In Situ and Operando Tools and Methods for Characterization of Heterogeneous Catalysts

By

Priya Darshini Srinivasan

Submitted to the graduate degree program in Chemical and Petroleum Engineering and the Graduate Faculty of the University of Kansas School of Engineering in partial fulfillment of the requirements for the degree of Doctor of Philosophy.

Chairperson: Juan J. Bravo Suárez

Bala Subramaniam

Raghunath V. Chaudhari

Kevin Leonard

Michael Rubin

Date Defended: May 3, 2019

The dissertation committee for Priya Darshini Srinivasan certifies that this is the approved version of the following thesis:

In Situ and Operando Tools and Methods for Characterization of Heterogeneous Catalysts

Chairperson: Juan J. Bravo Suárez

Date Approved:

Abstract

In situ and operando spectroscopic characterization of catalysts is a powerful tool to explore the nature of species that may be involved in a heterogeneous catalytic cycle. In combination with methodologies to discriminate passive and active species, it can inform researchers on the presence of spectator and true reaction intermediate species. Towards this goal, this dissertation encompasses novel tools and methods to detect adsorbed species, differentiate spectator species from likely intermediate species, and their application via in situ and operando spectroscopic methods at relevant reaction conditions. First, we introduce a commercial in situ diffuse reflectance (DR) mirror optics cell that was modified for use at high temperatures with fiber optics and with reduced void volume. Such design enabled the development of a technique named oxygen gold plasmon sensing (O_2-GPS). The O_2-GPS combines in situ/operando DR UV-Vis spectroscopy and the determination of gold surface plasmon resonance (Au SPR) peak shifts as a sensor for adsorption of oxygen on gold catalysts via a simple correlation based on Drude's free electron model for gold nanoparticles. Such method allowed, for the first time, the observation via in situ/operando UV-Vis spectroscopy of O_2 adsorbed at the gold-support interface during O_2 flow and under CO oxidation reaction conditions. This work also describes a unique and powerful mathematical framework for the discrimination of spectator species and likely intermediate species. The method is called modulation excitation-phase sensitive detection-diffuse reflectance Fourier infrared spectroscopy (ME-PSD-DRIFTS) as it is applied to in situ/operando DRIFTS data that has been collected under periodic changes of surface species coverages and processed via phase sensitive detection methods that employ Fourier analysis. Such approach allowed the collection of infrared spectra with enhanced signal-to-noise ratio of reacting species while avoiding the presence of spectator species. Here, it is also shown how ME-PSD-DRIFTS can be used to study surface reacting and likely intermediate species on a Co-Al_2O_3 catalyst with enhanced properties for ethanol dehydration. Along with ex situ characterization and kinetics measurements, ME-PSD-DRIFTS demonstrated the enhanced hydrophobic surface properties of this catalyst which reduced inhibition by water typical of the parent γ-Al_2O_3. The technique also allowed the sensitive detection of adsorbed ethanol and ethoxide species as well as terminal and bridging hydroxyls bonded to octahedral and tetrahedral Al on Al_2O_3 (100) and (110) facets as likely reaction intermediates in the conversion of ethanol to diethyl ether and ethylene.

Acknowledgments

I owe my deepest gratitude to all who have contributed towards the successful completion of my research work and had inspired and guided during my doctoral study. First of all, I would like to express my sincere gratitude for the guidance and support from my advisor, Dr. Juan J. Bravo Suárez. His encouragement, inspiring thoughts, and keen eyes on details in the results have been leading us to long lasting and impactful discoveries during my research at the Center for Environmentally Beneficial Catalysis (CEBC). Without his resourceful and continuous untiring supervision, this work would not have been possible.

I would like to thank the professors in my Doctoral Committee, Dr. Bala Subramaniam, Dr. Ragunath V. Chaudhari, Dr. Kevin Leonard and Dr. Michael Rubin for their precious time and valuable suggestions at every step of my doctoral study. I would like to thank Dr. Prem Thapa for his help on catalyst characterization with TEM and SEM. I am grateful to our collaborators, Dr. Hongda Zhu from the Center for Environmentally Beneficial Catalysis, Dr. Konstantin Khivantsev and Dr, John Tengco from the University of South Carolina for their valuable help with catalyst preparation. I would also like to thank Ed Atchison for his help in programming and machining of the in situ reaction cells.

I have spent almost five years in my lab and it has been a wonderful place where I worked with so many good people. I would like to express my special thanks to my lab mates Thomas Ofosu, Apexa Shah, Maria Ramirez and Bhagyesha Patil. I would like to thank my friends, Dr. Jianfeng Wu, Dr. Kakasaheb Nandiwale and Dr. Andrew Danby for helping me in all possible ways they can and their cheerful attitude.

Nothing appropriate can describe the love and support of my parents and my sister, whose constant encouragement and admiration sets new horizons for me to reach, in every facet of my life. Needless to say, it was because of the efforts and constant source of strength of my family today I stand where I am. Their cooperation helped me in pursuing the PhD course and no words are enough to acknowledge them.

Finally, I would like to acknowledge National Science foundation (NSF), without its financial assistance this work could not have been completed.

Table of Contents

List of Figures

List of Tables

General Introduction

Heterogenous catalysis is presently an essential tool in developing sustainable, safer, and greener chemical processes. For such a purpose, the rational design and synthesis of catalysts and the understanding of their intrinsic catalytic activity constitute some of the main interests in industry and academia. However, to achieve such level of understanding of catalytic activity and catalyst active sites at its working state are crucial for the improvement and development of new catalysts and processes. Recent advances in in situ and operando characterization techniques and sensitive spectroscopic methods are of great importance for the study of not only active sites but also the intermediate species that take part in the catalytic reaction cycle under reaction conditions [1-3]. However, at steady state conditions, identification of these short-lived active species and discriminating them from the strong spectroscopic fingerprints of spectator species which are not involved in the reaction but usually present is higher concentration than active species is a challenging task, making it difficult to derive information on the reaction mechanism and kinetics. Thus, an alternative strategy for obtaining selective information on active species involves transient techniques such as TAP (Temporal Analysis of products) [4], SSITKA (Steady State Isotopic Transient Kinetic Analysis) [5-8] and MES (Modulation Excitation Spectroscopy) [9, 10]. These characterization techniques in combination with spectroscopic methods such as UV-Vis, Fourier transform infrared, Raman and X-ray absorption spectroscopies can be a powerful tool for investigating the dynamically changing surface species and 'real' intermediates with enhanced signal to noise ratio [11-13]. In TAP studies, stimulations are introduced into the system by perturbing one or two parameters such as pressure, temperature, concentration and flow rate with a sub millisecond time resolution to influence the species of interest. Originally created by John Gleaves in 1988 [14], the technique uses gas pulses injected at high vacuum to influence the species of interest and to analyze reaction intermediates.

A novel modulation excitation (ME) method was developed by Baurecht and Fringeli [9] in 2001 which in combination with in situ and operando spectroscopic techniques was found to be a great tool for selective detection of active species with high temporal and spatial resolution while avoiding spectator species [10, 15, 16]. Modulation excitation spectroscopy (MES) is characterized by repeated periodic perturbations in feed parameters such as concentration, pH, temperature and rapid spectroscopic sampling of the surface species until the active species

concentration reaches a quasi-steady-state at which it oscillates at the same frequency as that of stimulation [10]. MES when combined with phase sensitive detection (PSD) via Fourier analysis has found to be effective for enhancing the sensitivity of the analytical method [9, 10, 15, 16]. Fourier transform (FT) has been applied to the analysis of spectra obtained from MES experiments, due to its powerful function to extract spectral components responding to a modulation (AC term) from those that do not respond to the modulation such as noise and background (DC term, by analogy with electrical signals as this would correspond to the direct current component) thus yielding a spectra with only reactive species [9, 17, 18]. For practical problems requiring FT, the most common method of solution involves the discrete Fourier transform algorithm using complex numbers. The most popular algorithm is the fast Fourier transform (FFT) and which is widely available for most modern programming languages and benchmarked [19]. In that respect, the objective of this work lies in developing tools and in situ and operando characterization techniques that helps us understanding intermediate surface species and catalyst active sites of heterogeneous catalysts at its working state.

This thesis is divided into five main parts, each of which is a reprint of five papers as a result of this dissertation and that represent the essential outcome of the research activity of the author. Four of these papers have already been published in peer-reviewed journals including Catalysis Reviews-Science and Engineering, Applied Catalysis A: General, Reaction Chemistry and Engineering, and Journal of Catalysis. Another one was submitted and is being currently reviewed.

The first chapter focuses on reaction cells for in situ/operando studies of heterogeneous catalysts by ultraviolet-visible (UV-Vis) and IR spectroscopies but mainly focuses on diffuse reflectance techniques. Its objective is to present a general overview of the most common commercial and home-made reaction cell designs, their main design characteristics, and limitations to serve as a guide for their selection or the design of new in situ/operando cells. It will be shown that an ideal reaction cell for a wide range of catalytic in situ and operando reaction conditions does not exist (yet), that is, with low dead volume (i.e., for fast dynamic response to process feed changes, within tens of seconds), high temperatures (> 500 ^{o}C), high pressures (>30 bar), low cost, enough sample capacity (for operando studies, in the tens of mg), good spectroscopic response, resemblance to laboratory scale reactors, and reactor wall inertness, among others.

Chapter 2 discusses UV-Vis spectroscopy as a common, powerful, and affordable technique for the characterization of heterogeneous catalysts followed by an improved design of the

commercial ubiquitous Harrick Scientific high temperature reaction cell for use in diffuse reflectance (DR) UV-Vis spectroscopy. The commercial cell possessed significant dead volume which was reduced by a homemade compact dome and by volume reduction of cell void space with simple addition of glass beads, thereby, enabling faster transfer of gases. This modified design and the use of an optical fiber DR probe in conjunction with a miniature concave-CCD combination-based spectrometer allowed fast acquisition of in situ UV-Vis spectra in the order of seconds and at temperatures up to about 500 °C. The flow dynamics of the reaction setup were followed by an analysis of residence time distributions (RTD) via pulse experiments and thermal analysis. Additionally, an example is presented to show the utility of the modified cell to monitor quickly (every 2 s) and continuously UV-Vis spectra over an extended period of time during the in situ dynamic response of gold surface plasmon resonance (Au-SPR) peak shifts on a Au(1 wt%)/ZrO_2 catalyst as it is exposed to controlled and cycling oxidizing and reducing environments. The reported modifications of the reaction cell setup were shown to enable in situ spectroscopic characterization of heterogeneous catalysts by DR-UV-Vis spectroscopy.

Chapter 3 covers the development of a simple and easy to implement in situ UV-Vis spectroscopic method based on gold surface plasmon resonance (Au SPR) to characterize oxygen adsorption on gold nanoparticles supported on various metal oxides (e.g., SiO_2, Al_2O_3, ZrO_2, ZnO, and TiO_2) for understanding activity trends in oxidation with gold catalysts. Drude's free electron model for gold nanoparticles will be used to derive a simple correlation between Au SPR and charge transfer from/to gold (a surrogate for adsorbed oxygen) during oxygen adsorption and titration with hydrogen. On the studied catalysts, it will be shown that oxygen adsorption does not depend solely on support reducibility, but also on particle size. Additionally, experimental evidence will be provided for the preferential adsorption of oxygen on all supports at the gold-support perimeter. The O_2-GPS results showed, however, that only a fraction of the oxygen adsorbed at the perimeter sites is active for CO oxidation at the studied conditions. It will be shown that CO oxidation catalytic activity increased with the amount of adsorbed oxygen, but it was distinct for catalysts with reducible and nonreducible supports.

Chapter 4 describes the application of in situ/operando modulation excitation-phase sensitive detection-diffuse reflectance Fourier transform spectroscopy (ME-PSD-DRIFTS) for characterization of heterogeneous catalysts. ME was enabled by a low void-volume diffuse reflectance cell which allowed rapid gas exchange (gas residence times < 2 s) and by periodic feed

concentration changes to the reaction cell by a simple switching valve system that provided quasi-square shaped modulation. A general description of ME-PSD principle, mathematical framework, guidelines for planning, running, and interpreting results will be provided while focusing on ME-PSD-DRIFTS. Aspects such as modulation frequency and amplitude, modulation waveform, sampling rate, in situ cell residence time, and future opportunities for ME-PSD-DRIFTS will also discussed, uncovering the use of frequency magnitude plots for evaluation of spectra baseline shifts, signal response to modulation, response waveform type, noise, and signal decay/growth.

Chapter 5 then describes the study of ethanol dehydration on γ-Al_2O_3 and a Co-Al_2O_3 catalyst prepared by the strong electrostatic adsorption (SEA) method. Specific surface area characterization indicated that the Co-Al_2O_3 catalyst possessed higher surface area because of opening of γ-Al_2O_3 occluded pores. It was found that the Co-Al_2O_3 catalyst, under identical reaction conditions, could achieve similar ethanol conversion and ethylene selectivity to ethylene at lower temperatures than the original γ-Al_2O_3 support. Analysis of apparent activation energies contributions and water co-feeding tests indicated that the Co-Al_2O_3 was less inhibited by water and that water dimers and trimers were required to explain the experimental data. Furthermore, in situ modulation excitation-phase sensitive detection-diffuse reflectance infrared Fourier transform spectroscopy (ME-PSD-DRIFTS) during ethanol dehydration at reaction conditions confirmed the enhanced hydrophobic properties of the Co-Al_2O_3, making this catalyst less propense to water inhibition at low to moderate temperatures. The enhanced surface hydrophobicity in combination with new micropore acidity allowed more active sites for reaction not accessible in the parent γ-Al_2O_3. Additionally, ME-PSD-DRIFTS also allowed the detection of adsorbed ethanol and ethoxide species as well as terminal and bridging hydroxyls bonded to octahedral and tetrahedral Al on Al_2O_3 (100) and (110) facets as likely reaction intermediates in the conversion of ethanol to diethyl ether and ethylene.

The last part of this work contains appendices and quick references of several important aspects that are highlighted throughout this thesis. To facilitate reading, the cited papers and books were cross-referenced at the end of each chapter.

References

1. Meunier, F.C., The design and testing of kinetically-appropriate operando spectroscopic cells for investigating heterogeneous catalytic reactions. *Chemical Society Reviews* **2010,** *39* (12), 4602-4614.
2. Weckhuysen, B.M., Snapshots of a working catalyst: possibilities and limitations of in situ spectroscopy in the field of heterogeneous catalysis. *Chemical Communications* **2002,** (2), 97-110.
3. Weckhuysen, B.M., Determining the active site in a catalytic process: Operando spectroscopy is more than a buzzword. *Physical Chemistry Chemical Physics* **2003,** *5* (20), 4351-4360.
4. Pérez-Ramírez, J. and Kondratenko, E.V., Evolution, achievements, and perspectives of the TAP technique. *Catalysis Today* **2007,** *121* (3), 160-169.
5. Jacobs, G. and Davis, B.H., Low temperature water–gas shift: Applications of a modified SSITKA–DRIFTS method under conditions of H2 co-feeding over metal/ceria and related oxides. *Applied Catalysis A: General* **2007,** *333* (2), 192-201.
6. Meunier, F.C., The power of quantitative kinetic studies of adsorbate reactivity by operando FTIR spectroscopy carried out at chemical potential steady-state. *Catalysis Today* **2010,** *155* (3), 164-171.
7. Olympiou, G.G., Kalamaras, C.M., Zeinalipour-Yazdi, C.D., and Efstathiou, A.M., Mechanistic aspects of the water–gas shift reaction on alumina-supported noble metal catalysts: In situ DRIFTS and SSITKA-mass spectrometry studies. *Catalysis Today* **2007,** *127* (1), 304-318.
8. Schweicher, J., Bundhoo, A., Frennet, A., Kruse, N., Daly, H., and Meunier, F.C., DRIFTS/MS Studies during Chemical Transients and SSITKA of the CO/H2 Reaction over Co-MgO Catalysts. *The Journal of Physical Chemistry C* **2010,** *114* (5), 2248-2255.
9. Baurecht, D. and Fringeli, U.P., Quantitative modulated excitation Fourier transform infrared spectroscopy. *Review of Scientific Instruments* **2001,** *72* (10), 3782-3792.
10. Urakawa, A., Bürgi, T., and Baiker, A., Sensitivity enhancement and dynamic behavior analysis by modulation excitation spectroscopy: Principle and application in heterogeneous catalysis. *Chemical Engineering Science* **2008,** *63* (20), 4902-4909.
11. Weckhuysen, B.M., *In-situ Spectroscopy of Catalysts*. American Scientific Publishers: **2004**.
12. Haw, J.F., *In-situ Spectroscopy in Heterogeneous Catalysis*. Wiley-VCH: **2002**.

13. Bravo-Suárez, J.J., Kidder, M.K., Schwartz, V., Energy, A.C.S.D.o., and Fuels, *Novel Materials for Catalysis and Fuels Processing*. American Chemical Society: **2013**.
14. Gleaves, J.T., Ebner, J.R., and Kuechler, T.C., Temporal Analysis of Products (TAP)—A Unique Catalyst Evaluation System with Submillisecond Time Resolution. *Catalysis Reviews* **1988,** *30* (1), 49-116.
15. Müller, P. and Hermans, I., Applications of Modulation Excitation Spectroscopy in Heterogeneous Catalysis. *Industrial & Engineering Chemistry Research* **2017,** *56* (5), 1123-1136.
16. Maeda, N., Meemken, F., Hungerbühler, K., and Baiker, A., Spectroscopic Detection of Active Species on Catalytic Surfaces: Steady-State versus Transient Method. *CHIMIA International Journal for Chemistry* **2012,** *66* (9), 664-667.
17. Peters, T.M. and Williams, J.C., *The Fourier Transform in Biomedical Engineering*. Birkhäuser Boston: New York, NY, **1998;** p 1-199.
18. Marchionni, V., Ferri, D., Kröcher, O., and Wokaun, A., Increasing the Sensitivity to Short-Lived Species in a Modulated Excitation Experiment. *Analytical Chemistry* **2017,** *89* (11), 5801-5809.
19. FFTW. http://www.fftw.org/ (accessed Dec. 16, 2018).

Chapter 1. Characteristics of In situ and Operando Spectroscopic Diffuse Reflectance Reaction Cells for Heterogeneous Catalysis

1.1. Introduction

Heterogeneous catalysis research is mainly focused on three general aspects: catalyst synthesis, characterization, and reactivity as supported by theoretical studies. These areas are interdependent and constitute the basis for the development of stable and selective catalysts for target reactions. With the advent of powerful computers and development of fundamental theories of catalysis, now we see a great synergy of these established experimental areas with advanced theoretical tools (e.g., molecular modelling, DFT, micro kinetics, etc) to further develop our understanding of catalyzed reaction mechanisms. Understanding of reaction intermediate species and catalysts' active sites from birth (cradle) to death (grave) and during their mature life (active state) has been classically studied by ex-situ static (pre-natal, post-mortem) and, more recently, by in situ/operando dynamic (e.g., at working conditions), kinetic (e.g., SSITKA), spectroscopic (e.g., FTIR, UV-Vis), diffraction, imaging (e.g., STM), and combined/hyphenated techniques (e.g., FTIR−UV-Vis, EXAFS−FTIR) [1]. Here, operando is understood in the sense of simultaneous measurement of reaction rates and spectroscopic data in the same reaction cell and catalyst bed [2, 3], whereas in situ at reaction conditions implies spectroscopic data acquisition at reaction conditions typical of laboratory scale reactors, but without reaction rate measurements. Undoubtedly, the ability to peak at catalysts with in situ (at reaction conditions) and/or operando techniques will help us get critical relevant information for the development of mechanistic hypothesis and ultimately of new and improved catalysts. Despite the great advances in in situ/operando characterization of catalysts there are still many challenges including the development of new techniques and reactors for single molecule/site characterization, for multiphasic reaction systems, and with increased spatial and time resolution, as well as spectrokinetic methodologies for discrimination of true reaction intermediates. This latter area will require a balanced approach between the development of reactors that operate at kinetically relevant conditions and with adequate dynamic response and designs that allow good spectroscopic and sampling rates among others. The reason for this is the often opposite requirements for obtaining good quality kinetic data while being able to collect meaningful spectroscopic signals of

adsorbed and catalyst species in the same reaction cell. It has been only until the past decades that the issues of spectroscopic cell design for kinetic measurements have been raised, for example, for data from spectroscopic reactors to be meaningful the same level of rigor applied to laboratory scale reactors for kinetic measurements should be performed (e.g., differential vs integral reactor analysis, absence of mass and heat transfer artifacts, etc.) [3-7].

1.2. Ultraviolet-visible spectroscopy

UV-Vis spectroscopy concerns the study of the interaction of ultraviolet (UV) (far UV: 6.2-124 eV, 200-10 nm; near UV: 3.3-6.2 eV, 380-200 nm) and visible (1.6-3.3 eV, 780-380 nm) radiation with matter. This interaction of UV-Vis light photons with matter can result in absorption processes which increase the energy of their atoms, ions, and/or molecules usually sufficiently enough to cause electronic transitions between different energy levels, orbitals, or bands [8, 9]. These electronic transitions can be of two types: metal-centered (MC) transitions such as d-d transitions in transition elements and charge transfer transitions such as ligand-to-metal (LMCT), metal-to-ligand (MLCT), and metal-to-metal (MMCT) charge transitions which manifest themselves in the corresponding material's spectrum [9]. Although the transitions should result in narrow absorbance bands, the resulting UV-Vis spectrum commonly has broadened bands because of the presence of superimposed vibrational and rotational phenomena, of many transitions with different energies, and contributions from solvent or solid support/matrix [8]. However, from the UV-Vis spectrum it is still possible to obtain solid catalysts chemical information, for example, on: 1) oxidation states, coordination of metals, and metal oxides; 2) band gaps of semiconductors; and 3) particle size and shape of metal nanoparticles (e.g., Au, Ag) from surface plasmon resonance [10].

For characterization, the technique requires UV-Vis spectrometers which are usually composed of the following components: 1) radiation (e.g., light) source; 2) wavelength selector (e.g., monochromator); 3) sample container; and 4) radiation detector (e.g., photomultiplier), as shown schematically in **Figure 1.1** [8, 11, 12].

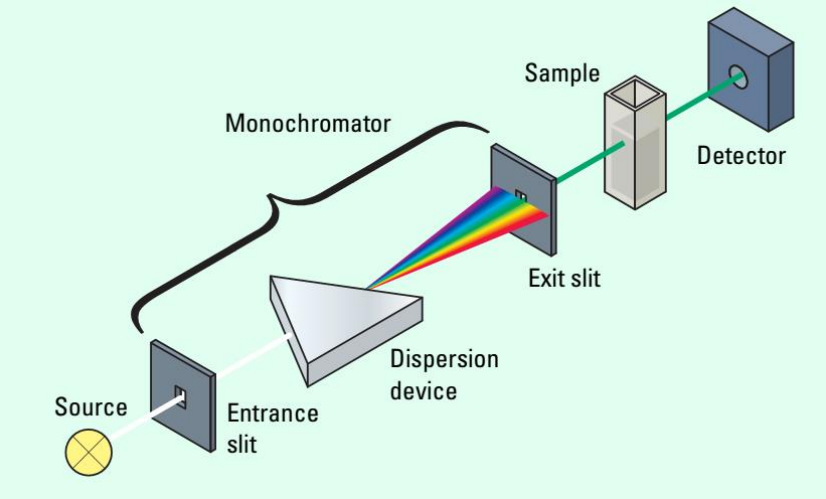

Figure 1.1. Schematics of a conventional single-beam UV-Vis spectrometer. Reprinted with permission from Agilent Technologies.

The design in **Figure 1.1** is that typically found in single-beam benchtop instruments (e.g., Agilent, Perkin-Elmer, etc.), whereas the one in **Figure 1.2** corresponds to that of miniature spectrometers (e.g., Ocean Optics, StellarNet, Avantes, etc.).

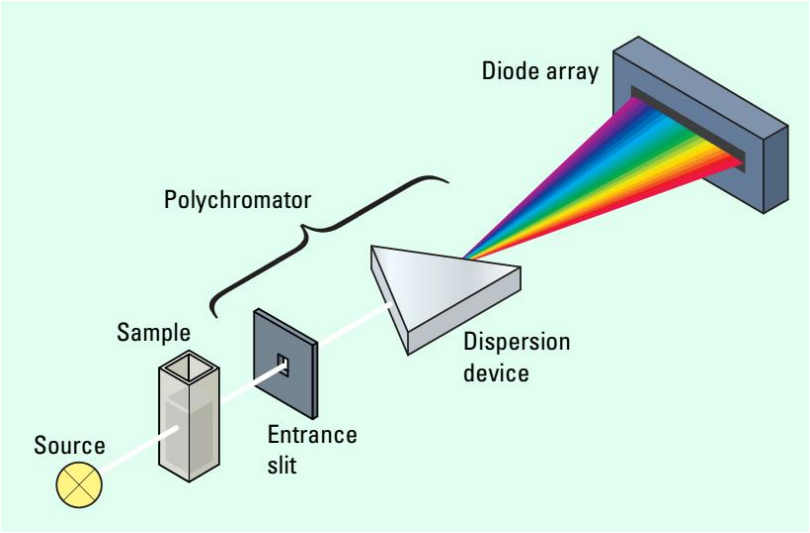

Figure 1.2. Schematics of a multichannel detector UV-Vis spectrometer. Reprinted with permission from Agilent Technologies.

In benchtop instruments the light wavelength selector is typically a monochromator (e.g., entrance slit, dispersion device such as a diffraction grating, and exit slit combination) to isolate a desired wavelength which is detected (e.g., commonly by a photomultiplier tube, PMT) and measured. In the design of **Figure 1.2**, the wavelength selector is a polychromator that disperses

the wavelengths so that they are all detected simultaneously in a multichannel detector (e.g., diode array detector, DAD; charge-coupled device, CCD, detector) [8, 11, 12].

Figure 1.3 shows the schematics of a typical commercial benchtop UV-Vis spectrometer. Several commercial ex situ and in situ accessories and reaction cells are available that can be fitted to such type of design. Some of these accessories and reactors will be described in later sections.

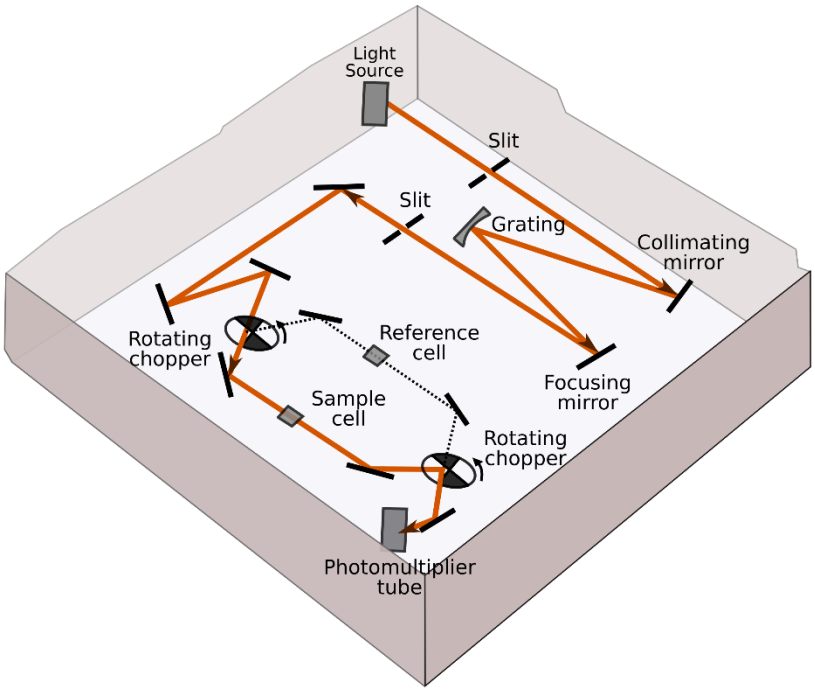

Figure 1.3. Schematics of a commercial benchtop UV-Vis spectrometer. Adapted from Reference [11].

Figure 1.4 and **1.5** show the schematics and details of a commercial miniature optical fiber UV-Vis spectrometer. This design is convenient for its portability, lower cost, modularity, and faster acquisition times over the whole UV-Vis range since all wavelengths are detected simultaneously, unlike that of most benchtop spectrometers that scan wavelengths in a stepwise mode, therefore, requiring much larger times.

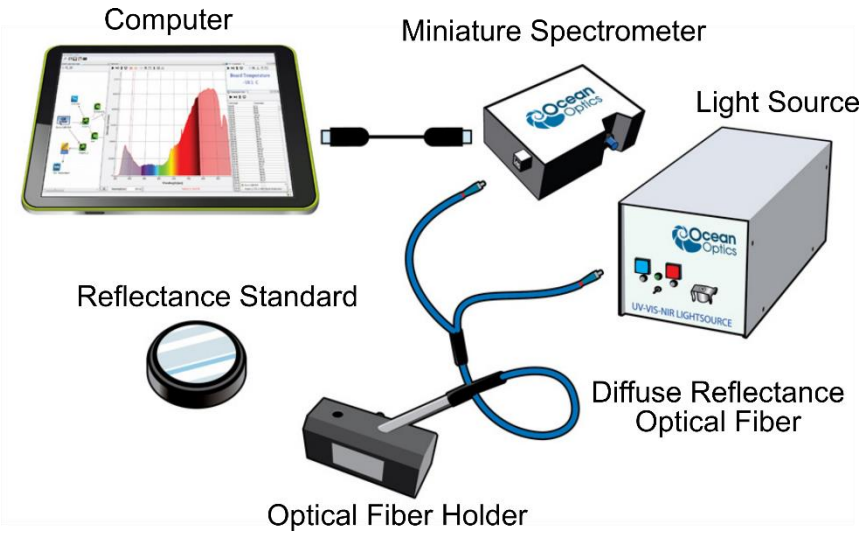

Figure 1.4. Schematics of a commercial miniature optical fiber UV-Vis spectrometer. Reprinted with permission from Ocean Optics.

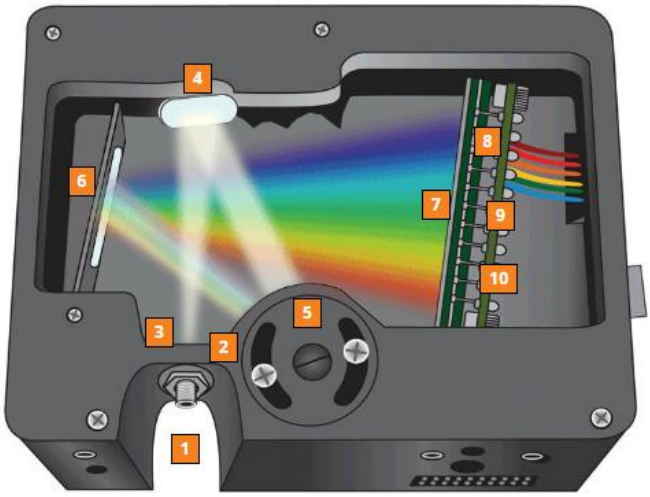

Figure 1.5. Schematics of a commercial miniature spectrometer (USB4000, Ocean Optics, shown in **Figure 1.4**). 1.Optical fiber connector; 2. Entrance slit; 3. Filter; 4. Collimating mirror; 5. Grating; 6. Focusing mirror; 7. Collection lens; 8. Detector; 9. Filter; and 10. Detector window. Reprinted with permission from Ocean Optics.

When a beam of light comes into contact with a solid the beam can undergo various phenomena including absorption, transmission, reflection, refraction, scattering, diffusion, and polarization (**Figure 1.6**) whose fate will depend on the angle of the incident light and the material being probed. To measure the different contributions of light absorbed/transmitted or reflected different UV-Vis-NIR equipment and techniques can be used. For characterization of catalytic

solid materials, these can be described broadly as transmission and reflectance (i.e., specular, internal, and diffuse) spectroscopic techniques.

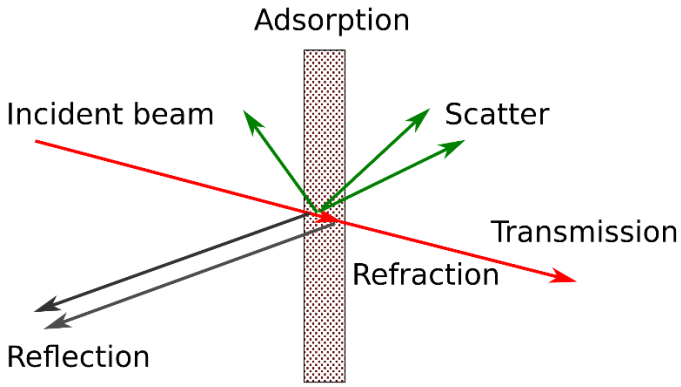

Figure 1.6. Interaction of light with a solid material.

UV-Vis spectra have been typically collected by different optical configurations that mainly collect transmitted or reflected light from the sample. Classically, the characterization of gas, liquid, and thin film samples by UV-Vis spectroscopy has been performed in transmission mode (**Figure 1.1**and **1.2**). The sample containers (e.g., cells or cuvettes) are made of materials that are transparent in the UV-Vis range. For this purpose, the material most commonly used is quartz or fused silica that can be employed in the UV range and in the visible region up to about 3000 nm (0.41 eV). For the characterization of solid catalyst powders, however, UV-Vis characterization in transmission mode is more problematic because of the need to prepare transparent thin wafers of high transmittance and the undesired effects of scattering (i.e., reflection, refraction, and diffraction) [13]. Albeit troublesome, there are literature examples demonstrating the successful UV-Vis characterization of solids in transmission mode such as in the case of zeolite materials [14]. For measuring UV-Vis spectra of powder catalysts in reflectance mode the two most common techniques are internal reflection [15, 16] and diffuse reflectance spectroscopies [9, 10, 13, 17, 18]. These latter techniques require the use of different theory for data analysis and interpretation as well as more sophisticated setups.

1.3. Infrared spectroscopy

Infrared spectroscopy concerns the study of structure and properties of molecules and materials from their vibrational transitions as a result of their interaction with infrared radiation [19]. Infrared (IR) radiation can be classified into three different regions [12]:

Near IR (NIR): 150-50 eV (12800-4000 cm^{-1}; 780-2500 nm)

Mid IR (MIR): 50-5 eV (4000-400 cm^{-1}; 2500-25000 nm)

Far IR (FIR): 5-0.1 eV (400-10 cm^{-1}; 25000-1000000 nm)

These IR regions corresponds to the energies of the vibrations and rotations of molecules [20]. In the in situ study of catalysts, these regions are used to study fundamental (MIR), combination (NIR), and lattice and heavy atom vibrations (FIR), as well as overtones (NIR) [11, 21]. The typical molecular vibrations that are studied include: (asymmetric and symmetric) stretching and (in-plane scissoring and rocking, out-of-plane twisting and wagging) bending vibrations. In molecules, adsorbed molecules, or solids, these vibrations can arise from the absorption (e.g., IR spectroscopy) or scattering of photons (e.g., Raman spectroscopy), electrons (e.g., electron energy loss spectroscopy, EELS), or neutrons (e.g., inelastic neutron scattering, INS) [22]. Infrared absorption is characterized by direct resonance of a photon frequency and the frequency of a given normal model of vibration [19]. In a typical IR spectra, many bands derived from molecules and solids under study typically arise and their number is a function of the number of elements involved (e.g., in linear molecules with N atoms, 3N-5 is the number of vibrational modes) [23]. In practice, the actual number of fundamental vibrations is much lower because of degeneration of some vibrational modes or limitations imposed by selection rules since IR photon absorption only occurs if a dipole moment change occurs [11, 22].

In heterogeneous catalysis, we are most commonly concerned with MIR spectroscopy because it is in this region where resonances with molecular vibrational frequencies occur [23]. This is in part the reason why mid IR range (4000-670 cm^{-1}) spectrometers are the most widely used to probe interactions of molecules, catalysts, and probe molecules on catalyst surfaces [24]. Additionally, since the 1980s the most common type of instrument for IR absorption in the MIR range are Fourier transform (FTIR) spectrometers because of its speed (all wavelengths are measured simultaneously), signal to noise advantage (same S/N as a dispersive IR spectrometer), precision and reliability [11, 21]. Dispersive instruments are still found for use in the NIR range

and are usually combined in UV-Vis-NIR spectrometers. These latter instruments will not be described here, but have been discussed in previous publications [11, 25].

An FTIR spectrometer is mainly designed such that interference between two beams yields an interferogram which is a signal produced from the change of path length between two beams. A Fourier transformation is then used to convert this distance into frequency (from which wavenumber is calculated) domains [25]. To obtain interferograms, a device called interferometer is employed. The most widely used interferometer in FTIR spectroscopy is the Michelson interferometer shown in **Figure 1.7**. As shown in the figure, it consists of: 1) a collimating mirror that collects and makes the radiation rays from the source parallel; 2) two perpendicular plane mirrors, the bottom one in the figure which is fixed and the right one which can move left and right in a direction perpendicular to the plane; 3) a beam splitter that bisects the planes of the two mirrors and which transmits and reflects some of the incident light. The light transmitted to the fixed mirror reflects back and recombines in the beam splitter with the light reflected to and from the moving mirror, which then leaves the interferometer; 4) light out of the interferometer that interacts with the sample; 4) and reaches the detector [25, 26]. The two most common types of detectors are the DTGS (deuterated triglycine sulfate) and the MCT (mercury cadmium telluride). The DTGS detector is convenient as it is inexpensive, and it does not require special treatments; however, it is a relatively slow and noisy detector, but useful for routine analysis. In in situ characterization of adsorbed species on catalysts, the MCT detector is more commonly used as it is orders of magnitude more sensitive, although it is more expensive and requires cooling with liquid nitrogen to reduce the noise [26]. **Figure 1.8** shows in more detail these internal parts in a commercial FTIR spectrometer.

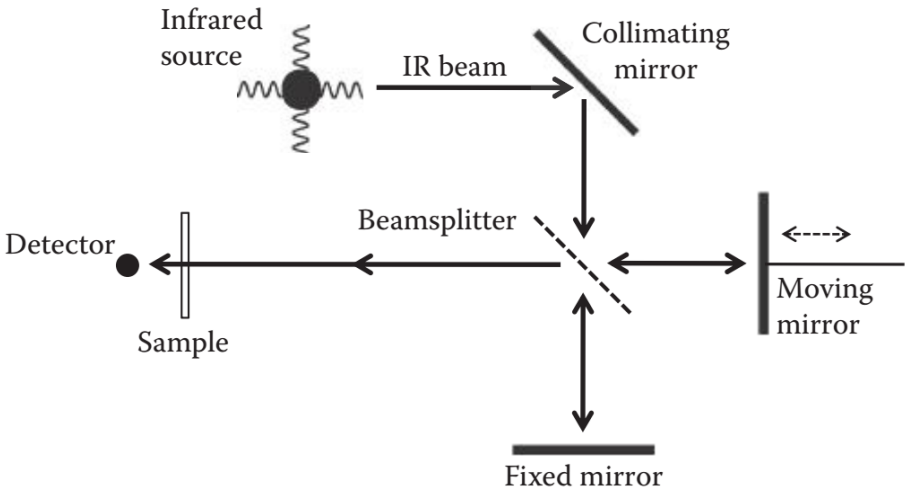

Figure 1.7. Schematic representation of a Michelson interferometer. With permission from Taylor & Francis, LLC [26].

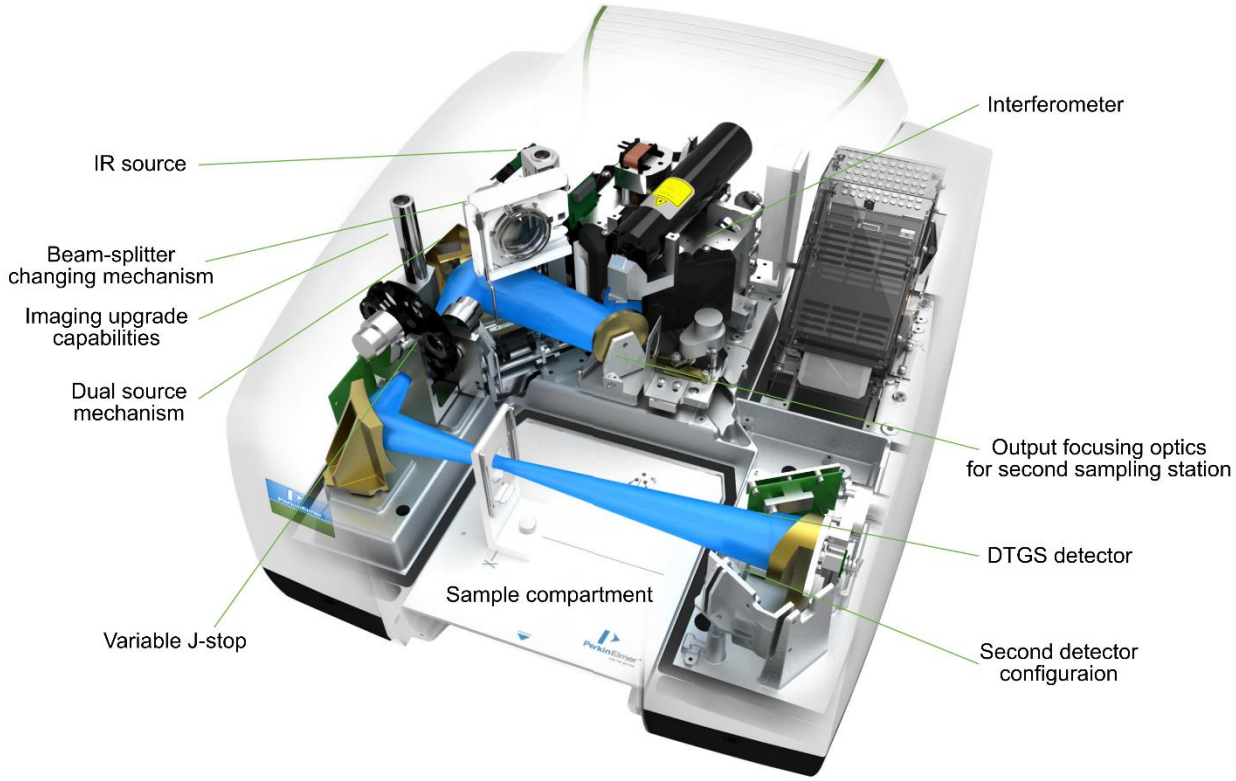

Figure 1.8. Photo of a PerkinElmer Frontier benchtop FTIR spectrometer. Courtesy of PerkinElmer, Inc.

IR spectroscopy can be operated in several forms including: transmission, diffuse reflection, emission, attenuated total reflection, reflection-absorption, Raman scattering, sum

frequency generation, and electron energy loss which are summarized in **Figure 1.9**. All these forms find applications in catalysis, but the most commonly applied for in situ studies in heterogenous catalysis are based on transmission and reflection techniques similarly to UV-Vis spectroscopy (see previous section). The reasons for the use of only transmission and reflection techniques appear to be related with the design of the reaction cells (e.g., flexibility of spectra acquisition at reaction conditions, reaction cell resemblance to laboratory reactors) than with the techniques [27].

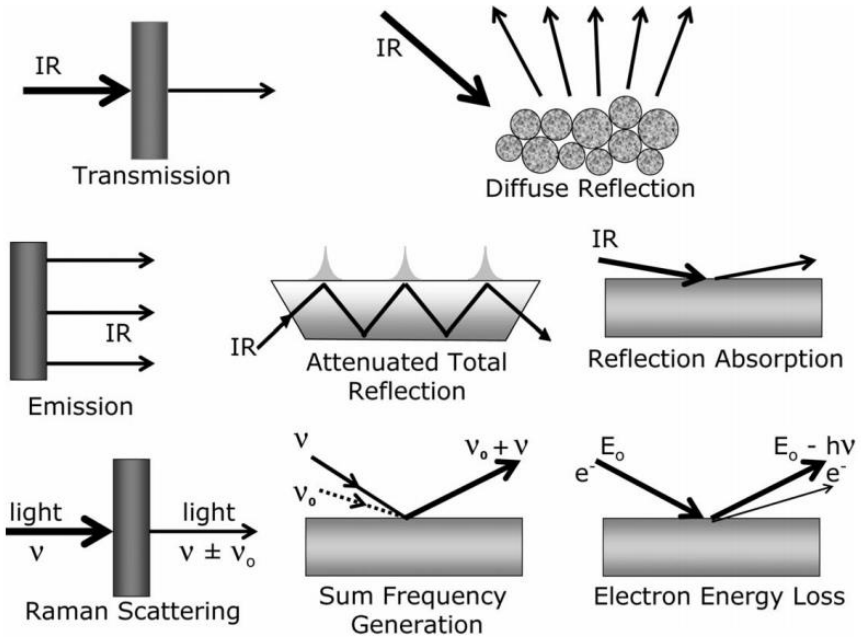

Figure 1.9. Different forms in which vibrational spectroscopy can be performed. With permission from Wiley [22].

Since our interest is in in situ and operando studies in heterogeneous catalysis, here we will describe jointly reaction cells for UV-Vis and IR spectroscopies because of the similarity in techniques and reactors for characterization of solid materials [28-31]. Most windows in current in situ IR reactors can be replaced for quartz windows that are transparent to UV-Vis light so the combination in single sections of both UV-Vis and IR reactors is justified despite the different shape of IR (i.e., circular) vs UV-Vis (e.g., slit-shaped) beams in benchtop spectrometers [13]. Therefore, three different modes of measuring in situ UV-Vis and IR of solids (and their variations) at reaction conditions can be identified: 1) Transmission; 2) Internal reflection; and 3) Diffuse reflectance. The latter technique will also be further divided by the type of optical accessories employed such as integrating spheres, mirror optics, and fiber optics.

1.4. Diffuse reflectance reaction cells

The UV-Vis and IR spectroscopic analysis of solids by diffuse reflectance mode is perhaps today the most common technique used today. Diffuse reflectance has many advantages over transmission since: 1) it can be applied to most solid materials possessing high absorption and scattering properties; 2) it does not require significant sample preparation; 3) there are many commercial accessories for sample analysis; 4) sample can be recycled for other uses; and 5) it is appropriate for in situ and operando characterization of catalysts as sample holders resemble the operation of fixed bed reactors, which in turn requires that spectroscopic reaction cells be operated in differential conditions for kinetic studies [3].

As seen from **Figure 1.6**, the interaction of light with a solid sample is a complex process involving absorption and scattering phenomena. In diffuse reflectance spectroscopy, light is partially absorbed and reflected from a solid in all directions without preference for any direction and whose distribution is the result of multiple scattering (**Figure 1.10**). The scattered reflected light arising from the catalyst sample is collected and analyzed as reflectance which can be related to absorption coefficients (similar to transmission spectroscopy) [10]. One such approaches is the Schuster-Kubelka-Munk theory which relates the absolute reflectance (R_∞, at infinite sample thickness) to the ratio of absorption (K) and scattering (S) coefficients via the Schuster-Kubelka-Munk or Kubelka-Munk function:

$$F(R_\infty) = \left[\frac{(1-R_\infty)^2}{2R_\infty}\right] = \frac{K}{S} = \frac{kC}{S}$$

R_∞ is taken approximately as the ratio of the experimentally measured light intensity reflected from the powdered sample to the light intensity reflected from a white reference standard that diffusely reflect light to 100% (e.g., $BaSO_4$, MgO, SiO_2, Spectralon®) [10]. If the absorption coefficient K is small and S does not vary with the absorber concentration and is constant over the studied wavelength range, then the Kubelka-Munk function is proportional to the absorption center concentration, and k is the molar absorption coefficient [10, 17].

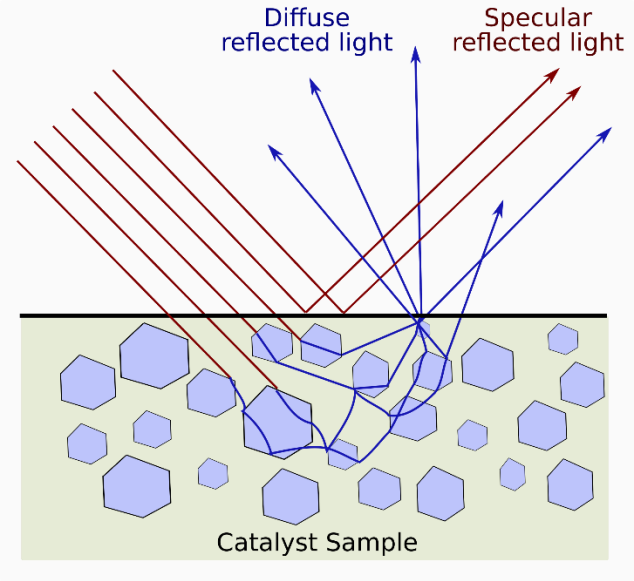

Figure 1.10. Schematic representation of diffuse reflection.

1.4.1. Experimental considerations for validity of F(R_∞) Function

Before expanding on some of the features of the most commonly available diffuse reflectance reaction cells, it is worth reviewing the limitations of the technique and the conditions at which the K-M expression is valid for quantification of adsorbed or bulk species.

1) Diffuse monochromatic incident radiation. This condition is met with samples that scatter strongly and absorb weakly by rendering diffuse the incident parallel light (common in many equipment with incident beams at 60º) [32]
2) An infinite layer thickness and infinite extent. Both conditions are generally easily met with thickness beyond 2-3 mm, conditions at which a further thickness increase causes no change in the K-M function F(R_∞) [32, 33].
3) No scattered photons totally internally reflected back in the sample. This can happen when a cover glass is used, or a sample has a continuous outer film both conditions leading to stronger absorption than expected. In diffuse reflectance samples do not need to be compacted, however, an increase in compaction of white samples will lead to similar effects of increase of absorption due to an increasingly smooth front surface [32].
4) Uniform distribution of absorbing centers. This is usually not an issue as most catalysts are usually highly dispersed.

5) Low concentration of absorbing centers or weakly absorbing sample. Weak absorption corresponds to roughly $F(R_\infty)<1$. This condition is important in limiting specular reflection and ensuring that when non diffuse radiation is used (condition 1) that scattering predominates over absorption. This can be accomplished by: a) collecting diffusely reflected light over a limited solid angle; b) employing finely ground powders; c) using polarized light and placing sample between cross polarizers; d) diluting the sample [10, 17, 32].
6) Isotropic light scattering. This condition is met when the medium consists of densely packed particles containing low amount of absorption centers [17].
7) Absence of fluorescence. For samples that fluoresce, this condition can be achieved instrumentally. For example, for instruments with integrating spheres, the sample can be irradiated with a non-diffuse dispersed beam with the source prior to the monochromator and a detector at the sphere or with a diffuse non disperse beam using a source directly attached to the sphere and the detector prior to the monochromator [32].
8) Scattering coefficient S is independent of wavelength (or photon energy). In general, finely ground particles (< 50 μm) are desirable for diffuse reflectance measurements [34], but not too fine such that particles are close in size to the wavelength, a condition is usually met with mean particle sizes > 2-3 μm [10, 32]. Therefore, fine powder catalyst samples in the ~5-50 μm range are recommended.

At the conditions stated above, the K-M function is expected to be proportional to the absorption coefficient and concentration ($0<F(R_\infty)<0.13$) [35]. However, in the analysis of adsorbate concentrations, it has been recently argued that at $F(R_\infty)<0.13$ the apparent absorbance $\log(1/R_\infty)$ seems more appropriate, whereas the Kubelka-Munk function appears to be proportional to concentration for strong signal absorptions ($F(R')>0.5$) [36]. Regardless of the range of proportionality of $F(R_\infty)$ with concentration or molar absorption coefficient, for proper development of correlations between spectroscopic and catalytic data from in situ and operando reactor experiments, this proportional relationship needs to be verified experimentally for each individual system [10].

Having covered the practical experimental conditions for application of diffuse reflectance to UV-Vis-NIR and IR, in what follows we will detail the corresponding in situ reaction cells to

collect spectral and kinetic data. Here, we have classified these reactors based on the accessories employed for collection of the diffused reflected light, namely, a) integrating spheres; b) optical accessories, and c) optical fibers.

1.4.2. Integrating spheres

Integrating spheres have been used commonly for ex situ diffuse reflectance analysis of solids. In diffuse reflectance mode, the sample is placed in the integrating sphere so that its surface matches that of the sphere (**Figure 1.11**). Light entering the sphere and hitting the sample is diffusely reflected in all directions and can bounce multiple times inside the sphere before reaching the detector. Baffles are sometimes part of the sphere to prevent direct specular reflections from the sample. Over 95% of the scattered light is collected in the integrating sphere, for such a purpose the inner surface of the sphere is coated with a high reflectance white material such as MgO, $BaSO_4$, or polymers (e.g., Spectralon®). Gold coatings may be used at wavelengths above 800 nm. Integrating spheres operate with high light yield, accuracy, and precision [10, 13, 17]. Despite these advantages, very few examples can be found in the literature of in situ or operando reactors combined with integrating spheres [37-43].

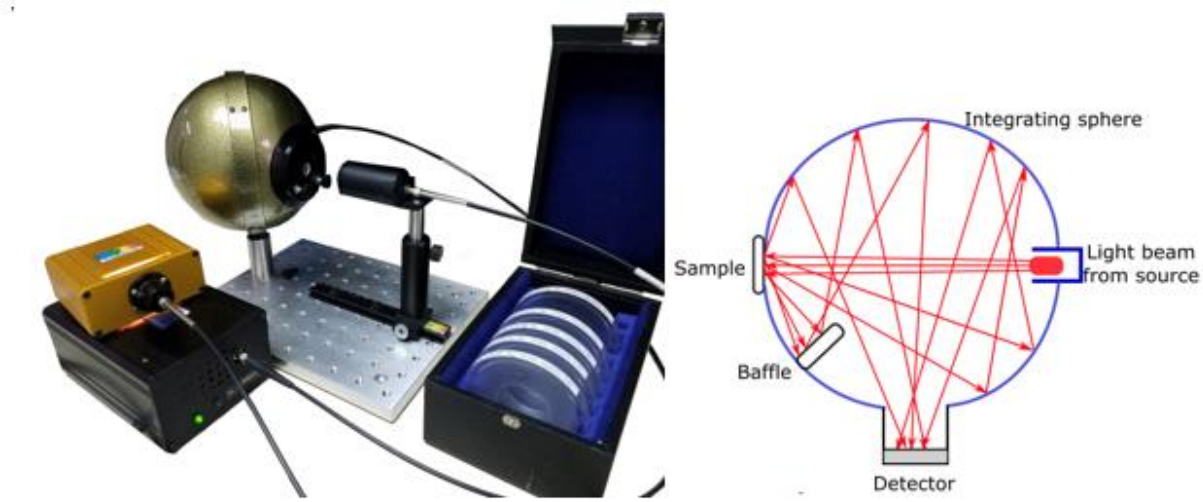

Figure 1.11 Spectrometer with integrating sphere system. A) StellarNet Inc's spectrometer, light source, optical fiber cables, and integrating sphere; B) Schematic representation of an integrating sphere, light beam, sample, baffle, and detector. Reprinted with permission from StellarNet Inc.

1.4.3. Mirror optics

In addition to integrating spheres, diffuse reflectance measurements can be carried out with mirror optics. Several commercially available optical benches exist. They can be used for spectra measurements from the UV to visible to MIR spectra range. As will be shown in a few examples next, most commercial mirror optics are composed of a total of four to six mirrors, 3-4 flat and 1-2 curved, but home-made designs can have a smaller number of mirrors [44, 45]. The purpose of the mirror optics is to direct the light beam from the source to the sample and to maximize the collection of diffuse reflected light while minimizing specular contributions and to direct it to the detector. One of the characteristics of the mirror optics is that they need to be aligned to maximize diffused reflected light, but in commercial designs this could be a relatively straight forward procedure. The mirror optics are advantageous as they provide a relatively good light throughput, with a maximum that can vary between 30-45% in the UV-Vis range and could be easily integrated with in situ/operando commercial or homemade reaction cell designs [10, 13].

1.4.3.1. Harrick scientific praying mantis UV-Vis and IR diffuse reflectance accessory and high temperature and pressure reaction cell

Harrick Scientific's combination of Praying Mantis diffuse reflectance accessory and high temperature and pressure reaction cell is perhaps one of the most popular reaction setup systems not only for catalyst characterization with UV-Vis, but also infrared and Raman spectroscopy [5]. The Praying Mantis accessory incorporates two 6:1, 90º off-axis ellipsoid mirrors (M3 and M4 in **Figure 1.12**). The near focal points of mirrors M3 and M4 coincide and arrange so that only diffusely reflected light is collected, which is achieved by placing the ellipsoid mirrors 60º away from the direction of the specularly reflected radiation. With this arrangement, the size of the beam spot on the sample is less than 2 mm in diameter, which is ideal for small samples and represents an advantage over traditional integrating spheres that usually require larger sampling areas. Additionally, samples can be placed horizontally, the reflective optics allow measurements over an extended wavelength range from UV to mid IR, and can be used with environmental cells for experiments in controlled gases, pressure, and temperature [46].

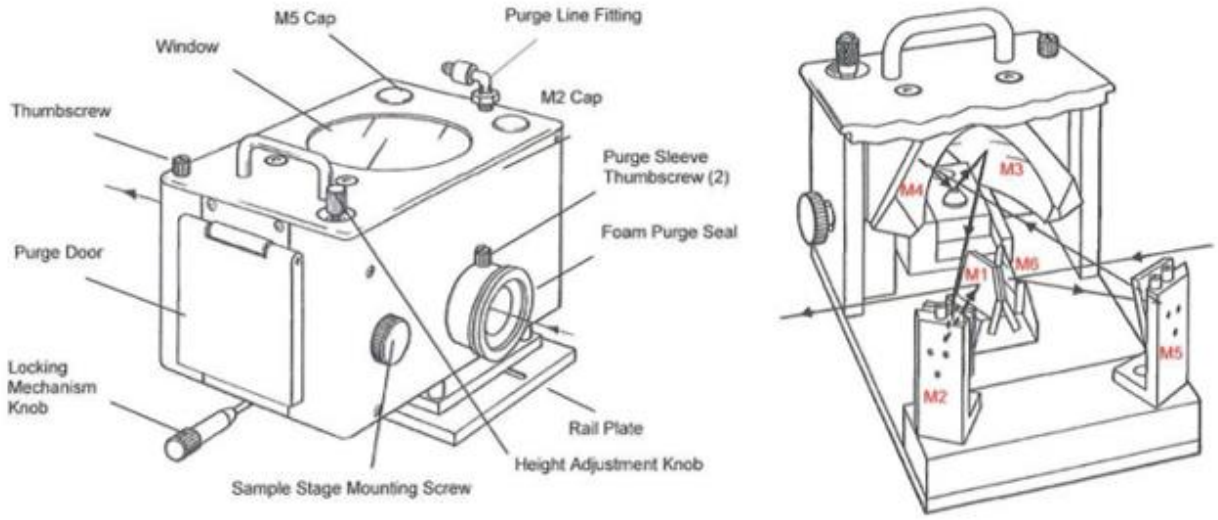

Figure 1.12 Harrick Scientific Praying Mantis UV-Vis and IR diffuse reflectance accessory. A) Front view; B) Interior view and optical diagram of beam path from light source to reflecting mirrors M6, M5, and M4 onto the solid sample and diffuse reflected light to M3, M2, and M1 to detector. M6, M5, M2, and M1 are flat mirrors; M4 and M3 are curved mirrors. Reprinted with permission from Harrick Scientific.

One of Harrick Scientific's environmental cells used in combination with the diffuse reflectance Praying Mantis accessory is presented in **Figure 1.13**. The cell is made of 316 stainless steel and features a water-cooled bottom block housing the sample cell, two side inlet/outlet and a single outlet port (1/4 inch VCO fittings) for evacuating (high vacuum), or pressurizing (up to 3.44 MPa with a high pressure dome) and flowing gas through the sample. Under flowing conditions, the gas feed enters via the side inlet port(s) and goes in a down flow pattern through the sample exiting the reaction cell via the central port. A thermocouple (K type) and cartridge heater (1 inch x 0.25 inch, 100W, 24V) is also present in the cell block to provide heat for a maximum high temperature operation up to 910 ºC under vacuum (and much lower temperatures at higher pressures and under gas flowing conditions usually above 350 ºC mainly depending on gas flow rates and thermal conductivities [47]. The reaction cell is quite flexible for spectroscopic studies as it can be used for UV-Vis, IR, or Raman operation provided that appropriate windows are used. **Figure 1.13** shows a high temperature (HVC) reaction chamber equipped with a three-windows dome. In a typical configuration, two of the windows are for radiation to enter and exit the reaction cell, and the third one (an observation window, usually the front one) is for viewing, illuminating, or

irradiating the sample. Depending on the material of the windows, the cell can be operated in the UV-Vis (all windows made of UV quartz) or IR range (observation window made of UV quartz and the two other made of an IR transparent material such as ZnSe, KBr, etc.) [46].

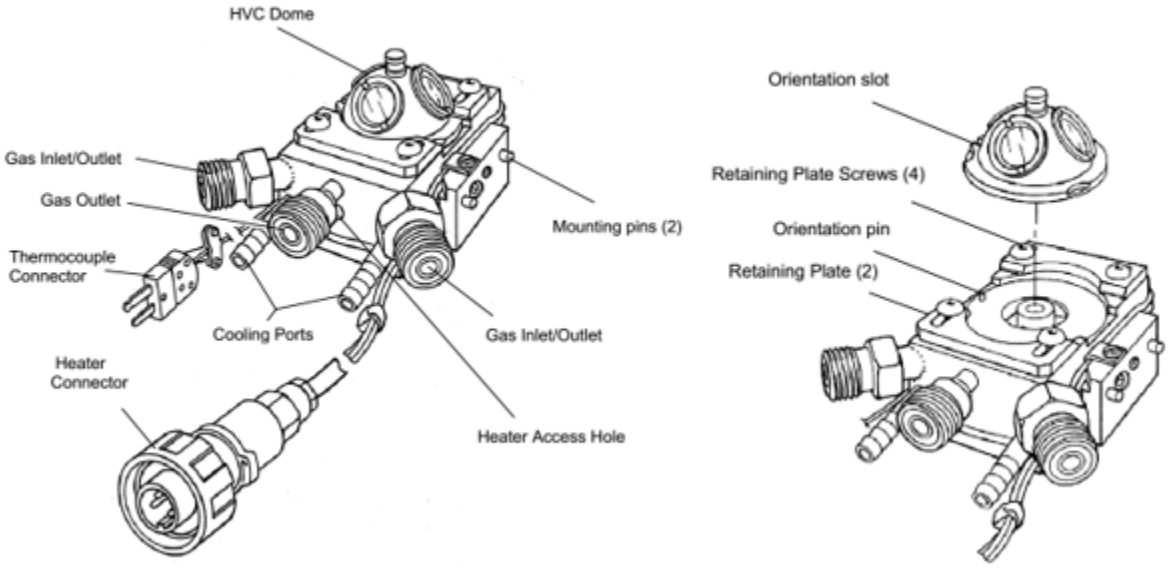

Figure 1.13. Harrick Scientific high temperature reaction chamber HVC for use in UV-Vis and IR diffuse reflectance measurements with the Praying Mantis accessory. Reprinted with permission from Harrick Scientific.

Figure 1.14 shows a schematic representation of the combined Praying Mantis accessory and high temperature and pressure environmental reaction cell. The whole set up can be incorporated in most commercial UV-Vis and IR spectrometers with appropriate mounting plates. Several issues, however, have been reported for the HVC design, which has resulted in custom modifications by several groups. For example, Venter and Vannice reported significant temperature differences between the sample and the reaction cell wall which led to modifications to the HVC-DRP design for measurement of strongly absorbing samples (e.g., carbon supported catalysts). Such modifications aimed at minimizing radiative, conductive, and convective heat losses included a modified sample cup or post, reduced size of outlet gas port, addition of a thermocouple for direct measurement of sample temperature, and changes to the thickness of the sample distributor plates (stainless steel mesh holding the sample in place) [47]. Additional issues have been reported such as gas bypassing, sample temperature homogeneity, large dead volume, and wall effects.

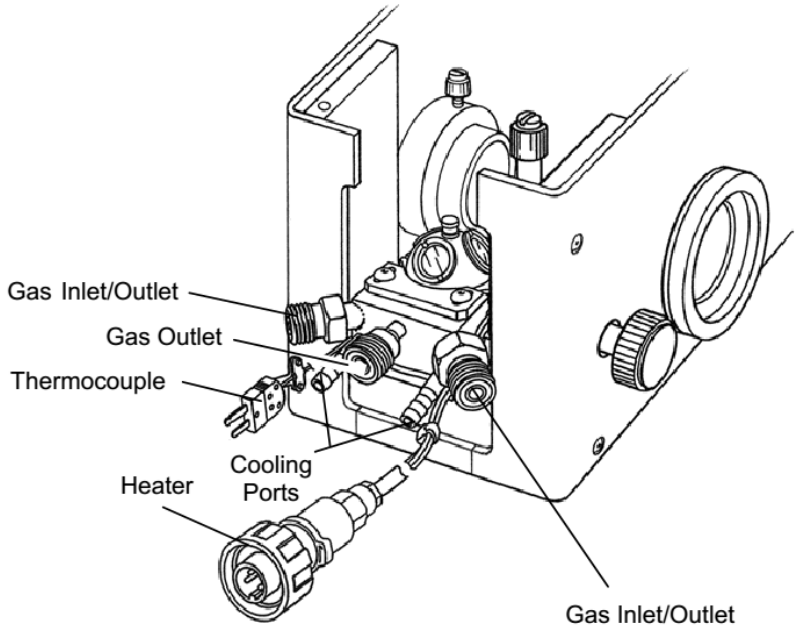

Figure 1.14 Harrick Scientific Praying Mantis and high temperature reaction chamber. Reprinted with permission from Harrick Scientific.

1.4.4. Fiber optics

Unlike integrating spheres and mirror optics, fiber optics have the flexibility to redirect the light beam from the source to the detector eliminating restrictions of space. For diffuse reflectance measurements, fiber optics probes exist that contain bundles of illuminating (taking the beam from the source to the sample) and reading (taking the reflected light from the sample to the detector) fibers that can be placed in the near proximity of the catalyst sample. This in combination with the availability of high temperature and pressure optical probes significantly enhances and widens application of these probes for in situ/operando measurements for heterogeneous catalysis. Another advantage of optical fibers in combination with rapid scan spectrometers is the increased time resolution (in the milliseconds range) allowing time-resolved studies, but at the expense of spectral resolution which is inferior to that of most scanning spectrometers [13, 48, 49].

1.4.4.1. Weckhuysen and co-workers' optical fiber UV-Vis diffuse reflectance reaction setup (2001-2003) [50-52]

Figure 1.15 shows a schematic representation of Weckhuysen and co-workers' reaction setup for in situ and operando UV-Vis spectroscopic measurements with optical fibers. In this setup, the

optical fiber probe is located inside and coaxially the center of a fixed-bed tubular reactor just slightly above (~1 mm) the catalyst particles to provide optimum signal to noise ratio [51, 53]. The optical setup consists of a miniature UV-Vis spectrometer, similar to those described above (**Figure 1.4** and **1.5**), equipped with a light source (Top Sensor Systems, DH-2000), detector (Ocean Optics, SD-2000), and optical fiber cable (Top Sensor Systems, FCB-UV400-ME) and high-temperature probe (Top Sensor Systems, FCB-UV400G-0.1-XHT). The probe sustained use in oxidation and reduction environments at 580 °C and 1 atm. Other high-temperature probes (Avantes, FCD-UV400-G-01CHT) have been used at temperatures as high as 800 °C [54]. One of the reported advantages of the optical fibers was the fast data collection of full UV-Vis scans in the 200-800 nm range within 1 second in comparison with more than 60 seconds with Harrick's Praying Mantis and a bench top scanning UV-Vis spectrometer (Varian Cary 5) [51, 53]. However, probe degradation after a few months at these high temperatures [51] and coke formation on the probe head [55] have been reported issues.

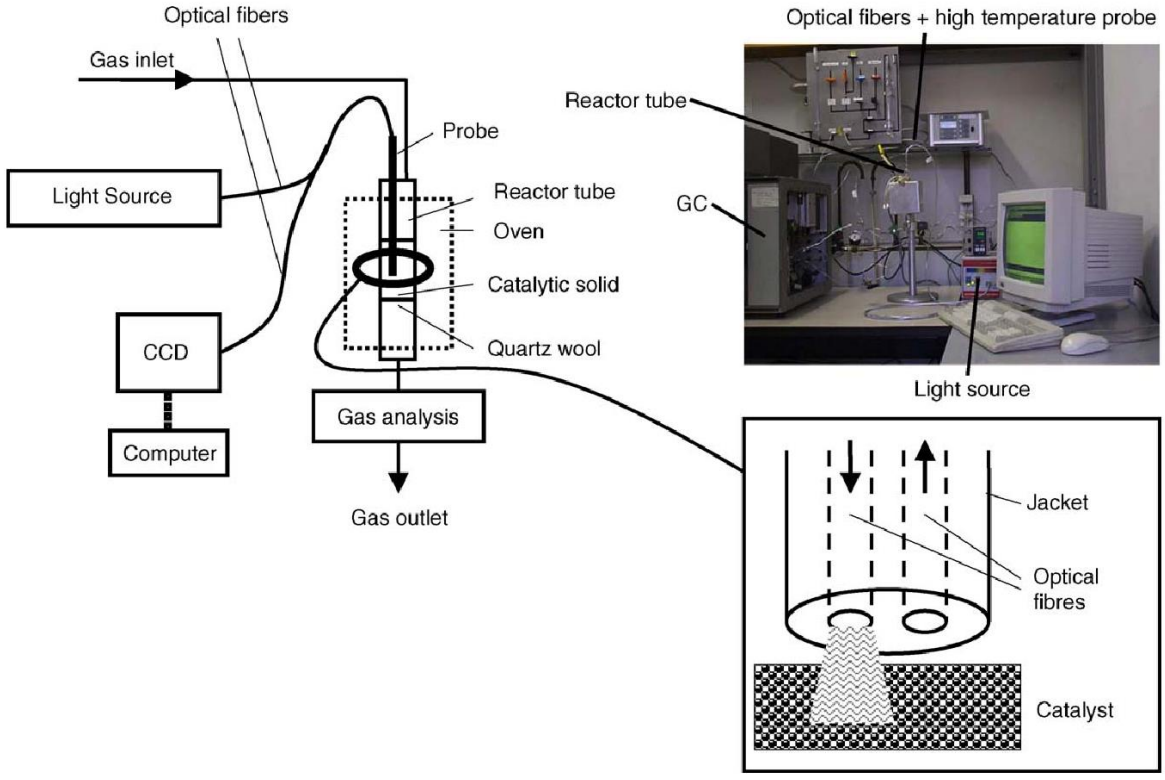

Figure 1.15 Weckhuysen and co-workers' optical fiber diffuse reflectance UV-Vis spectroscopy reaction setup (probe inside reactor and on top of catalyst approach). Reprinted with permission from reference [50]. Copyright © 2006 Elsevier.

1.4.4.2. Sobalík, Jíša, Jirglová, and Bernauer's optical fiber UV-Vis diffuse reflectance modification of ISRI's IR transmission cell (2007) [56]

Optical fiber diffuse reflectance probes for UV-Vis spectroscopy can also be incorporated in almost any transmission, ATR, or diffuse reflectance reaction cell designs. One such designs is that reported by Sobalík et al. that combined a transmission IR ISRI reactor with an UV-Vis optical fiber spectrometer (Avantes, AvaSpec-2048-TEC-FT-2) [56] for parallel IR and UV-Vis spectroscopic studies. The original ISRI cell design was modified such that the UV-Vis optical probe head could be placed just above the catalyst surface. An additional change included the addition of dual inlets to allow gas inlet flow to contact both sides of the pellet and a larger outlet gas tube. With such an arrangement and at high flow rates (> 100 cm^3/min) response times of the gas composition near the pellet was less than 1 s.

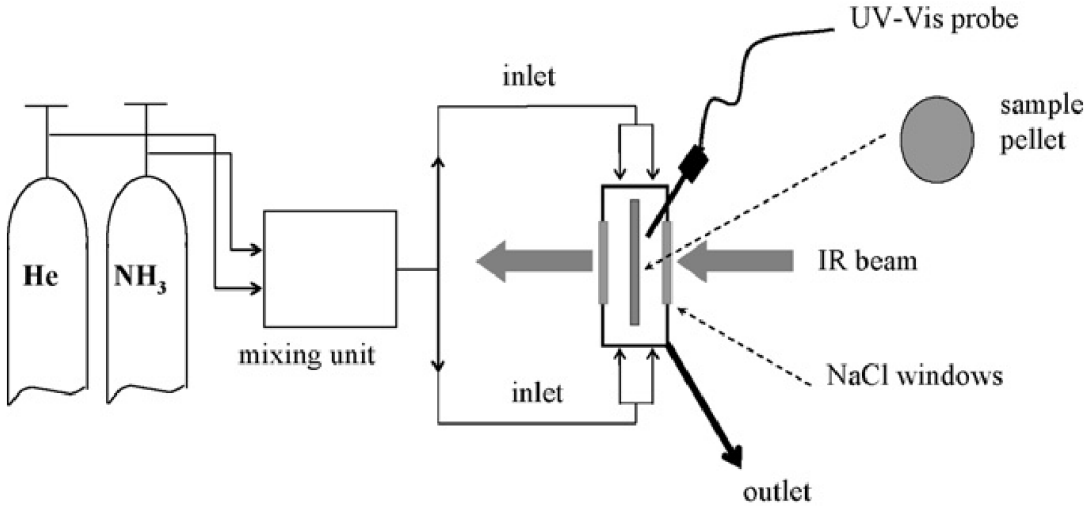

Figure 1.16 Sobalík, Jíša, Jirglová, and Bernauer's optical fiber diffuse reflectance UV-Vis spectroscopy combined with ISRI's IR transmission cell. Reprinted with permission from reference [56]. Copyright © 2007 Elsevier.

A new home-made design of a fiber optics diffuse reflectance in situ cell addressing some of the issues mentioned above will be described in Chapter 2.

1.5. In situ/operando reaction cells: limitations and opportunities

One of the biggest challenges in in situ and operando studies of heterogeneous catalysts is to obtain useful information at conditions mimicking bench scale and industrial reactors. This is a very difficult task because of the often-disparate characteristics of in situ/operando reaction cells and laboratory and industrial scale reactors. To get this catalyst fundamental information (e.g., reaction *true* intermediates, spectators, etc.) requires the use of proper tools (e.g., reaction cells and spectroscopy) at the right conditions and in the right manner (e.g., balancing reactor vs spectroscopic response, validating cell vs laboratory reactor data) [3, 4, 57, 58]. Although many issues can arise due to the reaction cells, catalyst system and reaction under consideration, spectroscopic and product stream sampling technique, data acquisition, and analysis of the data, this chapter focused on the reaction cells, whereas, some of these other issues have been dealt in prior publications [3, 28, 57].

As described here, reaction cells for in situ UV-Vis, IR, and Raman are by no means of universal application and that explains the large number of cell designs and modifications available in the literature and commercially. Some of the major design features of these reaction cells were briefly described above, but have been covered in great detail including their most salient features in a prior publication [59]. Clearly, all the (transmission, ATR, DR, and scattering) reaction cells briefly described here have their advantages and disadvantages and they should be carefully examined for any given application to get the most useful information out of an existing cell, or to consider them if modifications or new designs are required.

1.6. Further opportunities

At present, there are many areas of improvement for in situ and operando reaction cells, some of which include for example: 1) the development of new setups for the study of liquid-solid reactions with concentration homogeneity over the entire sample while ensuring absence of mass/heat transport effects and avoiding solvent effect contributions to spectroscopic signals; 2) the need for transport criteria in transmission, ATR, DR, and Raman cells; 3) the development of creative cell designs or modifications, in particular, for DR cells and Raman. 4) the need for CFD studies of reactions cells, in particular those exploring existing complex cell geometries (e.g.,

commercial DR cells) or for in silico design.; 5) the application of operando methodology while operating at differential conditions (e.g., differential or recycle reactors) for rigorous kinetic studies.

As we demand more from in situ and operando spectroscopic experiments, we expect better designed spectroscopic reaction cells and techniques to help us achieve that goal of studying and identifying surface (true or kinetically relevant) reaction intermediates or spectator species to elucidate reaction mechanisms. Certainly, significant advances have been realized in the past decades, but more are needed in spectroscopic techniques and computer assisted data mining and analysis for identification of adsorbed species to help us take full advantage of these tools more efficiently and to bring us closer to the ultimate goal of understanding how catalysts work.

1.7. Conclusions

Reaction cells for UV-Visible, IR, and Raman spectroscopic studies at steady or transient/dynamic state are available in many different configurations and for various applications in heterogeneous catalysis for gas-solid, gas-liquid-solid, and solid-liquid phases.

To fully exploit the potential of spectroscopy for the understanding of catalyst surface reaction species as spectators or true intermediates, active sites, and reaction mechanisms via spectrokinetic studies, proper reaction cell selection or design must be made. Many of the currently available cells, however, suffer from design issues including poor inlet/outlet and inner volume fluid dynamics, lack of thermal, and spectroscopic response homogeneity, just to name a few. These design deficiencies can result in poor mass and heat transfer which can limit in situ reaction cells kinetic rigor similar to that expected in bench scale heterogeneous catalytic reactors. Therefore, the acquisition of simultaneous kinetic and spectroscopic information of catalyst adsorbed species and active sites via in situ and operando characterization is still a long-sought goal. The construction of these reaction cells, however, have been mostly guided by intuition and similarity with laboratory reactors rather than a priori in silico design. That is why is not surprising that a large number of home-made and commercial cells are available, which are usually adapted and modified to meet specific spectroscopic and, sometimes, kinetic demands for specific catalytic applications. These in situ/operando reaction cells will continue to be used in heterogeneous catalysis, but full assessment of their kinetic relevance will need to be performed theoretically

and/or experimentally. Understandably, in situ and operando spectroscopic reaction cell design will be key to a continuing understanding of reaction mechanisms by acquiring data in a kinetically controlled regime.

This work was published as part of a comprehensive review on the design characteristics of in situ/operando reaction cells for heterogeneous catalysis in ***Catalysis Reviews-Science and Engineering***, 2017, 1-151, (DOI: 110.1080/01614940.01612017.01360071).

1.8. References

1. Thomas, J.M., Thomas, J.M., and Thomas, W.J., *Principles and Practice of Heterogeneous Catalysis*. 2 ed.; Wiley-VCH: Weinheim, Germany, **2015**.
2. Bañares, M.A., Operando methodology: combination of in situ spectroscopy and simultaneous activity measurements under catalytic reaction conditions. *Catalysis Today* **2005,** *100* (1–2), 71-77.
3. Meunier, F.C., The design and testing of kinetically-appropriate operando spectroscopic cells for investigating heterogeneous catalytic reactions. *Chemical Society Reviews* **2010,** *39* (12), 4602-4614.
4. Tsakoumis, N.E., York, A.P.E., Chen, D., and Ronning, M., Catalyst characterisation techniques and reaction cells operating at realistic conditions; towards acquisition of kinetically relevant information. *Catalysis Science & Technology* **2015,** *5* (11), 4859-4883.
5. Vannice, A., *Kinetics of Catalytic Reactions*. Springer: New York, NY, **2005**.
6. Topsøe, N.-Y. and Topsøe, H., In Situ methods in catalysis proceedings of the Surface Reactivity and Catalysis Group Meeting of the Royal Society of Chemistry Combined in-situ FTIR and on-line activity studies: applications to vanadia-titania DeNOx catalyst. *Catalysis Today* **1991,** *9* (1), 77-82.
7. Topsøe, H., Developments in operando studies and in situ characterization of heterogeneous catalysts. *Journal of Catalysis* **2003,** *216* (1–2), 155-164.
8. Owen, T., *Fundamentals of Modern UV-Visble Spectroscopy: Primer*. Agilent Technologies: Germany, **2000**.

9. Sojka, Z., Bozon-Verduraz, F., and Che, M., UV–Vis–NIR and EPR Spectroscopies. In *Handbook of Heterogeneous Catalysis*, G. Ertl, Knözinger, H., Schüth, F., and Weitkamp, J., Eds. Wiley-VCH Verlag GmbH & Co. KGaA: **2008;** pp 1039-1065.
10. Jentoft, F.C., Ultraviolet–Visible–Near Infrared Spectroscopy in Catalysis: Theory, Experiment, Analysis, and Application Under Reaction Conditions. *Advances in Catalysis* **2009,** *52*, 129-211.
11. Skoog, D.A., Holler, F.J., and Crouch, S.R., *Principles of Instrumental Analysis*. 6th ed.; Thomson Brooks/Cole: Belmont, CA, **2007**.
12. Skoog, D.A., West, D.M., Holler, F.J., and Crouch, S.R., *Fundamentals of Analytical Chemistry*. 9th ed.; Brooks/Cole: Belmont, CA, **2014**.
13. Jentoft, F.C., Electronic Spectroscopy: Ultra Violet-Visible and near IR Spectroscopies. In *Characterization of Solid Materials and Heterogeneous Catalysts*, Wiley-VCH Verlag GmbH & Co. KGaA: **2012;** pp 89-147.
14. Förster, H., UV/VIS Spectroscopy. In *Characterization I: -/-*, H.G. Karge and Weitkamp, J., Eds. Springer Berlin Heidelberg: Berlin, Heidelberg, **2004;** pp 337-426.
15. Mirabella, F.M., *Internal Reflection Spectroscopy: Theory and Applications*. Marcel Dekker, Inc.: New York, NY, **1993;** Vol. 15, p pp 1-374.
16. Räty, J.A., Peiponen, K.E., and Asakura, T., *UV-Visible Reflection Spectroscopy of Liquids*. Springer-Verlag: New York, NY, **2004;** Vol. 92, p pp 1-221.
17. Weckhuysen, B.M., Ultraviolet-Visible Spectroscopy. In *In-Situ Spectroscopy of Catalysts*, B.M. Weckhuysen, Ed. American Scientific Publishers: Stevenson Ranch, CA, **2004;** pp 255-292.
18. Schoonheydt, R.A., UV-VIS-NIR spectroscopy and microscopy of heterogeneous catalysts. *Chemical Society Reviews* **2010,** *39* (12), 5051-5066.
19. Banares, M.A., Raman Spectroscopy. In *In-Situ Spectroscopy of Catalysts*, B.M. Weckhuysen, Ed. American Scientific Publishers: Stevenson Ranch, CA, **2004;** pp 59-104.
20. Davydov, A.A. and Sheppard, N., *Molecular spectroscopy of oxide catalyst surfaces*. Wiley: **2003**.
21. Griffiths, P.R., Introduction to Vibrational Spectroscopy. In *Handbook of Vibrational Spectroscopy*, John Wiley & Sons, Ltd: **2006**.

22. Niemantsverdriet, J.W., Vibrational Spectroscopy. In *Spectroscopy in Catalysis: an Introduction*, 3rd ed.; J.W. Niemantsverdriet, Ed. Wiley-VCH: Weinheim, **2007;** pp 217-249.
23. Delgass, W.N., Haller, G.L., Kellerman, R., and Lunsford, J.H., Chapter 2: Infrared Spectroscopy. In *Spectroscopy in Heterogeneous Catalysis*, Academic Press: New York, NY, **1979;** pp 19-57.
24. Lamberti, C., Zecchina, A., Groppo, E., and Bordiga, S., Probing the surfaces of heterogeneous catalysts by in situ IR spectroscopy. *Chemical Society Reviews* **2010,** *39* (12), 4951-5001.
25. Stuart, B.H., *Infrared Spectroscopy: Fundamentals and Applications*. Wiley: **2004**.
26. Smith, B.C., *Fundamentals of Fourier Transform Infrared Spectroscopy, Second Edition*. Taylor & Francis: **2011**.
27. Lercher, J.A., Veefkind, V., and Fajerwerg, K., In situ IR spectroscopy for developing catalysts and catalytic processes. *Vibrational Spectroscopy* **1999,** *19* (1), 107-121.
28. Che, M. and Vedrine, J.C., *Characterization of Solid Materials and Heterogeneous Catalysts: From Structure to Surface Reactivity*. Wiley: Weinheim, Germany, **2012**.
29. Ryczkowski, J., IR spectroscopy in catalysis. *Catalysis Today* **2001,** *68* (4), 263-381.
30. Peri, J.B., Infrared Spectroscopy in Catalysis Research. In *Catalysis - Science and Technology. Vol 5.*, J.R. Anderson and Boudart, M., Eds. Springer-Verlag: Berlin, **1984;** Vol. 5, pp 171-220.
31. Basu, P., Ballinger, T.H., and Yates, J.T., Wide temperature range IR spectroscopy cell for studies of adsorption and desorption on high area solids. *Review of Scientific Instruments* **1988,** *59* (8), 1321-1327.
32. Delgass, W.N., Haller, G.L., Kellerman, R., and Lunsford, J.H., Chapter 4: Diffuse Reflectance and Photoacustic Spectroscopies. In *Spectroscopy in Heterogeneous Catalysis*, Academic Press: New York, NY, **1979;** pp 86-131.
33. Mondelli, C., Santo, V.D., Trovarelli, A., Boaro, M., Fusi, A., Psaro, R., and Recchia, S., An operando DRIFTS–MS study on model Ce0.5Zr0.5O2 redox catalyst: A critical evaluation of DRIFTS and MS data on CO abatement reaction. *Catalysis Today* **2006,** *113* (1–2), 81-86.
34. Pike Technologies - Diffuse Reflectance - Theory and Applications (Applications/Diffuse Reflectance/Theory & Applications). http://www.piketech.com/files/pdfs/DiffuseAN1313.pdf (accessed Jan. 26, 2017).

35. Klier, K., Absorption and Scattering in Plane Parallel Turbid Media. *Journal of the Optical Society of America* **1972,** *62* (7), 882-885.
36. Sirita, J., Phanichphant, S., and Meunier, F.C., Quantitative Analysis of Adsorbate Concentrations by Diffuse Reflectance FT-IR. *Analytical Chemistry* **2007,** *79* (10), 3912-3918.
37. Zou, W. and Gonzalez, R.D., Pretreatment chemistry in the preparation of silica-supported Pt, Ru, and Pt/Ru catalysts: An in situ UV diffuse reflectance study. *Journal of Catalysis* **1992,** *133* (1), 202-219.
38. Alerasool, S., Boecker, D., Rejai, B., Gonzalez, R.D., Del Angel, G., Azomosa, M., and Gomez, R., The role of preparative variables on the surface composition of supported platinum-ruthenium bimetallic clusters. *Langmuir* **1988,** *4* (5), 1083-1090.
39. Li, Y.-E., Boecker, D., and Gonzalez, R.D., CO oxidation on PtSiO2 and PdSiO2 catalysts: Rapid FTIR transient studies. *Journal of Catalysis* **1988,** *110* (2), 319-329.
40. Melsheimer, J., Thiede, M., Ahmad, R., Tzolova-Muller, G., and Jentoft, F.C., Improved experimental setup for in situ UV-Vis-NIR spectroscopy under catalytic conditions. *Physical Chemistry Chemical Physics* **2003,** *5* (20), 4366-4370.
41. Thiede, M. and Melsheimer, J., In situ UV/Vis/near-IR diffuse reflection measurement of catalysts at temperatures up to 673 K. *Review of Scientific Instruments* **2002,** *73* (2), 394-397.
42. Melsheimer, J. and Schlögl, R., On the sequence of events in H2S oxidation reactions. *Berichte der Bunsengesellschaft für physikalische Chemie* **1997,** *101* (4), 733-740.
43. Weckhuysen, B.M., Baetens, D., and Schoonheydt, R.A., Spectroscopy of the Formation of Microporous Transition Metal Ion Containing Aluminophosphates under Hydrothermal Conditions. *Angewandte Chemie International Edition* **2000,** *39* (19), 3419-3422.
44. Kazansky, V.B., Borovkov, V.Y., and Karge, H.G., Diffuse reflectance IR study of molecular hydrogen and deuterium adsorbed at 77 K on NaA zeolite Part 1.-Fundamentals, combination and vibrational-rotational modes. *Journal of the Chemical Society, Faraday Transactions* **1997,** *93* (9), 1843-1848.
45. Li, B. and Gonzalez, R.D., Design and Construction of a DRIFTS Accessory and an in Situ Heatable Sample Cell. *Applied Spectroscopy* **1998,** *52* (11), 1488-1491.
46. Harrick Scientific - Praying Mantistm High Temperature Reaction Chamber - User's Manual (UV-Vis/High Temperature Reaction Chambers) and

http://www.harrricksci.com/ftir/accessories/group/Praying-Mantis-High-Temperature-Reaction-Chambers.

47. Venter, J.J. and Vannice, M.A., Modifications of a Diffuse Reflectance Cell to Allow the Characterization of Carbon-Supported Metals by DRIFTS. *Applied Spectroscopy* **1988,** *42* (6), 1096-1103.
48. Jentoft, F.C., Chapter 3 Ultraviolet–Visible–Near Infrared Spectroscopy in Catalysis: Theory, Experiment, Analysis, and Application Under Reaction Conditions. In *Advances in Catalysis*, Academic Press: **2009;** Vol. 52, pp 129-211.
49. Weckhuysen, B.M., *In-situ Spectroscopy of Catalysts*. American Scientific Publishers: **2004**.
50. Tinnemans, S.J., Mesu, J.G., Kervinen, K., Visser, T., Nijhuis, T.A., Beale, A.M., Keller, D.E., van der Eerden, A.M.J., and Weckhuysen, B.M., Combining operando techniques in one spectroscopic-reaction cell: New opportunities for elucidating the active site and related reaction mechanism in catalysis. *Catalysis Today* **2006,** *113* (1–2), 3-15.
51. Puurunen, R.L., Beheydt, B.G., and Weckhuysen, B.M., Monitoring Chromia/Alumina Catalysts in Situ during Propane Dehydrogenation by Optical Fiber UV–Visible Diffuse Reflectance Spectroscopy. *Journal of Catalysis* **2001,** *204* (1), 253-257.
52. Groothaert, M.H., Lievens, K., Leeman, H., Weckhuysen, B.M., and Schoonheydt, R.A., An operando optical fiber UV–vis spectroscopic study of the catalytic decomposition of NO and N2O over Cu-ZSM-5. *Journal of Catalysis* **2003,** *220* (2), 500-512.
53. Weckhuysen, B.M., Verberckmoes, A.A., Debaere, J., Ooms, K., Langhans, I., and Schoonheydt, R.A., In situ UV–Vis diffuse reflectance spectroscopy — on line activity measurements of supported chromium oxide catalysts: relating isobutane dehydrogenation activity with Cr-speciation via experimental design. *Journal of Molecular Catalysis A: Chemical* **2000,** *151*, 115-131.
54. Nijhuis, T.A., Tinnemans, S.J., Visser, T., and Weckhuysen, B.M., Operando spectroscopic investigation of supported metal oxide catalysts by combined time-resolved UV-VIS/Raman/on-line mass spectrometry. *Physical Chemistry Chemical Physics* **2003,** *5* (20), 4361-4365.
55. Weckhuysen, B.M., Determining the active site in a catalytic process: Operando spectroscopy is more than a buzzword. *Physical Chemistry Chemical Physics* **2003,** *5* (20), 4351-4360.

56. Sobalík, Z., Jíša, K., Jirglová, H., and Bernauer, B., Simultaneous FTIR/UV-Vis study of reactions over metallo-zeolites: Approach to quantitative in situ studies. *Catalysis Today* **2007,** *126* (1), 73-80.
57. Weckhuysen, B.M., Snapshots of a working catalyst: possibilities and limitations of in situ spectroscopy in the field of heterogeneous catalysis. *Chemical Communications (Cambridge, United Kingdom)* **2002,** (2), 97-110.
58. Banares, M.A. and Mestl, G., Structural Characterization of Operating Catalysts by Raman Spectroscopy. In *Advances in Catalysis, Vol 52*, B.C. Gates and Knozinger, H., Eds. **2009;** Vol. 52, pp 43-128.
59. Bravo-Suárez, J.J. and Srinivasan, P.D., Design characteristics of in situ and operando ultraviolet-visible and vibrational spectroscopic reaction cells for heterogeneous catalysis. *Catalysis Reviews: Science and Engineering* **2017**, pp1-151, DOI: 10.1080/01614940.2017.1360071.

Chapter 2. Modified Harrick Reaction Cell for in Situ/Operando Fiber Optics Diffuse Reflectance UV-Visible Spectroscopic Characterization of Catalysts

2.1. Introduction

The fundamental pillars that constitute heterogenous catalysis are catalyst synthesis, characterization, and evaluation. Characterization of catalysts is particularly important during the synthesis of catalysts and during their reactivity evaluation as it provides insight into the genesis and working state of catalyst active sites. This is the so-called in situ characterization of catalysts. Among catalyst in situ characterization techniques, spectroscopic methods are of great relevance for the study of not only of active sites, but also of intermediate species that participate in catalytic cycles. Understanding the interrelation between active sites, adsorbed species, and reaction kinetics, nowadays supported by computational tools, informs researchers how to develop improved and novel catalysts for application in many different reactions of industrial and environmental interest. The study of catalysts with in situ spectroscopic techniques at reaction conditions helps us understand important steps such as adsorption of reactants on the surface, formation of reaction intermediates, and desorption of products from the catalytic surface. An example of commonly available in situ spectroscopic techniques include, for example, UV-Vis, FTIR, and Raman spectroscopies [1, 2]. When reactivity data is collected simultaneously in an in situ experiment, as typically done in laboratory reactors, the spectroscopic methodology is then called operando spectroscopy [3]. This combination of spectroscopic investigation with simultaneous monitoring of catalytic activity under reaction conditions in the same reaction cell is a powerful method that undoubtedly assists in the design and optimization of catalytic systems and has seen significant advances in recent years [3, 4]. One of the spectroscopic techniques of great use and widely available (although often not fully exploited) in catalysis laboratories is UV–Vis spectroscopy, which can be used for characterization of transition metal oxide catalysts, their metal oxidation states [5-10], kinetic parameters for elementary steps [11-13], and adsorption of surface species [14]. Despite all these advantages, there are still challenges in the design, construction, and application of in situ and operando UV-Vis spectroscopic cells for single and multiphasic reactions [2].

Over the years, many in situ reaction cells have been developed for characterization of solid materials. These spectroscopic cells operate in the most common modes of measurement: 1) transmission, as in the case of liquids and thin films [15-27] and 2) reflection, which includes internal reflectance [28-33] or diffuse reflectance. In the case of solid catalysts, however, UV-Vis analysis by diffuse reflectance is perhaps the most common technique as it does not require sample preparation, thus avoiding structural changes and sample scattering effects [2, 34]. Also, DR sample holders in these cells resemble fixed bed reactors, enabling their use for kinetic studies [4]. Although many popular reaction cells exist commercially [2], they do not often meet the time resolution required for fast dynamic experiments as limited by the sampling speed of the spectroscopic technique [2]. For UV-Vis spectroscopy, to achieve increased time resolution down to the millisecond level, one common approach has been to utilize cells employing diode array or charge coupled device (CCD) detector based spectrometers. In diffuse reflectance, unlike mirror optics, fiber optics coupled with diode array or CCD detectors offer such increased time resolution, which enhances the scope of in situ operando characterization. Weckhuysen and co-workers, for example, designed diffuse reflectance UV-Vis spectroscopy reaction cells with optical fibers for monitoring the catalyst surface on a movable platform in gas-solid reactions [13, 35]. Such reaction set up with optical fibers enabled fast data collection within 1 second. Chlebda et al. [36] recently reported the Harrick cell for use with a fiber optic probe, but details of the modified reaction cell were omitted. Another advantage of these probes is that they can be integrated into any of the ATR, transmission or diffuse reflectance reaction cells allowing for simultaneous multi spectroscopic in situ technique characterization of catalysts. For instance, Bürgi modified the trapezoidal-IRE ATR cell by adding a UV-Vis optical fiber probe, which fits on to a fused silica window in close proximity of the catalyst bed [37]; Sobalík et al. combined an in situ transmission FTIR cell with an UV-Vis optical probe [38]; and Brückner et al. reported the use of a modified in situ diffuse reflectance FTIR Harrick cell with addition of a UV-Vis optical fiber probe [39].

In addition to fiber optics, in situ diffuse reflectance UV-Vis spectroscopy has also been carried out with an integrating sphere [40] and mirror optics, commonly, with homemade or commercial cells. Mirror optics based cells can be versatile as they could be fitted for use in UV-Vis, FTIR, or Raman spectroscopy by proper selection of the cell windows [2]. Additionally, many homemade in situ mirror optics DR infrared spectroscopic cells could be adapted for UV-Vis as well, such as those by Li and Gonzalez low void volume cell [41], Schubert et al.'s cell that is compatible with

Harrick's Praying Mantis diffuse reflectance mirror optics [42], and Dal Santo et al.'s low dead volume diffuse reflectance cell inspired in Harrick's HV-DR2 cell [43], among others. These cells may have smaller dead volume adequate for most dynamic and transient studies, but are limited by poor UV-Vis spectroscopic time resolution as they use scanning spectrometers [2].

Finding an ideal diffuse reflectance reaction cell for a wide range of catalytic in situ and operando reaction conditions including small dead volume and for use with a fast-spectroscopic acquisition system is no easy task. While designing a new cell from scratch has indeed its merits, for most catalysis laboratories, this is usually tedious and not very practical due to the amount of design and machining work, cost, and safety checks required. Usually, but not necessarily always, commercial cells are preferred. In this work, we selected Harrick's reaction cell for its ubiquity (e.g., a Google Scholar search of Harrick+ "diffuse reflectance" yielded 5260 results, which is more than any other commercial cell: Spectra Tech = 2870, Pike = 2480, or Specac = 1110), operation at high temperature (~500-550 °C under flow conditions) and moderate pressure (up to 15 bar for IR with special windows), versatility (e.g., UV-Vis, IR, and Raman spectroscopy operation), enough sample capacity (in tens of mg), and resemblance to lab scale fixed bed reactors [2]. Here, we report an improved design of the commercial Harrick's in situ diffuse reflectance reaction cell with reduced dead volume and with fiber optics to reduce gas residence times and to improve time resolution for use with UV-Vis spectroscopy. Enough details are provided so that cell modifications can be easily reproduced. The reaction cell limitations and how to address them are also discussed. An example demonstrating its use in tracking plasmon resonance shifts of gold nanoparticles under cycling oxidizing/reducing environments using a ZrO_2 supported gold catalyst is presented to demonstrate the utility of the modified in situ DR UV-Vis reaction cell.

2.2. Experimental section

2.2.1. Catalyst preparation

Au/ZrO_2 catalyst with a Au loading of 1 wt% was prepared by a deposition-precipitation method. For the preparation, 1 g of the support (ZrO_2, Alfa Aesar, P/N 43814), was dispersed in 20 cm^3 of water (HPLC, Fisher Chemical, P/N W5-4) under stirring (MS-H-Pro Plus hotplate-stirrer, Scilogex). To this stirred slurry, 2.5 wt% NH_4OH (prepared from 14.8 N NH_4OH, Fisher, P/N A669-212) was added dropwise to reach a pH of 9.5 monitored with a DrDAQ pH measuring kit

(Pico Technology). After 5 min, about 20 mg of $HAuCl_4.3H_2O$ (Alfa Aesar, P/N 36400) dissolved in 8 cm^3 of water was added dropwise concurrently with 2.5 wt% NH_4OH until the pH was 9.5. The solution was stirred continuously for 1 h after which the solution was filtered and dried in vacuum for 12 h at room temperature. The dried catalysts were calcined in static air at 393 K for 2 h (5 K/min) and 673 K for 4 h (4.5 K/min) in a Thermolyne 48000 muffle furnace (Barnstead International). The calcined catalysts were stored in dark vials and in sealed plastic bags to minimize light and moisture exposure.

2.2.2. Catalyst characterization

The catalyst was characterized for N_2 adsorption-desorption isotherms at -196 °C using a Quantachrome Autosorb-iQ instrument. The Au/ZrO_2 catalyst was also examined by transmission electron microscopy (TEM). The samples were prepared by dispersing the catalyst in ethanol and suspending a drop on a carbon film supported by copper grid (Ted Pella Inc., P/N 01890-F). TEM analysis was performed using a FEI Tecnai F20 XT microscope at a 200 kV accelerating voltage.

2.2.3. Modified reaction cell design

A high temperature reaction chamber HVC (Harrick) made of chemically resistant 316 stainless steel (dimensions = 2.5" × 1.6" × 1") suitable for the diffuse reflectance UV-Vis spectroscopic characterization of heterogeneous catalysts, but originally designed for benchtop scanning spectrometers, was modified such that a new easy to machine low dead volume dome could fit a 1/4" UV-Vis spectroscopic fiber optics probe for faster spectroscopic data acquisition. **Figure 2.1** shows a detailed top view image of the improved reaction cell, whereas **Figure 2.2** shows a cut off and expanded view of the reaction cell internal parts. The bottom part (#8 in **Figure 2.2**) has a stainless-steel plate (with dimensions 6.4 cm × 4 cm × 0.5 cm) sealed by three O-rings that sit in their corresponding grooves (#7 in **Figure 2.2**). The reaction chamber has three ports for evacuating, pressurizing, and flowing gas (#1 and #2 in **Figures 2.1** and **2.2**). The gas enters through the inlet on one of the sides of the reactor, flows through the catalyst bed in a down flow pattern and exits through the central port below the catalyst bed (#2 in **Figures 2.1** and **2.2**). The outlet port consists of 1/4" Swagelok VCO fittings (#2 in **Figures 2.1** and **2.2**). The outlet gases are directed to a mass spectrometer through a 1/16" tubing and Swagelok connections for online analysis or directed to a vent for only in situ characterization at reaction conditions. Gas entering

in the cell can either flow through the reaction cell or can be bypassed using a manifold consisting of two three-way valves (**Figure A.1**, Appendix A). The reaction chamber and the catalyst are heated by a low power cartridge heater (0.25"× 1.25", 24V/100W, Harrick Scientific) located at the bottom part of the sample cup, but isolated from the internal volume of the cell (#5 **Figure 2.2**). A temperature controller box with cascade control capabilities (ATC-024-3, Harrick Scientific) delivers power to control the temperature of the block and catalyst bed by receiving feedback from two (1/32", OMEGA®) K-type thermocouples (#11, #12 in **Figure 2.2**). One thermocouple inserted into a small hole located in the heat cartridge wall inside the bottom part of the reactor half way through the cell (#11 in **Figure 2.2**), measures the temperature of the sample cup external wall. The second thermocouple inserted into the outlet port slips in to the catalyst bed (0.25" O.D.) through a metal screen (holding the catalyst powder and ensuring uniform flow of gases through the bed, made from 316 Stainless Steel, 38 µm opening, McMaster-Carr P/N 9319T189), measures the temperature of the catalyst bed (#12 in **Figure 2.2**). To prevent leaks through a 1/8" Swagelok tee, a 1/32" adapter was used to hold the thermocouple in place (Omega, P/N KMQXL-062G-6) and not over tightened to avoid damage to the thermocouple. A water cooling jacket controls the temperature of the chamber through an Isotemp 3006P programmable refrigerated recirculating bath (Fisher Scientific) set at 9 °C, which pumps coolant and prevents overheating of the sealing ring between the dome and the cell body.

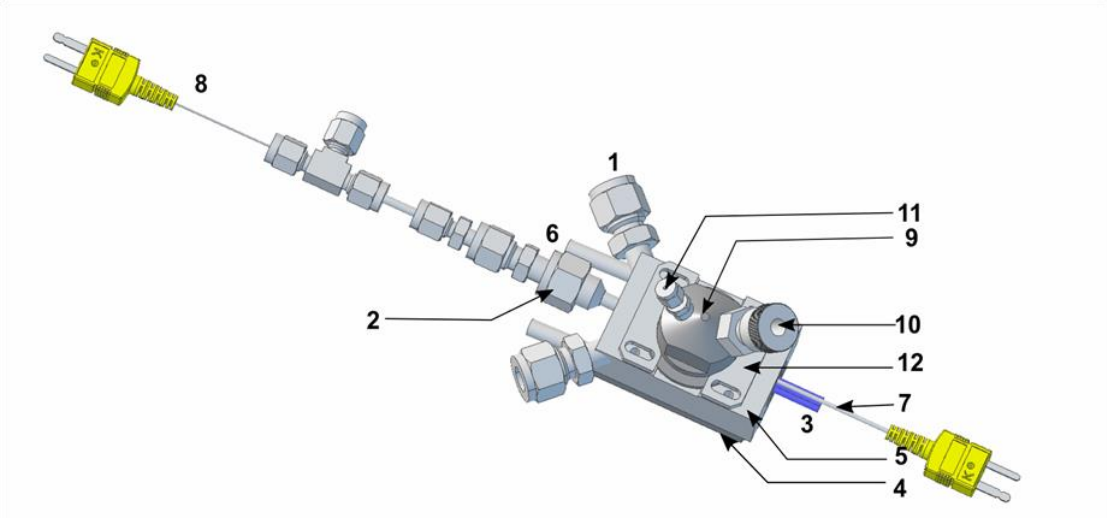

Figure 2.1. Top view of the modified diffuse reflectance UV-Vis cell with accessories. 1) Gas inlet/outlet; 2) gas outlet; 3) cartridge heater; 4) reaction cell bottom cover; 5) reaction cell body; 6) cooling port; 7) cell body thermocouple; 8) sample thermocouple; 9) UV-Vis optical fiber dome; 10) Swagelok fitting for optical fiber; 11) Swagelok fitting for thermocouple to monitor optical probe temperature; 12) retaining plates.

A metallic dome, resembling Harrick's ZnSe solid hemispherical window for FTIR, was designed to fit the reaction chamber (#13 in **Figure 2.2**). The dome is sealed by an O-ring on the groove at the bottom part of dome. The cell body has a pair of retaining plates which slide all the way over the rim of the dome and tightened by a pair of screws to secure the dome and provide a gas-tight seal (#12 in **Figure 2.1**). The dome holds an affordable laboratory grade diffuse reflectance fiber optic probe, Avantes (FCR-7UV400-2-ME-HT, 400 μm, < 200 °C, < 50 bar @ 25 °C) in direct proximity to the surface of the sample (~3.0-5.0 mm) and at an angle of 60 degrees to minimize specular reflectance. The fiber optic probe has a 400 μm core diameter with SMA 905 connectors and a ¼-inch diameter steel mono-coil armor that can be operated at a maximum temperature of 200 °C. On the opposite side of the dome, a K-type thermocouple (1/16") measures the temperature of the fiber optic probe surface close to the tip (#15 in **Figure 2.2**). Although this thermocouple monitors the probe temperature, it will be shown later that it could be omitted in further designs as the maximum measured probe temperature (~110 °C) was well below the Avantes probe maximum operating temperature of 200 °C. Because the Swagelok adapter (SS-4-UT-1-2, #14 in **Figure 2.2**) that holds the probe does not seat fully in the dome, an internal 010 O-ring is used to help seal the probe and avoid gas above the sample from entering that small cavity. Despite the quite small empty volume of this cavity, we found that this O-ring addition reduced a significant tailing during pulse experiments characteristic of contributing stagnant gases. Additional design details of the modified reaction cell and dome are provided in the appendix (**Figure A.1**, Appendix A) and 3D models that can be visualized and easily manipulated with most common pdf reader software.

The optical probe is illuminated by a preconfigured dual UV-Vis lamp setup that includes a SL3 Deuterium lamp and SL1-filter Halogen lamp (StellarNet Inc) that provides high output stable UV-Vis-NIR light in the 200-2300 nm range. This allows rapid acquisition of UV-Vis spectra through a Black-comet SR concave grating spectrometer + CCD detector (Model C, StellarNet Inc) operating in the range of 200-1080 nm that gives enhanced spectral imaging with low stray light and reasonable sensitivity. The spectrometer can deliver fast data acquisition (few milliseconds) and a high signal to noise ratio. Some other additional modifications were made to improve the performance of the diffuse reflectance cell as described below.

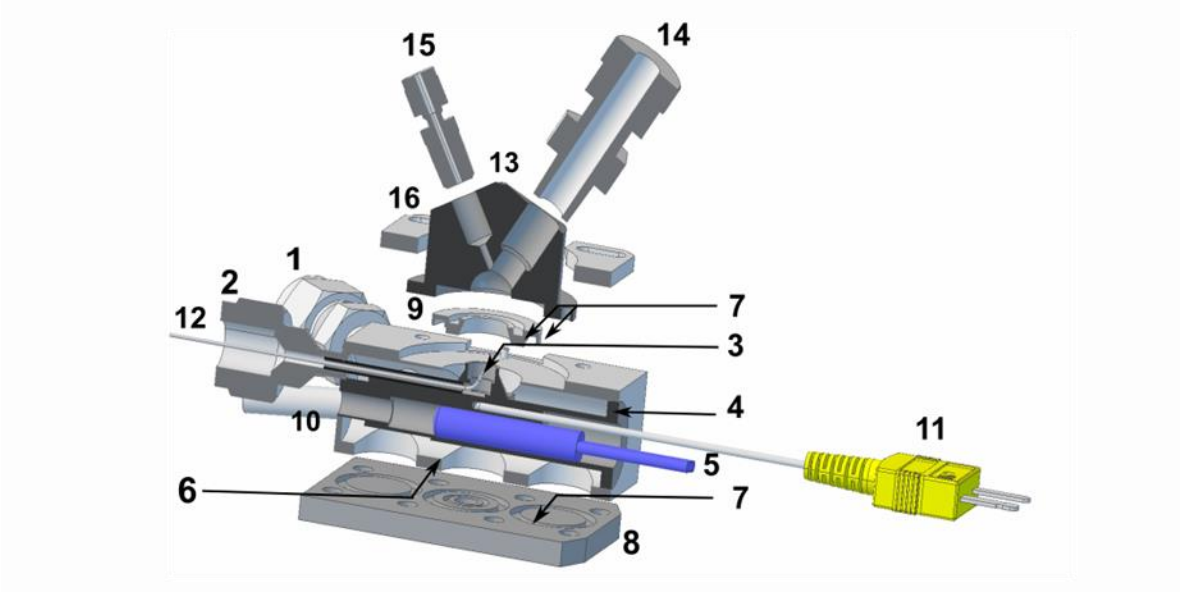

Figure 2.2. Cut off and expanded views of the optical fiber diffuse reflectance UV-Vis spectroscopy probe combined with Harrick's HVC reaction cell model. 1) Gas inlet/outlet; 2) Gas outlet; 3) Sample cup; 4) cartridge heater housing; 5) Cartridge heater; 6) Insulating void space; 7) O-ring groove; 8) Reaction cell bottom cover; 9) Reaction cell body; 10) Cooling port; 11) Cell body thermocouple; 12) Sample thermocouple; 13) UV-Vis optical fiber dome; 14) Swagelok fitting for optical fiber; 15) Swagelok fitting for thermocouple to monitor optical probe temperature; 16) Retaining plates.

2.2.4. DR UV-Vis spectroscopy technique

UV-Vis spectroscopic characterization of solid catalysts can provide information on the catalyst's oxidation state and coordination in metals and metal oxides, band gap in semiconductors, particle size and shape and surface adsorption in metal nanoparticles via surface plasmon resonance, among others [2, 14]. Characterization is more commonly carried out via (i.e., specular, internal, or diffuse) reflectance rather than by the typical transmission mode for liquid samples. Analysis via diffuse reflectance is particularly convenient because of it does not require sample preparation and, therefore, solids could be used in sample cells that resemble bench scale fixed bed reactors. For quantitative analysis, collected spectra are usually analyzed with the so-called Kubelka-Munk function (Equation 1) that relates the absolute reflectance (R_∞ at infinite sample thickness) to absorption (K) and scattering coefficients (S) [2, 14].

$$F(R_\infty) = \left[\frac{(1-R_\infty)^2}{2R_\infty}\right] = \frac{K}{S} = \frac{kC}{S} \quad (1)$$

The Kubelka-Munk function is expected to be proportional to the concentration of absorption centers and thus useful for characterization of solid catalysts. For quantitative purposes, such function, however, is limited to applications of densely packed and small particles (~5-50 μm), with uniform distribution and low concentration of absorbing centers, and with sample depths of 2-3 mm. The Kubelka-Munk function appears proportional to concentration at low values of $F(R_\infty) < 1$, however, the specific range can vary significantly and, in some cases, the apparent absorbance $\log(1/R_\infty)$ has been shown to be more adequate [2, 14, 44]. For the in situ cell and sample described here, small particle sizes <75 μm, small gold concentration (1 wt%), and sample bed depth of ~3.1 mm (~1/8") were used. In general, it is worth cautioning the implications of the Kubelka-Munk validity at infinite sample depth for in situ and operando studies which suggest that only a fraction of the bed will be probed by the light beam. At such conditions, application of the technique to draw rigorous structure/activity relationships will, therefore, require operation under differential conditions [2]. In this study, quantification of absorbing centers was not attempted by the Kubelka-Munk function, but rather the apparent absorbance was employed for simplicity and because the main monitored variable was the plasmon peak resonance shift (i.e., wavelength or photon energy) and not the observed reflectance intensity.

2.2.5. In situ DR UV-Vis reaction cell pulse experiments

Figure 2.3 shows the schematics of the in situ UV-Vis spectroscopic reaction setup. It consists of 3 main sections: (1) gas feeding system; (2) DR UV-Vis cell; and (3) analytical instrumentation (UV-Vis Spectrometer, OmniStar GSD 320 O Mass spectrometer). All lines are composed of 1/8" stainless steel tubing, except the one exiting the reaction cell towards the mass spectrometer (MS) which consisted of 1/16" stainless tubing to minimize dead volume between the cell and the MS. The gas feeding system consists of a series of rotameters (Cole Parmer) for the delivery of constant flow of gases to the diffuse reflectance cell. Each of these rotameters is fed by He (UHP, Matheson), H_2 (UHP, Matheson), O_2 (UHP, Matheson), CO (UHP, Matheson), and Ar (UHP, Matheson), respectively. All gas cylinders are provided with moisture (all gases: Matheson, 450B series, type 451), oxygen (He, H_2, Ar, CO: Perkin Elmer, P/N N9301179), and hydrocarbon (He, H_2, Ar, O_2: Matheson, 450B series, type 454) traps. The UV-Vis spectra are recorded with a black comet SR concave grating spectrometer (StellarNet Inc.), equipped with light sources (SL1, SL2,

StellarNet Inc.), whereas the outlet gas stream is analyzed online by an OmniStar GSD 320 O mass spectrometer (Pfeiffer Vacuum).

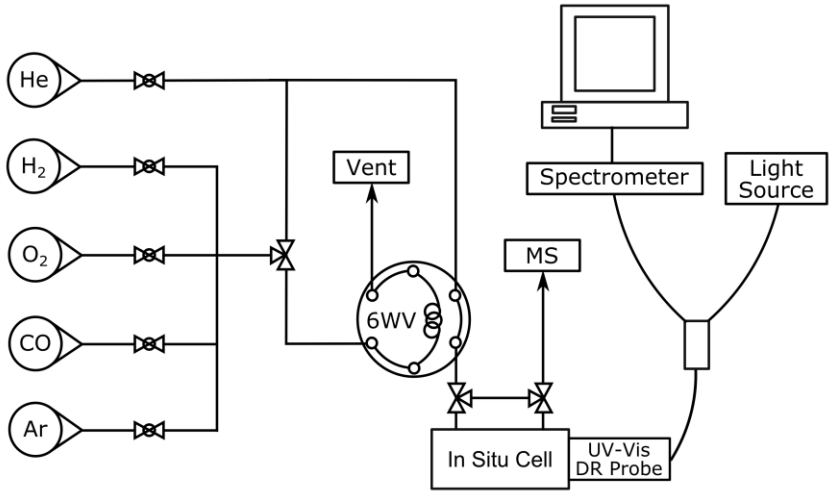

Figure 2.3. Scheme of the in situ UV-Vis experimental setup. MS=mass spectrometer; 6WV=VALCO 6 port valve; loop size = 50 μL.

Pulse experiments were performed at ambient temperature (25 °C) to characterize the in situ reaction cell flow performance. They were carried out by monitoring at the exit of the cell the concentration of different gas pulses using helium as the carrier gas. The outlet signal was tracked by a mass spectrometer with a data acquisition time interval of ~1 s. The flow rate of the carrier gas was kept constant at 45 cm^3/min. This flow rate was selected as a good compromise between fast exchange flow rate and low heat loss due to convection while achieving typical fixed bed reactor space velocities in the range of 350-600 $cm^3/min/g_{cat}$. Pulses of H_2, O_2, CO_2, and Ar were sent via a 6-port valve (VICI Cheminert Instruments, P/N C2-1006D) with a 50 μL loop volume at ambient temperature and 1 atm. They were monitored directly when bypassing the reaction cell or flowing through the reaction cell.

2.2.6. In situ Au surface plasmon resonance following H_2/O_2 cycle exposures to Au/ZrO_2 catalyst

Nanoparticles of metals such as Au, Ag, and Cu can exhibit a peak in the visible spectrum when excited with visible light due to localized surface plasmon resonance [45-49]. The position of this spectral position is sensitive to the metal nanoparticle size and changes in the embedding medium.

Gold nanoparticles larger than about 1.5 nm when supported on metal oxides often exhibit a peak in the visible spectral region due to surface plasmon resonance (SPR) [50]. In this work, gold NPs are chosen since they can act as excellent catalysts for oxidation reactions and Au SPR can be used as sensor for gas adsorption. Here, the modified UV-Vis diffuse reflectance cell enabled us to study the optical properties of supported gold nanoparticles and their dynamic spectral changes under oxidizing and reducing environments in real time.

For the gold SPR shift experiments, around 120 mg of catalyst was loaded in the reaction cell. UV-Vis light from the light source contacts the catalyst sample through a 400 µm core diameter fiber optics probe and gets reflected to the spectrometer for analysis via an inner fiber optics in the same probe. UV-Vis spectra were taken in situ at ambient pressures and referenced to $BaSO_4$ (Sigma Aldrich, P/N 243353). The spectrometer measured continuously absorbance spectra over the wavelength range of 230 to 1080 nm every 2 seconds (2000 ms, 1 scan) which enabled us to characterize very small changes in the plasmon resonance of gold nanoparticles as a function of time when switching from one gas to another. In a typical experiment, the catalyst was reduced in situ for 30 min at 200 °C with pure hydrogen at a flow rate of 45 cm^3/min. After reduction, the cell was flushed with He at a flow rate of 45 cm^3/min and the temperature of the sample was brought down to 125 °C (5 °C/min). The catalyst sample was then exposed to oxygen (99.98 %) for 30 min at a flow rate of 45 cm^3/min and then flushed with helium (99.999 %) for about 15-20 min, followed by exposure to hydrogen for 30 min (45 cm^3/min). This sequence of H_2-He-O_2 was repeated continuously for approximately 5 h to probe the reversibility of the Au-SPR gas adsorption process.

2.3. Results and discussion

2.3.1. Reaction cell volume vs pulse experiments: residence time distribution (RTD) properties

2.3.1.1. Reaction cell with large inner volume: RTD characteristics

The original reaction cell possesses a relatively large void volume from the chamber void space (6 in **Figure 2.2**, ~12.5 cm^3) that hinders the possibility of fast transient response experiments (within seconds at moderate flow rates). Here, the average residence time of several gases was determined to evaluate the reaction cell flow characteristics. Residence time distributions (RTDs)

are widely used to characterize mixing occurring in chemical reactors and hence measured here with gas pulse injection experiments by monitoring the corresponding pulse gas concentration changes (C(t)) with residence time, t. Following known techniques [51-53], the C vs t data was normalized to give an area of 1 which defines the RTD or so-called E(t) curve, where E(t) is given by Equation 2:

$$E(t) = \frac{vC(t)}{N_0} \tag{2}$$

Here v is the effluent volumetric flow rate and N_0 is the total amount of gas in the injected pulse. N_0 is conveniently determined experimentally by the total area of outlet concentration measurements of the pulse (Equation 3):

$$N_0 = \int_0^\infty v\, C(t)dt \tag{3}$$

In the pulse experiment, the volumetric flow rate v is assumed to be constant, thus, combination of Equations 2 and 3 results in Equation 4, which is used to determine the RTD, E(t), by normalization of C(t) data by its total area, $\int_0^\infty C(t)dt$.

$$E(t) = \frac{C(t)}{\int_0^\infty C(t)dt} \tag{4}$$

Figure 2.4 shows the RTD or E curve for argon pulse experiments bypassing (trace 1: by means of installed three-way valves) and through the reaction cell (trace 2: cell with added glass beads to reduce dead volume and trace 3: cell without glass beads). These traces displayed an initial time lag, a sharp peak, semi-symmetric peak width, and a mid-size to long tail, which are characteristic of plug flow in series with mixed flow and nonideal flow behavior (e.g., bypass or short-circuiting from inlet to outlet, stagnant gas due to dead volume pockets) [51-53]. RTDs for other gases including CO_2, H_2, and O_2 resulted in similar characteristic E curves and are not shown for the sake of brevity.

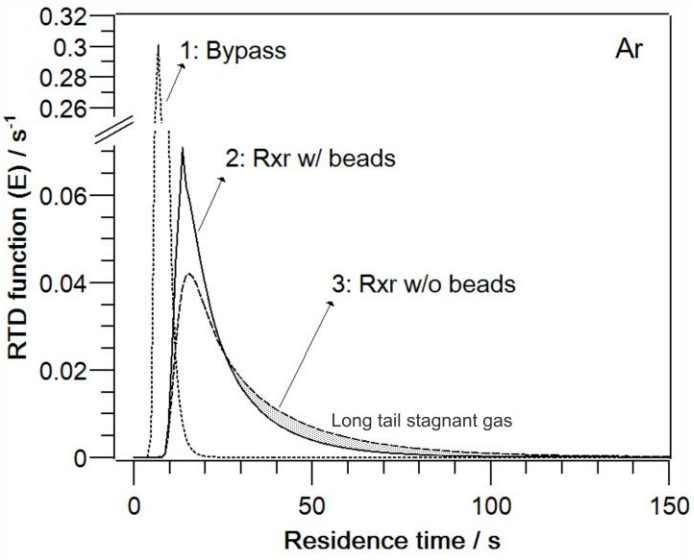

Figure 2.4. Residence time distribution (RTD) profiles of argon gas pulses at room temperature bypassing (trace 1: dotted line) and through the reaction cell with beads to reduce inner volume (trace 2: solid line), and in absence of beads (trace 3: dashed line). Conditions: ambient temperature, 1 bar, 50 μL loop, He flow of 45 std (ambient temperature and pressure) cm^3/min.

The presence of different RTD features for experiments bypassing and through the reaction cell unambiguously point out to coupling of different flow characteristics (e.g., plug flow and continuously-stirred tank reactors, PFR and CSTR behavior) between transfer lines, reaction cell, and detection system (MS detection chamber). The latter which appears to behave as a mixed tank. These results highlight the difficulties of characterizing flow dynamics in diffuse reflectance reaction cells due to nonevident and usually unaccounted-for contributions from transfer lines and detection system. To rigorously characterize the RTD of the reaction cell, these external contributions (e.g., transfer lines and MS detection chamber) must be considered.

Here, the different RTDs of the reaction cell are calculated by assuming different reactor model contributions for different sections in the reaction system. **Figure 2.5** shows, for example, the schematics of the assumed reactor models for the different reaction system sections, from the pulse injection to the MS detection point. For transfer lines from the pulse injection to the reactor (through-reactor mode) and from injection to MS detector (bypass mode), PFR behavior is assumed, whereas for the in situ reaction cell and MS detector chamber, CSTR models are considered. Additionally, since the flow conditions in the main transfer lines usually operate in the laminar flow (Re < 100), a laminar flow reactor (LFR) model was also employed for diagnostic of the reaction cell. To describe each section, the mean residence times (MRT) and the variance (σ)

are used as the main descriptors of the RTD. The MRT of the in situ reaction cell is, thus, determined by a combination of two experiments: bypass and through reaction cell pulses, which are also used to estimate transfer lines and MS detection contributions as described below.

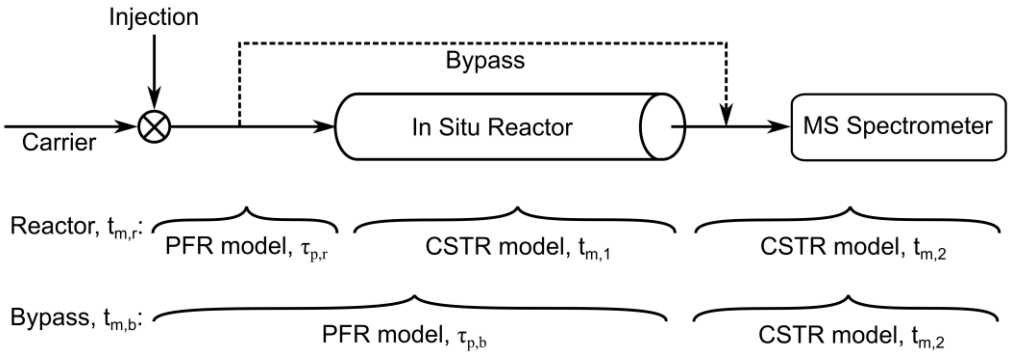

Figure 2.5. Residence time distribution models for the in situ reaction system in bypass and through reaction cell modes. Here, $t_{m,r}$ and $\tau_{p,r}$ are the overall and plug flow reactor (PFR) model mean residence times (MRT) for transfer lines to cell, respectively, resulting from flow through the reaction cell, whereas $t_{m,b}$ and $\tau_{p,b}$ are the overall and PFR model MRT for transfer lines to MS, respectively, when the gas bypasses the reaction cell (dashed line); and $t_{m,1}$ and $t_{m,2}$ are the in situ reaction cell and MS detection chamber MRTs, respectively.

It has been previously demonstrated that for ideal reactors in absence of dispersion and for constant volumetric flow (v), the nominal space time, $\tau = V/v$ (V = reactor volume) is equal to the mean residence time, t_m [51-53]:

$$t_m = \frac{\int_0^\infty tE(t)dt}{\int_0^\infty E(t)dt}$$

$$\text{Since } \int_0^\infty E(t)dt = 1 \quad \text{then}$$

$$t_m = \int_0^\infty tE(t)dt = \tau \tag{5}$$

Equation 4 shows that the mean residence time can be measured experimentally from the area of a t vs *tE(t)* plot. Additionally, the RTD standard deviation (σ) is defined by:

$$\sigma^2 = \int_0^\infty (t - t_m)^2 E(t)dt \tag{6}$$

Both magnitudes, t_m and σ, are determined experimentally from pulses through the reaction cell with large inner empty volume (~12.5 cm^3, $t_{m,rnb}$) and in bypass mode ($t_{m,b}$) using Equations 5 and 6.

Table 2.1. Residence time distribution characteristics through the reaction cell system with large empty volume (~12.5 cm3) summarizes the results from gas (Ar, CO_2, H_2, and O_2) pulses for the in situ reaction system for the case where the reaction cell with large internal void volume. The results include mean residence times of the overall system as well as individual section contributions shown in **Figure 2.5**. For all four pulsed gases no significant differences were observed for the overall MRTs and standard deviations (σ), with average values of 34.1 and 25.8 s, respectively. The similarity of MRTs, despite the two to three fold differences in the diffusion coefficients of the various gases (Ar/He: $0.747x10^{-4}$ m^2/s, CO_2/He: $0.596x10^{-4}$ m^2/s, H_2/He: $1.533x10^{-4}$ m^2/s, O_2/He: $0.744x10^{-4}$ m^2/s at 25 °C [54]), suggest that mass transfer due to molecular transport is not significant and rather controlled by convection and bulk transport. This similarity is also observed for the time required for detection of 90% of the pulsed gases (**Table 2.1**, t $RTD_{90\%}$) of about 64.5 s.

The MRT for the PRF model in the transfer lines from injection to reactor ($\tau_{p,r}$) and to the MS bypassing the reactor ($\tau_{p,b}$) were determined by the time lags observed in the corresponding E curves (see **Figure 2.4**). The two-fold larger average transfer time to the reactor, $\tau_{p,r}$ (8.8 s), with respect to that to the MS, $\tau_{p,b}$ (4.7 s), indicates a significant empty volume contribution from the feed line in the reaction cell (#1 in **Figures 2.1** and **2.2**), a volume that is larger than that in the 1/8" or 1/16" OD tubing in the transfer lines.

Another measured quantity was the MRT for the MS detection chamber ($t_{m,2}$) which was determined from the bypass experiment (**Table 2.1**, last column) by Equation 7. Finally, the MRT for the in situ reaction cell was calculated with Equation 8.

$$t_{m,2} = t_{m,b} - \tau_{p,b} \quad (7)$$

$$t_{m,1} = t_{m,r} - \tau_{p,r} - t_{m,2} \quad (8)$$

The results for $t_{m,1}$ and $t_{m,2}$ shown in **Table 2.1** were similar for all gases with average values of 21.3 and 4.1 s, respectively. The higher MRT for $t_{m,1}$ with respect to $t_{m,2}$ indicates that the empty volume in the reaction cell is larger than that in the MS detection chamber. More importantly, the mean residence time for the reaction cell of 21.3 s is significantly larger than those reported for in

situ transmission cells of less than a few seconds. This shows the significant disparity of flow operation between diffuse reflectance and transmission reaction cells and the need for further reduction of internal void volume in the former.

Table 2.1. Residence time distribution characteristics through the reaction cell system with large empty volume (~12.5 cm^3)

Gas	**$t_{m,rnb}$ (σ) (s)**	**t $RTD_{90\%}$ (s)**	**$\tau_{p,r}$ (s)**	**$\tau_{p,b}$ (s)**	**$t_{m,1}$ (s)**	**$t_{m,2}$ (s)**
Ar	34.2 (25.1)	66.1	8.8	3.9	21.2	4.2
CO_2	34.6 (25.6)	65.6	8.8	3.9	21.5	4.3
H_2	33.5 (24.7)	62.6	8.8	4.9	21.0	3.7
O_2	34.2 (27.6)	63.6	8.8	5.9	21.1	4.3
Average	34.1	64.5	8.8	4.7	21.2	4.1

$t_{m,rnb}$ = mean residence time of pulse gas to reach MS detector via in situ reaction cell without beads (rnb = reactor no beads), σ = standard deviation, t RTD90% = residence time required for 90% of the pulse gas to reach the MS detector, $\tau_{p,r}$ = space time for a plug flow reactor: tubing line before in situ reactor (with beads), $\tau_{p,b}$ = space time for a plug flow reactor: tubing line bypassing in situ reactor, $t_{m,1}$ = mean residence time of pulse gas through in situ reactor based on an ideal CSTR, $t_{m,2}$ = mean residence time of pulse gas in mass spectrometer before reaching detector based on an ideal CSTR. Experimental conditions: He carrier 45 cm^3/min, 500 μL gas pulse, 1 bar, 25 °C, reaction cell without glass beads (cell void volume ~12.5 cm^3).

2.3.1.2. Reaction cell with smaller inner void volume: RTD characteristics

Because of the significant empty volume, approximately 12.5 g of 3 mm-diameter glass beads (Fisher Scientific, Catalog No. 11-312A:) were added to the inner volume of the cell which reduced the void volume from ~12.5 to ~3.5 cm^3. The E curve of the reduced volume reaction cell as characterized by an Ar pulse experiment is shown in **Figure 2.4** (trace 2). Clear differences are observed when compared to the large inner void volume reaction cell (**Figure 2.4**, trace 3) including a sharper peak and shorter tail consistent with the reduced inner volume and less stagnant gas. The RTD characteristics of Ar and other gases (CO_2, H_2, and O_2) through this cell are summarized in **Table 2.2.** From these results, a reduced inner volume in the reaction cell is observed because of glass bead addition as shown by a substantial decrease in the overall mean residence time (MRT) and standard deviation through the reaction cell system to 26.2 and 17.5 s (from 34.1 and 25.8 s, **Table 2.1**), respectively. This is even more evident from the time required for the MS to detect 90% of the pulsed gas, which decreased from 64.5 to 44.7 s. Of more

relevance, however, is the MRT through the reaction cell ($t_{m,1}$) which decreased about 40% from 21.3 to 12.7 s with added glass beads. These values, although larger than those in many transmission reaction cells of a few seconds, are quite encouraging as they show a significant reduction in MRT and demonstrate that simple modifications could be of practical use for experiments requiring rapid cell gas exchange times. An additional experiment was carried out at carrier flow rates of 120 cm^3/min and same pulse volume (**Table A.1**, appendix A) to further confirm the smaller gas mean residence time (a factor of 2) obtained in the cell with the reduced volume (with beads ~4s *vs* without beads ~8s), although at the expense of sample heat loss due to convection which can result in larger temperature differences between the sample and surroundings as discussed in following sections.

Table 2.2. Residence time distribution of various gases in the in situ reaction system with a reduced inner volume cell (~3.5 cm^3, with glass beads added)

Gas	**$t_{m,r}$ (σ) (s)**	**t $RTD_{90\%}$ (s)**	**$\tau_{p,r}$ (s)**	**$\tau_{p,b}$ (s)**	**$t_{m,1}$ (s)**	**$t_{m,2}$ (s)**
Ar	25.3 (16.6)	44.3	8.9	3.9	12.2	4.2
CO_2	27.4 (22.0)	46.4	9.9	3.9	13.2	4.3
H_2	25.5 (15.5)	43.5	8.9	4.9	12.9	3.7
O_2	26.7 (15.9)	44.4	9.9	5.9	12.5	4.3
Average	26.2	44.7	9.4	4.7	12.7	4.1

$t_{m,r}$ = mean residence time of pulse gas to reach MS detector (via in situ reaction cell with beads), σ = standard deviation, t RTD90% = residence time required for 90% of the pulse gas to reach the MS detector, $\tau_{p,r}$ = space time for a plug flow reactor: tubing line before in situ reactor (with beads), $\tau_{p,b}$ = space time for a plug flow reactor: tubing line bypassing in situ reactor, $t_{m,1}$ = mean residence time of pulse gas through in situ reactor based on an ideal CSTR, $t_{m,2}$ = mean residence time of pulse gas in mass spectrometer before reaching detector based on an ideal CSTR. Experimental conditions: He carrier 45 cm^3/min, 50 μL gas pulse, 1 bar, 25 °C, reaction cell with glass beads (cell dead volume ~3.5 cm^3).

2.3.1.3. Reaction cell volume vs pulse experiments: ideal reactor models

To gain more insight into the flow mode in the in situ reaction cell with reduced inner volume, the residence time distribution (RTD) functions for several ideal reactor models were investigated. As shown in **Figure 2.5**, the reactor models for the reaction cell system include continuous-stirred tank reactor (CSTR), plug-flow reactor (PFR), as well as laminar flow reactor (LFR). For an ideal CSTR, the RTD can be derived from a material balance on the inert gas pulse and is given by:

CSTR:
$$E(t) = \frac{e^{-t/\tau}}{\tau} \quad (9)$$

This is a particularly important model as the relatively complex geometry of the reaction cell and the large size of the MS chamber relative to the size of the transfer tubing imply their RTD response should have such type of reactor behavior. In practice, a reactor RTD is likely to be better modelled by a series of CSTR reactors of equal volume as described in the literature [55]:

n CSTRs in Series:
$$E(t) = \frac{t^{n-1}}{(n-1)!}\frac{e^{-t/\tau}}{\tau^n} \quad (10)$$

Another simple useful model is the RTD model for two CSTR in series of different volumes [52]:

Two CSTRs in Series, $V_s \neq V_L$:
$$E(t) = \frac{1}{\tau(2m-1)}\left\{e^{-t/m\tau} - e^{-t/(1-m)\tau}\right\} \quad (11)$$

Where: m is the fraction of the smaller reactor (V_s) with respect to the combined volume of the reactors ($V_s + V_L$), $m = V_s/(V_s + V_L)$

The RTD function of an ideal PFR is given by a simple spike to infinite (as all molecules leaving the reactor spend and leave at the same time, τ, the nominal space time) as mathematically expressed by the Dirac delta function.

PRF:
$$E(t) = \delta(t-\tau) \quad (12)$$

Where δ(x) is the delta Dirac function with the following properties:

$$\delta(x) = 0 \qquad x \neq 0$$
$$\delta(x) = \infty \qquad x = 0$$

Lastly, since calculated Reynolds numbers were small (<100), the RTD model for a LFR was also considered as determined by:

LFR:
$$E(t) = 0 \qquad t < \frac{\tau}{2} \quad (13a)$$

$$E(t) = \frac{\tau^2}{2t^3} \qquad t \geq \frac{\tau}{2} \tag{13b}$$

Figure 2.6 presents the RTD response results for an Ar pulse (trace 2) and comparison to RTD models for CSTR (trace 3), PFR (trace 1), and LFR (trace 4) reactors. Qualitatively from the shape of the experimental RTD for bypass and through the in situ reaction cell (**Figure 2.3**), the results could be described by a CSTR model. A single (Equation 9) or two CSTR (Equation 10) in series of equal volume failed to fit the data (not shown), however, as expected from the larger MRT in the reaction cell ($t_{m,1}$) than the MS detection chamber ($t_{m,2}$) shown in **Table 2.2**, the two CSTR in series of different volume (Equation 11) gave a more reasonable fitting (**Figure 2.6**, trace 3). This model results in a MRT (τ) of 13.8 s and a value of m of 0.24. Although the MRT for the 2-CSTR model, τ = 13.8 s, tracks with the experimental results, is somewhat smaller than the values for $t_{m,1}+t_{m,2}$ = 16.4 s. This can be the result of non-ideal behavior of the reaction cell due to its rather complex geometry and empty voids in the packed beads that could promote a delayed response from stagnant gas in inner volume pockets [51, 52].

Additionally, the first observation from the experimental RTD is the evolution of a rapid and sharp peak (13.8 s in **Figure 2.6**, trace 2 or 4.9 s after correcting for $\tau_{p,r}$) corresponding closely to the reactor nominal space time ($\tau_n = V/\nu$ = 4.7 s) (**Figure 2.6**, trace 1), which suggests that only a small fraction of the gas feed rapidly evacuates the cell volume, likely in a laminar fashion (**Figure 2.6**, trace 4). The second observation, the long tail of the RTD response with respect to the ideal 2-CSTR ($V_s \neq V_L$) RTD model, indicates the presence of inner volume pockets where the pulse gas resides temporarily delaying its evacuation and detection in the MS. These results combined are consistent with a reduced inner volume due to the addition of glass beads and the formation of beads interstitial spaces. Lastly, the obtained value of m = 0.24 indicates that the reaction cell, with a larger MRT than that of the MS detection chamber ($t_{m,1} > t_{m,2}$), possesses an inner volume that is approximately three times larger that of the MS detection chamber.

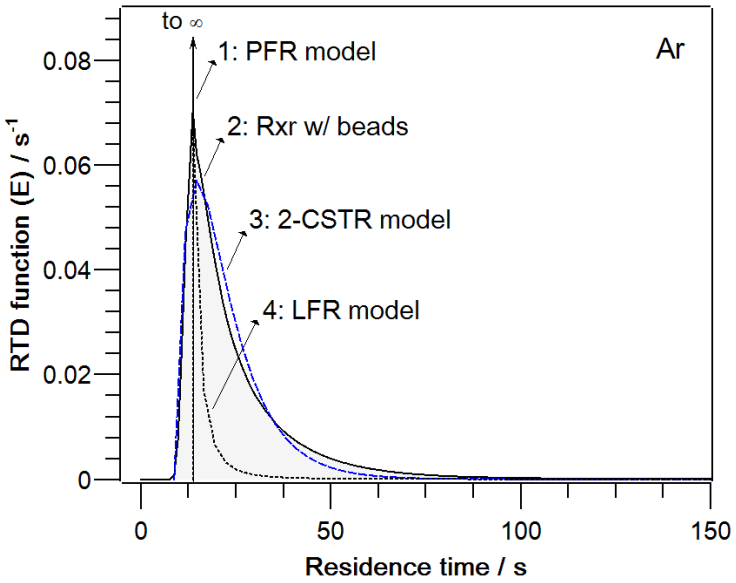

Figure 2.6. Residence time distribution (RTD) profiles of argon gas pulses at room temperature through the reaction cell with beads to reduce inner volume (trace 2) and corresponding reactor models: plug-flow reactor (PFR, trace 1), two continuous-stirred tank reactors (CSTR, trace 3) of different volume in series, and laminar flow reactors (LFR, trace 4). The residence time for the models corresponded to Residence time (in **Figure 1.6**) − $\tau_{p,r}$. Conditions: ambient temperature, 1 atm, 50 μL loop, He flow of 45 std cm^3/min.

In summary, the RTD responses of various pulsed gases in the in situ reaction cell indicated that it possesses a significant inner volume resulting in mean residence times (21.3 s) much larger than the nominal space time (4.7 s). This MRT can be significantly reduced (40%) to a value of 12.7 s by simple addition of glass beads which reduced the inner volume (~12.5 to ~3.5 cm^3). Although, the sample in the reaction cell is expected to resemble a fixed bed reactor, the flow dynamics and gas residence time are reasonably described by a CSTR RTD model. A previous report by Prairie et al. **[**56**]** has, understandably, treated the Harrick cell as a CSTR because it was modified to operate in recycle mode with flow rates of 2 L/min in the recycle loop. In other cases, however, when the cell was operated as a single pass reactor, as reported here, it was assumed the cell behaved as a CSTR [57, 58]. A report by Wulfers et al. **[**59**]** is, perhaps, one of the few studies that fitted gas exchanged data in the Harrick cell to a CSTR model to justify this behavior.

Overall, this analysis was possible by a detailed description of the RTD contributions from transfer lines and MS detection chamber that permitted isolation of the RTD of the reaction cell. While the described RTD analysis is specific to the current reaction setup (and which can be argued is the case for any in situ spectroscopy study), the method developed here demonstrates how to

isolate residence times in the reaction cell for comparison with other cells regardless of transfer lines dimensions and mass spectrometer analysis volume (as this is corrected by a bypass measurement). This method is, therefore, of general application to any reaction cell, including transmission and diffusion reflectance cells, which are the most commonly employed for spectroscopic studies heterogeneous catalysis. To the best of our knowledge, this is the first time such type of extensive analysis has been applied to the study of in situ spectroscopic reaction cells.

2.3.2. Sample vs external cell wall and probe temperatures

Another important aspect in the operation of in situ cells for catalysis research is the adequate measurement of a catalyst sample's temperature. This is not a trivial problem as very often temperature gradients exist between the catalyst bed and the heating source (e.g., heater cartridge, heating wire/blanket, usually placed outside the sample location) and also because the temperature monitoring is not in the sample itself [2, 60]. In such type of configuration, gradients between an external temperature and temperatures measured in the vicinity of the catalyst surface can be well over 100 °C when the catalyst bed temperature is close to 500 °C [61-63].

The Harrick diffuse reflectance reaction cell is originally configured with one thermocouple to monitor the temperature near the heat cartridge even though the current default temperature controller can handle two thermocouples and cascade control. This thermocouple location (thermocouple #11 in **Figure 2.2**) does not necessarily represent the sample temperature and this issue has been raised by several groups [2, 61-63] for many years and it is still quite surprising most in situ/operando studies do not report how sample temperature was measured. In this study, a second thermocouple was added (#8 in **Figure 2.1**, and #12 in **Figure 2.2**) to the sample cup, without requiring major modifications to the reaction cell, to monitor the sample temperature as it was in direct contact with the catalyst and placed just under the sample top surface. This thermocouple placing ensures improved sample contact and measurement of a representative sample surface temperature where spectroscopic measurements are being carried out. A recent extensive study by Meunier and co-workers [62] showed that in various cell configurations, a thermocouple in the middle of the catalyst bed (unlike that placed underneath the grid holding the sample bed) resulted in temperatures that closely resembled the sample surface temperature as measured by a pyrometer. This study clearly justifies our sample thermocouple placing and those reported by others to avoid flawed or falsified data [61, 63, 64].

To understand the thermal capabilities of the reaction cell, temperature profiles were measured by monitoring both thermocouples (#11 and #12 in **Figure 2.2**) for various sample temperature setpoints from 100 °C up to about 500 °C at a temperature ramp of 20 °C/min. The cell sample cup was filled with purified SiO_2 (<125 µm, Sigma Aldrich, P/N 84880) and heated under different flow rates of Ar and He from 5 to 100 std cm^3/min. For both gases, the temperature dependence was somewhat linear over the studied flow range, except for He at the highest flow rate (as shown in **Figure 2.7**). Under non-flow conditions, the maximum temperature of the catalyst bed was 520 °C, whereas the temperature near the heater core was 598 °C. Both temperatures can be linearly correlated with regression equations [42]. For all cases at lower temperatures, the temperature difference between the catalyst bed (e.g., @ 100 °C) and the heater core was moderate (e.g., T_{bed}-T_{core} ≈ 20-40 °C), but significantly higher at higher catalyst bed temperatures (e.g., 70-120 °C) (**Figure 2.7**). This temperature difference between the heater source (external part of the cell) and the sample bed can be attributed to excessive energy loss through the cell by radiation [24], conduction (due to cell material and geometry), and convection [24, 61]. These three loses collectively reduce the thermal efficiency of the cell.

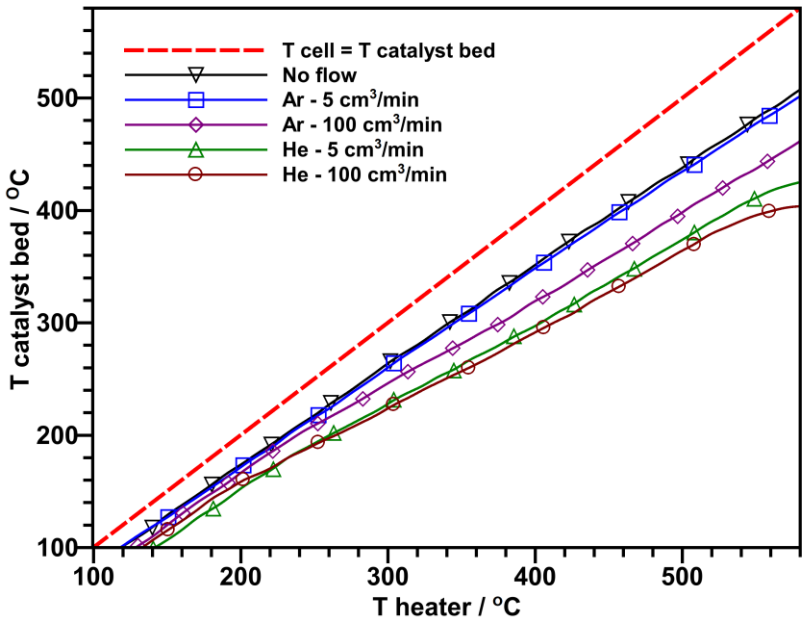

Figure 2.7. Correlation between reaction cell heating cartridge temperature and catalyst bed temperature. Sample is an amorphous low surface area <125 µm purified silica.

To minimize heat losses in the reaction cell, several approaches can be considered:

a) For radiative losses to the surroundings, the exposed surface of the reaction sample cup can be polished and/or shielded with a polished plate [61]. This reduces the surface emissivity (ε) which effectively decreases the rate of heat transfer due to radiation: $Q = \sigma\varepsilon A\ (T_h^4 - T_c^4)$. Alternatively, the surrounding temperature (cold side, T_c) can be increased to reduce the heat transfer driving force, however, in the case of diffuse reflectance cells, this is limited by the thermal stability of cell windows or in our case by the maximum operating temperature limitations of the fiber optics probe. These changes were not attempted in the present study and the surroundings were at ambient temperature. Meunier and co-workers [62] suggested that radiative losses are dominant in a related Spectra-Tech DR reaction cell operating with a windows-based dome, for which a reduction in the windows size could minimize heat losses at the expense of spectroscopic signal to noise ratio. Because of the fiber optics dome design reported here, radiative losses through dome windows was not an issue.

b) For conduction losses, as described by the one-dimension heat transfer equation by conduction: $Q = A(T_h - T_c)/R$ (R = heat resistance, e.g., δ/k for a slab), from the hot side (e.g., heater source, sample cup) to the cold side (e.g., sample cell surroundings), an increase in the thermal resistance can be explored by effective cell insulation with a poor heat conductor. For example, by adding, internally, a high temperature resistant and inert ceramic material around the sample cell. Both a decrease in the heat transfer area (A) and material thermal conductivity (k) is not possible in the current setup. A simple approach, however, is the increase in the cell temperature cold side (T_c) by, for example, increasing the cooling water temperature which would decrease the driving force and minimize sample gradient temperatures. These variations, however, would be at the expense of exposing cell windows and fiber optics probe to higher temperatures. These modifications were not tried in the current configuration, although they should be given further consideration for future new cell designs. Venter and Vannice [61] estimated that both radiative and conductive losses are not as pronounced (about one order of magnitude) as those expected for convection processes, thus, suggesting that efforts to improve reaction cell designs should be rather focused on the control of convective losses.

c) To reduce convective losses, for example, as implied from the general convective heat transfer equation: $Q = hA(T_h - T_c)$, it would require a decrease in the heat transfer coefficient (h), heat transfer area (A), or temperature driving force from the hot side (sample cup, T_h) to the cold side (inlet and outlet flow, $T_{c,in}$ and $T_{c,out}$) [61]. Changes to the heat transfer area are not possible in a

fixed commercial design, as in our case, but an increase to the temperature of the inlet gases by preheating feed lines would indeed contribute to reduce the (log-mean) average temperature during the heat transfer process. Lastly, the heat transfer coefficient (h) for convection in porous media at low (<2000) Reynolds numbers can be estimated from adimensional correlations of the type: $Nu = aRe^{0.6}Pr^{0.33}$, where $Nu = {hD}/{k}$, $Re = {\rho uL}/{\mu}$, and $Pr = {c_p\mu}/{k}$ are Nusselt, Reynolds, and Prandtl numbers [65]. Experimentally, it has been found that the heat transfer coefficient is only mildly dependent on Re number for Re below a few hundred (typical of lab scale reactors) [65], implying that control of heat losses due to convection can be addressed by a decrease of the cell characteristic length (D) or gas inlet composition and, therefore, gas properties (i.e., k, c_p, μ). Cell characteristics (e.g., D) are fixed for a given design, however, gas nature and inlet conditions will have a more marked effect on the heat transfer coefficient, h. This can be observed in **Figure 2.7**, where high gas flow and gas nature (Ar vs He) have a marked effect in the temperature difference between the catalyst bed and the cell heater as high flowrates and the use of a high thermal conductivity gas such as He (k = 0.157 W/m/K) is more efficient at cooling the catalyst sample than by employing low flowrates or Ar that has a thermal conductivity almost ten times lower (k = 0.018 W/m/K). Effective cooling by He of the catalyst sample leads to a wider temperature difference (which can be minimized by pre-heating of the incoming gas) leading to maximum attainable temperature of the catalyst bed much lower than with Ar. The large temperature differences between the catalyst bed and the cell heater shown in **Figure 2.7** represent worst case heat loss scenario as the in situ reaction cell gas feeding lines were all kept at ambient temperature (25 °C).

To better visualize the temperature profile in various parts of the reaction cell, especially in the region around the catalyst bed, a preliminary thermal simulation using Autodesk Fusion 360 was performed. Although the simulation mainly included radiation and free convection contributions, it still provided trends of temperature profiles in this relatively complex cell design. To achieve this, the exact geometry and dimensions of the modified cell were loaded in the software. The simulation determines the steady-state temperature distribution of the reactor and its components by use of a heat source (the heating rod) which was set to 550 °C to closely match the actual cell temperature maximum capacity. Certain parts of the reaction cell that are in contact with the atmosphere dissipate heat via convection and radiation such as the reactor body, the metal inlet and outlet, and the outer surface of the heater chamber that is in contact with the inlet gas. Heat

transfer through other solid sections and contacts were controlled by conduction via the cell stainless steel material.

The heat transfer by convection was calculated using the equation: $Q = hA(T_h - T_c)$, a value of 10 W/m^2/K was chosen for h in free convection into air since there was no forced cooling applied to the reactor setup (non-flow condition) [66]. For the calculation of heat transfer via radiation: $Q = \sigma\varepsilon A\,(T_h^4 - T_c^4)$, an emissivity value (ε) of 0.4 was chosen to represent this specific alloy of stainless steel [67], where σ is the Stefan-Boltzmann constant, and T_c is the ambient temperature of the surrounding environment. **Figure 2.8** shows the cut off and expanded views of temperature distribution for the cell in which the heating cartridge surface was set to 550 °C. As expected, the heater enclosure inside the reactor is hotter than the sample cup as some heat is lost as it conducts to the sample. A temperature difference between the sample cup and the heater surface of only 17 °C under non-flow conditions suggests the possible presence of significant internal radiation and convection in the cell void space (#6 in **Figure 2.2**), not considered in this simulation, which would account for the larger experimentally observed temperature difference (~70 °C, **Figure 2.7**). Losses due to gas nature and flow convection would also contribute significantly to the temperature differences observed with flowing He (~140 °C) and Ar (~100 °C). The results also show that the cell gas outlet temperature will be higher than that at the inlet, as observed experimentally. This points out to a feed preheating as a simple way of minimizing heat losses by reducing the convective heat transfer driving force. In summary, these preliminary results show that internal conduction and convection from the heater core to the surroundings also contributes to observed heat losses and temperature profile in the cell internals complex design. Heat losses due to gas flow are expected to contribute to a similar extent. Further simulations are under way for novel reaction cell designs to improve heat transfer to sample, sample temperature uniformity, and to minimize heat losses.

In addition to temperature measurements of the sample and cell heater, the temperature of the fiber optics probe was also monitored.

Table 2.3 summarizes probe temperature at the maximum temperatures achieved in the reaction cell with the given gases and flow rates. At the conditions studied, the maximum temperature of the UV-Vis probe was 110 °C, which is below the maximum operating temperature recommended by Avantes (200 °C) fiber optics probes.

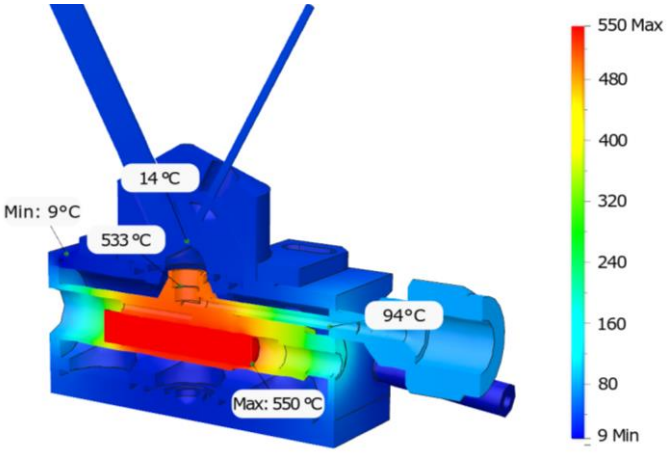

Figure 2.8. Cut off view of in situ reaction cell thermal simulation in non-flow condition. Conditions: Material = stainless steel, heating cartridge surface temperature = 550 °C, cooling line temperature = 9 °C, ambient temperature = 25 °C, convective heat transfer coefficient = 10 $W/m^2/K$, and emissivity = 0.4.

Here, it is worth noticing that the probe temperature does not correlate with the catalyst bed temperature, rather with the carrier gas ability to transport heat (thermal conductivity of He = 0.157 W/m/K vs Ar = 0.018 W/m/K). As He conducts heat more efficiently, the temperature of the probe (~3-5 mm above the sample) becomes hotter than when He is used as the carrier gas. All these results combined show that to avoid major temperature gradients (specially at high reaction temperatures), which may cause uncertainties during kinetic measurements, inert gases with relatively low thermal conductivities (e.g., Ar, N_2) should be employed. However, in experiments where safety plays a bigger role, for example, in the case of risk of runaway conditions, a gas with high thermal conductivity such as helium will be a safer choice.

Table 2.3. Maximum catalyst bed temperature *vs* UV-Vis probe temperature for different flow rates of argon and helium gas carrier

Gas	Flow rate / cm^3/min	T catalyst bed / °C	T probe / °C	$T_{bed} - T_{probe}$ / °C
None	0	520	93	427
Argon	5	519	52	467
	10	518	61	457
Helium	5	432	105	327
	10	425	110	315

2.3.3. In situ reaction cell reactivity testing H_2/O_2 cycles on Au/ZrO_2 catalysts

The modified in situ reaction cell was applied to the study of dynamic changes in the gold plasmon resonance peak position of a Au/ZrO_2 catalyst exposed to reducing and oxidizing cycling conditions. The tested Au/ZrO_2 catalyst had a specific surface area of 72.0 m^2/g and is composed of gold nanoparticles with an average particle size of 5.6 nm (**Figure 2.9**).

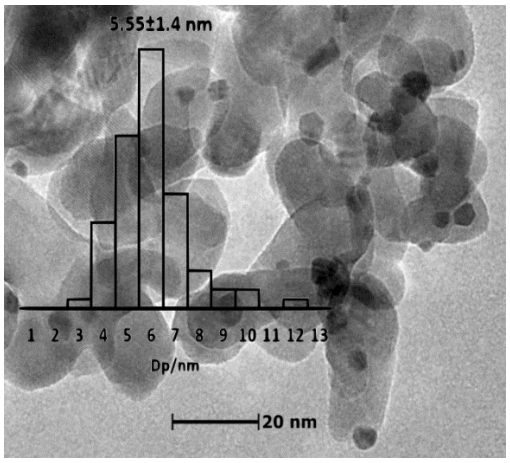

Figure 2.9. TEM image and particle size distribution of calcined $Au(1\%)/ZrO_2$ catalyst

In situ diffuse reflectance UV-Vis measurements of the catalyst were obtained in absorbance mode. Typical apparent absorbance *vs* wavelength spectra are shown in **Figure 2.10**. The figure shows the absorption spectra of the catalyst under oxidizing (O_2, red line) and reducing environments (H_2, blue line), where the peaks in the spectra correspond to gold's surface plasmon resonance (SPR) peak. The spectra show a sharp resonance between 400 and 650 nm, centered at 527 nm on exposure to O_2 which tails down above 700 nm. The peak position changes only slightly to ~526 nm on exposure to He as some O_2 desorbs. On exposure to H_2, the Au SPR peak position decreases as a likely result of O_2 reaction and/or desorption with time, stabilizing around 522 nm where blue shift or increase in the energy of peak position is seen. The changes in the Au SPR peak position are a likely result of changes to the dielectric function of the support and free electron density of the gold particles, both of which may change on catalyst exposure to different gases [45].

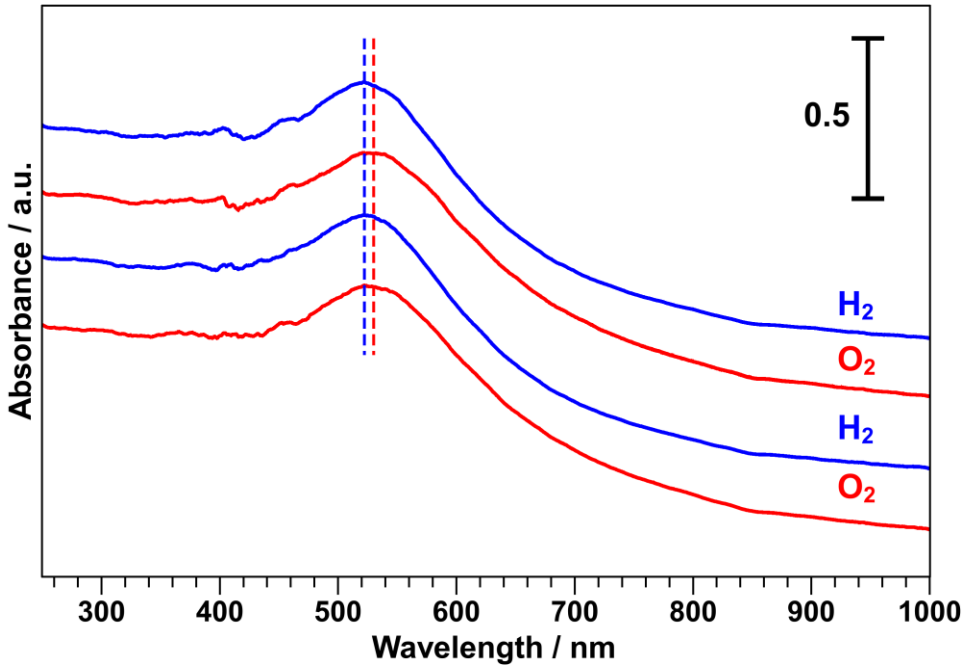

Figure 2.10. In Situ Au SPR During O_2/H_2 Adsorption Cycles on Au/ZrO_2 at 125 °C

Figure 2.11 shows the temporal changes in the Au SPR peak position on the $Au(1\%)/ZrO_2$ catalyst upon exposure to several cycles of O_2, H_2, and He over a continuing period of 5 h. The similarity in the Au SPR peak position after several cycles demonstrate that the observed Au SPR shifts are completely reversible. The magnitude of this temporal shift from oxidizing to reducing environment ($\Delta\lambda_{H2/O2}$ = 5 nm) reflects indirectly the amount of adsorbed oxygen near the gold nanoparticles as it desorbs or reduces with incoming hydrogen. The observed change in plasmon resonance upon exposure to O_2 can also be attributed to the transfer of charge from gold to oxygen species [50] adsorbed on specific sites of Au gold nanoparticles at the interface (e.g., periphery) with ZrO_2 support[68]. This plasmon resonance shift could help not only to account for adsorption of oxygen on gold but also to monitor Au adsorbed species in real time upon gas exposure. This initial study was possible by the modified cell with fiber optics UV-Vis probe described here that allowed continuous (for approximately 5 h) and rapid (every 2 s) monitoring of spectra to detect adsorption and desorption of surface species on gold nanoparticles. A more detailed description of the method extended to other gases and supported gold nanoparticles is currently in preparation.

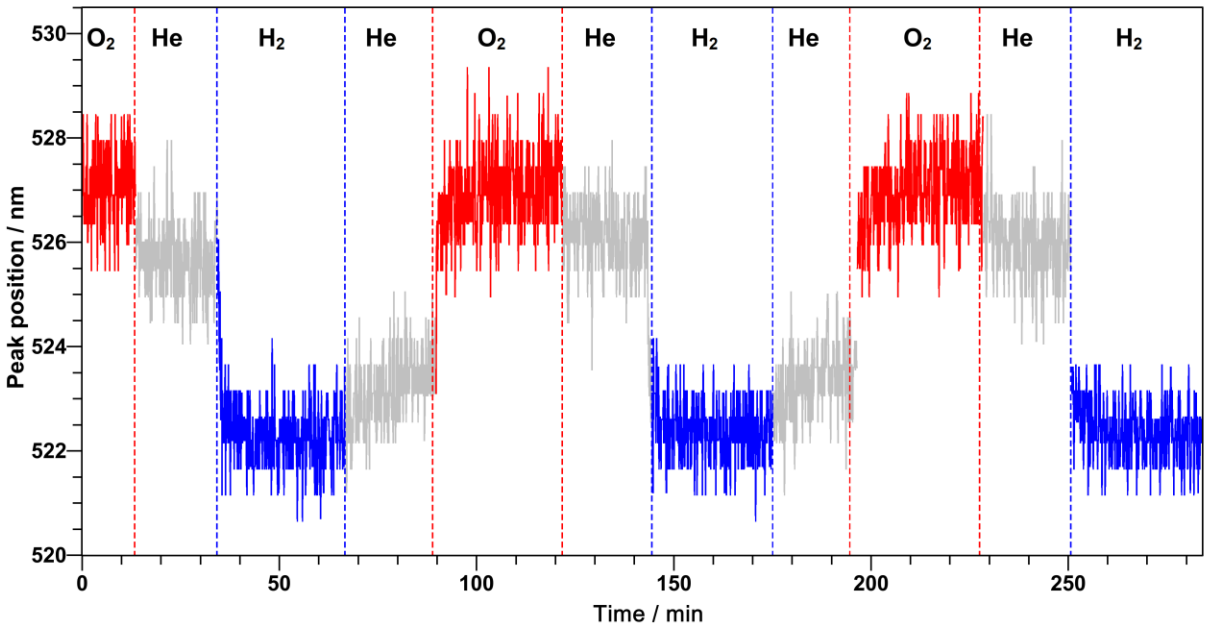

Figure 2.11. Change in Au SPR peak position on Au (1%)/ZrO_2 upon exposure to O_2, H_2 and He at 125 °C

2.4. Conclusions

In this study, a commercial Harrick diffuse reflectance reaction cell designed for mirror optics was modified for use with fiber optics and a miniature UV-Vis spectrometer equipped with a concave grating and CCD detector by addition of a low void volume home-made easily machinable dome to hold the probe. Other additional simple modifications were made to improve fluid dynamics (by reducing the cell void volume with addition of glass beads) and to monitor sample temperature (by addition of thermocouple in direct contact with the catalyst sample). A residence time distribution methodology to study the modified reaction cell via pulse experiments demonstrated a significant reduction in gas mean residence times in the reaction cell from 21 s to about 13 s with glass beads addition at carrier gas flow rate of 45 cm^3/min (or ~4 s at carrier gas flow rate of 120 cm^3/min). These results highlighted significant challenges in the design of similar reaction cells with a gas residence time scale required for fast transient and kinetic experiments of less than a few seconds without incurring in significant heat losses due to convection at high carrier flow rates. Reactor modelling of the RTD fluid dynamic results also suggested that the reaction cell primarily behaved as a CSTR reactor. A thermal experimental and simulation study on the modified cell pointed out to significant heat losses reflected by a significant gradient between the

sample bed and the heater temperatures. Heat losses due to radiation, conduction, and convection are expected, although convection was shown to be dominant and greatly affected by the nature of the carrier gas. For example, carrier gases possessing poor thermal conductivity (e.g., Ar) were expected and shown to decrease heat losses due to convection, effectively decreasing temperature differences with the cell heater source. Additional modifications to reduce heat losses including operation at higher cooling jacket temperatures, preheating of feed lines, and insulation of sample cup with poorly conductive materials were also discussed. The utility of the modified cell was also demonstrated to monitor temporal changes of UV-Vis spectra in a Au/ZrO_2 catalyst exposed to oxidizing (O_2) and reducing (H_2) environments at high temperature. More specifically, rapid changes to the gold surface plasmon resonance peak in the visible region were observed on switching from O_2 to H_2 gas as a likely result of O_2 reduction and/or desorption, a process that was fully reversible and reproducible over several cycles and an extended period. In summary, the modified Harrick cell for operation with diffuse reflectance fiber optics proved adequate for analysis of adsorption and desorption transients on gold catalysts and which under high flow conditions with gases of low thermal conductivity, with feed preheating, and high cooling liquid temperature, it can further minimize heat losses and temperature gradients in the sample bed, beneficial for in situ and operando spectroscopic studies.

This work was published in ***Applied Catalysis A: General,*** 2018, 561, 7-18 (DOI: 10.1016/j.apcata.2018.05.009).

2.5. References

1. Thomas, J.M. and Thomas, W.J., *Principles and Practice of Heterogeneous Catalysis*. 2nd ed.; Wiley-VCH: Weinheim, Germany, **2015;** p 1-744.
2. Bravo-Suárez, J.J. and Srinivasan, P.D., Design characteristics of in situ and operando ultraviolet-visible and vibrational spectroscopic reaction cells for heterogeneous catalysis. *Catalysis Reviews: Science and Engineering* **2017**, pp1-151, DOI: 10.1080/01614940.2017.1360071.

3. Bañares, M.A., Operando methodology: combination of in situ spectroscopy and simultaneous activity measurements under catalytic reaction conditions. *Catalysis Today* **2005,** *100* (1–2), 71-77.
4. Meunier, F.C., The design and testing of kinetically-appropriate operando spectroscopic cells for investigating heterogeneous catalytic reactions. *Chemical Society Reviews* **2010,** *39* (12), 4602-4614.
5. G. Centi, J.L.N., C. Iapalucci, K. Brückman, E.M. Serwicka, Selective oxidation of n-pentane on 12-molybdovanadophosphoric acids *Applied Catalysis* **1989,** *46*, 197-212.
6. Centi, G., Lena, V., Trifiro, F., Ghoussoub, D., Aissi, C.F., Guelton, M., and Bonnelle, J.P., Active form of 12-vanadomolybdophosphoric acids in n-butane selective oxidation. *Journal of the Chemical Society, Faraday Transactions* **1990,** *86* (15), 2775-2782.
7. D. Casarini, G.C., P. Jiru, V. Lena, Z. Tvaruzkova, Reactivity of Molybdovanadophosphoric Acids: Influence of the Presence of Vanadium in the Primary and Secondary Structure. *journal of catalysis* **1993,** *143*, 325-344.
8. M.N. Timofeeva, A.V.D., A.A. Davydov, I.V. Kozhevnikov, UV-Vis and ESR spectroscopic studies of the adsorption of arenes on the heteropoly acid $H_3PW_{12}O_{40}$. *Journal of Molecular Catalysis* **1993,** *79*, 21-28.
9. Melsheimer, J., Mahmoud, S.S., Mestl, G., and Schlögl, R., In situ UV-Vis diffuse reflectance spectroscopy of reduction–reoxidation of heteropoly compounds by methanol and ethanol: a correlation between spectroscopic and catalytic data. *Catalysis Letters* **1999,** *60* (3), 103-111.
10. Klokishner, S., Melsheimer, J., Ahmad, R., Jentoft, F.C., Mestl, G., and Schlögl, R., Influence of dehydration effects on the optical spectra of $H_4PVMo_{11}O_{40}$ in the visible and near infrared range: intra- and intercenter optical transitions in the V–Mo cluster. *Spectrochimica Acta Part A: Molecular and Biomolecular Spectroscopy* **2002,** *58* (1), 1-15.
11. Bensalem, A., Weckhuysen, B.M., and Schoonheydt, R.A., In Situ Diffuse Reflectance Spectroscopy of Supported Chromium Oxide Catalysts: Kinetics of the Reduction Process with Carbon Monoxide. *The Journal of Physical Chemistry B* **1997,** *101* (15), 2824-2829.
12. Grubert, G., Rathouský, J., Schulz-Ekloff, G., Wark, M., and Zukal, A., Reducibility of vanadium oxide species in MCM-411. *Microporous and Mesoporous Materials* **1998,** *22* (1–3), 225-236.

13. Weckhuysen, B.M., Verberckmoes, A.A., Debaere, J., Ooms, K., Langhans, I., and Schoonheydt, R.A., In situ UV–Vis diffuse reflectance spectroscopy — on line activity measurements of supported chromium oxide catalysts: relating isobutane dehydrogenation activity with Cr-speciation via experimental design. *Journal of Molecular Catalysis A: Chemical* **2000,** *151* (1–2), 115-131.
14. Jentoft, F.C., Ultraviolet–Visible–Near Infrared Spectroscopy in Catalysis: Theory, Experiment, Analysis, and Application Under Reaction Conditions. *Advances in Catalysis* **2009,** *52*, 129-211.
15. Leftin, H.P., Electronic Spectra Of Adsorbed Molecules: Stable Carbonium Ions On Silica Alumina. *The Journal of Physical Chemistry* **1960,** *64* (11), 1714-1717.
16. Tinker, H.B. and Morris, D.E., High Pressure, High Temperature Infrared-Ultraviolet-Visible Spectrophotometer Cell for in situ Catalyst Studies. *Review of Scientific Instruments* **1972,** *43* (7), 1024-1026.
17. Gallei, E. and Schadow, E., Ultrahigh-vacuum, high pressure and temperature infrared-ultraviolet-visible spectrophotometer cell. *Review of Scientific Instruments* **1974,** *45* (12), 1504-1506.
18. Hicks, R.F., Kellner, C.S., Savatsky, B.J., Hecker, W.C., and Bell, A.T., Design and construction of a reactor for in situ infrared studies of catalytic reactions. *Journal of Catalysis* **1981,** *71* (1), 216-218.
19. Edwards, J.F. and Schrader, G.L., In Situ FT-IR Spectroscopy of the Adsorption of CO on Methanol Catalysts. *Applied Spectroscopy* **1981,** *35* (6), 559-563.
20. Melsheimer, J. and Ziegler, D., Ethene transformation on HZSM-5 studied by combined UV-VIS spectroscopy and on-line gas chromatography. *Journal of the Chemical Society, Faraday Transactions* **1992,** *88* (14), 2101-2108.
21. Mirth, G., Eder, F., and Lercher, J.A., Design and Application of a New Reactor for in Situ Infrared Spectroscopic Investigations of Heterogeneously Catalyzed Reactions. *Applied Spectroscopy* **1994,** *48* (2), 194-197.
22. Weng, W.Z., Chen, M.S., Yan, Q.G., Wu, T.H., Chao, Z.S., Liao, Y.Y., and Wan, H.L., Mechanistic study of partial oxidation of methane to synthesis gas over supported rhodium and ruthenium catalysts using in situ time-resolved FTIR spectroscopy. *Catalysis Today* **2000,** *63* (2–4), 317-326.

23. Lesage, T., Verrier, C., Bazin, P., Saussey, J., and Daturi, M., Studying the NO-trap mechanism over a Pt-Rh/Ba/Al2O3 catalyst by operando FT-IR spectroscopy. *Physical Chemistry Chemical Physics* **2003,** *5* (20), 4435-4440.
24. Yang, Y., Disselkamp, R.S., Szanyi, J., Peden, C.H.F., Campbell, C.T., and Goodwin, J.G., Design and operating characteristics of a transient kinetic analysis catalysis reactor system employing in situ transmission Fourier transform infrared. *Review of Scientific Instruments* **2006,** *77* (9), 094104.
25. Clark, J.C., Dai, S., and Overbury, S.H., Operando studies of desorption, reaction and carbonate formation during CO oxidation by Au/TiO2 catalysts. *Catalysis Today* **2007,** *126* (1–2), 135-142.
26. Wang, J., Kispersky, V.F., Nicholas Delgass, W., and Ribeiro, F.H., Determination of the Au active site and surface active species via operando transmission FTIR and isotopic transient experiments on 2.3 wt.% Au/TiO2 for the WGS reaction. *Journal of Catalysis* **2012,** *289*, 171-178.
27. Kock, E.-M., Kogler, M., Pramsoler, R., Klotzer, B., and Penner, S., A high-temperature, ambient-pressure ultra-dry operando reactor cell for Fourier-transform infrared spectroscopy. *Review of Scientific Instruments* **2014,** *85* (8), 084102.
28. Fringeli, U.P., Goette, J., Reiter, G., Siam, M., and Baurecht, D., Structural investigations of oriented membrane assemblies by FTIR-ATR spectroscopy. *AIP Conference Proceedings* **1998,** *430* (1), 729-747.
29. Urakawa, A., Wirz, R., Bürgi, T., and Baiker, A., ATR-IR Flow-Through Cell for Concentration Modulation Excitation Spectroscopy: Diffusion Experiments and Simulations. *The Journal of Physical Chemistry B* **2003,** *107* (47), 13061-13068.
30. Meemken, F., Muller, P., Hungerbuhler, K., and Baiker, A., Simultaneous probing of bulk liquid phase and catalytic gas-liquid-solid interface under working conditions using attenuated total reflection infrared spectroscopy. *Review of Scientific Instruments* **2014,** *85* (8), 084101.
31. Aguirre, A., Kler, P.A., Berli, C.L.A., and Collins, S.E., Design and operational limits of an ATR-FTIR spectroscopic microreactor for investigating reactions at liquid–solid interface. *Chemical Engineering Journal* **2014,** *243*, 197-206.

32. Hamminga, G.M., Mul, G., and Moulijn, J.A., Real-time in situ ATR-FTIR analysis of the liquid phase hydrogenation of -butyrolactone over Cu-ZnO catalysts: A mechanistic study by varying lactone ring size. *Chemical Engineering Science* **2004,** *59* (22–23), 5479-5485.
33. Panella, B., Vargas, A., Ferri, D., and Baiker, A., Chemical Availability and Reactivity of Functional Groups grafted to Magnetic Nanoparticles monitored In situ by ATR-IR Spectroscopy. *Chemistry of Materials* **2009,** *21* (18), 4316-4322.
34. Jentoft, F.C., Electronic Spectroscopy: Ultra Violet-Visible and near IR Spectroscopies. In *Characterization of Solid Materials and Heterogeneous Catalysts*, Wiley-VCH Verlag GmbH & Co. KGaA: **2012;** pp 89-147.
35. Puurunen, R.L., Beheydt, B.G., and Weckhuysen, B.M., Monitoring Chromia/Alumina Catalysts in Situ during Propane Dehydrogenation by Optical Fiber UV–Visible Diffuse Reflectance Spectroscopy. *Journal of Catalysis* **2001,** *204* (1), 253-257.
36. Chlebda, D., Stachurska, P., Jędrzejczyk, R., Kuterasiński, Ł., Dziedzicka, A., Górecka, S., Chmielarz, L., Łojewska, J., Sitarz, M., and Jodłowski, P., DeNOx Abatement over Sonically Prepared Iron-Substituted Y, USY and MFI Zeolite Catalysts in Lean Exhaust Gas Conditions. *Nanomaterials* **2018,** *8* (1), 21.
37. Bürgi, T., Combined in situ attenuated total reflection infrared and UV–vis spectroscopic study of alcohol oxidation over Pd/Al2O3. *Journal of Catalysis* **2005,** *229* (1), 55-63.
38. Sobalík, Z., Jíša, K., Jirglová, H., and Bernauer, B., Simultaneous FTIR/UV-Vis study of reactions over metallo-zeolites: Approach to quantitative in situ studies. *Catalysis Today* **2007,** *126* (1), 73-80.
39. Brückner, A., Kondratenko, E., Kondratenko, V., Radnik, J., and Schneider, M., In Situ Non-Vibrational Characterization Techniques to Analyse Oxidation Catalysts and Mechanisms. In *Handbook of Advanced Methods and Processes in Oxidation Catalysis*, Imperial College Press: **2014;** pp 496-548.
40. Melsheimer, J., Thiede, M., Ahmad, R., Tzolova-Muller, G., and Jentoft, F.C., Improved experimental setup for in situ UV-Vis-NIR spectroscopy under catalytic conditions. *Physical Chemistry Chemical Physics* **2003,** *5* (20), 4366-4370.
41. Li, B. and Gonzalez, R.D., Design and Construction of a DRIFTS Accessory and an in Situ Heatable Sample Cell. *Applied Spectroscopy* **1998,** *52* (11), 1488-1491.

42. Schubert, M.M., Häring, T.P., Bräth, G., Gasteiger, H.A., and Behm, R.J., New DRIFTS Cell Design for the Simultaneous Acquisition of IR Spectra and Kinetic Data Using On-Line Product Analysis. *Applied Spectroscopy* **2001,** *55* (11), 1537-1543.
43. Dal Santo, V., Dossi, C., Fusi, A., Psaro, R., Mondelli, C., and Recchia, S., Fast transient infrared studies in material science: development of a novel low dead-volume, high temperature DRIFTS cell. *Talanta* **2005,** *66* (3), 674-682.
44. Weckhuysen, B.M., Ultraviolet-Visible Spectroscopy. In *In-Situ Spectroscopy of Catalysts*, B.M. Weckhuysen, Ed. American Scientific Publishers: Stevenson Ranch, CA, **2004;** pp 255-292.
45. Kreibig, U. and Vollmer, M., *Optical properties of metal clusters*. Springer: Berlin (Germany), **1995;** p 1-553.
46. Beitia, C., Borensztein, Y., Lazzari, R., Nieto, J., and Barrera, R.G., Substrate-induced multipolar resonances in supported free-electron metal spheres. *Physical Review B* **1999,** *60* (8), 6018-6022.
47. Noguez, C., Surface Plasmons on Metal Nanoparticles: The Influence of Shape and Physical Environment. *The Journal of Physical Chemistry C* **2007,** *111* (10), 3806-3819.
48. Sosa, I.O., Noguez, C., and Barrera, R.G., Optical Properties of Metal Nanoparticles with Arbitrary Shapes. *The Journal of Physical Chemistry B* **2003,** *107* (26), 6269-6275.
49. Myroshnychenko, V., Rodriguez-Fernandez, J., Pastoriza-Santos, I., Funston, A.M., Novo, C., Mulvaney, P., Liz-Marzan, L.M., and Garcia de Abajo, F.J., Modelling the optical response of gold nanoparticles. *Chemical Society Reviews* **2008,** *37* (9), 1792-1805.
50. Borensztein, Y., Delannoy, L., Djedidi, A., Barrera, R.G., and Louis, C., Monitoring of the Plasmon Resonance of Gold Nanoparticles in Au/TiO_2 Catalyst under Oxidative and Reducing Atmospheres. *The Journal of Physical Chemistry C* **2010,** *114* (19), 9008-9021.
51. Levenspiel, O., *The Chemical Reactor Omnibook*. 4th ed.; OSU Book Stores, Inc.: Corvallis, OR, **1993;** p pp. 1-750.
52. Fogler, H.S., Distribution of Residence Times for Chemical Reactors. In *Elements of Chemical Reaction Engineering*, 4th ed.; Prentice Hall: Upper Saddle River, NJ, **2005;** pp 867-944.
53. Levenspiel, O., *Chemical reaction engineering*. New York: John Wiley & Sons: **1999**.

54. Marrero, T.R. and Mason, E.A., Gaseous Diffusion Coefficients. *Journal of Physical and Chemical Reference Data* **1972,** *1* (1), 3-118.
55. Rawlings, J.B. and Ekerdt, J.G., *Chemical reactor analysis and design fundamentals*. Nob Hill Pub.: **2002**.
56. Prairie, M.R., Renken, A., Highfield, J.G., Ravindranathan Thampi, K., and Grätzel, M., A Fourier transform infrared spectroscopic study of CO_2 methanation on supported ruthenium. *Journal of Catalysis* **1991,** *129* (1), 130-144.
57. Aguirre, A. and Collins, S.E., Selective detection of reaction intermediates using concentration-modulation excitation DRIFT spectroscopy. *Catalysis Today* **2013,** *205*, 34-40.
58. Vecchietti, J., Baltanás, M.A., Gervais, C., Collins, S.E., Blanco, G., Matz, O., Calatayud, M., and Bonivardi, A., Insights on hydride formation over cerium-gallium mixed oxides: A mechanistic study for efficient H2 dissociation. *Journal of Catalysis* **2017,** *345*, 258-269.
59. Wulfers, M.J., Tzolova-Müller, G., Villegas, J.I., Murzin, D.Y., and Jentoft, F.C., Evolution of carbonaceous deposits on H-mordenite and Pt-doped H-mordenite during n-butane conversion. *Journal of Catalysis* **2012,** *296* (0), 132-142.
60. Meunier, F.C., Pitfalls and benefits of in situ and operando diffuse reflectance FT-IR spectroscopy (DRIFTS) applied to catalytic reactions. *Reaction Chemistry & Engineering* **2016,** *1* (2), 134-141.
61. Venter, J.J. and Vannice, M.A., Modifications of a Diffuse Reflectance Cell to Allow the Characterization of Carbon-Supported Metals by DRIFTS. *Applied Spectroscopy* **1988,** *42* (6), 1096-1103.
62. Li, H., Rivallan, M., Thibault-Starzyk, F., Travert, A., and Meunier, F.C., Effective bulk and surface temperatures of the catalyst bed of FT-IR cells used for in situ and operando studies. *Physical Chemistry Chemical Physics* **2013,** *15* (19), 7321-7327.
63. Gao, X., Jehng, J.-M., and Wachs, I.E., In Situ UV–vis–NIR Diffuse Reflectance and Raman Spectroscopic Studies of Propane Oxidation over ZrO2-Supported Vanadium Oxide Catalysts. *Journal of Catalysis* **2002,** *209* (1), 43-50.
64. Bravo-Suárez, J.J., Bando, K.K., Fujitani, T., and Oyama, S.T., Mechanistic study of propane selective oxidation with H-2 and O-2 on Au/TS-1. *Journal of Catalysis* **2008,** *257* (1), 32-42.

65. Kuwahara, F., Shirota, M., and Nakayama, A., A numerical study of interfacial convective heat transfer coefficient in two-energy equation model for convection in porous media. *International Journal of Heat and Mass Transfer* **2001,** *44* (6), 1153-1159.
66. Kreith, F., Manglik, R.M., and Bohn, M.S., *Principles of Heat Transfer*. 7th ed.; Cengage Learning: Stamford, CT, **2011;** p 1-784.
67. Gardner, L. and Ng, K.T., Temperature development in structural stainless steel sections exposed to fire. *Fire Safety Journal* **2006,** *41* (3), 185-203.
68. Liu, Z.-P., Gong, X.-Q., Kohanoff, J., Sanchez, C., and Hu, P., Catalytic Role of Metal Oxides in Gold-Based Catalysts: A First Principles Study of CO Oxidation on TiO2 supported Au. *Physical Review Letters* **2003,** *91* (26), 266102.

Chapter 3. In Situ/Operando Spectroscopic Gold Plasmon Sensing of Adsorbed Oxygen (O_2-GPS): Activity Trends in CO Oxidation on Supported Gold Catalysts

3.1. Introduction

For a long time, gold has attracted the interest of mankind as a valuable metal for use as jewelry and commodity money because of its relatively rareness, malleability, and apparent chemical inertness. Discoveries around the 1980s by Haruta, Hutchings, and others, however, showed that highly dispersed gold is active as a catalyst for several reactions including olefin hydrogenation [1], acetylene hydrochlorination [2], CO [3], olefin [4], and alcohol oxidation [5]. This has open a whole new world of possibilities in heterogeneous catalysis, in particular, for highly dispersed gold nanoparticles (NPs) [6, 7]. Among all the reactions, oxidation on gold catalysts has been perhaps the most studied for its environmental and industrial relevance in the selective conversion of CO, production of propylene oxide, hydrogen peroxide, and alcohol oxidation products at mild conditions [7, 8]. Due to its optical properties, gold has also found use as a plasmonic sensor in biomedical applications for the determination of kinetics of adsorption of biocompatible chemicals [9, 10] and more recently as plasmonic catalysts [11]. These applications exploit gold nanoparticles ability to absorb or scatter light in the visible spectrum resulting in strong electromagnetic fields around the nanoparticle [12].

In heterogeneous catalysis, in situ and operando spectroscopic characterizations are required to probe catalysts active sites and adsorbed species at relevant reaction conditions of temperature, pressure, and reactants partial pressures [13]. In combination with kinetic methods, they can be also used to evaluate the kinetic relevance of such surface species in a catalytic cycle [14, 15]. In CO oxidation by gold catalysts, in situ spectroscopic studies have provided a better understanding of intermediate adsorbed species, support oxygen vacancies, adsorbed oxygen, gold particle size and oxidation state, among others via Fourier transform infrared (FTIR) [16-26], Raman [22, 27], UV-visible [22, 25], and X-ray absorption spectroscopies (XANES, EXAFS) [17,28-33] .Complementary computational and kinetic studies have also helped elucidate the intricacies of the reaction mechanism of CO oxidation on gold catalysts [7, 16, 24, 34, 35]. For example, the existence of various catalytic mechanisms have been reported of the Langmuir-Hinshelwood or

Mars-van Krevelen type, involving dual active sites (Au and Au-M interface neighboring sites) or single Au sites only, whose predominance depends on the presence or absence of water [16, 24], reaction temperature [36-38], and support nature [37-39], At temperatures below 353 K (80 °C), kinetic data supports the presence of a Langmuir-Hinshelwood mechanism, whereas at higher temperatures and dry conditions a Au assisted Mars-van Krevelen has been proposed [37, 38, 40]. At the latter conditions, oxygen active species have been proposed to be present along the perimeter of the Au/TiO_2 interface which react with adsorbed CO in a rate controlling step to form CO_2 [40]. The coverage of such adsorbed oxygen species has been probed extensively by pulse experiments in a TAP (temporal analysis of products) reactor, from which a correlation between the oxygen storage capacity (OSC) and CO conversion was observed for several supported gold catalysts at similar reaction conditions [37-39, 41].

While TAP reactor measurements have provided valuable insights into gold catalyzed oxidation reactions and coverage of adsorbed oxygen species, the technique is not carried out at pressures typical of continuous reactors and the analytical equipment required is costly (close to ~US$1M), of relatively limited access to most catalysis research laboratories (there are fewer than 20 TAP reactors in the world, and only four in the US), and only a limited number of people can operate, collect, and interpret TAP results. An alternative technique for adsorbed oxygen species measurement is the conventional temperature programmed reduction/oxidation (TPR/TPO) or titration via alternate O_2/CO pulses, which tends to be limited to reducible supports [42, 43]. The rate of exchange of surface oxygen was also reported via $^{18}O/^{16}O$ isotopic exchange on Au/CeO_2 catalysts as a method to determine adsorbed oxygen, but it requires the use of expensive labeled oxygen [43]. Another technique that has been used for determination of adsorbed oxygen species on gold catalysts is XANES. For example, Bokhoven and co-workers detected adsorbed oxygen species from the whiteline increase on the Au L_3 XANES of Au/TiO_2 [32] and Au/Al_2O_3 [33] upon exposure to oxygen, which decreased when reacted with CO to form CO_2. Similar observations were reported by one of us for Au/TiO_2 and Au/TS-1 during in situ transients of propane oxidation with H_2 and O_2 [44-46]. These last report demonstrated a correlation between the Au L_3 XANES whiteline and shifts in the gold plasmon resonance peak as tracked by UV-Vis spectroscopy. The latter spectroscopic technique is clearly more accessible and relatively affordable, and which could yield information on adsorbed oxygen species. Similar plasmon techniques have been applied for sensing: 1) charge transfer from Au to oxygen on Au-YSZ (Yttria-stabilized zirconia) [47], 2) on

thin films of Au-CeO_2 [48, 49], Au-SiO_2 [50], Au-TiO_2 [51, 52], and Au-ZrO_2 [51], in H_2, CO, and NO_2 in oxygen containing environments; and 3) on Au/TiO_2 powders in O_2, H_2, and CO atmospheres [53, 54]. Recently, the method was exploited to study heterogeneous catalysts via in situ transmission UV-Vis spectroscopy of thin catalyst coatings deposited over a glass substrate covered with nanofabricated gold disks [55, 56]. Application examples of this method include monitoring adsorbate coverage during CO and H_2 oxidation on Pt nanoparticles [55, 57], NO_x storage kinetics on Pt/BaO [55], sintering of Pt nanoparticles on Pt/SiO_2 [58] and Pt/Al_2O_3 [59], oxidation/reduction [56] and hydrogen uptake/release in Pd nanoparticles [60]. Recently, Hutchings and co-workers also showed that gold plasmon peak shifts during CO adsorption on Au/TiO_2 correlated with CO oxidation activity [25]. With the exception of UV-Vis spectroscopy on powder catalysts, all other techniques are of limited access, relative expensive, complex, or performed on nanofabricated model thin films. UV-Vis spectroscopy and gold plasmon resonance of (powder) catalysts to sense changes in properties relevant to gold catalysis, for example, due to adsorption/desorption of surface species, nanoparticle sintering, and support properties have been rarely exploited [25, 44-46, 53, 54].

In this work, we focused on the development of a simple, sensitive, and relatively affordable in situ gold plasmon resonance technique to characterize O_2 adsorption on gold nanoparticles supported on a variety of materials including SiO_2, Al_2O_3, ZrO_2, ZnO, and TiO_2 to establish a correlation between oxygen adsorption, Au surface site statistics, and catalytic activity for a model CO oxidation reaction. Here, gold nanoparticles serve the rare simultaneous role of nanosensors and catalysts, allowing the study of their adsorptive properties at conditions relevant to catalysis such as high temperatures and pressures. It will be shown that the relative amount of adsorbed oxygen as tracked by in situ gold plasmon resonance shifts of the gold catalysts at high temperature correlated well oxygen adsorption at the gold-support interface. Additionally, analysis of the adsorbed oxygen by in situ GPS during CO oxidation and its dependence with particle size as well as CO oxidation turnover frequency with gold site statistics suggested that O_2 adsorbs preferentially at the gold-support interface, a fraction of which is active for CO oxidation, whereas CO likely adsorbs on the gold nanoparticle surface sites. These results highlight the utility of the proposed technique, opening the possibility of extending its application to more in-depth studies of CO oxidation and to other oxidation reactions on gold catalysts, their kinetics, and unique access

to adsorbed species and catalyst surface changes at reaction conditions via in situ/operando spectroscopic characterization.

3.2. Experimental section

3.2.1. Catalysts preparation

Five different Au catalysts with a nominal metal loading of 1 wt% were prepared by the deposition-precipitation (DP) method using ammonia as the base titrant and commercial metal oxides of intermediate surface area (~10-70 m^2/g): SiO_2 (Grace, Davisil XWP 1000A), Al_2O_3 (Norpro, SA31132), ZnO (Strem Chemicals, 30-1405), (monoclinic) ZrO_2 (Alfa Aesar, 43814), and TiO_2 (P25, Aldrich, 718467). In a typical preparation, 1 g of the support was dispersed in 20 cm^3 of water (Fisher Chemical, HPLC) under stirring (MS-H-Pro Plus hotplate-stirrer, Scilogex). To this stirred slurry, 2.5 wt% NH_4OH (prepared from 14.8 N NH_4OH, Fisher, A669-212) was added dropwise to reach a pH of 9.5 monitored with a DrDAQ pH measuring kit (Pico Technology). After 5 min, about 20 mg of $HAuCl_4.3H_2O$ (Alfa Aesar, 36400) dissolved in 8 cm^3 of water was added dropwise concurrently with 2.5 wt% NH_4OH until the pH was 9.5. NH_4OH was used as the added base (instead the usual NaOH employed in DP) to ensure that all gold was deposited on all supports (including SiO_2) and to avoid catalyst contamination by Na. The solution was then stirred continuously for 1 h after which it was filtered, washed with abundant water and dried in vacuum for 12 h at room temperature. The catalysts were treated in static air at 393 K for 2 h (5 K/min) and 673 K for 4 h (4.5 K/min) in a Thermolyne 48000 muffle furnace (Barnstead International). Finally, the calcined catalysts were stored in dark vials and in sealed plastic bags to minimize light and moisture exposure. For comparison with these catalysts, experiments were also performed with AUROlite^{TM} Au(1 wt%)/TiO_2 (Strem chemicals, 79-0165).

3.2.2. Catalysts characterization

Fresh and used catalysts were characterized by transmission electron microscopy (TEM) using a FEI Tecnai F20 XT microscope operating at a 200 kV. The TEM samples were prepared by dispersing the catalyst in ethanol and sonicating for about 10 min. A drop of the dispersed catalyst was then suspended on a 400 mesh copper grid containing ultra-thin carbon film on a lacey carbon support film (P/N 01824, Ted Pella Inc.) Particle size and distribution were calculated for about 50-100 particles from TEM images as counted and analyzed by ImageJ software

(https://imagej.nih.gov/ij/). Catalysts and supports were also characterized by N_2 physisorption, X-ray diffraction, and SEM-EDX (**Table B.1**, **B.2**, **Figure B.1**-**B.8**).

3.2.3. In Situ gold surface plasmon resonance following O_2/He/H_2 cycles

For the in situ gold plasmon resonance experiments, the catalyst samples were placed in a modified high temperature in situ/operando diffuse reflectance Harrick reaction cell [61]. Originally designed for bench top scanning spectrometers, the cell was modified to enable faster transfer of gases and faster acquisition of in situ UV-Vis spectra. A thorough description of the modifications to the cell (including 3D pdf models and blueprints), its thermal analysis, and its flow dynamics are described in Chapter 2 [61]. The UV-Vis light contacting the catalyst originates from a preconfigured dual UV-Vis lamp set up that includes an SL3 Deuterium lamp and an SL1-filter halogen lamp (Stellar Net) through a 600 µm core diameter high-temperature fiber optics probe (Avantes) and which gets reflected to a Black-comet SR concave grating spectrometer equipped with a CCD detector (Model C, Stellar Net) for analysis. The spectra (1300 ms integration time, 1 scan) were collected over the 230-1080 nm range with scans averaged every ~1.35 s (for better signal to noise ratio) to enable the characterization of small changes to the gold plasmon resonance peak in real time and in situ on exposure to different gas atmospheres. To avoid deuterium spikes around 485 nm originating from the lamp, a U-330 filter was used. Prior to the in situ experiments, a given amount (**Table B.2**) of the freshly calcined catalysts was loaded to the in situ cell sample cup (~0.15 cm^3) where it was reduced for 30 min at 473 K with pure hydrogen at a flow rate of 45 cm^3/min. After reduction, the cell was flushed with helium (45 cm^3/min) and the temperature of the sample was brought down to 398 K (5 K/min). The catalyst sample was then exposed to oxygen (Matheson, UHP, 99.98%) for 30 min at a flow rate of 45 cm^3/min, flushed with helium (Matheson, UHP, 99.999%) for about 15-20 min to purge the lines and cell, and exposed to hydrogen for 30 min (45 cm^3/min; Matheson, UHP, 99.999%). This H_2/He/O_2 sequence was repeated several times during 5 h for all the 6 catalysts to ensure the reproducibility of the results. The He purge after O_2 or H_2 contact is used to avoid possible artifacts by the presence of gas phase or weakly adsorbed adsorbates. All gas cylinders are provided with moisture (all gases: Matheson, 450B series, type 451), oxygen (He, H_2, CO: Perkin Elmer, P/N N9301179), and hydrocarbon (He, H_2, O_2: Matheson, 450B series, type 454) traps. The collected UV-Vis spectra were referenced to $BaSO_4$ at ambient conditions (Sigma Aldrich, P/N 243353). Lastly, the transient

changes of the Au SPR peak position were determined via a homemade Python (www.python.org) computer program by finding the maximum value of a polynomial fit (order 6) to the data within ~100 nm around the SPR peak. The program uses the *minimize scalar* and *polyfit* fitting functions available in the NumPy package (www.numpy.org). It is worth noting that although the response of the Au SPR band changes to different gas atmospheres has been previously studied in Au/YSZ, Au/TiO_2, and Au/CeO_2 in transmission mode, [48, 62-67] here, for simplicity the technique uses diffuse reflectance of powder catalysts since it does not require sample preparation.

3.2.4. Operando CO oxidation

In order to study the correlation between oxygen adsorption properties and catalytic activity, the gold catalysts were also tested for CO oxidation following the H_2/O_2 cycle exposures in the modified in situ/operando UV-Vis diffuse reflectance cell. A total gas flow rate of 60 cm^3/min (1 kPa CO, 2 kPa O_2, He balance) at 398 K and 101 kPa total pressure were employed so that a stoichiometric excess of O_2 was present. Oxidation of CO on gold catalysts has been extensively researched [6, 16, 19, 27, 39, 41, 68, 69] and was chosen since it has the advantage of taking place even at very low temperatures and because CO can act as a good probe molecule [70]. The conversion of CO in the in situ/operando cell was determined online by means of an Omnistar GSD 320 O mass spectrometer (MS, Pfeiffer Vacuum) using calibrated gas signals. Conversions were corrected for any CO_2 present in the gas mixture by subtracting baseline signals in a reactor bypass run. CO oxidation conducted on SiO_2 sand (Sigma-Aldrich, P/N 84878) showed negligible conversion demonstrating the inertness of the reaction cell at the studied conditions. Gold plasmon peak positions during CO oxidation and in oxygen flow after CO oxidation were also determined concomitantly in the same in situ/operando cell and also analyzed.

3.3. Results and discussion

3.3.1. Catalyst synthesis and characterization

We employed gold nanoparticles deposited on a variety of supports of intermediate surface areas (ZnO, ZrO_2, Al_2O_3, TiO_2, and SiO_2, ~10-70 m^2/g), prepared with the same synthesis method (ammonia deposition-precipitation) allowing similar gold loadings (~1 wt%) and close gold particle size range (~5.5-9 nm), while minimizing surface contamination with undesirable Na ion.

All supports and catalysts textural properties and X-ray diffractograms are reported in **Table B.1** and B.2 and **Table B.1**. They show the conservation of support integrity after ammonia-DP method as only small changes were noticed in the textural properties and crystal structure. Except for Au/Al_2O_3 and Au/SiO_2, which showed small peaks due to the presence of Au, all other catalysts lacked any noticeable XRD Au signals suggesting that Au dispersion was relatively high.

The synthetic approach employed in this work allowed us to carry a systematic study of gold surface plasmon resonance on supported (powder) catalysts and to study their consequences for adsorption phenomena in oxidizing (O_2) and reducing (H_2) gases. Au particle size and distribution of the prepared catalysts were measured by transmission electron microscopy and the images for each fresh catalyst are shown in **Figure 3.1**. It was found that, for all the supports, the ammonia DP method afforded gold average particle sizes in the range of 5.5-9.2 nm and with a relative close standard deviation (±1.0-2.0 nm) increasing in the following order: Au/ZnO (5.5±1.0 nm) < Au/ZrO_2 (6.4±1.5 nm) < Au/Al_2O_3 (7.6±1.2 nm) < Au/TiO_2 (7.8±1.6 nm) < Au/SiO_2 (9.2±2.0 nm). **Table B.2** also shows that the average particle size of the used gold catalysts only suffers minimum changes after exposure to O_2 and H_2 at reaction conditions for the duration of the experiments; therefore, for simplicity, only average particle sizes of the fresh catalysts will be used for subsequent calculations.

Figure 3.1 shows the presence of Au NPs at the external surface of single support particles and at grain boundaries between oxide support particles. This observation was also reported by Akita and Haruta where the interface between support particles served as sites for Au particles to get trapped and stop growing during calcination at high temperatures (> 573 K for Au/TiO_2) [71]. It is reasonable to assume this phenomenon may also occur for the catalysts reported in this work as calcination was at 673 K. Additionally, it is also possible that the apparent overlap of oxide particles seen in **Figure 3.1** could be from TEM sample preparation by solvent sonication, dispersion, deposition, and drying of the catalysts powders on the TEM grid before analysis. Regardless of the reasons why Au NPs could be sitting at grain boundaries between oxide particles, this should not be an issue for characterization of adsorbed O_2 with Au SPR because the obtained signals are an average of all Au nanoparticles. Additionally, since the majority of Au NPs are located at the external surface of single oxide particles [71], we do not expect significant contributions from trapped Au NPs (between support particles) to the overall count of Au

perimeter atom site as estimated from model structures (e.g., truncated octahedron or cuboctahedron).

The relatively large Au particle size obtained for the prepared catalysts, with respect to other common methods of preparation of gold catalysts (e.g., DP with NaOH as the basic titrant), follows previous reports of ammonia DP method for gold NPs deposition [72]. The reason for this is the formation of a surface ammonium cation [73]. on all oxide supports that serves as an anchor for $Au(OH)^{4-}$ and $AuCl(OH)^{3-}$ anions, which form from the $HAuCl_4$ gold precursor and are in equilibrium at the synthesis pH of 9.5 [74]. With the exception of Al_2O_3 that deposited ~80% of the nominal gold in the synthesis solution, all other supports resulted in Au deposition efficiencies of 95-100% due to ammonia surface modification (**Figures B.3-B.8**, **Table B.2**). Caution! it should be noted that the ammonia-DP synthesis method carries the risk of forming fulminating gold which is a shock-sensitive and explosive material [75]! We have used this synthesis method several times for ~1 wt% Au deposition on silicates, titanosilicates, and now on several oxidic supports (SiO_2, Al_2O_3, ZrO_2, ZnO, and TiO_2) without any safety incidents. This may be presumably because ammonia is contacted first with the supports forming surface ammonium ions [73], which seem to avoid formation of fulminating gold at the studied Au concentrations [75]. The relatively large Au NP sizes reported here are also in agreement with previous Au/SiO_2 preparations yielding Au NPs in the 2-16 nm range, whose final value depended on the synthesis pH, temperature, and reaction time [73].

Additionally, these larger particle sizes are expected to facilitate the measurement of Au SPR peak position as the SPR band will tend to be relatively symmetric and pronounced [76], while still demonstrating modest catalytic activity for a model test reaction such as CO oxidation at high reaction temperatures [7]. Moreover, in the obtained gold dispersion range (~11-18%, D ~ 1/*d*, *d* = average particle diameter in nm), CO oxidation activity dependence on particle size changes is not as pronounced as with smaller particle sizes (<3 nm) [77], It has been shown, for example, that CO oxidation activity dependence with gold particle size on various gold catalysts varies according to $1/d^3$ indicating significant contribution of low coordinated Au atoms whose surface fraction [77], important to catalysis, tend to tail off at gold particle sizes above 5 nm [78].

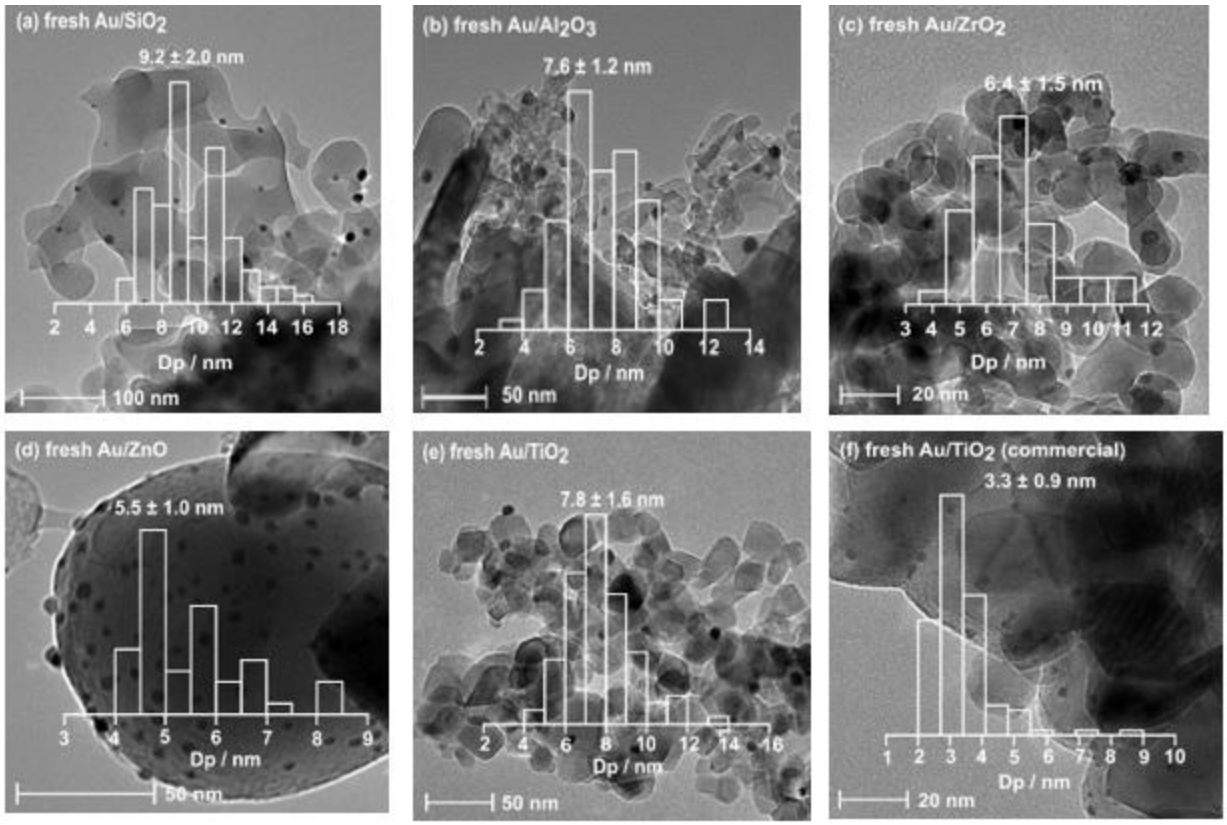

Figure 3.1. TEM images of calcined Au catalysts: Au/SiO_2, b) Au/Al_2O_3, c) Au/ZrO_2, d) Au/ZnO, e) Au/TiO_2, and f) Au/TiO_2 (commercial). Approximately 50-100 particles were counted to obtain the particle size distributions.

3.3.2. In Situ Au surface plasmon resonance during O_2/He/H_2 cycle exposures

Resonant oscillations occur on a metal surface due to interaction with visible light. These localized oscillations near metal nanoparticles (NPs), known as localized surface plasmon resonance [56]. result in a strongly enhanced electromagnetic field around the nanoparticle and manifest themselves as a broad band [79]. Metals commonly exhibiting surface plasmon resonance (SPR) are gold, silver, and copper which falls in the visible region of the electromagnetic spectrum. The peak position of the SPR band is sensitive to changes at the boundary of the metal nanoparticle and its surrounding medium. In this work, gold was chosen since it is also an excellent catalyst for many oxidation reactions [79]. The high sensitivity of Au surface plasmon resonance (Au SPR) peak position makes it an efficient tool for obtaining information on chemical properties around the gold NPs. Here, the changes in SPR peak position of supported gold nanoparticles are

monitored in real time with a modified in situ UV-Vis diffuse reflectance cell under oxidizing and reducing conditions [61].

The in situ diffuse reflectance UV-Vis spectra of the catalysts were measured under oxidizing and reducing atmospheres in absorbance mode at 398 K. **Figure 3.2** shows the typical (apparent) absorbance *vs* wavelength spectra of the Au/TiO_2 catalyst. A peak centered around 570 nm and generally broad between 400 and 650 nm corresponded to the gold SPR. When the catalyst was exposed to oxygen the peak position was centered at about 575 nm, whereas in the presence of H_2, the Au SPR peak position shifted to 566 nm (blue shift, or shift to higher photon energy). This blue shift can be explained as a result of charge transfer from hydrogen to Au [80]. Such shift is expected from an increase in the conduction electron concentration as derived from a simple analysis of the equation for the bulk plasmon frequency [12, 81]:

$$\omega_p^2 = \frac{Ne^2}{m_e \epsilon_0} \qquad (1)$$

Where ω_p is the bulk plasmon frequency, N is the concentration of conduction electrons, e is their electronic charge, m_e is their effective electron mass, and ϵ_0 is the permittivity of vacuum. While this equation is a simplistic view of the SPR phenomenon as it only reflects bulk and not surface properties of a catalyst's contributions from the support and the neighboring environment (e.g., dielectric properties, refractive index) as altered by adsorbing gases, it still shows in a simple manner the direct proportionality of the SPR peak position with charge transfer events (N). For example, an increase in the concentration of conduction electrons, N, (e.g., as a result of charge transfer from H_2 to gold) will result in an increase in the SPR frequency (ω_p) or increase in the energy (lower wavelength) of the peak position (blue shift). This is in concordance with experimental and modelling results of the SPR process on gold catalysts when exposed to oxidizing and/or reducing environments showing the preponderance of electron charge transfer to or from the gold nanoparticles [53, 80]. Similarly, DFT calculations of O_2 adsorption on $Au/TiO_2(101)$ demonstrated a weakening of the O-O bond as a result of charge transfer from Au to O_2 antibonding orbitals [82], whereas theoretical calculations showed electrochemical charge transfer from gold NPs to diffusing oxygen ions in a Au-YSZ thin film [47]. In the case of H_2 adsorption on Au, theoretical [83] and experimental evidence via Au SPR on Au/YSZ

nanocomposites [63, 84] and Au/Pt nanoparticles embedded in ZnO and TiO_2 [80] showed that H_2 is more likely to dissociate while transferring charge to Au, resulting in a blue shift (lower wavelength) as seen in **Figure 3.2** and **3.3**. In summary, the Au SPR peak position is sensitive to adsorption of oxidizing or reducing molecules as manifested by peak shifts determined in the present work primarily by charge transfer events. This phenomenon is exploited here to track adsorption of molecules on gold catalysts at reaction conditions via gold plasmon peak position shifts determined with in situ UV-Vis spectroscopy.

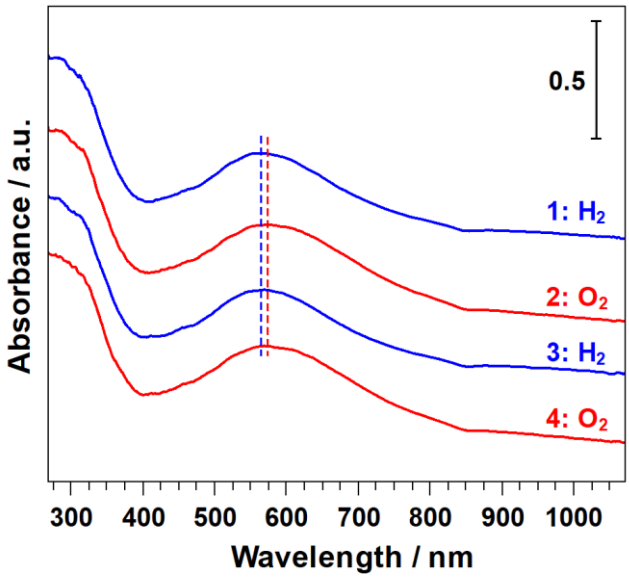

Figure 3.2. Typical in situ diffuse reflectance UV-Vis spectra of Au/TiO_2 catalyst upon exposure to H_2 and O_2 at 398 K. Numbers indicate the order of the measurement. He was used to flush gases in between H_2 and O_2 cycles.

Figure 3.1 shows the change in Au SPR peak position on the six gold catalysts (Au/SiO_2, Au/Al_2O_3, Au/ZrO_2, Au/ZnO, Au/TiO_2, and Au/TiO_2 (commercial)) as a function of exposure time to O_2, H_2, and He for a period of 5 h (average and standard deviation of Au SPR peaks provided in

Table B.3). Several observations can be made:

1. The Au SPR peak position was dependent on the support nature (e.g., in O_2: Au/SiO_2 ~ 517 nm < Au/Al_2O_3 ~ 526 nm < Au/ZrO_2 ~ 529 nm < Au/ZnO ~ 543 nm < Au/TiO_2 ~ 575 nm ≈ Au/TiO_2 (commercial) ~ 575 nm.), increasing with an increase in the index of refraction

of the support: SiO_2 ~ 1.54 [85] < Al_2O_3 ~ 1.76 [85] < (monoclinic) ZrO_2 ~ 1.90 [86] < ZnO ~ 2.01 [85] < (P25) TiO_2 ~ 2.56 [85].

2. The shift of the Au SPR between oxidizing and reducing atmospheres was completely reversible, indicating minimum irreversible changes to catalyst properties and gold average particle size as a result of gas exposure, which could affect the Au SPR peak position [87-89]. This is also evidenced by the similarity between average particle sizes of fresh and used catalysts (**Figure B.2**)
3. For all catalysts, the Au SPR peak position shifted towards higher wavelengths on exposure to O_2, decreased slightly in helium flow as a result of partial desorption of adsorbed oxygen, and decreased significantly on exposure to H_2. The change in Au SPR peak position in going from O_2 to H_2 exposure increased in the following order: Au/SiO_2 ~ 2 nm < Au/Al_2O_3 ~ 4 nm < Au/ZrO_2 ~ 6 nm < Au/TiO_2 ~ 9 nm < Au/ZnO ~ 11 nm > Au/TiO_2 (commercial) ~ 23 nm.

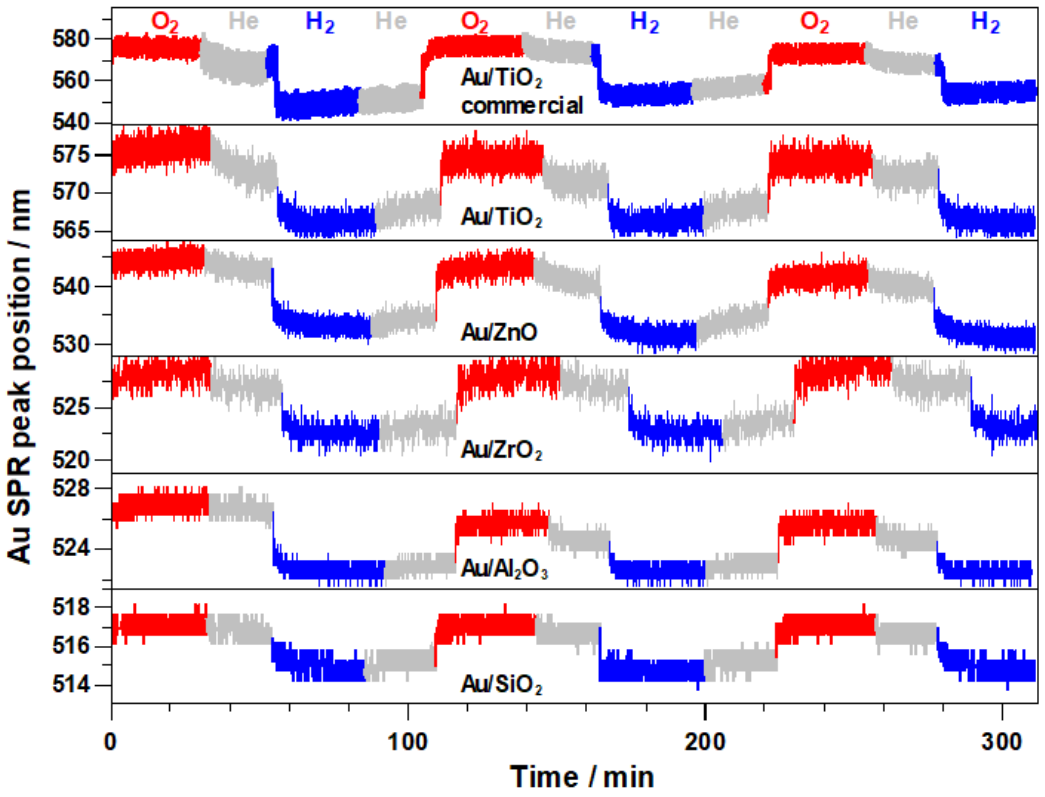

Figure 3.3. Gold catalysts characterization by Au SPR peak position changes after exposure to H_2 and O_2 gas environment at 398 K.

The observed Au SPR peaks shifts when catalysts were exposed to O_2 or H_2 are ascribed to O_2 and H_2 adsorption, respectively. When O_2 exposed catalysts were subsequently treated with H_2, all adsorbed O_2 species should react with H_2 to form water since gold nanoparticles are well known H_2 oxidation catalysts. Chemisorption of oxygen on Au nanoparticles has been reported for Au/TiO_2 and Au/Al_2O_3 exposed to oxygen as followed by in situ Au L3 XANES. The formation of Au-O species was evidenced by an increase in the intensity of the XANES white line due to the decrease of the electron count in the d orbital of Au as they transferred to the $2\pi^*$ orbital of O_2 [33, 45, 46, 90]. This charge transfer from Au to O_2 was also evidenced by a red shift of the Au SPR by in situ UV-Vis spectroscopy during propane partial oxidation on Au/TiO_2 and Au/TS-1 [45, 46]. While Au SPR appears to be quite sensitive to charge transfer due to O_2 chemisorption, the nature of the Au-O adsorbed species is still unclear because XANES and UV-Vis spectroscopies cannot discriminate among O_2, O^-, O_2^-, O^{2-}, hydroxyls, or hydroperoxo species which could form on Au or at the Au-support interface during O_2 chemisorption or after reaction with H_2 [45, 46]. Future experiments, for example, based on in situ EPR [91] or kinetic measurements for O_2 reaction order dependence [92, 93] followed by in situ Au SPR during oxidation reactions could also provide more clarity on the nature of these species.

Upon exposure to O_2, there is the possibility that Au in the catalysts of **Figure 3.3** become oxidized. However, this is less unlikely on these catalysts because of the relatively large Au NPs sizes which are more difficult to oxidize than smaller NPs (< 3 nm) [53, 94]. This is supported by previous in situ Au L3 XANES and UV-Vis spectroscopic characterization of Au/TiO_2 and Au/TS-1 during propane oxidation with H_2 and O_2 [44-46] which showed that O_2 adsorbed on Au, but that Au remained in a metallic state. Similar findings were also reported by Bokhoven's group from in situ Au L3 XANES on Au/TiO_2 and Au/Al_2O_3 (1-3 nm Au NPs) when exposed to CO/O_2 mixtures [32, 33]. Small amounts of cationic gold, however, were reported for Au/Al_2O_3 upon exposure to O_2, which may form a surface oxide on the small gold NPs [32]. Extensive theoretical modelling of metal and support effects on Au/TiO_2 exposed to O_2 by Borensztein et al [53] considered the formation of a Au NP oxide overlayer and adsorption of O_2 on TiO_2 support. They predicted changes to the Au SPR peak as a result of a reduction of the metallic Au NP volume (lower intensity), flattening of the Au NP (red shift), presence of a dielectric oxide layer (red shift and damping of the SPR), and changes to the dielectric function of the support (lower intensity). These

effects on the Au SPR, however, could not fit the experimental observations, which were better explained by charge transfer between Au and O_2 and a small flattening of the Au NPs rather than by a change in the oxidation state of Au or O_2 adsorption on TiO_2. The relatively small Au SPR peak changes observed for the gold catalysts on this work upon exposure to O_2 (**Figure B.9**), further suggest that O_2 species predominantly adsorb on Au or its vicinity, but not as an overlayer oxide and that Au is more likely to be in a metallic state. Additionally, any effect on the Au SPR peak due to adsorption of O_2 or H_2 on the supports reported here, which are less reducible than TiO_2, should be negligible.

3.3.2.1.Dependence of gold surface plasmon resonance peak position (λ_m) on support index of refraction (n_0) and Au charge transfer (N)

From **Figure 3.3**, it is worth noticing the increase of the Au SPR peak position with gold catalysts' support index of refraction, a trend that is similar to that reported for colloidal silver nanoparticles in various solvent environments [95, 96] This suggests that a relationship between gold nanoparticles properties and the support's index of refraction can be found based on similarities with well-known models for dilute colloids containing small absorbing nanoparticles in solution [95] or present within crystals [97, 98]. Thus, using the classical Drude's free electron model for the dielectric function to describe the metal's bulk plasma frequency, it can be shown that the relationship between the wavelength at which maximum absorption occurs (λ_m) and the nonadsorbing matrix (e.g., support) index of refraction (n_0) is given by (see Appendix for details on the derivation) [95, 97, 98]:

$$\lambda_m^2 = \lambda_p^2 \epsilon^\infty + \lambda_p^2 (2n_0^2) \qquad (2)$$

Where ϵ^∞ is the high frequency dielectric constant due to interband and core transitions and λ_p is the metal's bulk plasma wavelength: $\lambda_p^2 = {(2\pi c)^2}/{\omega_p^2}$. Here, c is the velocity of light and ω_p^2 is defined by Equation 1.

Equation 2 shows that the wavelength at which maximum absorbance occurs (λ_m) is a function of both the metal and the host medium (e.g., support in solid catalysts). This equation predicts a direct proportionality between the squared maximum absorbance wavelength and twice the square of the medium's refraction index. To verify that such dependence also holds for supported gold catalysts, a plot of (Au SPR maximum peak position)^2 *vs* $2n_0^2$ (n_0=support's refraction index) was

prepared for the gold catalysts in this work based on in situ UV-Vis measurements under flowing O_2 or H_2 at a high temperature of 398 K as shown in **Figure 3.4**. The results show an excellent linear fit to the data, which after use of Equation 2 yields $\lambda_p = 88.1$ nm and $\epsilon^{\infty} = 29.5$. These values are different from the expected gold's bulk plasma wavelength = 137.6 nm (9.01 eV) [99] and $\epsilon^{\infty} = 9.84$ [99]. A similar trend is observed for the catalysts after exposure to H_2 (**Figure 3.4**, solid symbols). The differences between the apparent values of λ_p(88.1 nm) and ϵ^{∞}(29.5) derived from the supported gold catalysts and the expected values for gold indicate that these parameters are strongly dependent on the supports and their interaction with the gold nanoparticles. The solid line in **Figure 3.4** for the predicted λ_m^2 shows close agreement with the experimental (Au SPR peak)^2 for Au/SiO_2 catalyst, but a deviation with other supports. This deviation increases with support type and follows expected trends of increased gold-support interaction with reducible supports: $SiO_2 > Al_2O_3 > ZrO_2 > ZnO > TiO_2$ [7]. The main reason for these differences are explained on the basis of the presence of electron charge transfer from the support to the gold nanoparticles, which result in a blue shift (lower wavelength) of the Au SPR with respect to Equation 2. As it will be shown next, there is a direct relationship between the $(\lambda_m^2 - \lambda^2)/\lambda_m^2$ or $(\lambda_m - \lambda)/\lambda_m$ relative deviation and the relative charge transfer change to the gold NP.

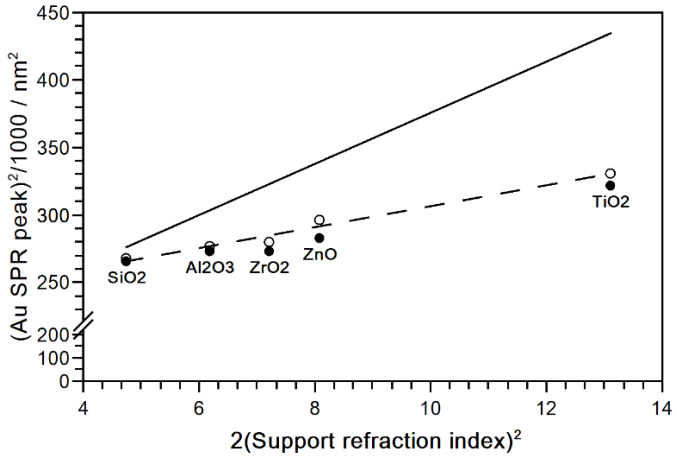

Figure 3.4. Plot of the squared Au SPR peak position (λ^2) for SiO_2, Al_2O_3, ZrO_2, ZnO, and TiO_2 supported Au catalysts as derived from in situ UV-Vis measurements under flowing O_2 (empty circles) and H_2 (solid circles) at 398 K as a function of twice the squared support index of refraction ($2n_0^2$, where the support dielectric medium $\epsilon_m = n_0^2$). Dashed line is a linear fit to the O_2 data (slope = 7.76; intercept = 228.9 nm^2; $R^2 = 0.978$) and solid line corresponds to the calculated λ_m^2 as given by $\lambda_m^2 = \lambda_p^2\epsilon^{\infty} + \lambda_p^2(2n_0^2)$, where λ_p = 137.6 nm (9.01 eV) [99] is gold's bulk plasma

wavelength and ϵ^{∞} = 9.84 [99] is the high frequency dielectric constant due to interband and core transitions in Drude's model for the dielectric function of the metal [95].

A relationship between gold nanoparticles plasmon absorption position (λ_m) and charge transfer (N) can be also found (see Appendix for derivation) [81, 95]:

$$\frac{\lambda_m^2 - \lambda^2}{\lambda_m^2} \approx \frac{\Delta N}{N} \quad (3)$$

Or alternatively:

$$\frac{\lambda_m - \lambda}{\lambda_m} \approx \frac{\Delta N}{2N} \quad (4)$$

Equation 3 shows that the relative change of the squared SPR peak position (λ) with respect to a reference wavelength (λ_m), in this case, the expected ideal Drude's model value, is proportional to the relative electron charge change in the gold NP. The alternate Equation 4 also shows that for small changes of charge transfer, $\Delta N/N \ll 1$, the relative change of the SPR peak position with respect to a reference λ_m value is proportional to half the relative charge transfer to/from the gold NP. Therefore, Equations 3 and 4 can be used to estimate the relative charge transfer change in a catalyst from two different conditions (e.g., Drude's model Au SPR peak prediction *vs* Au SPR peak experimental value, Au SPR peak position in O_2 *vs* Au SPR peak position in H_2, etc).

From **Figure 3.4**, it can be seen that the relative increase in the charge transfer ($\Delta N/N$) to gold NPs between Au SPR experimental and that derived from Drude's model (SiO_2 = 3% > Al_2O_3 = 9% > ZrO_2 = 14% > ZnO = 13% > TiO_2 = 24%) is usually more pronounced than that observed for a change between an oxidizing and a reducing gas environment (SiO_2 = 0.9% > Al_2O_3 = 1.1% > ZrO_2 = 2.3% > TiO_2 = 2.9% > ZnO = 4.5%). The former differences can be interpreted by the potential of the support to interact and transfer charge to the gold NPs, which is more favorable for reducible metal oxides, while the latter reflects the charge transfer between adsorbates and gold surface atoms. One important aspect of the interaction between reducible supports and gold NPs is the likely presence of oxygen vacancies, which can facilitate charge transfer to gold NPs [100]. A consequence of the above results is the possibility of employing Au SPR peak position shifts to correlate the presence of oxygen vacancies on supported gold catalysts. On gold catalysts, oxygen vacancies play an important role as gold nanoparticles will tend to nucleate at the site of oxygen vacancies which are electron rich resulting in charge transfer to the gold nanoparticle [100, 101].

This would explain the decreasing deviations between (Au SPR peak position)^2 for the theoretical and experimental supported gold catalysts as oxygen vacancies are expected to be more abundant on TiO_2 and ZnO than on ZrO_2, Al_2O_3, and SiO_2 [100].

A plot such as that shown in **Figure 3.4** could, therefore, be used as a tool for preliminary evaluation of the presence of oxygen vacancies and the degree to which the support can transfer electron charge to gold nanoparticles. This is an important aspect because the presence of oxygen vacancies and/or charged gold NPs in reducible and non-reducible supports has been correlated in some cases with catalytic activity, for example, in oxidation reactions [100, 102, 103].

3.3.2.2. Consequences of oxygen/hydrogen adsorption on gold surface plasmon resonance peak position

The results of **Figure 3.3** also showed that the Au SPR peak position is sensitive to switches in the gas environment from O_2 to H_2 as they interact with gold nanoparticles. When H_2 contacts gold NPs, the Au SPR peak position shifts to lower wavelengths as O_2 coverage decreases due to reaction with H_2. This resembles the O_2 titration with H_2 method developed by Benson and Boudart for Pt catalysts [104], and which is also commonly used for dispersion measurements of noble metal catalysts as it is more sensitive than direct O_2 or H_2 chemisorption [105]. The O_2 titration with H_2 has also been applied by Berndt and co-workers to Au/Al_2O_3 catalysts for estimations of gold dispersion. However, the method proved to be difficult due to the relatively small amounts of O_2 chemisorbed (<15 μmol/g) that need to be detected, high dependence on catalyst pretreatment and titration temperature, and requirements of relatively large amounts of catalyst (0.25-1.0 g) and high reduction pretreatment temperature (>673 K) [106]. Such complications likely make the method unreliable as these authors reported a very close agreement between TEM particle sizes and those calculated by chemisorption for various Au/Al_2O_3 samples with average TEM Au NP diameter of ~1.5 nm. As it will be shown in later sections, this is inconsistent with O_2 adsorption on only a fraction of the Au surface atoms (e.g., at the Au-support interface) which would result in calculated Au NP diameters (from chemisorption) larger than those expected from TEM observations. Since gold catalysts are effective hydrogen oxidation catalysts, water should form after O_2 titration with H_2 [107]. Attempts to monitor the water produced via MS, however, proved ineffective likely due to the small amounts of water formed whose concentrations are easily attenuated in the relatively large void volume of most in situ reaction cells and in the corresponding

gas phase streams [108]. Despite this, it was shown that Au SPR peak position is sensitive to adsorbates-gold interaction. The largest changes in Au SPR peak position in **Figure 3.3** from O_2 to H_2 gas switches on the prepared Au catalysts were found for ZnO (11 nm) and TiO_2 (9 nm) supported catalysts. This is in line with prior reports indicating that oxygen adsorption is more favorable on gold or gold-support interface with reducible supports [38, 39, 42, 43, 109].

The larger shift for Au/ZnO with respect to Au/TiO_2 (both supports are reducible) would at first look unusual as TiO_2 is known to be a more reducible support (and with potentially more oxygen vacancies) than ZnO (also seen in **Figure 3.4**). This lack of correlation of support reducibility with its ability to adsorb oxygen and oxidize CO has been also reported by Schüth and co-workers for various supported gold catalysts with similar average particle size [110]. These authors suggest that, in addition to the support's reducibility, other factors could be at play such as particle shape changes induced by the support. In our case, average Au particle sizes of the prepared catalysts varied although not in a significant dispersion range (5.5-9.2 nm). Therefore, as discussed above, the observed results are consistent with a larger adsorption of O_2 (i.e., charge transfer) on the Au/ZnO catalyst. This points to a larger gold surface or gold-support interface on Au/ZnO than that on the Au/TiO_2 that is available for O_2 adsorption, in this case, as a result of a smaller average Au NP size on Au/ZnO ($d \approx 5.5$ nm) than on the Au/TiO_2 ($d \approx 7.8$ nm) sample. This is further supported by the observed shift (23 nm) in a Au/TiO_2-commercial ($d \approx 3.3$ nm) that resulted in the expected trend for a more reducible support. This result clearly shows that the Au SPR is able to sense differences in O_2 adsorption for apparently similar catalysts. It suggests that reducibility alone is not a good descriptor of catalytic activity on gold catalysts and which possibly also holds for other noble metal supported nanoparticles.

As discussed above, the large deviations observed in **Figure 3.4** between the gold catalysts' experimental and calculated $(\text{Au SPR peak})^2$ by Drude's model indicate the possible presence of oxygen vacancies, which anchor and transfer charge to the Au NPs. These differences alone, although useful in recognizing a support's potential to transfer charge to the Au NP, do not provide a direct measure of the adsorbed oxygen that can be titrated and likely available for reactions such as oxidation. However, up to this point we can qualitatively say, from **Figure 3.4** trends, that support properties (i.e., index of refraction) have a larger effect on the Au SPR peak position than those observed for gas environment switches, as indicated from the larger deviation from ideal Drude's model (**Figure 3.4**, solid *vs* dashed line) *vs* peak shifts with gas change (**Figure 3.4**, solid

vs empty circles). For example, **Figure 3.4** suggests that TiO_2 should be the support with the most oxygen vacancies available and therefore the one that would adsorb the most oxygen; however, as previously discussed, the Au/ZnO catalyst shows a larger amount of adsorbed oxygen because of the difference in particles sizes for Au/TiO_2 and Au/ZnO catalysts. This result suggest the possibility of optimizing the density of oxygen adsorption sites at the interface or in the vicinity of the Au NPs deposited on reducible supports, which should be a function of the gold particle size [6, 7, 100].

On supported gold catalysts, the role of metal-support interface in the activation of reactants in various reactions has been typically linked to high catalytic activity. This was first suggested by Haruta more than 20 years ago [6] and more experimental and theoretical evidence has accumulated since then to support this hypothesis [7]. For instance, Yates and co-workers [21] and Chandler and co-workers [16], based on DFT calculations on Au/TiO_2, surmised that CO oxidation occurs at the $Au\text{-}TiO_2$ interface. Behm and co-workers also offered kinetic evidenced for the catalytic relevance of the Au-support interface for CO oxidation based on transient TAP reactor measurements [38]. For the water gas shift reaction on gold catalysts, Ribeiro and co-workers also offered kinetic evidence for the importance of gold corner atoms at the gold-support interface [111]. Based on these prior works, it is reasonable to expect that gold-support perimeter sites play a significant role in CO oxidation; however, a kinetic study by Iglesia and co-workers showed that all Au sites (under "wet" conditions), not just perimeter sites, are required for CO oxidation [112]. This brings up questions on the reasons for these discrepancies. Since Haruta's discover of Au catalysts for CO oxidation over 30 years ago [3], several theoretical and kinetic studies in the literature have offered evidence for the involvement of gold-support perimeter in oxidation reactions; however, to date there has not been a single in situ/operando spectroscopic evidence on the site location of adsorbed O_2 on supported Au nanoparticles at oxidation reaction conditions.

From a kinetics point of view, it is worth noting the relevance of adsorbed oxygen in catalytic activity and the importance of the catalyst support. For example, in CO oxidation on gold catalysts the reaction rate order with respect to oxygen was shown to be positive for reducible (e.g., Au/TiO_2) and non-reducible supports (e.g., Au/Al_2O_3) [68], Such dependency implies that O_2 is involved in rate determining steps suggesting that O_2 surface coverage is expected to correlate with oxidation activity. Recent CO oxidation kinetic studies on Au/Al_2O_3 and Au/TiO_2 showed a mechanism that is consistent with oxygen activation at the gold-support interface regardless of the

support nature [24]. Similar observations were reported for the water-gas shift reaction by Ribeiro and co-workers on Au/Al_2O_3 and Au/TiO_2 who used a combination of kinetics and site statistics analysis to show that the most active sites are corner Au sites at the perimeter regardless of support and particle size (1-7 nm range) [111]. Recently, Uchiyama et al. [113] also reported ETEM experiments on Au/SiO_2 (5.7 nm) and two different Au/CeO_2 (4.1 and 10.4 nm) catalysts showing that there is a strong correlation between O_2 adsorption on gold nanoparticles (more likely at the Au-support perimeter), as implied by smoothening of the gold NPs in O_2 atmosphere, and CO oxidation catalytic activity. Such activity trends were reported to be also independent of the nature of the support. The reported magnitude of Au NPs changes and CO TOFs decreased in the following order Au/CeO_2 (4.1 nm) > Au/CeO_2 (10.4 nm) > Au/SiO_2 (5.7 nm). [113] Theoretical calculations of Au SPR by Borensztein et al.[53] showed that O_2 interaction with Au on Au/TiO_2 mainly resulted in charge transfer from Au to oxygen and to a smaller extent in a flattening of the gold NPs as evidenced by a red shift in the Au SPR peak position from in situ UV-Vis experiments. If the activation of O_2 on Au catalysts occurs predominantly on the same type of Au sites, namely Au-support perimeter, then, altogether these results and theoretical calculations predict a correlation between the relative charge transfer change ($\Delta N/N$) (as a result of oxygen adsorption) and the fraction of Au perimeter sites regardless of the type of support.

To test the assertion that O_2 activation on Au NPs occurred at the Au-support perimeter regardless of the nature of the support, we plotted: 1) the relative change of electron density in the gold NPs resulting from O_2 to H_2 gas environment switch, $\Delta N/N$, and 2) Au site statistics for (top) surface (S), perimeter (P), and (perimeter) corner (C) atoms, as a function of Au NP size, d. These correlations of Au (surface, perimeter, and corner) atoms in a NP for gold particle sizes in the 1.7-14 nm range were determined from geometry considerations from the top slice of a truncated octahedron [114]. This relationship between average particle size (d) and gold atoms sites should let us assess the effect of gold NP size and location for adsorption of oxygen on the catalysts. More specifically, it is expected that experimental data for the tested catalysts' electron charge change should track with specific sites on such type of plot and therefore allow us to determine the location of oxygen adsorption on the supported gold catalysts. Such type of plot is presented in **Figure 3.5**. The results from this figure show a clear trend for the $\Delta N/N$ values of the prepared catalysts and even the commercial Au/TiO_2c which overlaps with those for the dispersion of Au perimeter sites,

indicating that at 398 K in a flow of O_2, O_2 is predominantly adsorbed at the Au-support interface. A similar conclusion is found when $\Delta N/N$ is calculated with Au SPR peaks (

Table B.3) in He after O_2 and H_2 flow (**Figure B.12**). This agrees with the above predictions and theoretical and experimental kinetic and reactivity studies that suggested that oxygen atoms adsorb preferentially at the boundary region between Au and the support metal oxide where they can then be removed with low energy barriers, for example, via oxidation reactions [6, 7, 16, 21, 38, 100, 115-117]. The application of this method of gold plasmon sensing of adsorbed O_2 (O_2-GPS) to find trends for the location of O_2 adsorption on the prepared gold catalysts is quite remarkable considering that the Au SPR peak position is not strongly dependent on the particle size in the studied range (5.5-9 nm), which makes it robust and amenable for potentially studying other properties that can affect oxygen adsorption such as support morphology, acidity/basicity, and composition including presence of promoters/dopants and mixed metal oxides, among others. This methodology relating the dependence of the coordination of Au atoms as a function of particle size with catalytic activity (but not with spectroscopic data) was also proven useful for suggesting Au sites more likely involved in CO oxidation [77, 117] and the water-gas shift reaction [111]. The method described here expands the application of site statistics correlation to in situ/operando spectroscopic data demonstrating its utility and power to understand adsorbed species on catalyst active sites in its working state giving unprecedented access to specific adsorption sites on practical catalysts. Moreover, the O_2-GPS, which is a deceivingly simple yet powerful technique, has the potential for widespread use as it can be applied directly to powder catalysts that exhibit plasmon resonance requiring only a relatively inexpensive reaction setup [61] and in situ reaction cell [61, 118].

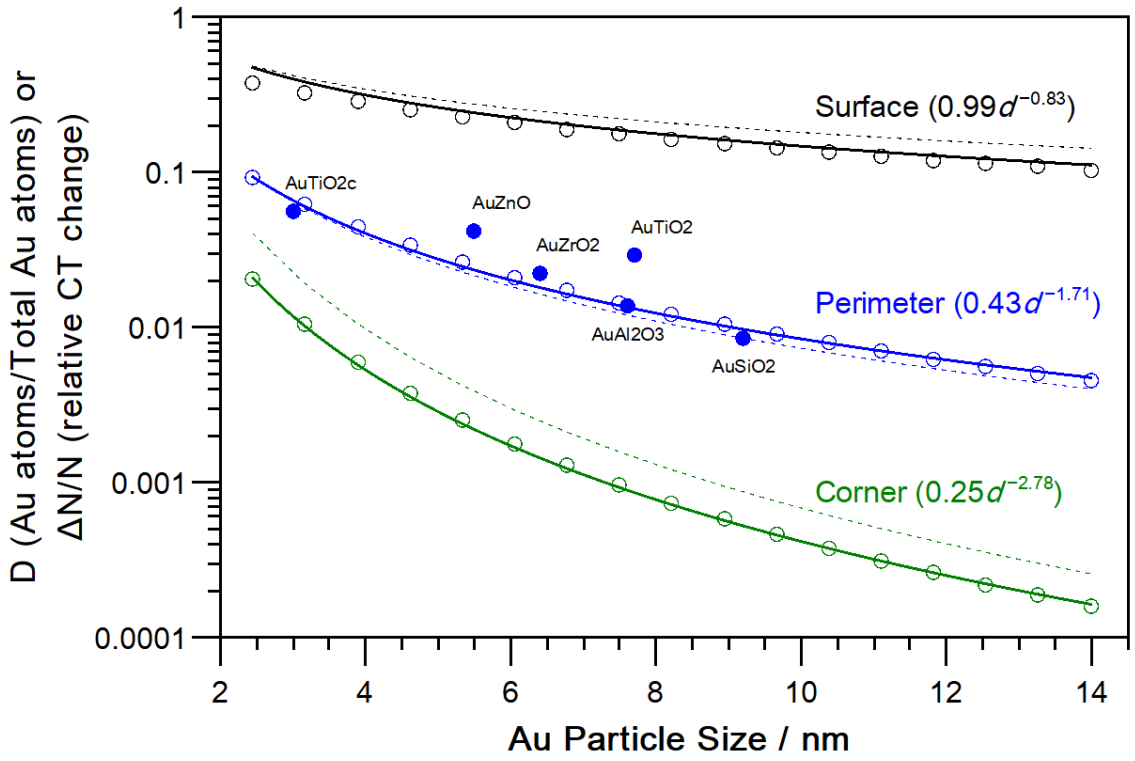

Figure 3.5. Correlation between gold average particle diameter *vs* dispersion (D) = fraction of surface gold atoms with respect to the total amount of Au in a NP (empty circles, calculated from site statistics for a Au NP with truncated octahedron geometry, detailed calculations can be found in the Appendix B: **Table B.4-B.7**) and $\Delta N/N$ = fraction of electron density change (charge transfer, CT) from Au SPR peaks (Equation 3, **Table B.3**) in flowing O_2 and H_2 (blue solid circles) on gold catalysts at 398 K. Here, D is the dispersion or fraction of surface sites which are proportional to $1/d^m$, where d is the average gold nanoparticle size in nm and m=0.83 for the (top) surface atoms (coordination number = 6−9), m=1.71 for perimeter atoms (coordination number = 5−7), or m=2.78 for (perimeter) corner atoms (coordination number = 5). Values of m were calculated from best fit (solid lines) to atom site statistics for a gold nanoparticle modeled as the top slice of a truncated octahedron (empty circles) as shown by the equations in parentheses [114]. For comparison, the corresponding site statistics for Surface ($0.90d^{-0.70}$), Perimeter ($0.90d^{-1.8}$), and Corner ($0.90d^{-2.9}$) atoms in a Au nanoparticle with truncated cuboctahedron geometry were also added (dotted line) as reported by Ribeiro and co-workers [111].

The Au site statistics shown in **Figure 3.5** (empty symbols, solid lines) were based on calculations for the top slice of a truncated octahedron. From DFT calculations, the truncated octahedron was postulated by Curtiss and co-workers as the most energetically favored structure for particles above 3 nm [119]. Such geometry was also found stable for 1-2 nm Au NPs along with the octahedron structure, but not below 1 nm, where the cuboctahedron was found to be the

most stable [120]. This is also in agreement with calculations by Wang et al. [121] and McKenna [122] showing that the truncated octahedron was favorable for Au NPs larger than 2 and 5 nm, respectively. Ex situ TEM characterization also showed the presence of truncate octahedron structures on Au/TiO_2 (1.5-4.8 nm) [123, 124] and Au/Fe_2O_3 (2.2-3.5 nm), [125] however, the truncated cuboctahedron was also reported for Au/TiO_2 (~2-4 nm) [126, 127] and Au/Al_2O_3 (~2-4 nm) [127] catalysts. Recent ETEM studies on Au/TiO_2 (3-4 nm) [128] and Au/CeO_2 (~3-4 nm) [129, 130] in O_2 and CO atmospheres reported structures that also resemble a truncated octahedral geometry.

From **Figure 3.1**, ex situ TEM images show that Au NPs are quasi spherical. Because of the relatively large Au NP size in these catalysts (5.5-9 nm), they are more likely to be described reasonably well by a truncated octahedron. In situ diffuse reflectance UV-Vis spectra of the supported gold catalysts in flowing O_2 and H_2 at 398 K (**Figure B.9**) shows that the Au SPR peak is symmetric for Au/SiO_2, Au/Al_2O_3, and Au/ZrO_2. Such symmetry is characteristic of Au NPs with regular morphology and with a relatively narrow size distribution [131]. In the case of Au/ZnO and Au/TiO_2 the Au SPR band appeared slightly broadened to lower energies. This could be assigned to a stronger interaction between Au NPs and reducible supports [132]. A small broadening of the Au SPR band during exposure to O_2 appears to be related to charge transfer to gold and a slight flattening [133] of the gold NPs as proposed by Borensztein et al. [53] In summary, the Au NPs morphology for the gold catalysts studied here, which possess large average Au NP sizes, is likely to be that of a truncated octahedron, with that for reducible supports being slightly flattened as a result of a stronger Au-support interaction. At high temperatures and in O_2 and H_2, the Au NPs morphology remained fairly unchanged as evidenced from the gold plasmon peak shape (**Figure B.9**). Even if minor changes in morphology were present in the reducible supports, because of the relatively large NP size and low dispersion (11-18%), they should not affect significantly the surface site distribution, amount of adsorbed oxygen, and therefore the relative change of charge transfer reported in **Figure 3.4.** A detailed description of the Au sites, count, and formulas is given in **Table B.4**-**B.7** and **Figures B.10**-**B.11**. For comparison, the site statistics of a truncated cuboctahedron are also presented in **Figure 3.5** (dotted lines). It is clear that even if Au NPs of truncated cuboctahedron geometry are present in the catalysts, the O_2-GPS results are still consistent with oxygen adsorption at the Au-support perimeter.

Lastly, it is worth noting that the O_2-GPS is of general application and can be applied to determine adsorption of O_2 at in situ/operando conditions as it will be demonstrated in the following section. An important consideration is the low detection limit of the O_2-GPS technique. This was not explored in the present work, but it will ultimately depend on the quality of the gold catalysts and the signal-to-noise ratio of the analytical equipment. However, results from Carpenter's group on gas sensing of H_2 (100-1000 ppm), CO (20-2000 ppm), or NO_2 (2-100 ppm) in air and O_2 mixtures from 0.1-21% on thin films of Au/TiO_2 [134], Au/YSZ [47, 49, 134], and Au/CeO_2 [48, 134], indicate that GPS on powder gold catalysts could potentially be extended to very low gas concentrations (in the ppm level) which are below the range of most typical conditions found in oxidation catalysis.

3.3.3. Activity trends of CO oxidation on supported gold catalysts

We now refer to the application of the supported gold catalysts to CO oxidation reaction to derive catalytic activity trends based on the differences in gold nanoparticles and support properties. CO oxidation on gold catalysts is a widely studied reaction whose mechanism is still a matter of debate [7]. The reasons for this arise from the wide range of reaction conditions tested (low *vs* high temperature mechanisms [38, 135]), [68] different Au particle size (corner [116, 117] *vs* surface [135] *vs* perimeter atoms [6, 7, 116]) and support (reducible *vs* nonreducible [39, 110]; presence of oxygen vacancies [100], bulk defects [136]) effects, presence or absence of water [16, 24], carbonate poisoning [19, 24, 137], etc. Several mechanistic proposals have been put forward for CO oxidation on gold catalysts which usually depend on the nature of the support, gold nanoparticle sizes, and reaction conditions (e.g., low and high temperature, water-assisted or water-free mechanisms). The most commonly proposed mechanism has been that where Au-support perimeter interface sites (primary reaction zone) and nearby gold atoms or oxide support (secondary reaction zone) are considered key reaction sites where oxygen is adsorbed and activated prior to reaction with CO on gold or at the periphery of gold NP. Theoretical and experimental evidence has been put forward to support this general mechanism [6, 7, 16, 21, 24, 38]. While the nature of the adsorbed and activated oxygen species is not completely clear, it has been suggested that at high temperatures (>353 K) and dry conditions, lattice oxygen in reducible supports is the active species which react with CO via a Mars-van Krevelen type mechanism [37-39]. On nonreducible supports, however, a Au-only mechanism has been hypothesized [38]. At high

temperatures, CO oxidation TOFs have been reported to be similar for Au/TiO_2 when normalized by Au perimeter atoms [38] and for $Au/TiO_2(110)$ when normalized by the total surface Au atoms [135]. At lower temperatures (< 353 K), molecularly adsorbed oxygen species (e.g., peroxide, superoxides) [43] are assumed to be prevalent at the Au perimeter sites [21, 38]. In the presence of water, hydroperoxide species, which result from O_2 activation with water or hydroxyl groups, seem to be oxygen active species for reducible (e.g., TiO_2) and nonreducible (e.g., Al_2O_3) supports during CO oxidation [16, 24]. A Langmuir-Hinshelwood based on noncompetitive adsorption on two different types of sites was shown to be in agreement with experimental data [24]. At low temperatures, CO oxidation has been reported to occur predominantly at the Au NP perimeter and its vicinity [16, 21, 24, 116, 135] or at corner sites [116, 117]. Variation with Au loading on Au/TiO_2 catalysts affected the TOF dependence on the type of Au sites. A high Au loading (7.2 wt%) with varying particle size catalysts resulted in a dependence favoring corner Au sites, whereas lower loading catalysts (4.5 wt%) TOFs were found more dependent on Au perimeter sites [116]. Overall, it can be seen that gold chemistry, even for a seemingly well-studied reaction such as CO oxidation, is quite rich and still open to scientific inquiries.

3.3.3.1. CO adsorption sites and support effects.

The gold catalysts (i.e., Au/SiO_2, Au/Al_2O_3, Au/ZrO_2, Au/ZnO, Au/TiO_2) prepared in this work by the DP method using ammonia as the base titrant resulted in relatively large average Au nanoparticles in the 5.5-9 nm diameter range. These catalysts, in addition to a Au(1 wt%)/TiO_2 (Strem) commercial catalyst which was used for reference purposes, allowed a preliminary evaluation of the effect of particle size on CO turnover frequency (TOF) normalized to different low-coordinated Au sites: corner (at perimeter) (TOF-C), perimeter (TOF-P), and top surface Au atoms (TOF-S, excluding perimeter) from data collected in the in situ/operando reaction cell as shown in **Figure 3.6**. The main findings were:

1. The turnover normalized per total surface Au atoms (TOF-S) appeared to vary less as a function of Au particle size.
2. The presence of two correlations of TOF vs *d* as a function of support reducibility, the first one for reducible (**Figure 3.6**, empty symbols: Au/TiO_2, Au/ZnO, and Au/TiO_2-commercial) and the second for nonreducible (**Figure 3.6**, filled symbols: Au/SiO_2, Au/Al_2O_3, and Au/ZrO_2) supports.

3. TOFs are larger for gold catalysts with reducible supports than nonreducible supports.

Studies based on the dependence of TOF with the coordination of Au sites have been used in the past to assess the location and nature of more likely active sites during CO oxidation [38, 41, 116, 135]. Behm and co-workers reported that at high temperature (353 K) and on Au(3.4wt%)/TiO_2 catalysts (1 kPa CO, 1 kPa O_2, balance N_2), TOFs normalized to the amount of perimeter Au atoms resulted in similar TOF-P values for catalysts with particle sizes ranging from 4~12 nm [38, 41]. Similarly, Fujitani and Nakamura also reported similar TOF-P and TOF-S for Au/TiO_2 in CO oxidation at 300 and 400 K, respectively, (25 torr CO, 625 torr O_2, 0.5 torr H_2O) for gold particle sizes in the 1.5-10 nm range [135]. Despite the limited number of catalysts, our results suggest that at the studied reaction conditions (398 K, 1 kPa CO, 2 kPa O_2, balance He) CO oxidation is predominantly dependent on the availability of Au atoms at the NP top surface (as evidenced by the almost independent TOF-S trend *vs* Au NP diameter), not just perimeter sites, which is in agreement with Fujitani and Nakamura's results, but in apparent contradiction with Behm and co-workers' findings. At present, the reasons for this disagreement are unknown, although it is possible that the lower Au loadings of the catalysts in **Figure 3.6** with respect to Behm's may affect, in part the Au site dependence as reported by Overbury et al. [116] who observed a switch of TOF dependence from corner to perimeter sites in going from Au(7.2wt%)/TiO_2 to Au(4.5wt%)/TiO_2. Alternatively, it also seems likely that CO oxidation at the studied conditions is not only controlled by the amount of oxygen species at the periphery as inferred from **Figure 3.5**, but also by the availability of CO molecules on the gold NP surface which need to diffuse to the reaction zone at the perimeter sites where oxygen is present.

While CO oxidation at high temperatures (>320-353 K) [38, 135] has been suggested to proceed with a mechanism different from that at lower temperatures, and presumably different for reducible and nonreducible supports, it is unclear if that is the case for the catalysts reported here as oxygen adsorption sites (perimeter) and trends (not absolute values) for TOF-S are similar for both reducible and nonreducible supports (**Figure 3.6**), despite the latter's lower catalytic activity. Overall, given the different apparent dependences on oxygen adsorption at the perimeter of Au NPs (inferred from **Figure 3.5**) and of CO adsorbed on the Au surface (from **Figure 3.6**), our results suggest that both oxygen and CO are involved in rate determining steps on Au for reducible and nonreducible supports. Such type of rate controlling step has been proposed for CO oxidation

on Au/TiO_2 and Au/Al_2O_3 at low temperatures by Chandler and co-workers [16, 24], Yates and co-workers [21], and Laursen and Linic [138] however, more systematic kinetic studies are required to shed light into the controlling mechanisms at high temperatures, on reducible and nonreducible supports, and in presence or absence of co-fed water.

The apparent mismatch between reducible and nonreducible supports shown in **Figure 3.6** is not unique to CO oxidation. For example, a similar lack of correlation was reported recently for Au/TiO_2 and Au/Al_2O_3 in the water-gas shift (WGS) reaction by Ribeiro and co-workers for Au NPs sizes between about 1 and 5 nm [111]. In that case, reaction rates on Au/TiO_2 were 20 times higher than those for the Au/Al_2O_3 catalyst. For WGS, significant differences in the reaction rates orders with respect to co-fed water indicated that, in addition to Au sites, water activation also occurred on the support or at the Au-support interface. In **Figure 3.6**, gold catalyst's TOFs with reducible supports are approximately 12 times higher than for non-reducible supports. These differences in CO oxidation with support reducibility also support Ribeiro et al.'s [111] hypothesis on the involvement of the support in gold catalyzed reactions. Recent ETEM experiments with Au/CeO_2, Au/SiO_2, and Au/TiC in O_2 or CO/air also offered additional evidence for this hypothesis of reactants (e.g., O_2 and CO) activation at the Au/support perimeter. In this report, for CO oxidation on Au/SiO_2, which was less active than Au/CeO_2, it was hypothesized that only a partial number of active sites at the perimeter is present as a result of a specific (and currently unknown) local structure that promotes adsorption and dissociation of O_2 [113]. To explain such activity differences, match [113] or mismatch [100] between the oxide support and gold NP structure has been invoked. The latter of which can result in strain that reduces the cost of oxygen vacancy formation at the gold-support interface [100].

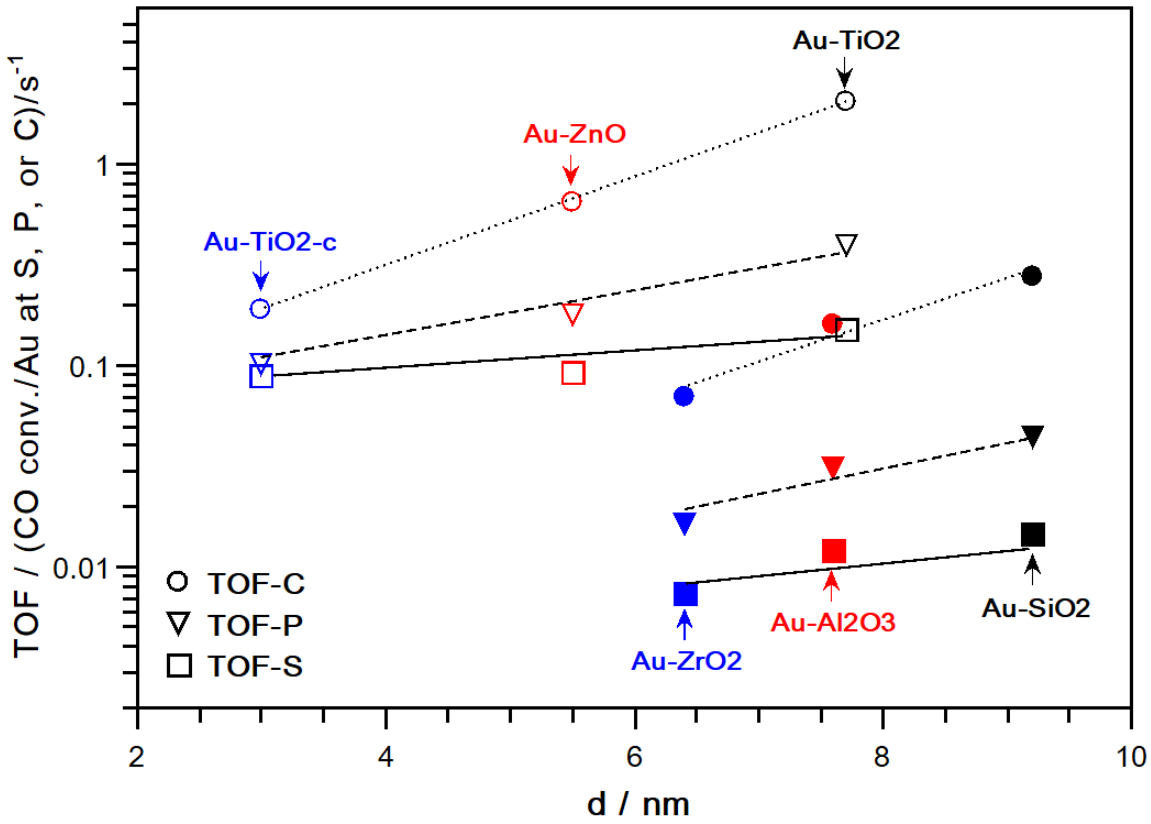

Figure 3.6. Correlation between the number of molecules of CO converted per second per total number of Au atoms at the top (excluding perimeter) surface (TOF-S; squares, solid lines; dispersion, D = $0.99/d^{0.83}$), at the Au-support perimeter (TOF-P; triangles, dashed lines, D = $0.43/d^{1.71}$), or nanoparticle corners (only at perimeter) (TOF-C; circles, dotted lines, D = $0.25/d^{2.78}$) as a function of the average gold particle size in reducible (empty symbols) and nonreducible (filled symbols) catalysts. Each catalyst' results are reported under or above each name (same *d*). Data collected in in situ/operando reaction cell. CO oxidation conditions: 398 K and 101 kPa total pressure (1 kPa CO, 2 kPa O_2, balance He). CO conversion varied between 1-25%. Lines added to guide the eye. Detailed Au site statistics are provided in **Tables B.4-B.7** and **Figures B.10** and **B.11**.

3.3.3.2. Oxygen adsorption sites.

In previous sections, it has been shown that the amount of adsorbed oxygen can be related to the amount of charge transferred from gold (ΔN) as estimated from Equations 3 or 4. These equations require the measurement of Au SPR peak in O_2 and H_2 gas environments, which was done here during consecutive exposure of gold catalysts to oxygen and hydrogen flowing gas while tracking the Au SPR peak position via in situ UV-Vis spectroscopy (**Figure 3.3**). A related idea was reported by Mulvaney and co-workers to study electron charging by chemical reduction in

colloidal solutions of gold nanorods [81, 139] and later extended to ellipsoids [140], nanodisks [141], and nanoshells [141] for plasmonic device applications. Unlike Mulvaney's application to colloidal gold which was reduced in solution, the present work demonstrated that charge transfer in Au NPs can be extended to the in situ characterization of supported gold catalysts in powder form as followed by diffuse reflectance UV-Vis spectroscopy. The method resembles somewhat conventional chemisorption techniques such as Benson and Boudart's [104] titration of adsorbed O_2 with H_2 for determining Pt dispersion, except that here the changes of the adsorbed species on the catalyst surface were monitored via in situ spectroscopy. One of the advantages of the Au SPR methodology as applied to heterogeneous catalysts via UV-Vis spectroscopy is its ability and potential to track not only the effect of adsorbed species to Au SPR peak position, but also to monitor redox events at in situ and operando conditions [142, 143].

While evidence was shown in Section 3.3.2.2 that O_2 adsorbs at the Au-support interface in O_2 flow and in Section 3.3.3.1 that CO adsorbs mostly on the top surface of the gold nanoparticles (from TOF measurements in the in situ/operando cell vs Au site statistics), it can be argued that O_2 may not adsorb at the Au-support interface during CO oxidation as the experimental conditions are different. To verify the O_2 adsorption sites at reaction conditions, we also performed in situ/operando UV-Vis during CO oxidation, that is, by carrying simultaneous reactivity and spectroscopic measurements. In this case, the relative change of charge transfer in the catalysts was estimated from changes in the Au SPR peak position at CO oxidation conditions (λ, related to adsorbed oxygen at reaction conditions) and when subsequently exposed to a flow of O_2 (λ_m, related to maximum amount of oxygen that can adsorb on Au at reaction conditions) by applying Equation 3. This relative change in charge transfer thus reflects the amount of O_2 that was consumed during CO oxidation. Compared with **Figure 3.5** (solid circles), the results presented in **Figure 3.7** (solid triangles) indicate that a significant fraction of the adsorbed O_2 at the Au-support interface is utilized for CO oxidation. These findings are in agreement with prior DFT calculations [16, 21] TAP [38], and kinetic studies [111] that suggested that at reaction conditions O_2 adsorbed at the Au-support interface. A report by Iglesia's group, however, indicated that CO oxidation (at wet conditions, 0.12-0.53 kPa H_2O) occurred on all Au sites, not just perimeter sites [112]. This apparent contradiction can be reconciled by considering Chandler and co-workers' concept of surface "flooding" [24] where under "wet" conditions water can cover the Au-support interface blocking access to these sites and only leaving the (top) surface Au sites available for reaction

likely via the formation of water-assisted hydroperoxy intermediates [112]. Additional kinetic and in situ/operando UV-Vis spectroscopic studies on gold catalysts under identical dry and wet conditions should help verify this hypothesis.

Figure 3.7 also compares the in situ O_2-GPS results at CO oxidation conditions with O_2 adsorption data (O atom/Au atom; solid squares) calculated from Behm's group TAP reactor data [39, 41]. These authors measured the oxygen storage capacity of various supported gold catalysts calcined at 523 K (Au/Al_2O_3, Au/ZrO_2, Au/ZnO, Au/TiO_2) and 673 (400 °C), 773 (500 °C), 873 (600 °C), and 973 K (700 °C) (Au/TiO_2-400, Au/TiO_2-500, Au/TiO_2-600, and Au/TiO_2-700, respectively) in a TAP reactor via CO multi-pulse titration of adsorbed O_2 at 353 or 393 K. The agreement between both set of data, in situ O_2-GPS during CO oxidation at 398 K and TAP CO titration of adsorbed O_2 at 353 and 393 K, is quite reasonable and provides strong spectroscopic and kinetic evidence for oxygen adsorption at the Au-support interface during CO oxidation at relatively high temperatures. This agreement also validates the O_2-GPS approach as a powerful yet simple in situ spectroscopic technique to determine adsorbed O_2 on gold catalysts. In summary, the combined analysis of O_2-GPS via Au SPR *vs* Au site statistics not only was in line with TAP reactor characterization of gold catalysts but also revealed the likely high reactivity of a limited number of adsorbed oxygen species for CO oxidation at the Au-support interface.

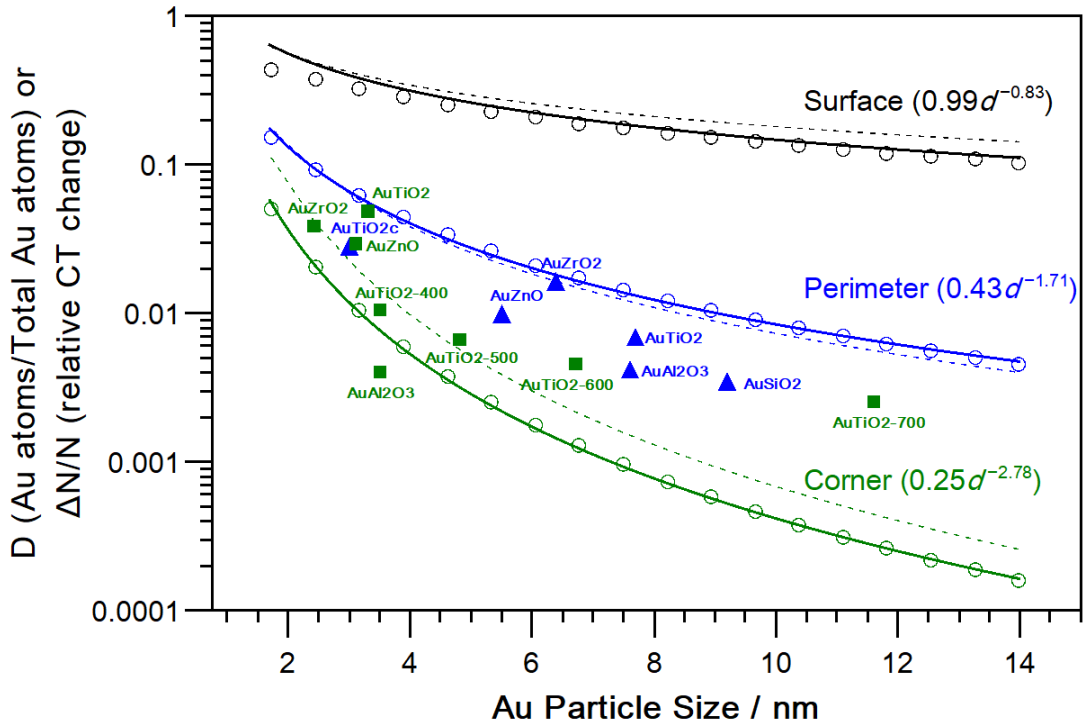

Figure 3.7. Correlation between gold average particle diameter *vs* Au (surface, perimeter, perimeter corner) atom dispersion (D) (empty circles) calculated from a Au NP with truncated octahedron geometry. Solid and dotted lines are the best fit to Au NPs with truncated octahedron and truncated cuboctahedron geometry, respectively. $\Delta N/N$ is the fraction of relative change of charge transfer (CT) determined by Au SPR peak position changes (Equation 3) from CO oxidation and flowing O_2 conditions (blue solid triangles) at 398 K. Behm and co-workers data (O atom/Au atom) was also plotted (green solid squares) as determined from oxygen storage capacity measurements using a TAP reactor by titration of adsorbed O_2 with CO via multi-pulse experiments at 353 (Au/TiO_2-400, Au/TiO_2-500, Au/TiO_2-600, and Au/TiO_2-700) [41] or 393 K (Au/TiO_2, Au/ZrO_2, Au/ZnO, and Au/Al_2O_3) [39].

To investigate a possible correlation between gold catalysts reactivity and the amount of adsorbed oxygen available for reaction, a plot of CO conversion vs the amount of reacted oxygen was prepared. For such a purpose, the total amount of charge transferred is used as a surrogate for the reacted oxygen. *ΔN/N* was already calculated and shown in **Figure 3.7**, but it is now scaled to the total gold atoms in the sample to take into account the catalyst weight differences during CO oxidation runs and to give an estimate of the total amount of charge transferred as a result of oxygen consumed. **Figure 3.8** thus explores the results of CO conversion *vs* the total charge transferred due to reacted adsorbed oxygen on the catalysts. In this figure, similar results to those in **Figure 3.6** were found: distinct trends for catalysts with reducible and nonreducible supports. For each group of supports, CO conversion correlated with the charge transferred to gold due to

the oxygen available for reaction. In the case of reducible supports, Au/ZnO was more active than Au/TiO_2 (but less active than the commercial Au/TiO_2-c), despite the higher reducibility of TiO_2, as a result of the smaller particle sizes present in Au/ZnO. This is in agreement with Schüth, Behm, and co-workers who reported that for gold catalysts of similar particle size, support reducibility is not a good descriptor of catalytic activity [110], but rather the catalyst's oxygen adsorption capacity as demonstrated by systematic and extensive TAP (temporal analysis of products) reactor measurements [39].

On the reported catalysts in **Figure 3.8**, whose supports are inactive for CO oxidation, CO conversion is expected to become zero for $\Delta N/N \times n_{Au} = 0$ (see Appendix B for derivation) because of the positive non-zero reaction rate order dependence of O_2 as reported in the literature [68]. The correlation of CO conversion with adsorbed oxygen available for reaction shown in **Figure 3.8** also suggests that oxygen should be present in rate limiting steps along with CO (**Figure 3.6**) during CO oxidation at the studied reaction conditions (398 K, 1 kPa CO, 2 kPa O_2). **Figure 3.8** also shows the often-reported reactivity differences between gold NPs supported on reducible and nonreducible supports (Au/TiO_2(commercial) > Au/ZnO > Au/TiO_2 >>> Au/ZrO_2 > Au/Al_2O_3 > Au/SiO_2). These differences are even present for catalysts that have similar amount of available oxygen for reaction such as in the case of Au/TiO_2-c and Au/ZrO_2. The reasons for these differences are unclear, although several hypothesis could be put forward where the support can affect NPs shape [110], or adsorption properties of O_2 [38, 115], CO [25, 136] or CO_2 [19, 24, 137]. Changes to the gold nanoparticle shape could introduce new active sites for CO adsorption which could be more energetically favored for diffusion towards the Au-support periphery where it can react with activated oxygen species [21]. Similarly, reducible supports could also facilitate the formation of oxygen species that are more reactive than those on nonreducible supports [38, 115]. On the other hand, inhibition by strong adsorption of CO derived species such as carbonates could also explain the significantly lower reactivity of the Au/ZrO_2 [19, 24, 39, 137]. Further research, thus, is granted to resolve all these prevailing questions.

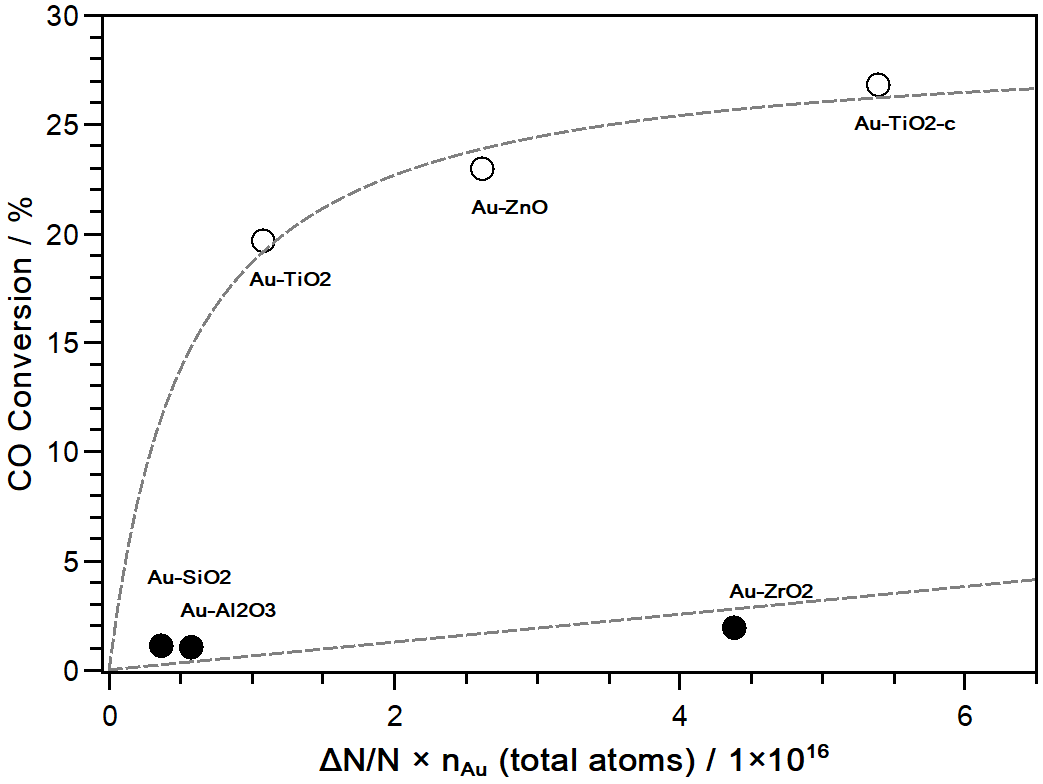

Figure 3.8. Correlation between CO conversion and the total amount of charge transferred from gold catalysts during CO oxidation. Data were collected in the same operando UV-Vis experiment. Amount of charge transferred scaled by the total atoms of gold per sample loaded in the in situ cell to correct for differences in catalyst weight during runs. Catalysts with reducible (empty symbols, top curve) and nonreducible (filled symbols, bottom curve) supports. CO oxidation conditions are the same as those in **Figure 3.6**: 398 K, 101 kPa total pressure (1 kPa CO, 2 kPa O_2, balance He), and total gas flow rate of 60 cm^3/min. CO conversion varied between 1-25%. Lines added to guide the eye.

In summary, we have shown evidence for adsorption of oxygen at the Au-support perimeter (**Figure 3.5**). A fraction of the oxygen species on these sites (**Figure 3.7**), whose nature cannot be assessed by the Au SPR method, react at high temperatures (398 K) in rate limiting steps with CO, which more likely adsorbs on gold surface sites and diffuse to the Au-support perimeter (**Figure 3.6**). The mechanism by which CO is oxidized at this high temperature appears to be similar for gold on reducible and nonreducible supports; however, the higher activity of reducible supports cannot be explained by the catalysts' oxygen adsorption capacity alone, rather, we hypothesize that support surface properties, including reducibility and acid-base properties, can affect active sites and the adsorption/desorption strength of O_2, CO_x or CO_x derived species which can result in more or less active species or block access to active sites. Additional kinetics, in situ/operando

spectroscopic characterization, and theoretical studies are thus required to further clarify these differences in an apparently widely studied but not fully understood reaction.

3.4. Conclusions

We have developed a simple characterization method based on gold surface plasmon resonance to correlate oxygen adsorption properties of supported gold catalysts, we named this technique gold plasmon sensing of adsorbed oxygen or simply O_2-GPS. The technique was applied under flowing O_2 and CO oxidation conditions and in combination with Au nanoparticle site statistics analysis provided the first in situ UV-Vis spectroscopic evidence for adsorption of O_2 at the Au-support interface. The O_2-GPS technique is based on monitoring the changes of the gold surface plasmon resonance peak position in real time in an in situ/operando diffuse reflectance UV-Vis reaction cell under oxidizing (e.g., O_2) and reducing (e.g., H_2) or less oxidizing environments. The gold catalysts were prepared by the deposition-precipitation method using ammonia as the base reagent to minimize sodium contamination in the catalysts, to prepare catalysts with similar gold content, and supported on metal oxides of similar surface area including SiO_2, Al_2O_3, ZrO_2, ZnO, and TiO_2. This synthetic methodology allowed us to reduce the number of experimental variables to probe the catalysts for oxygen adsorption and catalytic reactivity during CO oxidation at high temperature (398 K). A simple charge transfer model based on the support's dielectric constant and Drude's free electron model for gold nanoparticles dielectric function was employed to estimate the relative charge transfer change from/to gold during oxygen adsorption and titration with hydrogen. This relative charge transfer change was used as a surrogate of adsorbed oxygen in flowing O_2 (in situ UV-Vis) and at CO oxidation (operando UV-Vis) reaction conditions to correlate with gold particle size, support, and catalytic activity. The method proved simple and confirmed the large effect of support reducibility on gold charge transfer; however, reducibility alone was not sufficient to explain a catalyst's oxygen adsorption properties, which also depended on gold particle size and increased with smaller gold particle sizes. A correlation was found between charge transfer from gold to oxygen and gold nanoparticle size suggesting that for reducible and nonreducible supports at 398 K oxygen adsorption primarily occurred at the Au-support perimeter, a fraction of which is available for CO oxidation. At reaction conditions, CO oxidation turnover frequencies showed distinct linear trends for reducible and nonreducible

supports, which were less dependent on gold particle size when normalized by the total number of surface gold atoms. CO conversion followed the same trend when compared to the total charge transferred due to oxygen available for reaction at the same reaction temperature. Overall, the presented results provide evidence of oxygen participation at the Au-support perimeter and CO or CO_x intermediate species on (top) surface gold atoms in rate limiting steps with reducible and nonreducible supports. Our study also rises additional questions regarding the enhancement of catalytic activity when reducible supports are used as the amount of charge transfer (or adsorbed oxygen) does not fully account for the significantly different catalytic activity. We hypothesize that support acid-base properties and presence of oxygen vacancies may be at play as they could influence the adsorption/desorption of O_2 and CO or CO_x derived intermediates which could adsorb strongly on active sites and inhibit the reaction. The simple yet powerful in situ O_2-GPS technique developed here along with future kinetic and in situ/operando spectroscopies (e.g., IR, Raman) should shed additional light to our understanding of gold-support effects, particle size, and reactant/product inhibition in CO and other oxidation reactions enabled by gold catalysts.

This work was submitted for publication and is currently under review

3.5. References

1. Bond, G.C., Sermon, P.A., Webb, G., Buchanan, D.A., and Wells, P.B., Hydrogenation over supported gold catalysts. *Journal of the Chemical Society, Chemical Communications* **1973,** (13), 444-445.
2. Nkosi, B., Coville, N.J., and Hutchings, G.J., Reactivation of a supported gold catalyst for acetylene hydrochlorination. *Journal of the Chemical Society, Chemical Communications* **1988,** (1), 71-72.
3. Haruta, M., Kobayashi, T., Sano, H., and Yamada, N., Novel Gold Catalysts for the Oxidation of Carbon Monoxide at a Temperature far Below 0 °C. *Chemistry Letters* **1987,** *16* (2), 405-408.
4. Hayashi, T., Tanaka, K., and Haruta, M., Selective vapor-phase epoxidation of propylene over Au/TiO2 catalysts in the presence of oxygen and hydrogen. *Journal of Catalysis* **1998,** *178* (2), 566-575.

5. Prati, L. and Rossi, M., Gold on carbon as a new catalyst for selective liquid phase oxidation of diols. *Journal of Catalysis* **1998,** *176* (2), 552-560.
6. Haruta, M., Size- and support-dependency in the catalysis of gold. *Catalysis Today* **1997,** *36* (1), 153-166.
7. Takei, T., Akita, T., Nakamura, I., Fujitani, T., Okumura, M., Okazaki, K., Huang, J.H., Ishida, T., and Haruta, M., Heterogeneous Catalysis by Gold. *Advances in Catalysis* **2012,** *55*, 1-126.
8. Haruta, M., Gold rush. *Nature* **2005,** *437*, 1098.
9. Dykman, L. and Khlebtsov, N., Gold nanoparticles in biomedical applications: recent advances and perspectives. *Chemical Society Reviews* **2012,** *41* (6), 2256-2282.
10. Zeng, S.W., Baillargeat, D., Ho, H.P., and Yong, K.T., Nanomaterials enhanced surface plasmon resonance for biological and chemical sensing applications. *Chemical Society Reviews* **2014,** *43* (10), 3426-3452.
11. Linic, S., Aslam, U., Boerigter, C., and Morabito, M., Photochemical transformations on plasmonic metal nanoparticles. *Nature Materials* **2015,** *14* (6), 567-576.
12. Kreibig, U. and Vollmer, M., *Optical properties of metal clusters*. Springer: Berlin (Germany), **1995;** p 1-553.
13. Bravo-Suárez, J.J., Chaudhari, R.V., and Subramaniam, B., Design of Heterogeneous Catalysts for Fuels and Chemicals Processing: An Overview. In *Novel Materials for Catalysis and Fuels Processing*, J.J. Bravo-Suárez, Kidder, M.K., and Schwartz, V., Eds. American Chemical Society: Washington, D.C., **2013;** Vol. Volume 1132, pp 3-68.
14. Bravo-Suárez, J.J., Bando, K.K., Lu, J.I., Haruta, M., Fujitani, T., and Oyama, S.T., Transient technique for identification of true reaction intermediates: Hydroperoxide species in propylene epoxidation on gold/titanosilicate catalysts by X-ray absorption fine structure spectroscopy. *Journal of Physical Chemistry C* **2008,** *112* (4), 1115-1123.
15. Oyama, S.T. and Zhang, W., True and spectator intermediates in catalysis: The case of ethanol oxidation on molybdenum oxide as observed by in situ laser Raman spectroscopy. *Journal of the American Chemical Society* **1996,** *118* (30), 7173-7177.
16. Saavedra, J., Doan, H.A., Pursell, C.J., Grabow, L.C., and Chandler, B.D., The critical role of water at the gold-titania interface in catalytic CO oxidation. *Science* **2014,** *345* (6204), 1599-1602.

17. Henao, J.D., Caputo, T., Yang, J.H., Kung, M.C., and Kung, H.H., In situ transient FTIR and XANES studies of the evolution of surface species in CO oxidation on Au/TiO_2. *Journal of Physical Chemistry B* **2006,** *110* (17), 8689-8700.
18. Piccolo, L., Daly, H., Valcarcel, A., and Meunier, F.C., Promotional effect of H-2 on CO oxidation over Au/TiO2 studied by operando infrared spectroscopy. *Applied Catalysis B-Environmental* **2009,** *86* (3-4), 190-195.
19. Clark, J.C., Dai, S., and Overbury, S.H., Operando studies of desorption, reaction and carbonate formation during CO oxidation by Au/TiO_2 catalysts. *Catalysis Today* **2007,** *126* (1–2), 135-142.
20. Wang, Y.C., Widmann, D., and Behm, R.J., Influence of TiO_2 Bulk Defects on CO Adsorption and CO Oxidation on Au/TiO_2: Electronic Metal-Support Interactions (EMSIs) in Supported Au Catalysts. *ACS Catalysis* **2017,** *7* (4), 2339-2345.
21. Green, I.X., Tang, W.J., Neurock, M., and Yates, J.T., Spectroscopic Observation of Dual Catalytic Sites During Oxidation of CO on a Au/TiO_2 Catalyst. *Science* **2011,** *333* (6043), 736-739.
22. Schilling, C. and Hess, C., CO Oxidation on Ceria Supported Gold Catalysts Studied by Combined Operando Raman/UV-Vis and IR Spectroscopy. *Topics in Catalysis* **2017,** *60* (1-2), 131-140.
23. Panayotov, D.A., Burrows, S.P., Yates, J.T., and Morris, J.R., Mechanistic Studies of Hydrogen Dissociation and Spillover on Au/TiO_2: IR Spectroscopy of Coadsorbed CO and H-Donated Electrons. *Journal of Physical Chemistry C* **2011,** *115* (45), 22400-22408.
24. Saavedra, J., Pursell, C.J., and Chandler, B.D., CO Oxidation Kinetics over Au/TiO_2 and Au/Al2O3 Catalysts: Evidence for a Common Water-Assisted Mechanism. *Journal of the American Chemical Society* **2018,** *140* (10), 3712-3723.
25. Lari, G.M., Nowicka, E., Morgan, D.J., Kondrat, S.A., and Hutchings, G.J., The use of carbon monoxide as a probe molecule in spectroscopic studies for determination of exposed gold sites on TiO_2. *Physical Chemistry Chemical Physics* **2015,** *17* (35), 23236-23244.
26. Kung, M.C., Davis, R.J., and Kung, H.H., Understanding Au-catalyzed low-temperature CO oxidation. *Journal of Physical Chemistry C* **2007,** *111* (32), 11767-11775.

27. Lohrenscheit, M. and Hess, C., Direct Evidence for the Participation of Oxygen Vacancies in the Oxidation of Carbon Monoxide over Ceria-Supported Gold Catalysts by using Operando Raman Spectroscopy. *Chemcatchem* **2016,** *8* (3), 523-526.
28. Schwartz, V., Mullins, D.R., Yan, W.F., Chen, B., Dai, S., and Overbury, S.H., XAS study of Au supported on TiO2: Influence of oxidation state and particle size on catalytic activity. *Journal of Physical Chemistry B* **2004,** *108* (40), 15782-15790.
29. Hutchings, G.J., Hall, M.S., Carley, A.F., Landon, P., Solsona, B.E., Kiely, C.J., Herzing, A., Makkee, M., Moulijn, J.A., Overweg, A., Fierro-Gonzalez, J.C., Guzman, J., and Gates, B.C., Role of gold cations in the oxidation of carbon monoxide catalyzed by iron oxide-supported gold. *Journal of Catalysis* **2006,** *242* (1), 71-81.
30. Weiher, N., Bus, E., Delannoy, L., Louis, C., Ramaker, D.E., Miller, J.T., and van Bokhoven, J.A., Structure and oxidation state of gold on different supports under various CO oxidation conditions. *Journal of Catalysis* **2006,** *240* (2), 100-107.
31. Guzman, J. and Gates, B.C., Catalysis by Supported Gold: Correlation between Catalytic Activity for CO Oxidation and Oxidation States of Gold. *Journal of the American Chemical Society* **2004,** *126* (9), 2672-2673.
32. van Bokhoven, J.A., Louis, C., T Miller, J., Tromp, M., Safonova, O.V., and Glatzel, P., Activation of oxygen on gold/alumina catalysts: In situ high-energy-resolution fluorescence and time-resolved X-ray spectroscopy. *Angewandte Chemie-International Edition* **2006,** *45* (28), 4651-4654.
33. Weiher, N., Beesley, A.M., Tsapatsaris, N., Delannoy, L., Louis, C., van Bokhoven, J.A., and Schroeder, S.L.M., Activation of oxygen by metallic gold in Au/TiO2 catalysts. *Journal of the American Chemical Society* **2007,** *129* (8), 2240-2241.
34. Costello, C.K., Kung, M.C., Oh, H.S., Wang, Y., and Kung, H.H., Nature of the active site for CO oxidation on highly active Au/gamma-Al2O3. *Applied Catalysis a-General* **2002,** *232* (1-2), 159-168.
35. Calla, J.T. and Davis, R.J., Oxygen-exchange reactions during CO oxidation over titania- and alumina-supported Au nanoparticles. *Journal of Catalysis* **2006,** *241* (2), 407-416.
36. Widmann, D., Krautsieder, A., Walter, P., Bruckner, A., and Behm, R.J., How Temperature Affects the Mechanism of CO Oxidation on Au/TiO2: A Combined EPR and TAP Reactor

Study of the Reactive Removal of TiO2 Surface Lattice Oxygen in Au/TiO2 by CO. *ACS Catalysis* **2016,** *6* (8), 5005-5011.

37. Widmann, D. and Behm, R.J., Active Oxygen on a Au/TiO2 Catalyst: Formation, Stability, and CO Oxidation Activity. *Angewandte Chemie-International Edition* **2011,** *50* (43), 10241-10245.
38. Widmann, D. and Behm, R.J., Activation of Molecular Oxygen and the Nature of the Active Oxygen Species for CO Oxidation on Oxide Supported Au Catalysts. *Accounts of Chemical Research* **2014,** *47* (3), 740-749.
39. Widmann, D., Liu, Y., Schuth, F., and Behm, R.J., Support effects in the Au-catalyzed CO oxidation - Correlation between activity, oxygen storage capacity, and support reducibility. *Journal of Catalysis* **2010,** *276* (2), 292-305.
40. Widmann, D. and Behm, R.J., Dynamic surface composition in a Mars-van Krevelen type reaction: CO oxidation on Au/TiO2. *Journal of Catalysis* **2018,** *357*, 263-273.
41. Kotobuki, M., Leppelt, R., Hansgen, D.A., Widmann, D., and Behm, R.J., Reactive oxygen on a Au/TiO2 supported catalyst. *Journal of Catalysis* **2009,** *264* (1), 67-76.
42. Fu, Q., Deng, W.L., Saltsburg, H., and Flytzani-Stephanopoulos, M., Activity and stability of low-content gold-cerium oxide catalysts for the water-gas shift reaction. *Applied Catalysis B-Environmental* **2005,** *56* (1-2), 57-68.
43. Lakshmanan, P., Averseng, F., Bion, N., Delannoy, L., Tatibouet, J.M., and Louis, C., Understanding of the oxygen activation on ceria- and ceria/alumina-supported gold catalysts: a study combining O-18/O-16 isotopic exchange and EPR spectroscopy. *Gold Bulletin* **2013,** *46* (4), 233-242.
44. Bravo-Suárez, J.J., Bando, K.K., Akita, T., Fujitani, T., Fuhrer, T.J., and Oyama, S.T., Propane reacts with O-2 and H-2 on gold supported TS-1 to form oxygenates with high selectivity. *Chemical Communications* **2008,** (28), 3272-3274.
45. Bravo-Suárez, J.J., Bando, K.K., Fujitani, T., and Oyama, S.T., Mechanistic study of propane selective oxidation with H-2 and O-2 on Au/TS-1. *Journal of Catalysis* **2008,** *257* (1), 32-42.
46. Bravo-Suárez, J.J., Bando, K.K., Lu, J., Fujitani, T., and Oyama, S.T., Oxidation of propane to propylene oxide on gold catalysts. *Journal of Catalysis* **2008,** *255* (1), 114-126.

47. Rogers, P.H., Sirinakis, G., and Carpenter, M.A., Direct observations of electrochemical reactions within Au-YSZ thin films via absorption shifts in the an nanoparticle surface plasmon resonance. *Journal of Physical Chemistry C* **2008,** *112* (17), 6749-6757.

48. Joy, N.A., Nandasiri, M.I., Rogers, P.H., Jiang, W.L., Varga, T., Kuchibhatla, S., Thevuthasan, S., and Carpenter, M.A., Selective Plasmonic Gas Sensing: H-2, NO2, and CO Spectral Discrimination by a Single Au-CeO2 Nanocomposite Film. *Analytical Chemistry* **2012,** *84* (11), 5025-5034.

49. Dharmalingam, G., Joy, N.A., Grisafe, B., and Carpenter, M.A., Plasmonics-based detection of H-2 and CO: discrimination between reducing gases facilitated by material control. *Beilstein Journal of Nanotechnology* **2012,** *3*, 712-721.

50. Ohodnicki, P.R., Buric, M.P., Brown, T.D., Matranga, C., Wang, C.J., Baltrus, J., and Andio, M., Plasmonic nanocomposite thin film enabled fiber optic sensors for simultaneous gas and temperature sensing at extreme temperatures. *Nanoscale* **2013,** *5* (19), 9030-9039.

51. Ohodnicki, P.R., Brown, T.D., Holcomb, G.R., Tylczak, J., Schultz, A.M., and Baltrus, J.P., High temperature optical sensing of gas and temperature using Au-nanoparticle incorporated oxides. *Sensors and Actuators, B: Chemical* **2014,** *202*, 489-499.

52. Della Gaspera, E., Bersani, M., Mattei, G., Nguyen, T.L., Mulvaney, P., and Martucci, A., Cooperative effect of Au and Pt inside TiO2 matrix for optical hydrogen detection at room temperature using surface plasmon spectroscopy. *Nanoscale* **2012,** *4* (19), 5972-5979.

53. Borensztein, Y., Delannoy, L., Djedidi, A., Barrera, R.G., and Louis, C., Monitoring of the Plasmon Resonance of Gold Nanoparticles in Au/TiO2 Catalyst under Oxidative and Reducing Atmospheres. *The Journal of Physical Chemistry C* **2010,** *114* (19), 9008-9021.

54. Borensztein, Y., Delannoy, L., Barrera, R.G., and Louis, C., Kinetics of the plasmon optical response of Au nanoparticles/TiO2 catalyst under O-2 and H-2 followed by differential diffuse reflectance spectroscopy. *European Physical Journal D* **2011,** *63* (2), 235-240.

55. Larsson, E.M., Langhammer, C., Zorić, I., and Kasemo, B., Nanoplasmonic probes of catalytic reactions. *Science* **2009,** *326* (5956), 1091-1094.

56. Langhammer, C. and Larsson, E.M., Nanoplasmonic In Situ Spectroscopy for Catalysis Applications. *ACS Catalysis* **2012,** *2* (9), 2036-2045.

57. Wettergren, K., Hellman, A., Cavalca, F., Zhdanov, V.P., and Langhammer, C., Unravelling the Dependence of Hydrogen Oxidation Kinetics on the Size of Pt Nanoparticles by in Operando Nanoplasmonic Temperature Sensing. *Nano Letters* **2015,** *15* (1), 574-580.
58. Larsson, E.M., Millet, J., Gustafsson, S., Skoglundh, M., Zhdanov, V.P., and Langhammer, C., Real Time Indirect Nanoplasmonic in Situ Spectroscopy of Catalyst Nanoparticle Sintering. *ACS Catalysis* **2012,** *2* (2), 238-245.
59. Adibi, P.T.Z., Pingel, T., Olsson, E., Gronbeck, H., and Langhammer, C., Pt Nanoparticle Sintering and Redispersion on a Heterogeneous Nanostructured Support. *Journal of Physical Chemistry C* **2016,** *120* (27), 14918-14925.
60. Langhammer, C., Larsson, E.M., Kasemo, B., and Zoric, I., Indirect Nanoplasmonic Sensing: Ultrasensitive Experimental Platform for Nanomaterials Science and Optical Nanocalorimetry. *Nano Letters* **2010,** *10* (9), 3529-3538.
61. Srinivasan, P.D., Nitz, S.R., Stephens, K.J., Atchison, E., and Bravo-Suárez, J.J., Modified Harrick reaction cell for in situ/operando fiber optics diffuse reflectance UV–visible spectroscopic characterization of catalysts. *Applied Catalysis A: General* **2018,** *561*, 7-18.
62. Sirinakis, G., Siddique, R., Manning, I., Rogers, P.H., and Carpenter, M.A., Development and Characterization of Au−YSZ Surface Plasmon Resonance Based Sensing Materials: High Temperature Detection of CO. *The Journal of Physical Chemistry B* **2006,** *110* (27), 13508-13511.
63. Joy, N.A., Settens, C.M., Matyi, R.J., and Carpenter, M.A., Plasmonic Based Kinetic Analysis of Hydrogen Reactions within Au−YSZ Nanocomposites. *The Journal of Physical Chemistry C* **2011,** *115* (14), 6283-6289.
64. Rogers, P.H., Sirinakis, G., and Carpenter, M.A., Plasmonic-based Detection of NO2 in a Harsh Environment. *The Journal of Physical Chemistry C* **2008,** *112* (24), 8784-8790.
65. Rogers, P.H. and Carpenter, M.A., Particle Size Sensitivity Dependence of Nanocomposites for Plasmonic-Based All-Optical Sensing Applications. *The Journal of Physical Chemistry C* **2010,** *114* (25), 11033-11039.
66. Buso, D., Post, M., Cantalini, C., Mulvaney, P., and Martucci, A., Gold Nanoparticle-Doped TiO2 Semiconductor Thin Films: Gas Sensing Properties. *Advanced Functional Materials* **2008,** *18* (23), 3843-3849.

67. Della Gaspera, E., Guglielmi, M., Martucci, A., Giancaterini, L., and Cantalini, C., Enhanced optical and electrical gas sensing response of sol–gel based NiO–Au and ZnO–Au nanostructured thin films. *Sensors and Actuators, B: Chemical* **2012,** *164* (1), 54-63.
68. Aguilar-Guerrero, V. and Gates, B.C., Kinetics of CO Oxidation Catalyzed by Supported Gold: A Tabular Summary of the Literature. *Catalysis Letters* **2009,** *130* (1-2), 108-120.
69. Wang, Y.G., Yoon, Y., Glezakou, V.A., Li, J., and Rousseau, R., The Role of Reducible Oxide-Metal Cluster Charge Transfer in Catalytic Processes: New Insights on the Catalytic Mechanism of CO Oxidation on Au/TiO2 from ab Initio Molecular Dynamics. *Journal of the American Chemical Society* **2013,** *135* (29), 10673-10683.
70. Mihaylov, M., Knoezinger, H., Hadjiivanov, K., and Gates, B.C., Characterization of the oxidation states of supported gold species by IR spectroscopy of adsorbed CO. *Chemie Ingenieur Technik* **2007,** *79* (6), 795-806.
71. Akita, T., Lu, P., Ichikawa, S., Tanaka, K., and Haruta, M., Analytical TEM study on the dispersion of Au nanoparticles in Au/TiO2 catalyst prepared under various temperatures. *Surface and Interface Analysis* **2001,** *31* (2), 73-78.
72. Nijhuis, T.A., Visser, T., and Weckhuysen, B.M., Mechanistic study into the direct epoxidation of propene over gold/titania catalysts. *Journal of Physical Chemistry B* **2005,** *109* (41), 19309-19319.
73. Phonthammachai, N. and White, T.J., One-step synthesis of highly dispersed gold nanocrystals on silica spheres. *Langmuir* **2007,** *23* (23), 11421-11424.
74. Moreau, F., Bond, G.C., and Taylor, A.O., Gold on titania catalysts for the oxidation of carbon monoxide: control of pH during preparation with various gold contents. *Journal of Catalysis* **2005,** *231* (1), 105-114.
75. Steinhauser, G., Evers, J., Jakob, S., Klapötke, T.M., and Oehlinger, G., A review on fulminating gold (Knallgold). *Gold Bulletin* **2008,** *41* (4), 305-317.
76. Nealon, G.L., Donnio, B., Greget, R., Kappler, J.-P., Terazzi, E., and Gallani, J.-L., Magnetism in gold nanoparticles. *Nanoscale* **2012,** *4* (17), 5244-5258.
77. Lopez, N., Janssens, T.V.W., Clausen, B.S., Xu, Y., Mavrikakis, M., Bligaard, T., and Nørskov, J.K., On the origin of the catalytic activity of gold nanoparticles for low-temperature CO oxidation. *Journal of Catalysis* **2004,** *223* (1), 232-235.

78. Bond, G.C. and Thompson, D.T., Catalysis by gold. *Catalysis Reviews - Science and Engineering* **1999,** *41* (3-4), 319-388.
79. Larsson, E.M., Edvardsson, M.E.M., Langhammer, C., Zorić, I., and Kasemo, B., A combined nanoplasmonic and electrodeless quartz crystal microbalance setup. *Review of Scientific Instruments* **2009,** *80* (12), 125105.
80. Collins, S.S.E., Cittadini, M., Pecharroman, C., Martucci, A., and Mulvaney, P., Hydrogen Spillover between Single Gold Nanorods and Metal Oxide Supports: A Surface Plasmon Spectroscopy Study. *ACS Nano* **2015,** *9* (8), 7846-7856.
81. Mulvaney, P., Pérez-Juste, J., Giersig, M., Liz-Marzán, L.M., and Pecharromán, C., Drastic Surface Plasmon Mode Shifts in Gold Nanorods Due to Electron Charging. *Plasmonics* **2006,** *1* (1), 61-66.
82. Romero-Sarria, F., Plata, J.J., Laguna, O.H., Marquez, A.M., Centeno, M.A., Sanz, J.F., and Odriozola, J.A., Surface oxygen vacancies in gold based catalysts for CO oxidation. *Rsc Advances* **2014,** *4* (25), 13145-13152.
83. Takagi, S., Hoshino, J.-i., Tomono, H., and Tsumuraya, K., Electron Transfer from Hydrogen Molecule to Au(111) During Dissociative Adsorption: A First-Principles Study. *Journal of the Physical Society of Japan* **2008,** *77* (5), 054705.
84. Baltrus, J.P., Ohodnicki, P.R., Joy, N.A., and Carpenter, M.A., Examination of charge transfer in Au/YSZ for high-temperature optical gas sensing. *Applied Surface Science* **2014,** *313*, 19-25.
85. Shannon, R.D., Shannon, R.C., Medenbach, O., and Fischer, R.X., Refractive Index and Dispersion of Fluorides and Oxides. *Journal of Physical and Chemical Reference Data* **2002,** *31* (4), 931-970.
86. Liu, W.C., Wu, D., Li, A.D., Ling, H.Q., Tang, Y.F., and Ming, N.B., Annealing and doping effects on structure and optical properties of sol-gel derived ZrO2 thin films. *Applied Surface Science* **2002,** *191* (1-4), 181-187.
87. van Dijk, M.A. Nonlinear-optical studies of single gold nanoparticles. Dissertation, Universiteit Leiden, **2007**.
88. Lee, K.-S. and El-Sayed, M.A., Gold and Silver Nanoparticles in Sensing and Imaging: Sensitivity of Plasmon Response to Size, Shape, and Metal Composition. *The Journal of Physical Chemistry B* **2006,** *110* (39), 19220-19225.

89. Xu, H. and Käll, M., Modeling the optical response of nanoparticle-based surface plasmon resonance sensors. *Sensors and Actuators, B: Chemical* **2002,** *87* (2), 244-249.
90. Bus, E., Miller, J.T., and van Bokhoven, J.A., Hydrogen chemisorption on Al2O3-supported gold catalysts. *Journal of Physical Chemistry B* **2005,** *109* (30), 14581-14587.
91. Chowdhury, B., Bravo-Suárez, J.J., Mimura, N., Lu, J.Q., Bando, K.K., Tsubota, S., and Haruta, M., In situ UV-vis and EPR study on the formation of hydroperoxide species during direct gas phase propylene epoxidation over Au/Ti-SiO2 catalyst. *Journal of Physical Chemistry B* **2006,** *110* (46), 22995-22999.
92. Herrmann, J.M., The electronic factor and related redox processes in oxidation catalysis. *Catalysis Today* **2006,** *112* (1-4), 73-77.
93. Herrmann, J.-M., Applications of Electrical Conductivity Measurements in Heterogeneous Catalysis. In *Catalyst Characterization: Physical Techniques for Solid Materials*, B. Imelik and Vedrine, J.C., Eds. Springer US: Boston, MA, **1994;** pp 559-584.
94. Fierro-Gonzalez, J.C. and Gates, B.C., Catalysis by gold dispersed on supports: the importance of cationic gold. *Chemical Society Reviews* **2008,** *37* (9), 2127-2134.
95. Mulvaney, P., Surface Plasmon Spectroscopy of Nanosized Metal Particles. *Langmuir* **1996,** *12* (3), 788-800.
96. McFarland, A.D. and Van Duyne, R.P., Single Silver Nanoparticles as Real-Time Optical Sensors with Zeptomole Sensitivity. *Nano Letters* **2003,** *3* (8), 1057-1062.
97. Doyle, W.T., Absorption of Light by Colloids in Alkali Halide Crystals. *Phys. Rev.* **1958,** *111* (4), 1067-1072.
98. Doremus, R.H., Optical Properties of Small Gold Particles. *The Journal of Chemical Physics* **1964,** *40* (8), 2389-2396.
99. Derkachova, A., Kolwas, K., and Demchenko, I., Dielectric Function for Gold in Plasmonics Applications: Size Dependence of Plasmon Resonance Frequencies and Damping Rates for Nanospheres. *Plasmonics* **2016,** *11* (3), 941-951.
100. Ruiz Puigdollers, A., Schlexer, P., Tosoni, S., and Pacchioni, G., Increasing Oxide Reducibility: The Role of Metal/Oxide Interfaces in the Formation of Oxygen Vacancies. *ACS Catalysis* **2017,** *7* (10), 6493-6513.

101. Chretien, S. and Metiu, H., Density functional study of the charge on Au-n clusters (n=1-7) supported on a partially reduced rutile TiO2(110): Are all clusters negatively charged? *Journal of Chemical Physics* **2007,** *126* (10).

102. Molina, L.M., Rasmussen, M.D., and Hammer, B., Adsorption of O-2 and oxidation of CO at Au nanoparticles supported by TiO2(110). *Journal of Chemical Physics* **2004,** *120* (16), 7673-7680.

103. Sanchez, A., Abbet, S., Heiz, U., Schneider, W.D., Hakkinen, H., Barnett, R.N., and Landman, U., When gold is not noble: Nanoscale gold catalysts. *Journal of Physical Chemistry A* **1999,** *103* (48), 9573-9578.

104. Benson, J.E. and Boudart, M., Hydrogen-oxygen titration method for the measurement of supported platinum surface areas. *Journal of Catalysis* **1965,** *4* (6), 704-710.

105. Bergeret, G. and Gallezot, P., Particle Size and Dispersion Measurements. In *Handbook of Heterogeneous Catalysis*, 2nd ed.; G. Ertl, Knözinger, H., Schüth, F., and Weitkamp, J., Eds. Wiley-VCH: Weinheim, **2008;** pp 738-765.

106. Berndt, H., Pitsch, I., Evert, S., Struve, K., Pohl, M.M., Radnik, J., and Martin, A., Oxygen adsorption on Au/Al2O3 catalysts and relation to the catalytic oxidation of ethylene glycol to glycolic acid. *Applied Catalysis a-General* **2003,** *244* (1), 169-179.

107. Haruta, M., Yamada, N., Kobayashi, T., and Iijima, S., Gold catalysts prepared by coprecipitation for low-temperature oxidation of hydrogen and of carbon monoxide. *Journal of Catalysis* **1989,** *115* (2), 301-309.

108. Srinivasan, P.D., Patil, B.S., Zhu, H., and Bravo-Suárez, J.J., Application of modulation excitation-phase sensitive detection-DRIFTS for in situ/operando characterization of heterogeneous catalysts. *Reaction Chemistry & Engineering* **2019,** *DOI: 10.1039/C9RE00011A*.

109. Fu, Q., Weber, A., and Flytzani-Stephanopoulos, M., Nanostructured Au-CeO2 catalysts for low-temperature water-gas shift. *Catalysis Letters* **2001,** *77* (1-3), 87-95.

110. Comotti, M., Li, W.C., Spliethoff, B., and Schuth, F., Support effect in high activity gold catalysts for CO oxidation. *Journal of the American Chemical Society* **2006,** *128* (3), 917-924.

111. Shekhar, M., Wang, J., Lee, W.S., Williams, W.D., Kim, S.M., Stach, E.A., Miller, J.T., Delgass, W.N., and Ribeiro, F.H., Size and Support Effects for the Water-Gas Shift

Catalysis over Gold Nanoparticles Supported on Model Al2O3 and TiO2. *Journal of the American Chemical Society* **2012,** *134* (10), 4700-4708.

112. Ojeda, M., Zhan, B.Z., and Iglesia, E., Mechanistic interpretation of CO oxidation turnover rates on supported Au clusters. *Journal of Catalysis* **2012,** *285* (1), 92-102.
113. Uchiyama, T., Yoshida, H., and Kamiuchi, N., Correlation of catalytic activity with the morphology change of supported Au nanoparticles in gas. *Surface Science* **2017,** *659*, 16-19.
114. Carlsson, A., Puig-Molina, A., and Janssens, T.V.W., New Method for Analysis of Nanoparticle Geometry in Supported fcc Metal Catalysts with Scanning Transmission Electron Microscopy. *The Journal of Physical Chemistry B* **2006,** *110* (11), 5286-5293.
115. Widmann, D. and Behm, R.J., Formation and removal of active oxygen species for the non-catalytic CO oxidation on Au/TiO2 catalysts. *Chinese Journal of Catalysis* **2016,** *37* (10), 1684-1693.
116. Overbury, S.H., Schwartz, V., Mullins, D.R., Yan, W., and Dai, S., Evaluation of the Au size effect: CO oxidation catalyzed by Au/TiO2. *Journal of Catalysis* **2006,** *241* (1), 56-65.
117. Janssens, T.V.W., Clausen, B.S., Hvolbaek, B., Falsig, H., Christensen, C.H., Bligaard, T., and Norskov, J.K., Insights into the reactivity of supported Au nanoparticles: combining theory and experiments. *Topics in Catalysis* **2007,** *44* (1-2), 15-26.
118. Patil, B.S., Srinivasan, P.D., Atchison, E., Zhu, H., and Bravo-Suárez, J.J., Design, Modelling, and Application of a Low Void-Volume in Situ Diffuse Reflectance Spectroscopic Reaction Cell for Transient Catalytic Studies. *React. Eng. Chem.* **2019,** *4*, 667-678.
119. Barnard, A.S., Lin, X.M., and Curtiss, L.A., Equilibrium Morphology of Face-Centered Cubic Gold Nanoparticles >3 nm and the Shape Changes Induced by Temperature. *The Journal of Physical Chemistry B* **2005,** *109* (51), 24465-24472.
120. Barnard, A.S. and Curtiss, L.A., Predicting the Shape and Structure of Face-Centered Cubic Gold Nanocrystals Smaller than 3 nm. *Chem Phys Chem* **2006,** *7* (7), 1544-1553.
121. Wang, B.Y., Liu, M.X., Wang, Y.T., and Chen, X.S., Structures and Energetics of Silver and Gold Nanoparticles. *Journal of Physical Chemistry C* **2011,** *115* (23), 11374-11381.

122. McKenna, K.P., Gold nanoparticles under gas pressure. *Physical Chemistry Chemical Physics* **2009,** *11* (21), 4145-4151.
123. Zanella, R., Giorgio, S., Shin, C.-H., Henry, C.R., and Louis, C., Characterization and reactivity in CO oxidation of gold nanoparticles supported on TiO2 prepared by deposition-precipitation with NaOH and urea. *Journal of Catalysis* **2004,** *222* (2), 357-367.
124. Shao, B., Zhang, J., Huang, J., Qiao, B., Su, Y., Miao, S., Zhou, Y., Li, D., Huang, W., and Shen, W., Size-Dependency of Gold Nanoparticles on TiO2 for CO Oxidation. *Small Methods* **2018,** *2* (12), 1800273.
125. Wei, X.J., Shao, B., Zhou, Y., Li, Y., Jin, C.C., Liu, J.Y., and Shen, W.J., Geometrical Structure of the Gold-Iron(III) Oxide Interfacial Perimeter for CO Oxidation. *Angewandte Chemie-International Edition* **2018,** *57* (35), 11289-11293.
126. Williams, W.D., Shekhar, M., Lee, W.-S., Kispersky, V., Delgass, W.N., Ribeiro, F.H., Kim, S.M., Stach, E.A., Miller, J.T., and Allard, L.F., Metallic Corner Atoms in Gold Clusters Supported on Rutile Are the Dominant Active Site during Water−Gas Shift Catalysis. *Journal of the American Chemical Society* **2010,** *132* (40), 14018-14020.
127. Delannoy, L., Chantry, R.L., Casale, S., Li, Z.Y., Borensztein, Y., and Louis, C., HRTEM and STEM-HAADF characterization of Au-TiO2 and Au-Al2O3 catalysts for a better understanding of the parameters influencing their properties in CO oxidation. *Physical Chemistry Chemical Physics* **2013,** *15* (10), 3473-3479.
128. Kuwauchi, Y., Yoshida, H., Akita, T., Haruta, M., and Takeda, S., Intrinsic Catalytic Structure of Gold Nanoparticles Supported on TiO2. *Angewandte Chemie-International Edition* **2012,** *51* (31), 7729-7733.
129. Uchiyama, T., Yoshida, H., Kuwauchi, Y., Ichikawa, S., Shimada, S., Haruta, M., and Takeda, S., Systematic Morphology Changes of Gold Nanoparticles Supported on CeO2 during CO Oxidation. *Angewandte Chemie International Edition* **2011,** *50* (43), 10157-10160.
130. Kuwauchi, Y., Takeda, S., Yoshida, H., Sun, K., Haruta, M., and Kohno, H., Stepwise Displacement of Catalytically Active Gold Nanoparticles on Cerium Oxide. *Nano Letters* **2013,** *13* (7), 3073-3077.
131. Lu, J.Q., Bravo-Suárez, J.J., Takahashi, A., Haruta, M., and Oyama, S.T., In situ UV-vis studies of the effect of particle size on the epoxidation of ethylene and propylene on

supported silver catalysts with molecular oxygen. *Journal of Catalysis* **2005,** *232* (1), 85-95.

132. Jana, J., Ganguly, M., and Pal, T., Enlightening surface plasmon resonance effect of metal nanoparticles for practical spectroscopic application. *RSC Advances* **2016,** *6* (89), 86174-86211.

133. Guler, U. and Turan, R., Effect of particle properties and light polarization on the plasmonic resonances in metallic nanoparticles. *Optics Express* **2010,** *18* (16), 17322-17338.

134. Joy, N.A., Rogers, P.H., Nandasiri, M.I., Thevuthasan, S., and Carpenter, M.A., Plasmonic-Based Sensing Using an Array of Au–Metal Oxide Thin Films. *Analytical Chemistry* **2012,** *84* (23), 10437-10444.

135. Fujitani, T. and Nakamura, I., Mechanism and Active Sites of the Oxidation of CO over Au/TiO2. *Angewandte Chemie International Edition* **2011,** *50* (43), 10144-10147.

136. Wang, Y., Widmann, D., Heenemann, M., Diemant, T., Biskupek, J., Schlogl, R., and Behm, R.J., The role of electronic metal-support interactions and its temperature dependence: CO adsorption and CO oxidation on Au/TiO2 catalysts in the presence of TiO2 bulk defects. *Journal of Catalysis* **2017,** *354*, 46-60.

137. Chang, B.K., Jang, B.W., Dai, S., and Overbury, S.H., Transient studies of the mechanisms of CO oxidation over Au/TiO2 using time-resolved FTIR spectroscopy and product analysis. *Journal of Catalysis* **2005,** *236* (2), 392-400.

138. Laursen, S. and Linic, S., Geometric and electronic characteristics of active sites on TiO2-supported Au nano-catalysts: insights from first principles. *Physical Chemistry Chemical Physics* **2009,** *11* (46), 11006-11012.

139. Sardar, R., Funston, A.M., Mulvaney, P., and Murray, R.W., Gold Nanoparticles: Past, Present, and Future. *Langmuir* **2009,** *25* (24), 13840-13851.

140. Liow, C., Meng, F., Chen, X., and Li, S., Dependence of Plasmonic Properties on Electron Densities for Various Coupled Au Nanostructures. *The Journal of Physical Chemistry C* **2014,** *118* (47), 27531-27538.

141. Juluri, B.K., Zheng, Y.B., Ahmed, D., Jensen, L., and Huang, T.J., Effects of Geometry and Composition on Charge-Induced Plasmonic Shifts in Gold Nanoparticles. *The Journal of Physical Chemistry C* **2008,** *112* (19), 7309-7317.

142. Jentoft, F.C., Ultraviolet–Visible–Near Infrared Spectroscopy in Catalysis: Theory, Experiment, Analysis, and Application Under Reaction Conditions. *Advances in Catalysis* **2009,** *52,* 129-211.

143. Bravo-Suárez, J.J. and Srinivasan, P.D., Design characteristics of in situ and operando ultraviolet-visible and vibrational spectroscopic reaction cells for heterogeneous catalysis. *Catalysis Reviews: Science and Engineering* **2017**, pp1-151, https://doi.org/10.1080/01614940.2017.1360071.

Chapter 4. Application of Modulation Excitation-Phase Sensitive Detection-DRIFTS for in Situ/Operando Characterization of Heterogeneous Catalysts

4.1. Introduction

A great number of environmentally and industrially relevant reactions are heterogeneously catalyzed and occur in the gas phase [1]. To develop new or improve current catalysts for these reactions, a better understanding of catalyst requirements and catalytic cycle are required. This can be accomplished by a combination of in situ and operando spectroscopic characterization along with kinetic and computational studies [1]. Some of the most commonly available in situ spectroscopic techniques in catalysis laboratories are UV-Visible (UV-Vis), Fourier transform infrared (FTIR), and Raman spectroscopies [2-4]. However, in situ FTIR is perhaps the most ubiquitous because of its moderate cost, relatively simple use, and ability to probe powder catalyst's surface for adsorbed species and active sites at reaction conditions [5]. Such ability is crucial for identification of reaction intermediates to support reaction mechanisms; however, this is challenging in FTIR because the spectra arise from contributions of catalyst background, spectator species, noise, and reactive intermediate species which are usually present in small amounts and are difficult to disentangle [6]. Therefore, advances in in situ and operando characterization techniques and sensitive spectroscopic methods are of great importance for the study of not only active sites but also the intermediate species that take part in the catalytic reaction cycle [7, 8]. However, at steady state conditions, identification of these short-lived active species and discrimination from the strong fingerprints of spectator species and catalyst support, which are not involved in the reaction, but usually present in high concentration, is quite complex making difficult to derive any information on mechanism and kinetics [9, 10].

Some of the current strategies to obtain selective information on surface intermediate species include transient techniques such as TAP (temporal analysis of products) [11, 12], SSITKA (steady state isotopic transient kinetic analysis) [13, 14], pure transient methods [15-17], and MES (modulation excitation spectroscopy) [6, 10, 18]. The main characteristic of these techniques is the introduction of a rapid perturbation (e.g., in temperature, pressure, concentration) in the system via pulses (TAP), step (SSITKA, pure transient methods), or periodic changes (MES). In TAP

studies, stimulations are introduced into the system by perturbing one or two parameters such as pressure, temperature, concentration and flow rate with a sub millisecond time resolution to influence the species of interest and to analyze reaction intermediates [12], In SSITKA [19-21], the catalyst operates at steady state chemical potential conditions, but at isotopic transients as introduced by a step change in concentration of one of the components isotope. Kinetic analysis of the resulting data thus provides information of reactive species pools. These techniques in combination with spectroscopic methods such as UV-Vis, FTIR, Raman, and X-ray absorption spectroscopies can be a powerful tool for investigating the dynamically changing surface species and true reaction intermediates [3, 22], The likelihood that these spectroscopically detected surface species are involved in a catalytic cycle is usually studied by tracking changes of spectral signals to determine reaction rates, rate constants, or activation energies and match with expectations from online or bench scale reactor activity studies [13, 15, 17, 23]. A more recent approach to detect surface reacting species has been the combination of in situ/operando spectroscopies and (e.g., concentration, temperature, pressure, etc) modulation excitation (ME) coupled with phase sensitive detection (PSD) analysis to enhance the spectra signal-to-noise ratio of reacting species while avoiding the presence of spectator species [6, 10, 18, 24],

In the application of ME-PSD methodology, a periodic concentration perturbation around a middle value is typically introduced in the reaction system. At this condition, the system operates in a quasi-steady state while allowing the monitoring of surface species from the transient changes [10, 18]. While ME was initially employed as a frequency response technique for the determination of adsorption/desorption rates on heterogeneous catalysts [25, 26] and later combined with in situ DRIFTS spectroscopy for characterization of heterogeneous catalysts [27-34], it was not until the early 2000's that Baurecht and Fringeli [6] reported a numerical method to apply ME-PSD to in situ infrared spectroscopy. Since then, a similar ME-PSD methodology has been combined and extended to ATR [35], PM-IRRAS [24], DRIFTS [36-39], Raman [40], and X-ray absorption spectroscopies [41] and X-ray diffraction [40, 42]. The original PSD methodology directly transforms in situ ME-IR spectra perturbed sinusoidally from the time-domain into the phase domain with only signals that responded to the modulation frequency [6]. Urakawa, Bürgi, and Baiker later extended the methodology to squared waveform perturbations [24].

While ME-PSD, as implemented via Baurecht and Fringeli's methodology [6], has proved to be a major advance in the development of sensitive techniques for detection of surface reacting

species in heterogeneous catalysis [10, 18], it is not yet widely available and has been only confined to a handful of research groups worldwide. One of the reasons for this is perhaps the apparent complexity of the numerical method and the cumbersome software code implementation to analyze large data sets [18]. Inspired by Baurecht and Fringeli [6], we will report here a relatively simpler development of PSD also based on Fourier analysis following a procedure that is more familiar and widely available in engineering and which is not limited to a specific modulation waveform. This ME-PSD methodology is schematically shown in Figure 4.1. for in situ DRIFTS spectroscopy. Briefly, this PSD method uses Fourier transform (FT) to convert data from the time domain to the frequency domain, filters frequency or frequencies of interest (e.g., avoiding those of spectators), and recovers the filtered data via inverse Fourier transform (IFT) (into the so-called phase domain). This approach is well-known in the analysis of weak signals in the presence of a large noise as applied to mechanics (e.g., vibration analysis, nuclear power plant modeling), sonic and acoustics (e.g., passive sonar, music synthesis), biomedical engineering (e.g., cardiac patients diagnosis, ECG data compression), signal processing (e.g., real-time spectra analysis, speech synthesis and recognition), and instrumentation (e.g., microscopy, spectroscopy), among others [43-46]. For practical problems requiring FT, the most common method of solution involves the discrete Fourier transform (DFT) algorithm using complex numbers. The most popular algorithm is the fast Fourier transform (FFT), which is widely available for most modern programming languages and benchmarked [47].

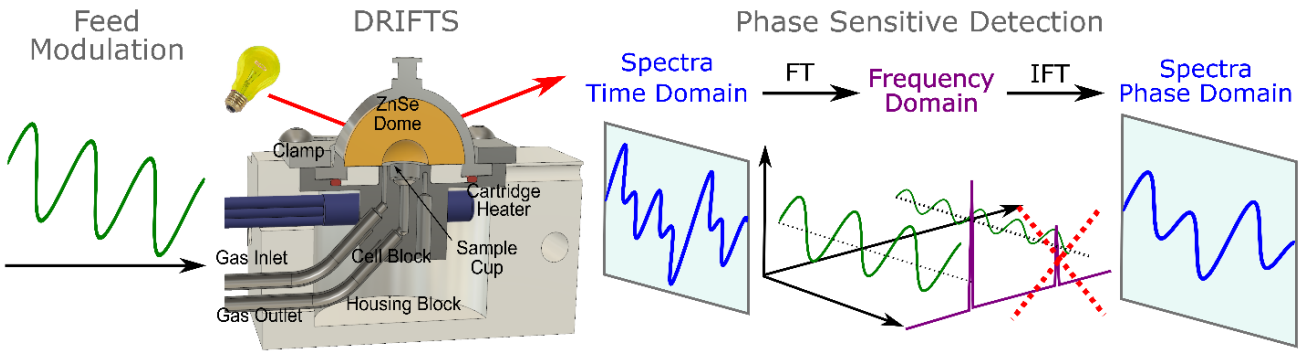

Figure 4.1. General schematic representation of modulation excitation-phase sensitive detection-diffuse reflectance infrared Fourier transform spectroscopy (ME-PSD-DRIFTS) methodology.

In this work, the application of in situ/operando ME-PSD-DRIFTS via DFT/IDFT for characterization of heterogeneous catalysts is discussed. The principle and mathematical framework used in ME-PSD is also described. Moreover, general guidelines for planning, running, and interpreting results from ME-PSD-DRIFTS are provided including aspects such as modulation frequency and amplitude, modulation waveform, sampling rate, and in situ cell residence time. Further, ethanol dehydration on γ-Al_2O_3 is used as an example of the application of Fourier transform/inverse Fourier transform for PSD analysis of DRIFTS spectra submitted to feed concentration modulation methodology. Finally, an outlook on future opportunities to further develop the ME-PSD-DRIFTS methodology is presented. We hope this work will contribute to the catalysis community to better understand the application of Fourier analysis for implementation of in situ/operando ME-PSD techniques for understanding of reaction intermediates and active sites in heterogeneous catalysis.

4.2. Experimental

4.2.1. Reaction setup

As shown in Figure 4.1., the experimental setup is in principle relatively simple and similar to most heterogeneous catalysts in situ spectroscopic characterization systems. It is made of a feed system that allows control of the flow rates such that a periodic concentration signal can be sent to the in situ reaction cell where surface species are monitored online. Unlike typical in situ or operando setups, there are some special requirements for feed modulation, in situ reaction cell, and spectra sampling, which will be discussed in the following sections. Regarding the feed modulation, one of the simplest systems to introduce a periodic signal is that composed of a four-way valve where two feeds are switched periodically as shown in **Figure 4.2**. . In the case of the in situ cell (and transfer lines), it is preferable that the void volume is minimized, mainly to allow rapid exchange of gases in the cell and to facilitate data analysis as gas concentration within the cell will tend to follow that of the input concentration. Also, the infrared spectrometer should be capable of collecting spectra rapidly (e.g., rapid scan). Additionally, an online mass spectrometer is usually available to facilitate the rapid monitoring of gas phase products for operando studies.

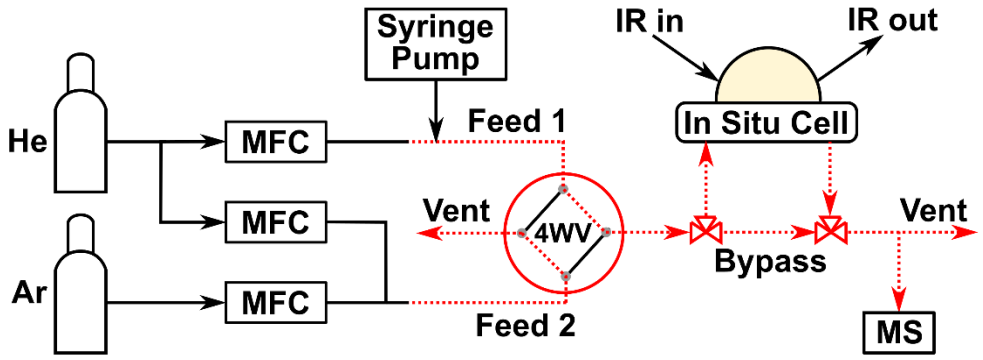

Figure 4.2. Schematics of the in situ experimental setup for ME-DRIFTS. MFC = mass flow controller; MS = mass spectrometer; IR = infrared beam; 4WV = 4-port two-position (dotted and solid lines) switching valve. Dotted lines and red color indicate that transfer lines are heated to avoid possible condensation of liquid injected via the syringe pump.

For the in situ DRIFTS application described in this work (e.g., ethanol dehydration on a commercial γ-Al_2O_3 (SBa-200)) a detailed description of the reaction setup is available elsewhere including the details on the design and operation of a new low-void volume in situ diffuse reflectance cell [48]. Briefly, mass flow controllers (Omega) were used to deliver and control gases flow rates to feed lines. Gas feed lines were periodically switched with a six-way switching valve (VICI) instead of a 4WV to (optionally) allow in situ cell's gas residence time distribution studies [49]. The new in situ cell resembles Harrick Scientific's HVC high reaction chamber (except it has a void volume of ~1.2 cm^3) so that it can fit Harrick's mirror optics (Praying Mantis™). The cell possesses a monolithic ZnSe dome window (which is a special Harrick's fabrication part) that has a bottom small semi-sphere (1 cm ID) providing minimum void volume (~0.5 cm^3) above the sample cup. Sample temperature in the cell was monitored by a thermocouple that is in direct contact with the sample. Infrared data was acquired with an FTIR spectrometer (Vector 70, Bruker) equipped with a mercury-cadmium-telluride detector (MCT D316/BP) and with rapid scan capabilities. The outlet gases were analyzed via an online mass spectrometer (Pfeiffer, OmniStar GSD 320 O, MS).

4.2.2. Modulation experiment

As an example of the application of the modulation excitation-phase sensitive detection-diffuse reflectance infrared Fourier transform spectroscopy (ME-PSD-DRIFTS) methodology, ethanol

conversion in the vapor phase on a commercial γ-Al_2O_3 will be described. In a typical experiment, about 45 mg of a calcined (static air, 623 K, 5 K/min, 2 h) γ-Al_2O_3 (SBa-200, Sasol, BET area = 189 m^2/g) catalyst (38-75 μm) were loaded to the cell. The catalyst was then heated in He (45 NTP cm^3/min, Feed 2) to 473 K. For the modulation experiment, Feed 1 (consisted of ~1 kPa ethanol, which was introduced via a syringe pump (60 μL/h of liquid ethanol at ambient temperature) and carried by 40 NTP cm^3/min of He for a total flow rate of ~40.4 NTP cm^3/min. Feed 2 was composed of a mixture of Ar/He = (10.4 NTP cm^3/min)/(30 NTP cm^3/min), where Ar was used as internal standard for mass spectrometry. Feed concentration modulation was started by switching periodically between Feed 2 and Feed 1 flows every 45 s (via a LabVIEW 2018 VI program routine) to yield a period of 90 s (f = 1/90 = 0.011 Hz). This frequency falls within the range of typical reaction TOFs for the reaction at this condition. A total of 15 periods were repeated. IR spectra were also collected simultaneously via rapid scan, about every 1 s (16 scans, 4 cm^{-1}) to match the average gas residence in the reaction cell (~ 1 s) [48]. More details on the catalyst, reactivity, and in situ DRIFTS characterization have been recently reported [48, 50].

4.3. Modulation excitation-phase sensitive detection (ME-PSD) methodology

In a typical infrared spectrum many peaks are usually present that arise from contributions due to background, baseline shift, noise, and surface (e.g., spectator, intermediate) species that are often difficult to discriminate. Detecting intermediate species thus becomes an even more complex task as the intensity of these species tends to be small. This problem resembles the analysis of small signals in the presence of a large noise, which has been studied via a phase sensitive detection (PSD) method using a lock-in amplifier which makes use of Fourier transform (FT) [51, 52]. Thus, application of FT to periodic changes of in situ infrared spectra of heterogeneous catalysts is expected to enhance the signal of intermediate species.

In the application of ME-PSD to in situ DRIFTS, the main interest is to extract with high sensitivity spectral information on surface reacting species. More specifically, one would like to detect species that could be involved in elementary steps. Here, the ME-PSD methodology employs a two-step approach. First, it introduces an external periodic perturbation to the catalyst surface (modulation excitation), which could be modulation of feed concentration, temperature, pressure, among others [53, 54] and second, it proceeds to perform data analysis on the spectra of

the perturbated catalyst surface to track only species that respond to the periodic perturbation (phase sensitive detection) [6]. This periodic change on the catalyst surface is what enables the application of Fourier transform analysis on the modulated spectroscopic data. In general, the ME in DRIFTS is most often performed via feed concentration modulation [18], which can be done without sophisticated controls by simply switching between two flows of different gas phase concentrations or by computer programmed (e.g., LabVIEW) periodic changes of feed gases concentration via control of flow rates with mass flow controllers. Once in situ DRIFTS data is collected over the ME experiment, the data is processed via PSD to extract information on species that respond to the frequency of feed modulation. The PSD method requires application of FT to time domain data of a periodic function resulting in a new set of data in the frequency domain. Once in the frequency domain, a filter is applied to restrict signals, usually, to the frequency of modulation, and then an inverse FT is applied to obtain the reconstructed spectroscopic data (in what is called the phase domain) with only the species that respond to the feed modulation frequency.

4.3.1. Fourier analysis

In FT analysis, a periodic function $f(t)$ that varies with time and with some period T can be expressed, with little restrictions, as a Fourier series expansion in terms of an infinite sum of sines and cosines [6, 45, 55]:

$$f(t) = \frac{1}{2}a_0 + \sum_{k=1}^{\infty}[a_k \cos(k\omega_0 t) + b_k \sin(k\omega_0 t)] \quad (5)$$

Where the angular frequency is: $\omega_0 = \frac{2\pi}{T} = 2\pi f_0$, f_0 is the fundamental frequency, k is a positive integer (k=1 for the fundamental frequency and $k > 1$ for higher frequency harmonics), a_0, a_k, and b_k are known as Fourier coefficients. In Equation 5, the first term $\frac{1}{2}a_0$ represents the average value of $f(t)$ over the period *T*. It is also interpreted as the DC term (i.e., static component of the signal) arising from contributions of species that do not respond to modulation and represented by a frequency equal to 0. The a_k, and b_k are the amplitudes of the cosine (real part) and sine (imaginary part) components with frequency $k\omega_0$ needed to form the signal $f(t)$, respectively. Additionally, the set of a- and b-coefficients are called the real, Re[$f(t)$], and imaginary, Im[$f(t)$], parts, respectively, whereas the set of all a- and b-coefficients is called the Fourier

transform of $f(t)$, denoted here as $\mathcal{F}(f)$. In analogy with a polynomial equation: $p(t) = a_0 + \sum_{n=1} a_n\, t^n$ that is fitted to *N* points in the *x*-*t* Cartesian coordinates, the set of a-coefficients could be now called the "polynomial transform of x". Thus, the Fourier transform could be simply viewed as a curve fitting of a signal by a series of cosines (real part in the complex FT) and sines (imaginary part in the complex FT) and whose a_k and b_k coefficients are given by [6, 55, 56]:

$$a_0 = \frac{2}{T}\int_{-T/2}^{T/2} f(t)\, dt \tag{6}$$

$$a_k = \frac{2}{T}\int_{-T/2}^{T/2} f(t)\cos(k\omega_0 t)dt; \quad k \geq 1 \tag{7}$$

$$b_k = \frac{2}{T}\int_{-T/2}^{T/2} f(t)\sin(k\omega_0 t)dt; \quad k \geq 1 \tag{8}$$

There are other convenient ways of writing the Fourier series, for example, in polar coordinates, by writing $a_k = r_k\cos(\phi_k)$ and $b_k = r_k\sin(\phi_k)$ so that Equation 5 becomes:

$$f(t) = \frac{1}{2}a_0 + \sum_{k=1}^{\infty} r_k \sin(k\omega_0 t + \phi_k) \tag{9}$$

Where r_k and ϕ_k are the amplitude and phase angle of the k^{th} harmonic, respectively. Here, a single sinusoid replaces each sine and cosine, and the amplitude and phase replace the previous a_k, and b_k as the quantities that define the harmonics [57]. The amplitude, r_k, is proportional to the square root of the amplitude of the oscillation, whereas $|r_k|^2$ is a measure of the power contained in each harmonic. The phase angle, ϕ_k, can be useful to compare two waves. They are said to be "in-phase" when both waves' crest are in sync or "out-of-phase" if they have a phase difference of 180° [57]. These quantities will become more apparent in ME-PSD-DRIFTS when studying the kinetic response of various surface species responding to a modulation frequency. The amplitudes a_k and phase angles (or phase shift or phase lag or argument) ϕ_k are given by Equations 10 and 11, respectively [6, 56]:

$$r_k = \sqrt{(a_k^2 + b_k^2)} \tag{10}$$

$$\phi_k = \tan^{-1}\left(\frac{b_k}{a_k}\right) = \tan^{-1}\left(\frac{\text{Imaginary part}}{\text{Real part}}\right) \tag{11}$$

Despite the trigonometric and polar representation of the Fourier series, the complex exponentials is perhaps the most common way of representing the series expansion because it is easier to manipulate algebraically. By using Euler's equation: $e^{\mathrm{i}k\omega_0 t} = \cos k\omega_0 t + \mathrm{i}\sin k\omega_0 t$ and the definitions: $c_k = {}^1/_2\, a_k + {}^1/_{2\mathrm{i}}\, b_k$, Equation 5 can then be expressed as [55]:

$$f(t) = \sum_{k=-\infty}^{\infty} c_k e^{\mathrm{i}k\omega_0 t} \tag{12}$$

Where the c_k coefficients are given by:

$$c_k = \frac{2}{T}\int_{-T/2}^{T/2} f(t)\, e^{-\mathrm{i}k\omega_0 t} dt \tag{13}$$

4.3.2. Fourier and discrete Fourier transforms

The Fourier series (e.g., Equation 12) can be used to analyze periodic functions with a period of T and a fundamental frequency of $f_0 = {}^1/_T = \frac{\omega_0}{2\pi}$. A more general Fourier series, which can be also employed for analysis of non-periodic functions, is obtained from Equations 12 and 13 by letting the period to tend to infinity and the fundamental frequency to zero [45, 55]:

$$f(t) = \int_{-\infty}^{\infty}\left[\frac{1}{2\pi}\int_{-\infty}^{\infty} f(t')\, e^{-\mathrm{i}\omega t'} dt'\right] e^{\mathrm{i}\omega t} d\omega \tag{14}$$

$$f(t) = \int_{-\infty}^{\infty} F(\omega)\, e^{\mathrm{i}\omega t} d\omega \tag{15}$$

$$F(\omega) = \frac{1}{2\pi}\int_{-\infty}^{\infty} f(t)\, e^{-\mathrm{i}\omega t} dt \tag{16}$$

The coefficient function $F(\omega)$ is known as the Fourier transform (FT) of $f(t)$. Thus, Equation 16 is employed to transform the function $f(t)$ in the time domain to the same function $F(\omega)$ in the frequency domain, it is also called the analysis equation. On the other hand, Equation 15 is used to recover $f(t)$ from $F(\omega)$ and it is known as inverse Fourier transform (IFT) or the synthesis equation [55]. Together, the analysis (Equation 16) and synthesis (Equation 15) equations form what is known as the Fourier transform pair [45, 55, 56].

When dealing with in situ infrared spectra, data is collected as a finite series of discrete points whose explicit FT is unknown. In this case, FT is computed numerically for which Equation

16 integral term is approximated by finite sums. A FT calculated in this manner is called a discrete Fourier transform. For a finite-duration discrete-time signal f_m with a total of N samples, the discrete FT (DFT) and IFT (DFT-IDFT) pair equations are given by [46, 56].

$$F_n = \frac{1}{N}\sum_{m=0}^{N-1} f_m e^{-\mathrm{i}\frac{2\pi}{N}mn} \tag{17}$$

$$f_m = \sum_{k=0}^{N-1} F_n e^{\mathrm{i}\frac{2\pi}{N}mn} \tag{18}$$

Where,

F_n= n^{th} DFT output component (i.e., $F_0, F_1, F_2, \ldots, F_{N-1}$)

n = DFT output index in the frequency domain ($n = 0, 1, 2, \ldots, N-1$)

f_m= sequence of input samples (i.e., $f_0, f_1, f_2, \ldots, f_{N-1}$)

m = time-domain index of input samples ($m = 0, 1, 2, \ldots, N-1$)

$\mathrm{i} = \sqrt{-1}$, and

N = number of samples in the input sequence and number of frequency points in the DFT output

In Equation 16, the Fourier component $\mathrm{Re}(F_0) = \sum f_m$ captures the static (DC) component of the signal ($\mathrm{Im}(F_0)$ is assumed to be zero), whereas the coefficients F_n are the DFT or frequency domain representation of the discrete time signal [56]. The DFT equation described above converts in a straight manner a time-domain sequence into the corresponding frequency domain, but it is inefficient. However, an algorithm called the fast Fourier transform (FFT) developed in the 1960's significantly reduced the computational time to solve the DFT equation and is now widely available and has been implemented in many popular programming languages [44, 58].

4.3.3. DFT method

In the application of ME-PSD-DRIFTS, we used the exponential representation of the DFT as it is the standard adopted for FFT libraries. It is worth mentioning that the definitions of DFT and IDFT may differ in various references and libraries (e.g., various possibilities of assigning summation factors and exponential negative sign). These conventions should be carefully examined when applying various FFT libraries. Without loss of generality, the discussion hereinafter adopts Equation 17 as the DFT definition. The most commonly available programming

languages already have available libraries or packages with handy functions for application of the phase sensitive detection methodology, that is for FT, selection of frequency or frequencies range, and IFT via the FFT algorithm, namely, FFT, IFFT, FFT shift, and IFFT shift. The last two functions sort the frequencies from minimum to maximum values. This facilitates the application of a filter to select a frequency range for IDFT in the analysis of MES data. In general, programming languages with FFT and matrix support will reduce the code length for the necessary manipulations. The use of an appropriate software language is quite convenient as it will reduce programming time to solve the DFT and IDFT equations by simply applying existing functions (e.g., FFT, IFFT) rather than by writing cumbersome homemade code to solve equations numerically as implied with previously reported approaches [6, 10, 18]. In this work, we applied the numpy, matplotlib, and wxPython libraries for Python for a homemade program that aids the analysis of DRIFTS data obtained from concentration modulated experiments.

4.4.MES-PSD-DRS key considerations

Figure 4.3. General considerations in a modulation excitation spectroscopy experiment shows a general set of decisions, not necessarily in the order presented, that need to be made before running a ME experiment including:

a) What modulation frequency and amplitude should be applied?
b) What modulation waveform should be used?
c) What variable should be modulated?
d) What is the minimum spectra sampling rate?
e) Does the cell void volume matter? If so, what is the minimum residence time that should be used?

To answer these questions, there does not appear to be a given set of rules to follow. Here, we will summarize some basic guidelines based on prior advances in this area for similar type of ME-ATR and ME-DRIFTS experiments [10, 18] and their similarity with well-known periodic [54, 59] and relaxation kinetic methods [60, 61] for the study of chemical reactions. As in the study of periodic or frequency response methods, modulation excitation can be performed via pressure, temperature, and concentration perturbations [60]; however, our focus here, for simplicity, is on concentration modulation strategies [59, 62, 63]. This, however, does not preclude the use of pressure,

temperature, or other previously used approaches as the data collection and analysis will still be similar to those described here [54, 59, 60, 63].

At first look, it is difficult to realize that all questions and steps in **Figure 4.3**. are interrelated [60]. For example, it will be shown in the following sections that ultimately the experimental variables need to be chosen such that quality and amount of the collected data is sufficient to draw qualitative (e.g., presence of possible intermediate species and their interrelationship) and quantitative (e.g., elementary reaction rate constants) information from the studied system as limited by the sensitivity and noise level of the available analytical equipment [60, 64]. For frequency response experiments, for example, the following observations have been reported that need to be taken into account for a measurable (chemical relaxation) effect:

a) *Frequency.* If the oscillation frequency is much larger than the reciprocal of the relaxation time, the amplitude of the response is zero and the system remains at steady state [60].
b) *Frequency.* Experimental frequencies should be selected such that their inverse values are within the range of the characteristic relaxation times (for fast and slow processes) of the system under study [54, 59, 60, 65].
c) *Amplitude.* The amplitude of the input perturbation is usually kept small to simplify quantitative kinetic data analysis (often <5–20%, but dependent on system) [54, 60, 63]. However, under specific circumstances (e.g., reactions can be expressed as first order or pseudo first order processes) it is possible to employ larger perturbations which result in higher precision of the measurements because of the larger observed concentration changes [60].
d) *Sampling*. Data needs to be acquired rapidly to collect a sufficient number of points per period (>50) [54].
e) *Sampling.* Amplitude changes and phase lags need to be collected over several (>5-10) steady-state cycles [6, 10, 54].
f) *Analytical equipment.* Analysis methods must detect accurately phase lags (<0.1%) and amplitude attenuations (~1% of total amplitude change), specially at low and high frequencies when phase lags are small [54].
g) *Reactor*. System volume should minimize hydrodynamic delays and allow modulation frequencies >0.01 Hz [54].
h) *Reactor*. In mixed reactors, cycling periods are usually around 60 s (~0.017 Hz) [59].

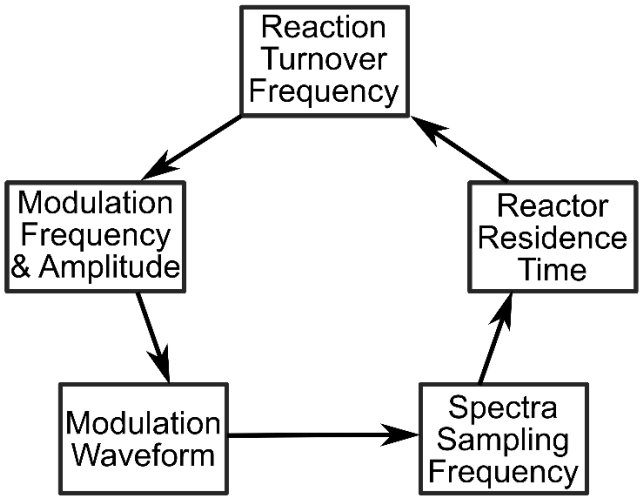

Figure 4.3. General considerations in a modulation excitation spectroscopy experiment

4.4.1. TOF vs modulation frequency and amplitude

One of the decisions to plan a ME-PSD-DRIFTS experiment requires the selection of the type of modulation and its frequency and amplitude. Although a modulation in a reactive system could be imposed by perturbations to reaction temperature, pressure, feed composition and others [54, 60, 62, 64], our work and that of others on ME-PSD spectroscopic techniques over the past 16 years have focused on feed composition modulation because of the flexibility and better control on the perturbation [6, 10, 18, 65]. The answer to what magnitude of the frequency and amplitude of the modulation to be used, however, it is not a trivial one. Chemical intuition would suggest, for example, that modulation frequency should be at least of the same order of magnitude of the reaction turnover frequency and this is indeed in agreement with requirements in relaxation methods, in part because too low or too high frequencies may result in responses that are too weak or that produce minimum phase lags which preclude kinetic analysis of the data [54, 59, 60, 65]. It is worth noting that even if significant differences exist between the reaction TOF and the modulation frequency, it may still be possible to obtain qualitative information on the detected species. While TOFs are known to vary over a wide range, for example, 10^{-6} to 10^{0} s^{-1} [66], it may be possible to modify the reaction conditions such as temperature and pressure to match TOFs with feasible modulation frequencies in the in situ reaction cell and with the available analytical equipment. For example, cycling frequencies in mixed reactors have been reported to be in the

order of 10^{-2} Hz [59], which would place limits on the possible modulation frequencies available for testing in in situ cells. Moreover, the decision of the modulation frequency is also dependent on the sensitivity and time resolution of the analytical equipment such that a good spectral response signal to noise ratio can be obtained. In turn, spectra quality depends on data sampling requirements. Also, it is possible that higher frequency harmonics maybe available in a single experiment depending on the modulation waveform used. This can further extend the range of frequencies available for evaluating surface species responses. For example, it is expected that by controlling the modulation to specific waveforms (e.g., square [24], triangular, sawtooth) higher frequency harmonics will result that could be used to discern short lived (fast reacting) species [9]. All these variables, modulation waveform, sampling frequency, and the effect of mixing (i.e., residence time) in a ME-PSD experiment will be discussed in the following sections.

Similar to the requirements for modulation frequency, the size of the perturbation change for the amplitude of the selected variable (e.g., a given reactant concentration in the feed) should be high enough that it results in measurable responses, but not too high as to oversaturate the catalyst surface or to introduce gas phase signals that could mask surface species (e.g., in ME-PSD-DRIFTS). Also, the response quality, in turn, will depend on the sensitivity and time resolution of the analytical equipment. Changes as high as 100% in the modulation amplitude with respect to an average (concentration) value have been reported for ME-PSD-DRIFTS or frequency response methods [27, 28, 31, 38, 48]. However, changes in the order of 5–20%, which will be dependent on the system under study, have been estimated to be required to linearize rate equations (via the assumption of *small perturbations*) which simplify kinetic models to determine chemical relaxation times (related to reaction rate constants) [54, 60]. Examples of development of kinetic models to frequency response (feed concentration modulation) experiments applied to heterogeneous catalysis have been reported by the groups of Renken [28], Wokaun [31-34], and Gonzalez [27].

4.4.2. Waveform vs frequency harmonics

The most common waveforms described in concentration ME-PSD experiments are the sine [6, 10, 31] and square [9, 24, 65] waveforms. The main reason for the use of the sine waveform is because of a simpler mathematic analysis of the FT equations allowing more manageable numerical methods implementation [6, 10, 24], however, at the expense of a more sophisticated

computer controlled feed delivery system for precise control of concentration in a sine periodic fashion. The opposite is true for a square waveform, a slightly more complicated mathematical solution of the FT equations, but which can be generated with a simpler feed control system by switching between two feeds of different concentrations. As described above, the use of a square waveform has the additional advantage of generating higher frequency harmonics which could be used for inquiring the response of faster reacting surface species [9]. While introducing a sine or square perturbation in the feed to an in situ cell does not warrant that the response of surface species will be of the same form, it should introduce a periodicity on the surface species and active sites enabling FT type analysis as that required in the PSD methodology. Therefore, regardless of the obtained periodic form on the surface and active site species, those species that respond to the modulation frequency will be more likely to be involved in reaction elementary steps.

In previous reported ME-PSD approaches, very little attention was given to the resulting frequency domain of the response, which is expected to contain additional information of the response waveform, spectra baseline shifts, noise, signal decay, among others. **Table 4.1.**, for example, presents some common nonperiodic and periodic waveforms and their corresponding time and frequency domain DFT-pairs. These pairs will help later in the interpretation of ME-PSD frequency domain data. For example, during feed ME-PSD only species that respond to the feed modulation are more likely to be intermediate species. On the other hand, species that do not respond, namely, spectator species, and spectra background will show up in a frequency domain magnitude plot, but with a frequency of zero (Entry 1). Therefore, contributions due to spectators and background will be excluded during application of the IDFT with a frequency or frequencies larger than the (fundamental) modulation frequency.

Entry 2 in **Table 4.1**. indicates that noise, except that which may be periodic and with frequency higher or lower than the modulation frequency, will contribute to some extent to the reconstructed IDFT spectra. Entry 3 could be interpreted, for example, as a linear shift in the spectra baseline, and which could be assessed from the broadening around the zero frequency. Entries 4 and 5 correspond to sine or cosine waveforms showing that the corresponding frequency domain magnitude plot results in a single frequency (e.g., the modulation frequency), whereas that for the square waveform in Entry 6 shows the presence not only of the fundamental frequency, but also higher frequency harmonics. This frequency domain magnitude plot clearly shows the advantage of using a square waveform as higher frequency harmonics will be present (equivalent

to single sine waveform experiments of 2*k*-1 modulation frequency) and which could be employed to evaluate faster reacting surface species [9, 24], but at the expense of a response in the phase domain of lower signal to noise ratio quality. In general, depending on the chemical response (e.g., relaxation time) of surface species, their resulting waveform could be slightly different from that of a sine or square and possibly looking more like a triangle or sawtooth like waveform. In that case, higher 2*k*-1 and *k* harmonics may be expected as shown from Entries 7 and 8, respectively.

In summary, regardless of the modulation waveform, the frequency domain magnitude plot of the spectral response can provide additional information to assess the quality of the collected data such as the presence of baseline shifts and deviations from the modulation waveform, but more importantly if the species selected (e.g., a given wavenumber) responds to the perturbation, in which case, the observed fundamental frequency (i.e., the most intense) should match the modulation frequency. Also, application of DFT and IDFT via commonly available FFT algorithms (implemented in widely available software packages) further facilitate the use of almost any type of periodic modulation form and its corresponding analysis, further increasing our ability to extract more information of surface species that respond to periodic perturbations and their possible relevance in elementary steps of catalytic cycles. For example, based on Entry 9, and in analogy with NMR spectroscopy, a decaying sine waveform will result in a broad fundamental frequency similar to that observed in free induction decay (FID) signal and its corresponding frequency domain. Thus, we anticipate that, at least in principle, from a decaying response waveform it is possible to determine the relative kinetic response (e.g., relaxation time) of different species from the broadening of the fundamental frequency in a frequency domain magnitude plot. This is particularly interesting as kinetic information of surface species could be obtained in a single experiment with a decaying waveform with a single frequency and not in multiple experiments with varying modulation frequencies as it has been usually performed [27, 31-34]. Another consequence of the presence of a decaying waveform (not introduced deliberately as a feed modulation) is that ME-PSD could in theory be also expanded to the study of deactivating catalysts. This is a broadly unexplored area where we expect ME-PSD techniques to make further contributions to the understanding of active sites and intermediate species in heterogeneous catalysis.

Table 4.1. Common nonperiodic signals and periodic waveforms, time domain, and their frequency domain magnitude [44, 67]

Nonperiodic signals and periodic waveforms	**Time domain signal**	**Frequency domain - magnitude**
1: Constant ($f \equiv 1$)	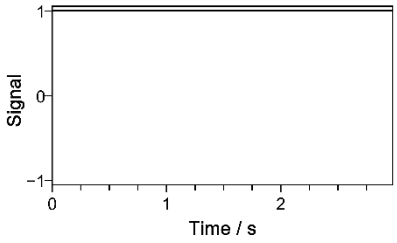	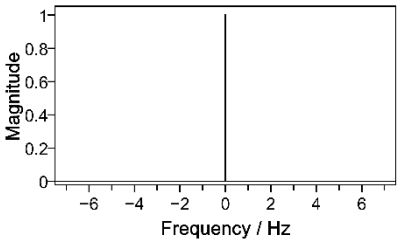
2: Noise (random)	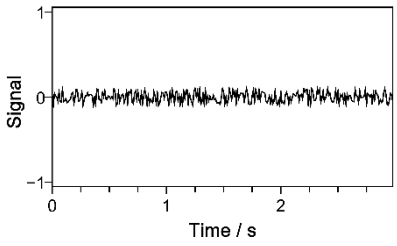	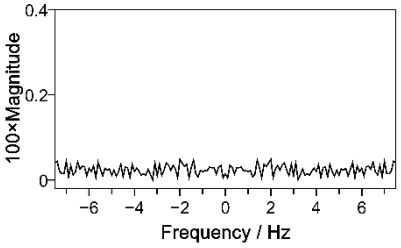
3: Linear	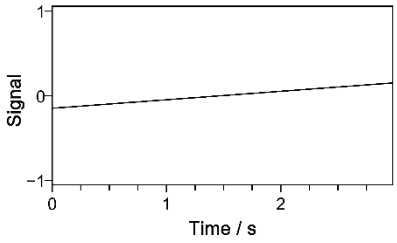	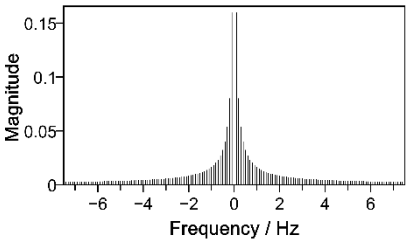
4: Sine (amplitude=1, period=1) $f(t) = \sin(\omega_0 t)$ $= \frac{1}{2\mathrm{i}}[\exp(\mathrm{i}\omega_0 t) - \exp(-\mathrm{i}\omega_0 t)]$	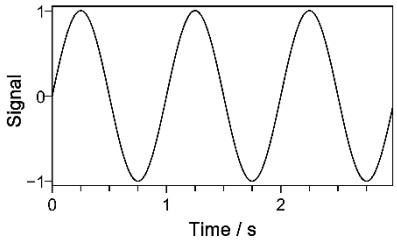	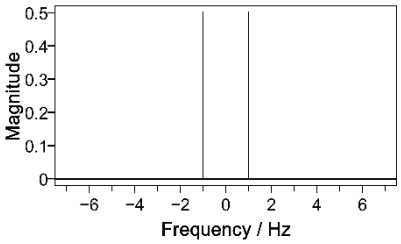

5: Cosine (amplitude=1, period=1)

$$f(t) = \cos(\omega_0 t)$$

$$= \frac{1}{2}[\exp(\mathrm{i}\omega_0 t) + \exp(-\mathrm{i}\omega_0 t)]$$

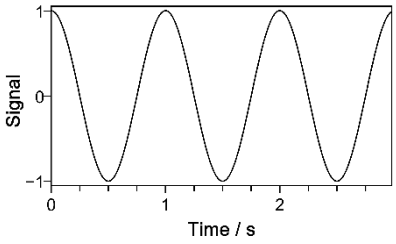

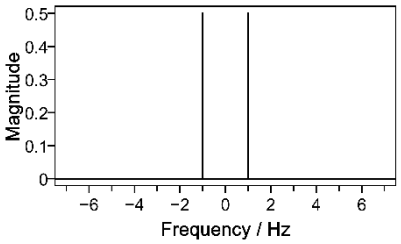

6: Square (amplitude=1, period=1)

$$f(t) = \frac{4}{\pi}\sum_{k=1}^{\infty}\frac{\sin[(2k-1)\omega_0 t]}{2k-1}$$

$$= \frac{2}{\pi\mathrm{i}}\sum_{k=-\infty}^{\infty}\frac{\exp[\mathrm{i}(2k-1)\omega_0 t]}{2k-1}$$

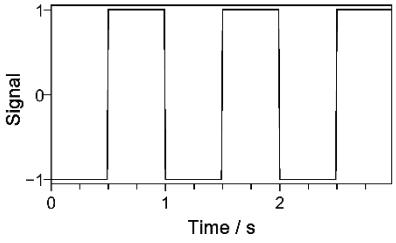

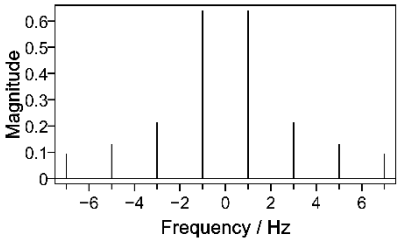

7: Triangular (amplitude=1, period=1)

$$f(t)$$

$$= \frac{8}{\pi^2}\sum_{k=1}^{\infty}\frac{(-1)^{k+1}\sin[(2k-1)\omega_0 t]}{(2k-1)^2}$$

$$= \frac{4}{\pi^2\mathrm{i}}\sum_{k=-\infty}^{\infty}\frac{(-1)^{k+1}\exp[\mathrm{i}(2k-1)\omega_0 t]}{(2k-1)^2}$$

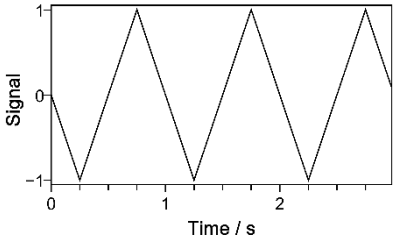

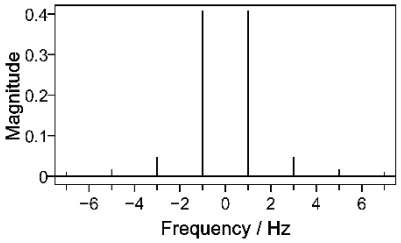

8: Sawtooth (amplitude=1, period=1)

$$f(t) = \frac{2}{\pi}\sum_{k=1}^{\infty}\frac{(-1)^{k+1}\sin(k\omega_0 t)}{k}$$

$$= \frac{1}{\pi\mathrm{i}}\sum_{k=-\infty,k\neq 0}^{\infty}\frac{(-1)^{k+1}\exp(\mathrm{i}k\omega_0 t)}{k}$$

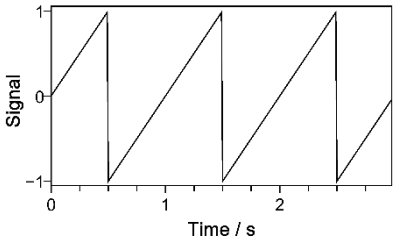

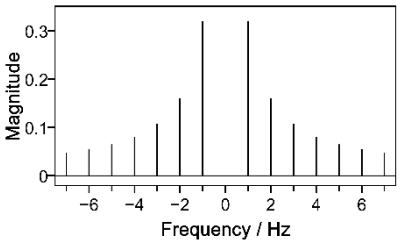

9: Decaying sine (initial amplitude=1, period=1, decay constant=0.5 s^{-1})

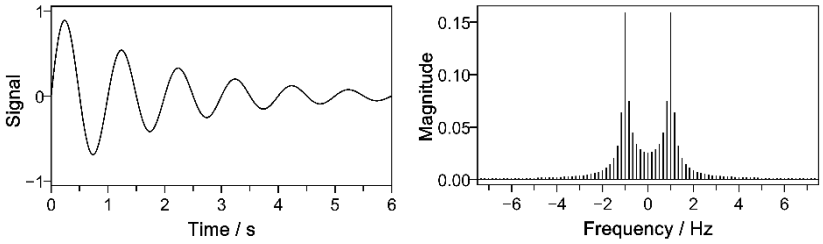

$$f(t) = e^{-k_d t}\sin(\omega_0 t)$$

$$= \frac{e^{-k_d t}}{2\mathrm{i}}[\exp(\mathrm{i}\omega_0 t) - \exp(-\mathrm{i}\omega_0 t)]$$

4.4.3. Minimum sampling rate

An additional question to ask in planning ME-PSD experiments is how fast should data be collected? While the obvious answer would be as fast as possible with the available analytical equipment, this is not satisfactory because of the nature of the sampling of a continuous signal. To answer this question, we refer to the theory of signal processing and more specifically to the Nyquist-Shannon sampling theorem that states that proper sampling of a continuous function requires a sampling frequency that is at least twice that of the highest frequency in the signal [67]. When such condition is met, the original signal form can be recreated from the sampled data via Fourier analysis, otherwise the reconstructed signal form will be different from the original where high frequencies appear as artifacts at low frequencies in the sampled signal (aliasing) [46]. In a ME-PSD-DRIFTS experiment, for example, when employing a sine waveform, one would reasonably expect the response to follow the fundamental modulation frequency (**Table 4.1**., Entry 4). Therefore, at the very least a sampling frequency of $2f_0$ would suffice. In the case of a square waveform, because of the presence of higher harmonic frequencies (**Table 4.1.**, Entry 6), the highest frequency of the response signal is unknown, but often it will likely not exceed $9f_0$. Therefore, in such a case, $18f_0$ could be used as a safe minimum sampling frequency.

4.4.4. Reaction cell residence time

Another aspect that requires careful consideration is the fluid dynamic characteristics of the in situ reaction cell employed in the ME-PSD-DRIFTS experiments. It is expected that diffuse reflectance (DR) reaction cells with minimum void volume (<1–2 cm^3), as encountered in bench scale fixed bed reactors or in transmission reaction cells [2], will be favorable for ME-PSD experiments as gas exchange within the cell should be rapid (i.e., low residence time) following concentration changes due to feed perturbation introduced in the reaction system. Such stringent low void volume requirements for in situ DR cells bring experimental complications as low void volume cells (<1–2 cm^3) are not currently commercially available [2] and those which have been reported in the literature are not easy reproducible [68-71]. Despite these limitations, ME-PSD-DRIFTS experiments have been reported in the literature with commercial cells (e.g., Spectra-Tech [32, 72], Specac [31, 34, 73], Pike [29, 38], Harrick [36, 37, 74-78]). Based on the design specifications of these cells [2], and our recent study of mean residence time distribution in a modified Harrick DR cell [49], it is very unlikely that any of these reaction cells is able to achieve rapid exchange of feed gases within a couple of seconds or less at reasonable gas flow rates (<100 $cm^3\ min^{-1}$, to avoid pressure drop through the cell). For this reason, we recently reported the design (including the blueprints) of a new low void-volume (~1.0 cm^3) DR reaction cell, that is relatively easy to reproduce in most catalysis laboratories with machining capabilities, and that exhibited an average gas residence time in the cell of ~1.3 s at a total gas flow rate of 45 cm^3/min [48]. If ME-PSD-DRIFTS experiments have been reported with large void volume reaction cells, then, a question to ask would be: is a low void volume cell required for these experiments? or in other words, what is the average residence time required for ME-PSD-DRIFTS?

An obvious answer to the above question would be the lowest residence time possible. However, as discussed in previous sections, there is not a simple answer because of the interrelationship between gas residence time and feed modulation frequency and amplitude to yield a good spectral response with the time resolution limitations of the available analytical equipment (e.g., rapid scan FTIR, mass spectrometer). For frequency response techniques, for example, previous authors have reported that void volume should be minimized to obtain frequencies above 0.01 Hz [54]. which appears to be the case for mixed reactors where cycling periods of around 60 s (~0.017 Hz) are achievable [59]. If we follow previous suggestions of at least 50 data points (i.e.,

spectra) per period or the minimum number of samples based on a square waveform (assuming conservatively that the highest frequency is ~10f_0 ≈ 0.017 Hz) [54], then at least a sampling frequency of 0.35 Hz (0.35 samples/s) would be needed or the equivalent of 1 spectra every 3 s. This sampling frequency (1–3 spectra/s) is readily achievable in most current FTIR spectrometers with rapid scan capabilities at a reasonable resolution. Therefore, a time of <1–3 s would probably be a good first guess of the average residence time in the reaction cell to match the time resolution of the spectrometer.

It can be argued that large void volume cells can yield similar results as those of low void volume ones. In analogy with the system behavior to different modulation frequencies, intuitively one would expect this to be true. For example, in low void volume cells the gas phase modulation frequency and concentration amplitude within the cell should match closely that expected from the input waveform because of the rapid gas exchange. In a larger void volume cell, the gas phase concentration frequency will still match that of the waveform, thus allowing ME-PSD analysis. However, the gas phase concentration amplitude should be attenuated because of the slower gas phase exchange within the cell [48]. Therefore, large void volume cells could be used for ME-PSD-DRIFTS experiments, but because of attenuation the system response could likely have a lower signal to noise ratio under the experimental reaction conditions. To match the performance of a low void volume cell, larger concentration amplitude changes would be needed, which carry the risk of introducing significant gas phase contributions in the resulting spectra. Overall, this suggests that large void volume cells will require more careful preliminary tests to ensure proper performance and the absence of gas phase contributions. In order to better explore the interrelation between cell void volume (i.e., residence time) and modulation frequency and amplitude, next section explores the in situ cell gas phase concentration and the recorded outlet concentration in a mass spectrometer as modelled by a two CSTR reactors in series. Such model roughly represents the reaction cell setup shown in **Figure 4.2**. as demonstrated in recent reports for a homemade low void-volume [48] and large void-volume commercial Harrick cell [49].

4.4.4.1.Feed modulation and in situ reaction cell frequency response model

In the study of residence time distribution for the in situ reaction cell shown in **Figure 4.2**, it has been shown that the cell and the MS analysis chamber can be approximated as continuously

stirred tank reactors in series [48, 49]. We are interested in investigating the output concentration behavior from the in situ cell as a function of the cell average residence time and modulation frequency for a given modulation waveform. This is a classical type of problem used in process control to study the response to a disturbance in a continuously stirred tank reactor (its solution is available in many textbooks), for example, to attenuate concentration changes in an upstream process stream before delivery to a downstream plant [79]. Below, a solution of the problem is presented based on Fourier series with a fundamental angular frequency $\omega_0 = 2\pi f_0$, bounded by [−1, 1], and for a square waveform (**Table 4.1**, Entry 6).

For a square waveform, the input signal is given by:

$$f(t) = \frac{4}{\pi}\sum_{k=1}^{\infty}\frac{\sin[(2k-1)\omega_0 t]}{2k-1} = \frac{2}{\pi \mathrm{i}}\sum_{k=-\infty}^{\infty}\frac{\exp[\mathrm{i}(2k-1)\omega_0 t]}{2k-1} \tag{19}$$

Thus, after solution of the two CSTR model the following Fourier series express the outputs from the CSTR1 (in situ cell) and CSTR2 (MS) after the modulation is steady.

$$f_1(t) = \frac{2}{\pi \mathrm{i}}\sum_{k=-\infty}^{\infty}\frac{\exp[\mathrm{i}(2k-1)\omega_0 t]}{(2k-1)[1+\mathrm{i}(2k-1)\omega_0\tau_1]} \tag{20}$$

$$f_2(t) = \frac{2}{\pi \mathrm{i}}\sum_{k=-\infty}^{\infty}\frac{\exp[\mathrm{i}(2k-1)\omega_0 t]}{(2k-1)[1+\mathrm{i}(2k-1)\omega_0\tau_1][1+\mathrm{i}(2k-1)\omega_0\tau_2]} \tag{21}$$

A detailed derivation, description of the equations, and the solution for other waveform types are provided in Appendix C. Equations 20 and 21 are then used to predict the output concentrations of the in situ cell (CSTR1) and MS (CSTR2) characterized by average residence times τ_1 and τ_2, respectively, which are forced to a square input modulation of frequency ω_f as given by Equation 19. Based on the in situ cell characteristics described above, a τ_1=1 s is used to characterized a low void-volume cell [48] and a τ_1=25 s is used to describe a relatively large void-volume cell at moderate gas flow rates (~45 cm^3/min) [49].

Figure 4.4 shows the residence time distribution in a typical low void-volume (τ_1 = 1 s) in situ cell subjected to a square waveform input signal of frequencies f_0 = 0.011, 0.033, and 0.10 Hz and an amplitude of 0.5. The conditions of **Figure 4.4**. are typical of ME-PSD-DRIFTS experiments [48]. The results show that the concentration within the cell (solid orange line) tracks closely with the input waveform (solid black line) at the f_0 between 0.011 and 0.033 Hz. Only

when f_0 = 0.10 Hz is used, the feed concentration in the cell (i.e., same as the CSTR1 output in absence of reaction) takes more of a triangular shape (with slightly reduced amplitude) despite the use of square waveform as the input. This result highlights the interrelation between modulation frequency and amplitude and mixing in the reaction cell. Clearly, for a cell with a residence time = 1 s (i.e., low void-volume), concentration attenuation (slight change in amplitude) only becomes significant after an almost tenfold increase in the modulation frequency in the 0.01–0.1 Hz range, but with a distortion in the response modulation waveform. It is worth noticing that these results only account for the effect of mixing within the cell; however, it is likely that the waveform shape may be more accentuated once adsorption and reaction (i.e., chemical relaxation time) are also taken into account. If the sought concentration amplitude changes within the cell with respect a central value are based on the changes from the input signal, then the results here illustrate that preliminary testing is not necessary for typical modulation frequencies (e.g., 0.01–0.1 Hz) in a low void-volume cell as the concentration changes tracked with those expected from the input modulation. Additionally, if mixing within the MS analysis chamber was minimum at the studied modulation frequency, then one would expect output concentrations CSTR1 (solid orange line) and CSTR2 (dashed black line) to be only slightly delayed as observed for **Figure 4.4A** and **4.4B**. These results highlight possible risks of analyzing phase shifts based on MS data without taking into account the effect of mixing within the MS analysis chamber at relatively high modulation frequencies [48, 49].

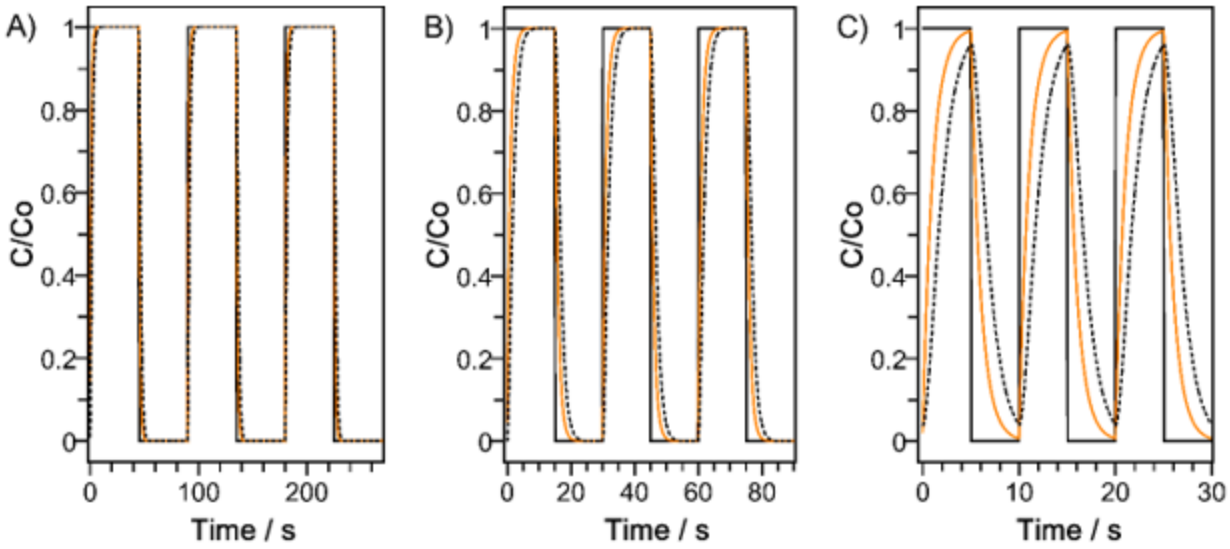

Figure 4.4. Residence time distribution simulation of two CSTR reactors in series (in absence of reaction) by inducing a square waveform with a periodic concentration change in the feed with periods of: A) 90 s (f_0 = 0.011 Hz), B) 30 s (f_0 = 0.033 Hz), and C) 10 s (f_0 = 0.1 Hz). First reactor simulates a low void-volume reaction cell and the second simulates the mass spectrometer mixing chamber. Concentration exiting CSTR #1 = orange, solid line; concentration exiting CSTR #2 = black, dotted line. Conditions: (CSTR #1 average residence time) τ_1 = 1 s; (CSTR #2 average residence time) τ_2 = 1 s; (feed modulation low relative concentration) C_{low}/C_o = 0; (feed modulation low relative concentration) C_{high}/C_o = 1.

Figure 4.5 also shows the residence time distribution in a relatively large void-volume (τ_1 = 25 s) in situ cell subjected to a square waveform input signal of frequencies f_0 = 0.011, 0.033, and 0.10 Hz and an amplitude of 0.5 [49]. Unlike the results in **Figure 4.4**. for a low void-volume cell, these results indicate that, as expected, a larger void-volume can significantly attenuate the cell feed concentration. At comparable conditions, a larger void-volume at 0.011 Hz (**Figure 4.5A**) will have a large concentration amplitude variation, despite the relatively lower modulation frequency. Further increases in modulation frequencies will simply continue to attenuate the output signal such that only about 10% of the original amplitude will be noticeable at a modulation frequency of 0.1 Hz. Such dramatic concentration amplitude changes within the cell make it more difficult to plan ME-PSD-DRIFTS experiments in absence of a mixing description of the reaction cell used. Also, if the analytical equipment is unable to capture the smaller amplitude changes of the response (e.g., spectra, output concentrations) within the cell, then higher input concentrations will be required. This presents additional experimental issues as gas phase contributions may be more prominent and could affect the resulting phase domain spectra results.

In summary, significant attenuation of the response waveform (i.e., concentration amplitude), with respect to that of the input modulation within the cell, was observed at relatively high enough modulation frequencies and at large cell residence times such as those usually found at typical flow conditions (e.g., 45 cm^3/min) in large void-volume (e.g., 13 cm^3) commercial reaction cells [49]. Such effects are minimized when using low void-volume cells (~1 cm^3) in which lower residence times (~1 s) are more easily achievable [48]. Another advantage of low void-volume cells is that amplitude changes within the cell are expected to track more closely with those expected from the input periodic perturbation, which greatly facilitates the planning of ME-PSD-DRIFTS experiments and further quantitatively analysis of the results.

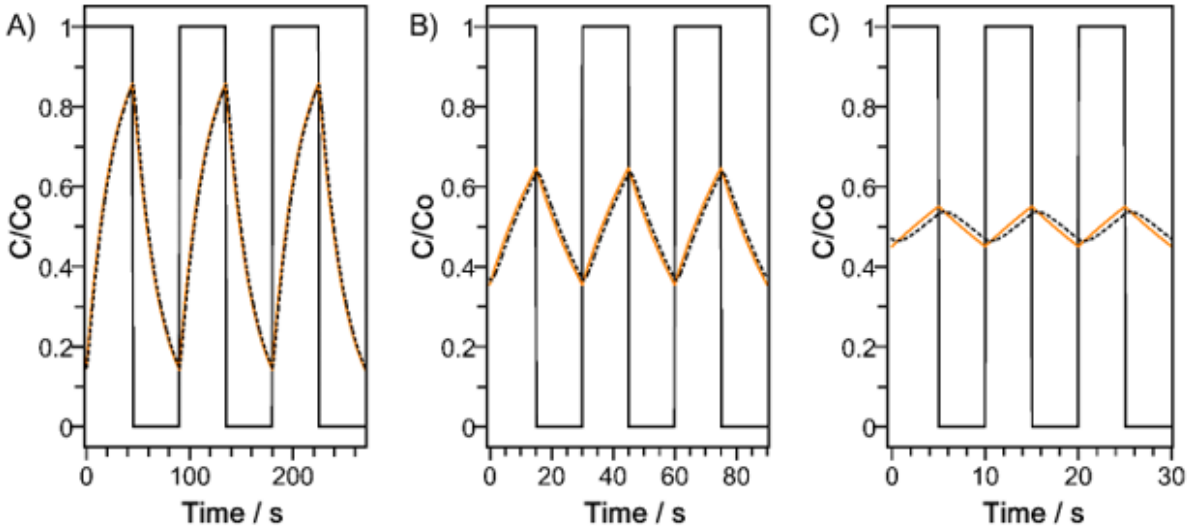

Figure 4.5. Residence time distribution simulation of two CSTR reactors in series (in absence of reaction) by inducing a square waveform with a periodic concentration change in the feed with periods of: A) 90 s (f_0 = 0.011 Hz), B) 30 s (f_0 = 0.033 Hz), and C) 10 s (f_0 = 0.1 Hz). First reactor simulates a large void-volume reaction cell and the second simulates the mass spectrometer mixing chamber. Concentration exiting CSTR #1 = orange, solid line; concentration exiting CSTR #2 = black, dotted line. Conditions: (CSTR #1 average residence time) τ_1 = 25 s; (CSTR #2 average residence time) τ_2 = 1 s; (feed modulation low relative concentration) C_{low}/C_o = 0; (feed modulation low relative concentration) C_{high}/C_o = 1.

4.5.ME-PSD-DRIFTS application example: ethanol dehydration on γ-Al_2O_3

Ethanol dehydration on γ-Al_2O_3 was selected as an example to demonstrate the application of ME-PSD-DRIFTS [50]. On γ-Al_2O_3, ethanol conversion to diethyl ether at low temperatures has been hypothesized to occur via an S_N2 mechanism in which adsorbed ethanol and an incipient ethoxide species react to produce diethyl ether and water [80, 81]. Additionally, ethanol conversion

to ethylene is usually favored at higher temperatures via an E2 mechanism with adsorbed ethanol as intermediate species [80, 81]. Also, the active sites are believed to be strong Lewis acid-weak Brønsted base pair sites present on several facets of Al_2O_3 [80, 82-89]. Here, the conversion of ethanol at 473 K and total pressure of 101 kPa is reported. At these conditions, the main product of reaction was diethyl ether (5.9 mmol/g_{cat}/h) and ethylene to a lesser extent (0.2 mmol/g_{cat}/h) as determined in a fixed bed reactor (473 K, 1 kPa EtOH, total gas flow rate ≈ 80 cm^3/min, catalyst weight = 76 mg). Additional catalyst characterization, reactivity and kinetic tests were communicated recently [50], but here the focus is on the application of ME-PSD-DRIFTS as discussed below. **Figure 4.6** shows possible reaction intermediates in the conversion of ethanol to ethylene and diethyl ether which may be detected via in situ ME-PSD-DRIFTS as described in the following sections.

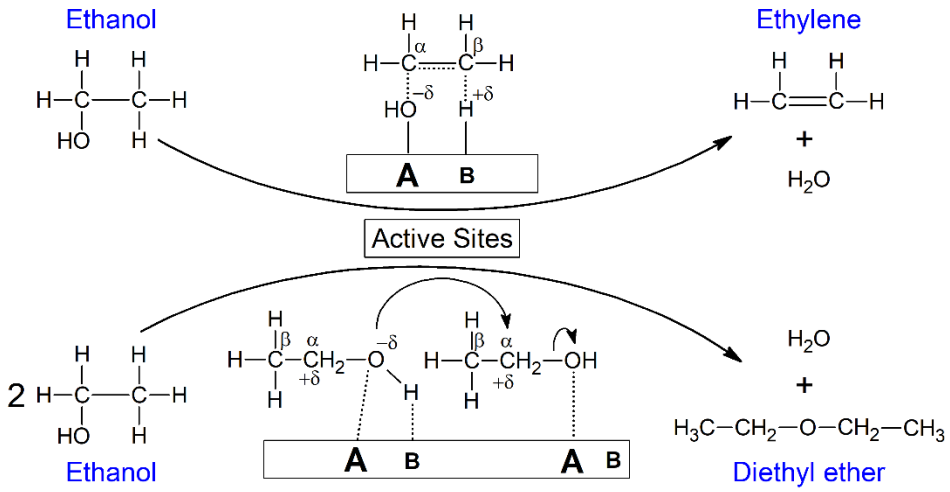

Figure 4.6. Ethanol conversion to ethylene and diethyl ether via E2 (adsorbed ethanol intermediate) and S_N2 (incipient ethoxide species and adsorbed ethanol intermediates) mechanisms, respectively [80].

4.5.1. Time domain spectra

Figure 4.7 shows the in situ time domain ME-DRIFTS spectra during ethanol dehydration on γ-Al_2O_3 at 473 K as ethanol concentration rises to a maximum within the reaction cell during the first 45 s (0–45 s: He/EtOH(1 kPa) and 45–90 s: Ar/He) of the 12th ME periodic cycle. Small changes can be seen as ethanol concentration increases, however, these are not obvious as spectra is dominated by strong sample background and peaks that do not change significantly during the

transient change. The peaks identified in **Figure 4.7** correspond closely to some of those that will be shown to respond to the feed modulation (e.g., 3730, 3674, 3230, 2975, 2929, 2873, 1445, and 1385 cm^{-1}) and some that did not change significantly (e.g., ~1700–1500 cm^{-1}). Also, the spectra showed noise in the region below 1200 cm^{-1}, that will also persist to some extent in the frequency and phase domains.

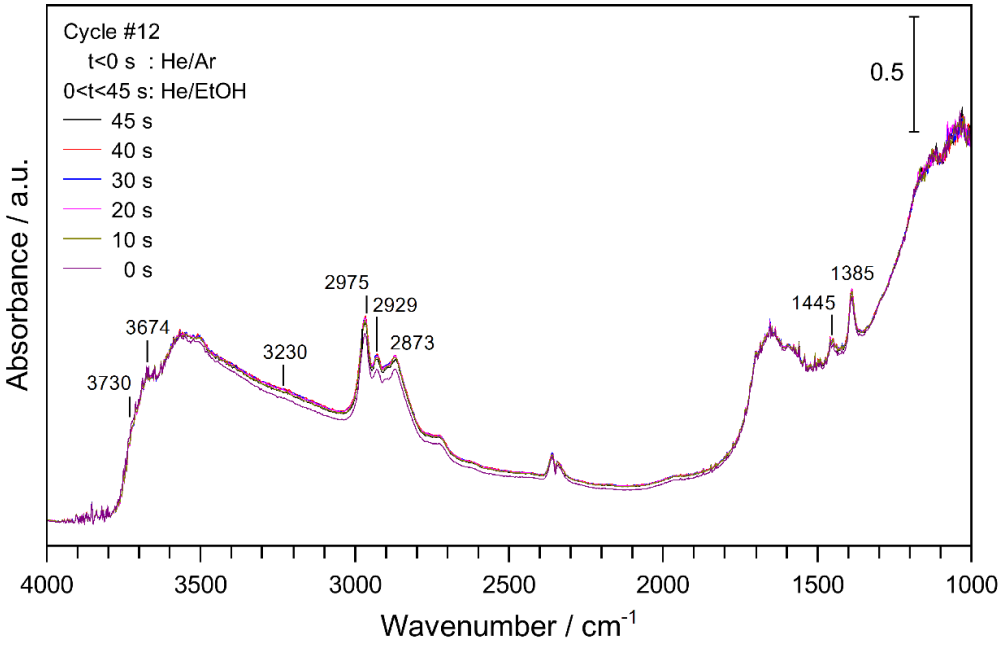

Figure 4.7. In situ time domain of ME-PSD-DRIFTS during ethanol conversion on γ-Al_2O_3. Conditions: 473 K, 101.3 kPa, feed modulation from He/Ar → He + EtOH (1 kPa), modulation frequency = 1/90 Hz, total gas flow ~45 NTP cm^3/min, catalyst weight ~45 mg.

4.5.2. Fourier transform (FT): time domain, MS response, and frequency domain results

The in situ ME-DRIFTS results in **Figure 4.8A** show the evolution of ethanol derived adsorbed species as tracked by the C–H stretching signal at 2967 cm^{-1}. The results indicate that it took approximately 4 cycles to reach a quasi-steady state. In typical ME-PSD-DRIFTS experiments, these first 4 cycles would be usually discarded and only the last 11 be used for PSD analysis. As implied from Section 4, there is no need to discard this data when performing PSD via DFT + frequency filtering + IDFT process. When kept, these subtle spectral changes (small decrease in amplitude and baseline shift) in the time domain data will be reflected in the obtained frequency domain magnitude plot as broad frequency peaks (at k=0 for background, and k=1, 2, 3, …, for

fundamental and higher frequency harmonics), for example, as shown for linear shifts and periodic decaying (or growth) of signals (**Table 4.1.**, Entries 3 and 9).

Figure 4.8B presents the MS signals due to the outlet gases from the in situ cell as ethanol reacted on γ-Al_2O_3 during the periodic changes from He/Ar to EtOH/He gas environments. The ethylene (*m*/*z*=28) and diethyl ether (*m*/*z*=59) gas phase concentration changes tracked with the adsorbed surface species and ethanol (*m*/*z*=31) outlet concentration, indicating that ethylene and diethyl ether formed from ethanol, that their formation is dependent on ethanol partial pressure, and that ethanol adsorbed reversibly on the catalyst surface. The results of the internal standard (Ar) and of cycles bypassing the cell (not shown) indicated that the input signal is dominated by a quasi-square waveform, which is similar to that observed for the ethanol adsorbed species (**Figure 4.8A**). Such response form indicates that the corresponding expected frequency domain magnitude plot should have peaks mostly due to the fundamental frequency and 2*k*-1 higher frequency harmonics.

Figure 4.8C shows the frequency domain magnitude plot for the peak corresponding to wavenumber = 2967 cm^{-1} from the in situ ME-DRIFTS during ethanol conversion on γ-Al_2O_3. In agreement with expectations from the results of **Figure 4.8A** and **Figure 4.8B** and the discussion above, the frequency domain magnitude plot (**Figure 4.8C**) is mainly constituted by the main frequency peaks of $1f_0$, $3f_0$, $5f_0$, and $7f_0$ (f_0 = feed modulation frequency) as the square waveform dominates the C–H stretching response (**Figure 4.8A**). The presence of even (2*k*) higher frequency harmonics indicates that the response is not a perfect square waveform and that it is somewhat distorted with likely contributions of a sawtooth waveform (**Table 4.1**., Entry 8). In general, the observation of fundamental and higher harmonic frequencies in **Figure 4.8C** confirmed that the species defined by the peak at 2967 cm^{-1} responded to the feed concentration modulation change and it is likely to be an intermediate species during ethanol conversion. Additionally, the broad frequency peak at $0f_0$ confirmed the presence of a constant background signal, spectator species (which do not respond to feed modulation), and a shifting baseline as shown in **Figure 4.8A** (**Table 4.1.**, Entries 1 and 3). Moreover, the slight broadening of the fundamental and higher harmonic frequencies indicate a moderate decay/growth of the signal (**Table 4.1.**, Entry 9) as also observed from **Figure 4.8A.**

To summarize:

1) The feed modulation of 0.011 Hz used in the ME-PSD-DRIFTS experiments was within the same order of magnitude of typical TOFs for ethanol dehydration at moderate temperatures [50].
2) The amplitude change of the feed modulation was about 60% of a middle ethanol concentration of ~0.45 kPa, which is relatively large but sufficient to produce a measurable response of the surface species as shown later. This amplitude change is in line with previous ME-DRIFTS works that reported changes of around 50–100% [27, 28, 31, 38, 48]. At these conditions, it is possible to carry out kinetic analysis of intermediate species as previously reported by Renken [28], Wokaun [31-34], and Gonzalez [27]. For kinetic analysis such as in the determination of reaction rate constants, it is also possible to apply chemical relaxation techniques, for which it is more convenient to employ modulation amplitude changes within 5–20% [60, 64]. At these relatively small periodic concentration changes, rate equations can be simplified by linearization allowing the direct determination of chemical relaxation times and their relationship to reaction rate constants [60, 64]. In the present work, no attempt was made to carry out kinetic analysis of the data, but it is a current topic of research in our group.
3) The results in **Figure 4.8** indicated that a feed modulation of 0.011 Hz results in response frequencies as high as ~0.08 Hz ($7f_0$). This corresponds to a sampling frequency of 0.16 Hz or 6.3 samples/s in concordance with Shannon-Nyquist minimum sampling requirement. Because the rapid scan measurements reported here allowed sampling of ~1 spectra/s, our data sampling surpass the minimum required and can be rigorously used for PSD analysis via the DFT+IDFT methodology.

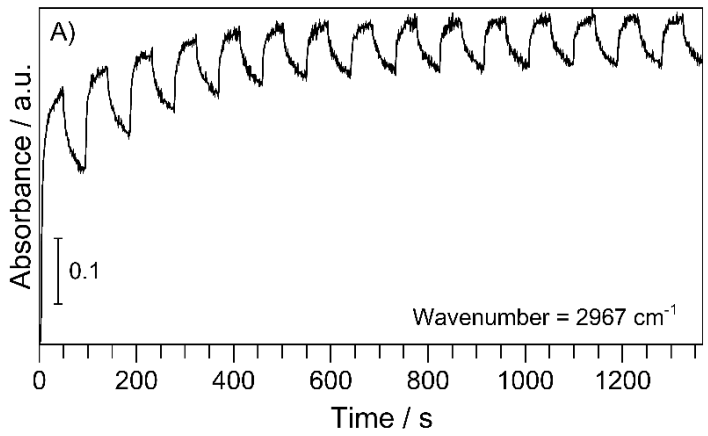

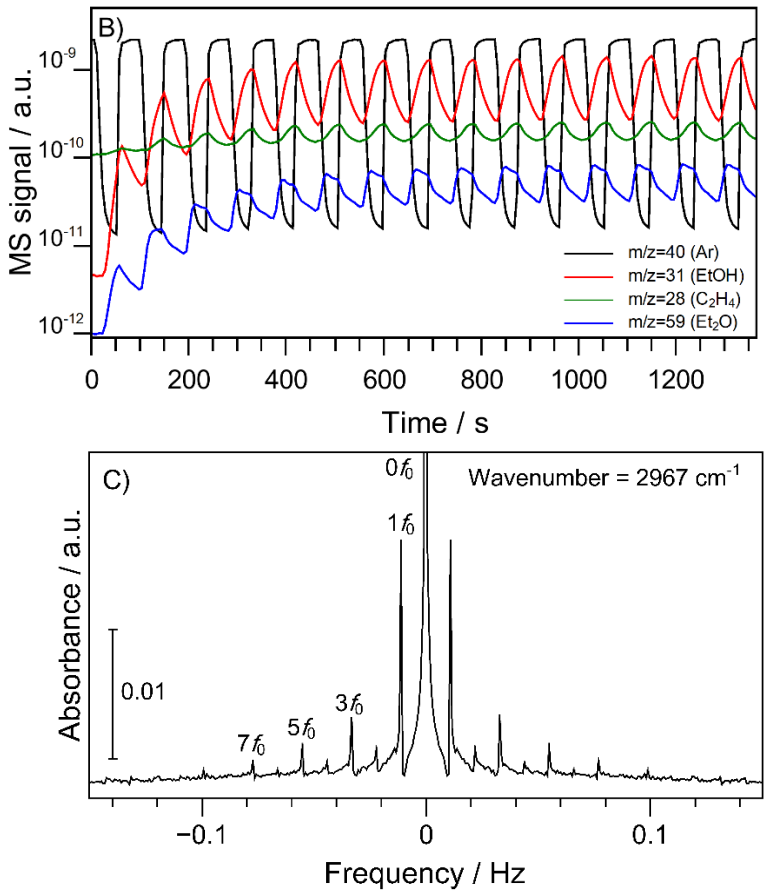

Figure 4.8.In situ ME-PSD-DRIFTS during ethanol conversion on γ-Al_2O_3. A) Time domain response plot for peak at wavenumber = 2967 cm^{-1}; B) MS signal response plot of cell outlet gases; C) Frequency domain magnitude plot for peak at wavenumber = 2967 cm^{-1}. Conditions: 473 K, 101.3 kPa, feed modulation from He/Ar → He + EtOH (1 kPa), modulation frequency = 1/90 Hz, total gas flow ~45 NTP cm^3/min, catalyst weight ~45 mg.

4.5.3. Inverse fourier transform (IFT) results

In the previous section, it was shown that the DFT of the ME-DRIFTS data results, among other information, in the determination of frequency domain magnitude plots (**Figure 4.8.C**) which allow a critical assessment of the quality of the data and the spectral response to the feed modulation. This step was usually omitted in prior applications of ME-PSD [10, 18, 24]. It was shown above that such plot is rich in information about spectra background, modulation and response waveforms, decaying/growing spectral signal trends, and signal response to modulation. In prior reports of ME-PSD methodology, the focus was on the resulting phase domain and phase

shift of spectral signals, in other words, the IDFT of the FT spectral data after restricting the response only to that of signals responding to the frequency of modulation. With the information shown so far, the phase domain plots as well as phase shift (argument) plots at a given modulation frequency can be determined. In the example of **Figure 4.8C**, it is clear that the data can be filtered at the fundamental frequency ($1f_0$) or higher frequency harmonics ($3f_0$, $5f_0$, $7f_0$) allowing the study of slow and faster reacting surface species and/or the changes in surface coverages.

4.5.3.1.IFT frequency filtering results

Figure 4.9. presents the in situ ME-PSD-DRIFTS phase domain spectra at different response frequencies of ethanol conversion on γ-Al_2O_3. **Figure 4.9A**, for example, shows the phase domain spectra for frequencies in the $0f_0$–$1f_0$ (0–0.011 Hz) range for the maximum C–H stretching at a cycle time of 35 s (140° phase angle). The spectra is similar to the time domain spectra shown in **Figure 4.7**, as expected, since the $0f_0$ captures all signals in the spectra that do not respond to feed modulation (e.g., baseline, background, spectators, etc), whereas, the $1f_0$ response frequency captures species responding to the periodic perturbation at a modulation frequency of $1f_0$. Essentially, the original spectrum was reproduced to a great extent by including $0f_0$ in the range of frequencies for IDFT. While no new information was gained in this process, it is important from a pedagogic point of view to illustrate the PSD methodology and its ability to restrict IDFT of the ME data to a selected range of frequencies.

Figure 4.9B shows more clearly the effect of frequency selection for IDFT. In this figure, the phase domain spectrum has been restricted to only the fundamental frequency, $1f_0$ (i.e., 0.011 Hz). Here, the phase domain spectrum reflects only the species that respond to the fundamental frequency and which are more likely to be intermediate species in ethanol conversion on γ-Al_2O_3 at 473 K. While the absorbance intensity is significantly smaller in **Figure 4.9B** than the original time domain spectrum (**Figure 4.7** or **Figure 4.9A**), it does highlight the power of the PSD methodology as various peaks are now discernible which were not easily observed in the time domain spectrum (**Figure 4.9A**). Assignment of these peaks will be made in more detail in the following section as here the focus is to highlight the selection of different modulation frequencies for phase domain (i.e., IDFT) spectra reconstruction.

Figure 4.9C shows the phase domain spectrum for maximum C–H stretching signal during ethanol conversion on γ-Al_2O_3 at 473 K and as limited to the higher frequency harmonic $3f_0$ (i.e., 0.033 Hz). It has been recently reported that the ME-PSD analysis at frequencies higher than the fundamental one allows discrimination of faster reacting reaction species [9]. Comparison of **Figure 4.9B** and **Figure 4.9C** indicates that both spectra are almost identical, except with a slight decrease in the intensity of broad peaks around 3300–3200 cm^{-1} and an increase in the noise of the signal below 1200 cm^{-1}. Such differences suggest the existence of species in the 3300–3200 cm^{-1} that adsorb or react at different rates [9] and of a decrease in the signal-to-noise ratio as a result of the smaller intensity of the $3f_0$ response frequency [24].

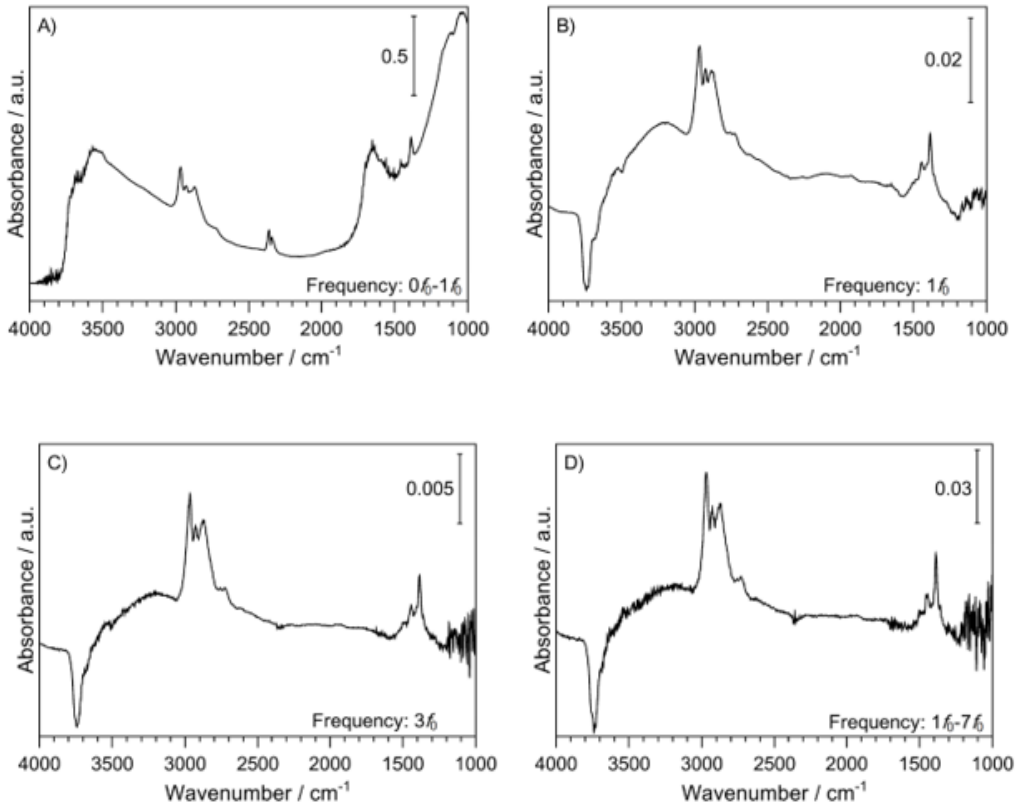

Figure 4.9. In situ ME-PSD-DRIFTS phase domain spectra during ethanol conversion on γ-Al_2O_3. A) frequency response: $0f_0$–$1f_0$ (at maximum C–H stretching cycle time, 35 s); B) frequency response: $1f_0$ (at maximum C-H stretching cycle time, 35 s); C) frequency response: $3f_0$ (at maximum C–H stretching cycle time, ~16 s); D) frequency response: $1f_0$–$7f_0$ (at maximum C-H stretching cycle time, 35 s). Conditions: 473 K, 101.3 kPa, feed modulation from He/Ar → He + EtOH (1 kPa), modulation frequency = 1/90 Hz (period = 90 s), total gas flow ~45 NTP cm^3/min, catalyst weight ~45 mg. Phase angle = (time in s/period in s)×360°.

4.5.3.2.IFT phase domain results

It was shown in the previous section that spectra reconstruction is adequately performed via IDFT after filtering of signals that respond to the fundamental modulation frequency. Here, **Figure 4.10** shows the in situ ME-PSD-DRIFTS phase domain spectra filtered at the fundamental modulation frequency ($1f_0$ = 0.011 Hz) over an entire period cycle during ethanol conversion on γ-Al_2O_3. While **Figure 4.9B** shows a single spectrum at the maximum C–H stretching (2967 cm^{-1}) at the frequency response of $1f_0$, **Figure 4.10A** presents the phase domain contour plot which reflects spectra changes over one modulation period (90 s) as indicated in the Y axis. It is worth noting that, for simplicity, a sine waveform was added to this plot to guide the eye for gas phase concentration modulation, despite not being the actual modulation form. In general, this plot can be quite useful (if wavenumber and high and low ranges are selected appropriately) as it allows a quick visual evaluation of the possible presence of peaks and their possible relationships. In **Figure 4.10A**, color contrast between blue and red regions correlate with low and high surface coverage of species with respect to a mid-point in the periodic modulation. More specifically, it can be quickly noticed that at high concentrations of ethanol in the gas feed (between ~25–60 s) there is an abundance of ethanol derived species as inferred from the C–H stretching at 3000–2800 cm^{-1}. These species seem to follow an opposite behavior to Al hydroxyl species in the 3800–3700 cm^{-1} region as shown by the blue color indicating a negative signal with respect to the average value during the periodic feed oscillation. Additionally, adsorbed water and ethanol bonded to hydroxyl groups were visible at high ethanol gas phase concentration as indicated by the orange region between 3500 and 3100 cm^{-1}. The opposite observations can be also made when the concentration of ethanol is low (i.e., 60–90 s) because of the symmetry of the feed modulation and, therefore, the phase-domain spectra around a mid-concentration reference point. Such rapid evaluation of trends is only possible in this contour plot, which is not obvious from time domain spectra (**Figure 4.7**).

More detailed observations can be made from individual in situ ME-PSD-DRIFTS phase domain traces shown in **Figure 4.10.B**. In contrast with the time domain plot (**Figure 4.7**), the surface species observed in this plot respond to the fundamental feed concentration modulation and are likely to be reaction intermediates. This plot also shows that the PSD procedure significantly reduced the noise level and enhanced the definition of weak peaks, not easily

discernible in the time domain spectra. At the reaction temperature investigated (473 K), the predominant product of reaction was diethyl ether followed by smaller amounts of ethylene. Therefore, from **Figure 4.6** several surface species would be expected in the DRIFTS spectra such as adsorbed ethanol and ethoxide species. The following peaks were observed in **Figure 4.10B**: 1) 2968, 2925, 2880, 1448, 1388, and very weak 1063 cm^{-1}, assigned to adsorbed ethanol [50, 84, 90-94]; 2) 2968, 2925, 2880, 1448, 1388, and very weak 1137, 1063, and 1033 cm^{-1}, assigned to an incipient ethoxide species [50, 84, 90-94]; 3) 3754, 3741, 3720, and 3680 cm^{-1} assigned to terminal and bridging hydroxyls in Al_{IV} and Al_{V} [50, 85, 86, 95, 96]; and 4) broad peak at 3500–3000 cm^{-1} assigned to ethanol and water H-bonded to surface hydroxyls in terminal and triply bridging positions on tetrahedral and octahedral Al [50, 85, 86, 95-97]; These results are consistent with the conversion of ethanol to diethyl ether on γ-Al_2O_3 via an S_N2 mechanism involving an ethanol and an incipient ethoxide species (**Figure 4.6**) in agreement with previous reports [80, 81, 84, 94, 98-101]; Additionally, the results of **Figure 4.10B** clearly show that several types of Al hydroxyl species, not just one, are likely active sites for ethanol conversion on γ-Al_2O_3. Also, the presence of the broad band at 3500–3000 cm^{-1} indicates that ethanol and water molecules covered the catalyst surface to a larger extent. As shown in **Figure 4.9C**, some of these species respond much more slowly than other observed surface species. Such differences suggest the involvement of these species in the reaction mechanism, but not necessarily in the ethanol conversion catalytic cycle. This is in agreement with the involvement of these species as inhibitors during ethanol dehydration reactions as previously reported for ethanol, *n*-propanol, and isopropanol conversion on γ-Al_2O_3 [81, 83, 88, 102];

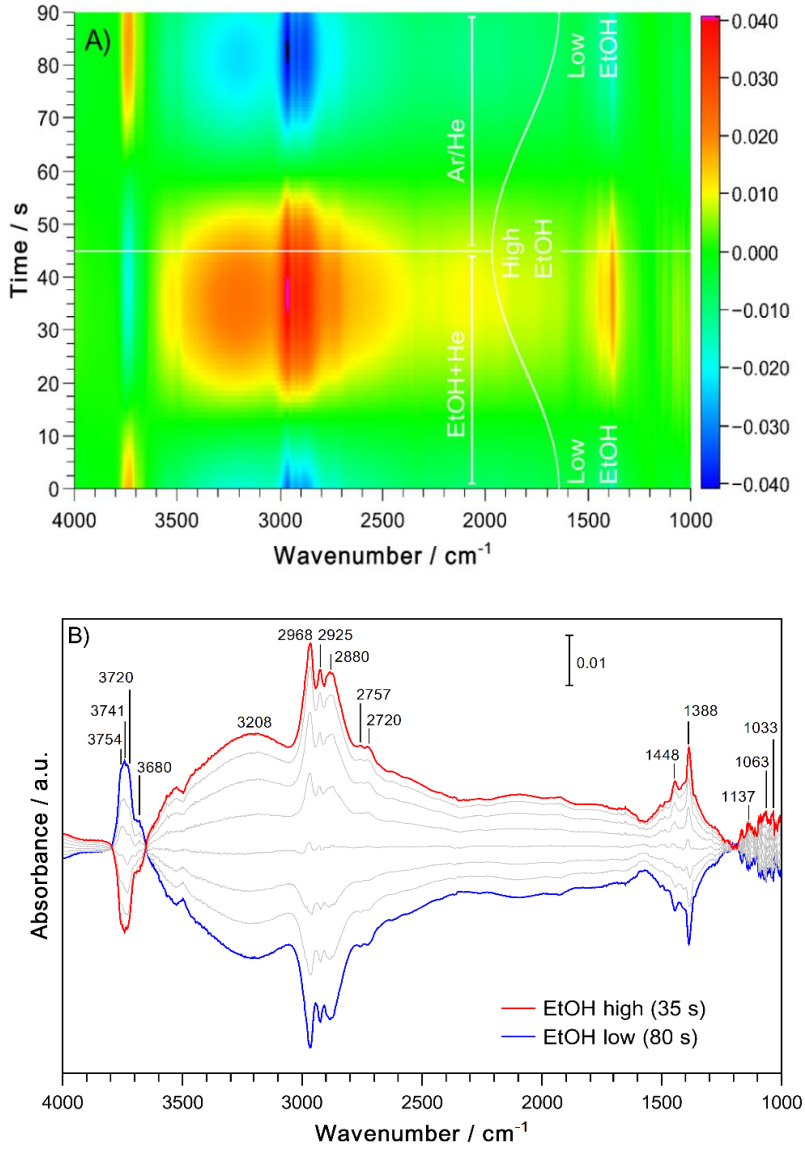

Figure 4.10. In situ ME-PSD-DRIFTS spectra during ethanol conversion on γ-Al_2O_3. A) Phase domain contour plot; B) Phase domain trace plot. Conditions: 473 K, 101.3 kPa, feed modulation from He/Ar → He + EtOH (1 kPa), modulation frequency = 1/90 Hz (period = 90 s), frequency response = 1/90 Hz (1f_0), total gas flow ~45 NTP cm^3/min, catalyst weight ~45 mg. Phase angle = (time in s/period in s)×360°. EtOH sine wave feed composition curve added to contour plot to guide the eye.

4.5.3.3.IFT phase angle (argument) results

Another advantage of ME-PSD methodology is the possibility of discriminating surface species that have different kinetic responses in a catalytic cycle. This is seen as a phase lag in the

response signal of the surface species with respect to the input signal waveform [10, 18, 24, 35]. Such time or phase lag of surface species with different kinetic characteristics (i.e., time constant or relaxation time of reaction) resembles that observed in **Figure 4.4** and **Figure 4.5** (and Appendix C) as a result of different gas residence times in the in situ cell. Additionally, analysis of different peaks in a phase angle plot, that is, if they are in-sync (in-phase) or out-of-sync (out-of-phase) will provide information of the relationships of different species and thus of reaction pathways [10, 35, 37]. A typical qualitative analysis of the kinetic response of different signals consists of comparing the relative response of the different species (e.g., peaks) at different times during a modulation period, as typically shown in: 1) a wavenumber vs absorbance phase domain plots with traces at different times (or phase angle) [35] (**Figure 4.10B**) or 2) wavenumber vs phase angle plot (or phase shift or argument plot) at the frequency of interest (**Figure 4.11A**) [10, 37].

The phase domain plot (e.g., **Figure 4.10B**) is quite useful because it only shows the signals of species that respond to input (e.g., feed concentration) modulation and which are likely to be intermediate species. When a phase domain spectrum presents species that are consumed and produced concomitantly, and which are interrelated, then both peaks will show opposite trends at different times (or phase angle) in a periodic cycle. Such kinetic differentiation should be then observed in a phase angle (argument) plot such as that shown in **Figure 4.11A**. For example, this figure shows:

1) That all peaks in the 3600–1200 cm^{-1} range are in-sync (in-phase) as they present the same phase angle. This suggests that these species have the same kinetic response (e.g., time constant) or that they all have fast kinetics (but not necessarily the same) so that they are able to follow the input modulation such as adsorbed ethanol or ethoxide species. Also, **Figure 4.9C** indicated that some of the water and/or ethanol species H-bonded to surface hydroxyls in terminal and triply bridging positions on tetrahedral and octahedral Al adsorbed more slowly than others, but those that adsorb faster do so at similar rates as ethanol or ethoxide species on terminal and bridging hydroxyls in Al_{IV} and Al_{V}.
2) That adsorbed ethanol or ethoxide species (3600–1200 cm^{-1}) are out-of-sync (out-of-phase) by almost π radians (180°) indicating that they are oppositely related, such that ethanol/ethoxide species form on terminal and bridging hydroxyls in Al_{IV} and Al_{V} (3760–3650 cm^{-1}), these latter

which are consumed in this process. This result agrees with the same observations in the phase domain contour plot (**Figure 4.10A**).

3) The different terminal and bridging hydroxyls in Al_{IV} and Al_V (3760–3650 cm^{-1}) kinetic response is similar, with the hydroxyls at 3720 cm^{-1} (25.6°) showing a slightly larger kinetic response than 3755 cm^{-1} (30.0°) ≈ 3741 cm^{-1} (27.8°) ≈ 3680 cm^{-1} (28.5°). These results suggest that at the studied conditions, terminal and bridging hydroxyls are likely reaction intermediates, but with the HO-μ_1-Al_V (110) (@ 3720 cm^{-1}) [85, 86, 95, 96] reacting at a slightly faster rate.
4) The species in the 1200–1000 cm^{-1} are more likely to be in-sync ethanol and ethoxide species, but the noise in this region precluded further detailed analysis.
5) The apparent significant phase lag observed around 1200 cm^{-1} is an artifact calculated from noise as no peaks are observed in this region. To confirm or rule out the presence of peaks, a phase domain magnitude plot at the same response frequency of 0.011 Hz such as that shown in **Figure 4.11B** is quite useful. The figure serves as a guide to confirm all observed peaks in the phase domain (**Figure 4.10B**) as they all showed in the positive direction. Then, this figure confirms the absence of a peak at 1200 cm^{-1}.

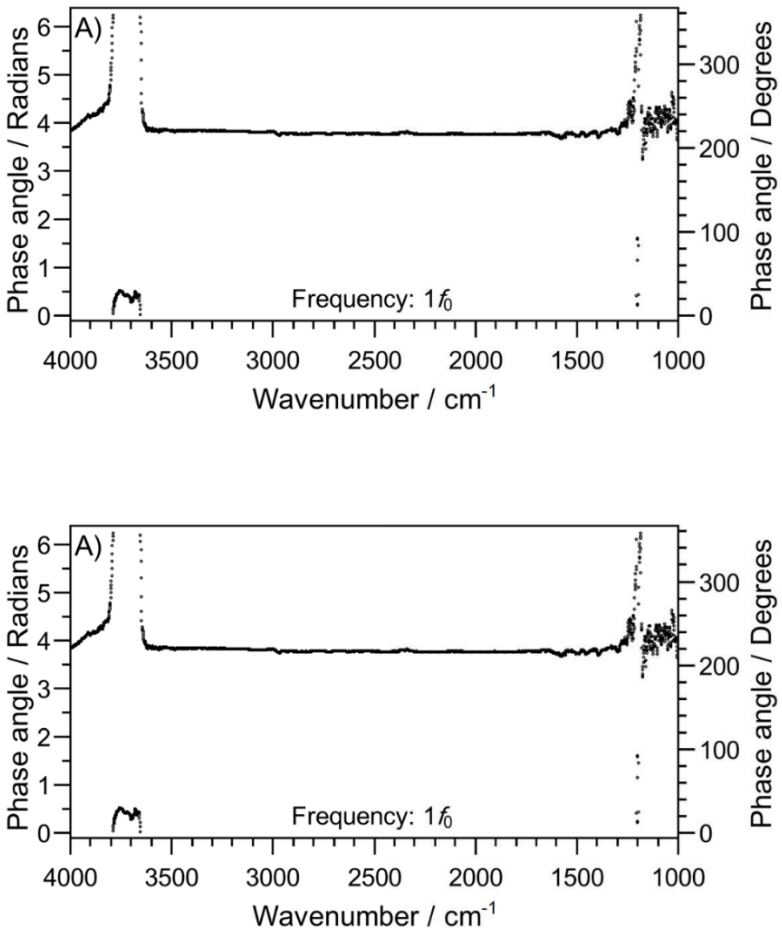

Figure 4.11. In situ ME-PSD-DRIFTS during ethanol conversion on γ-Al_2O_3. A) phase angle (argument) plot at a frequency of 0.011 Hz; B) phase domain magnitude plot (showing all positive observed peaks) at a frequency of 0.011 Hz. Conditions: 473 K, 101.3 kPa, feed modulation from He/Ar → He + EtOH (1 kPa), modulation frequency = 1/90 Hz, total gas flow ~45 NTP cm^3/min, catalyst weight ~45 mg. Phase angle = (radians/2π)×360°.

4.6.Conclusions

In this work, the application of modulation excitation-phase sensitive detection-diffuse reflectance Fourier transform spectroscopy (ME-PSD-DRIFTS) via discrete Fourier transform (DFT)/inverse discrete Fourier transform (IDFT) was described in detail including a general mathematical framework, basic guidelines for planning, running, and interpreting ME-PSD-DRIFTS results with aspects such as required modulation frequency and amplitude, modulation waveform, sampling rate, and in situ cell residence time. The described ME-PSD technique was based on the introduction of a periodic perturbation in the reaction system so that PSD can be applied via Fourier

analysis. For this analysis the resulting spectroscopic data was converted from time domain to frequency domain via DFT, followed by selection of a proper response frequency (or frequencies), and reconstruction of the filtered signal via IDFT. Because spectator species do no respond to rapid modulation frequencies in the range of reaction turnover frequencies, the methodology allows the sensitive detection of reacting species that respond to the modulation frequency, which are, thus, likely reaction intermediates. The resulting filtered spectra in the so-called phase domain and phase angle (i.e., argument) plots permitted the study of the relative response of the various detected species. Additionally, the use of frequency domain plots provided information on the reaction system such as baseline shifts (e.g., due to accumulation of spectator species on the catalyst surface), signal response to modulation, response waveform type, noise, and signal decay/growth, which were not explored in previous applications of ME-PSD. Because the described DFT/IDFT procedure can be applied to any periodic modulation, in theory, any input modulation waveform (not just sine and square waveforms) can be used to introduce a perturbation in the reaction system. In practice, this is quite convenient as a single software code can be used to handle ME-PSD responses regardless of the type of perturbation. Because of the general application of the ME-PSD methodology, we also expect this work to promote its popularization and application to other in situ/operando spectroscopic techniques and thus contribute to the further understanding of active sites and intermediate species in heterogeneous catalysis.

This work was published in ***Reaction Chemistry and Engineering***, 2019 4, 862-883 (DOI: 10.1039/C9RE00011A)

4.7.References

1. Bravo-Suárez, J.J., Chaudhari, R.V., and Subramaniam, B., Design of Heterogeneous Catalysts for Fuels and Chemicals Processing: An Overview. In *Novel Materials for Catalysis and Fuels Processing*, J.J. Bravo-Suárez, Kidder, M.K., and Schwartz, V., Eds. American Chemical Society: Washington, D.C., **2013;** Vol. Volume 1132, pp 3-68.

2. Bravo-Suárez, J.J. and Srinivasan, P.D., Design characteristics of in situ and operando ultraviolet-visible and vibrational spectroscopic reaction cells for heterogeneous catalysis. *Catalysis Reviews: Science and Engineering* **2017**, pp1-151, https://doi.org/10.1080/01614940.2017.1360071.

3. Weckhuysen, B.M., *In-Situ Spectroscopy of Catalysts*. American Scientific Publishers: Stevenson Ranch, CA, **2004;** p 1-332.

4. Che, M. and Vedrine, J.C., *Characterization of Solid Materials and Heterogeneous Catalysts: From Structure to Surface Reactivity*. Wiley: Weinheim, Germany, **2012**.

5. Lamberti, C., Zecchina, A., Groppo, E., and Bordiga, S., Probing the surfaces of heterogeneous catalysts by in situ IR spectroscopy. *Chemical Society Reviews* **2010,** *39* (12), 4951-5001.

6. Baurecht, D. and Fringeli, U.P., Quantitative modulated excitation Fourier transform infrared spectroscopy. *Review of Scientific Instruments* **2001,** *72* (10), 3782-3792.

7. Meunier, F.C., The design and testing of kinetically-appropriate operando spectroscopic cells for investigating heterogeneous catalytic reactions. *Chemical Society Reviews* **2010,** *39* (12), 4602-4614.

8. Weckhuysen, B.M., Determining the active site in a catalytic process: Operando spectroscopy is more than a buzzword. *Physical Chemistry Chemical Physics* **2003,** *5* (20), 4351-4360.

9. Marchionni, V., Ferri, D., Krocher, O., and Wokaun, A., Increasing the Sensitivity to Short-Lived Species in a Modulated Excitation Experiment. *Analytical Chemistry* **2017,** *89* (11), 5802-5810.

10. Urakawa, A., Bürgi, T., and Baiker, A., Sensitivity enhancement and dynamic behavior analysis by modulation excitation spectroscopy: Principle and application in heterogeneous catalysis. *Chemical Engineering Science* **2008,** *63* (20), 4902-4909.

11. Pérez-Ramírez, J. and Kondratenko, E.V., Evolution, achievements, and perspectives of the TAP technique. *Catalysis Today* **2007,** *121* (3), 160-169.

12. Morgan, K., Maguire, N., Fushimi, R., Gleaves, J.T., Goguet, A., Harold, M.P., Kondratenko, E.V., Menon, U., Schuurman, Y., and Yablonsky, G.S., Forty years of temporal analysis of products. *Catalysis Science & Technology* **2017,** *7* (12), 2416-2439.

13. Meunier, F.C., The power of quantitative kinetic studies of adsorbate reactivity by operando FTIR spectroscopy carried out at chemical potential steady-state. *Catalysis Today* **2010,** *155* (3), 164-171.

14. Kalamaras, C.M., Americanou, S., and Efstathiou, A.M., "Redox" vs "associative formate with -OH group regeneration" WGS reaction mechanism on Pt/CeO2: Effect of platinum particle size. *Journal of Catalysis* **2011,** *279* (2), 287-300.

15. Bravo-Suárez, J.J., Bando, K.K., Lu, J.I., Haruta, M., Fujitani, T., and Oyama, S.T., Transient technique for identification of true reaction intermediates: Hydroperoxide species in propylene epoxidation on gold/titanosilicate catalysts by X-ray absorption fine structure spectroscopy. *Journal of Physical Chemistry C* **2008,** *112* (4), 1115-1123.

16. Oyama, S.T. and Li, W., Absolute determination of reaction mechanisms by in situ measurements of reaction intermediates. *Topics in Catalysis* **1999,** *8* (1), 75-80.

17. Gott, T. and Oyama, S.T., A general method for determining the role of spectroscopically observed species in reaction mechanisms: Analysis of coverage transients (ACT). *Journal of Catalysis* **2009,** *263* (2), 359-371.

18. Müller, P. and Hermans, I., Applications of Modulation Excitation Spectroscopy in Heterogeneous Catalysis. *Industrial & Engineering Chemistry Research* **2017,** *56* (5), 1123-1136.

19. Shannon, S.L. and Goodwin, J.G., Characterization of catalytic surfaces by isotopic-transient kinetics during steady-state reaction. *Chemical Reviews (Washington, DC, United States)* **1995,** *95* (3), 677-695.

20. Ledesma, C., Yang, J., Chen, D., and Holmen, A., Recent Approaches in Mechanistic and Kinetic Studies of Catalytic Reactions Using SSITKA Technique. *ACS Catalysis* **2014,** *4* (12), 4527-4547.

21. Chuang, S.S.C. and Guzman, F., Mechanistic Investigation of Heterogeneous Catalysis by Transient Infrared Methods. *Topics in Catalysis* **2009,** *52* (10), 1448-1458.

22. Rodriguez, J.A., Hanson, J.C., and Chupas, P.J., *In-situ Characterization of Heterogeneous Catalysts*. Wiley: **2013**.

23. Kopelent, R., van Bokhoven, J.A., Szlachetko, J., Edebeli, J., Paun, C., Nachtegaal, M., and Safonova, O.V., Catalytically Active and Spectator Ce3+ in Ceria-Supported Metal Catalysts. *Angewandte Chemie International Edition* **2015,** *54* (30), 8728-8731.

24. Urakawa, A., Bürgi, T., and Baiker, A., Kinetic analysis using square-wave stimulation in modulation excitation spectroscopy: Mixing property of a flow-through PM-IRRAS cell. *Chemical Physics* **2006,** *324* (2), 653-658.

25. Polinski, L. and Naphtali, L., Dynamic Methods for Characterization of Adsorptive Properties of Solid Catalysts. *Advances in Catalysis* **1969,** *Volume 19*, 241-291.

26. Jones, R.H., Olander, D.R., Siekhaus, W.J., and Schwarz, J.A., Investigation of Gas–Solid Reactions by Modulated Molecular Beam Mass Spectrometry. *Journal of Vacuum Science & Technology* **1972,** *9* (6), 1429-1441.

27. Li, Y.-E., Willcox, D., and Gonzalez, R.D., Determination of rate constants by the frequency response method: CO on Pt/SiO2. *AIChE Journal* **1989,** *35* (3), 423-428.

28. Marwood, M., Doepper, R., and Renken, A., Modeling of surface intermediates under forced periodic conditions applied to CO2 methanation. *The Canadian Journal of Chemical Engineering* **1996,** *74* (5), 660-663.

29. Cavers, M., Davidson, J.M., Harkness, I.R., Rees, L.V.C., and McDougall, G.S., Spectroscopic Identification of the Active Site for CO Oxidation on Rh/Al2O3 by Concentration Modulation in situ DRIFTS. *Journal of Catalysis* **1999,** *188* (2), 426-430.

30. Cavers, M., Davidson, J.M., Harkness, I.R., McDougall, G.S., and Rees, L.V.C., Novel frequency response techniques for the study of kinetics in heterogeneous catalysis. *Studies in Surface Science and Catalysis* **1999,** *122*, 65-72.

31. Ortelli, E.E., Wambach, J., and Wokaun, A., Use of periodic variations of reactant concentrations in time resolved DRIFT studies of heterogeneously catalysed reactions. *Applied Catalysis a-General* **2000,** *192* (1), 137-152.

32. Ortelli, E.E. and Wokaun, A., Use of periodic variations of reactant concentrations in time resolved FTIR studies of heterogeneously catalysed reactions. *Vibrational Spectroscopy* **1999,** *19* (2), 451-459.

33. Kritzenberger, J. and Wokaun, A., Time resolved FTIR study of the catalytic CO oxidation under periodic variation of the reactant concentration. *Journal of Molecular Catalysis a-Chemical* **1997,** *118* (2), 235-245.

34. Ortelli, E.E., Wambach, J., and Wokaun, A., Methanol synthesis reactions over a CuZr based catalyst investigated using periodic variations of reactant concentrations. *Applied Catalysis A: General* **2001,** *216* (1–2), 227-241.

35. Bürgi, T. and Baiker, A., In Situ Infrared Spectroscopy of Catalytic Solid−Liquid Interfaces Using Phase-Sensitive Detection: Enantioselective Hydrogenation of a Pyrone over Pd/TiO2. *The Journal of Physical Chemistry B* **2002,** *106* (41), 10649-10658.

36. Kydd, R., Ferri, D., Hug, P., Scott, J., Teoh, W.Y., and Amal, R., Temperature-induced evolution of reaction sites and mechanisms during preferential oxidation of CO. *Journal of Catalysis* **2011,** *277* (1), 64-71.

37. Aguirre, A. and Collins, S.E., Selective detection of reaction intermediates using concentration-modulation excitation DRIFT spectroscopy. *Catalysis Today* **2013,** *205*, 34-40.

38. Müller, P., Burt, S.P., Love, A.M., McDermott, W.P., Wolf, P., and Hermans, I., Mechanistic Study on the Lewis Acid Catalyzed Synthesis of 1,3-Butadiene over Ta-BEA Using Modulated Operando DRIFTS-MS. *ACS Catalysis* **2016,** *6* (10), 6823-6832.

39. Maeda, N., Meemken, F., Hungerbühler, K., and Baiker, A., Spectroscopic Detection of Active Species on Catalytic Surfaces: Steady-State versus Transient Method. *CHIMIA International Journal for Chemistry* **2012,** *66* (9), 664-667.

40. Urakawa, A., Van Beek, W., Monrabal-Capilla, M., Galán-Mascarós, J.R., Palin, L., and Milanesio, M., Combined, Modulation Enhanced X-ray Powder Diffraction and Raman Spectroscopic Study of Structural Transitions in the Spin Crossover Material [Fe(Htrz)2(trz)](BF4). *The Journal of Physical Chemistry C* **2011,** *115* (4), 1323-1329.

41. Ferri, D., Newton, M.A., and Nachtegaal, M., Modulation Excitation X-Ray Absorption Spectroscopy to Probe Surface Species on Heterogeneous Catalysts. *Topics in Catalysis* **2011,** *54* (16-18), 1070-1078.

42. Ferri, D., Newton, M.A., Di Michiel, M., Chiarello, G.L., Yoon, S., Lu, Y., and Andrieux, J., Revealing the Dynamic Structure of Complex Solid Catalysts Using Modulated Excitation X-ray Diffraction. *Angewandte Chemie-International Edition* **2014,** *53* (34), 8890-8894.

43. *Transform techniques in chemistry* edited by Peter R. Griffiths. Plenum Press: New York, **1978;** p 1-385.

44. Brigham, E.O., *The Fast Fourier Transform and Its Applications*. Prentice Hall: Englewood Cliffs, NJ, **1988;** p 1-448.

45. Kauppinen, J. and Partanen, J., *Fourier Transforms in Spectroscopy*. Wiley: Berlin, Germany, **2001;** p 1-271.

46. Peters, T.M. and Williams, J.C., *The Fourier Transform in Biomedical Engineering*. Birkhäuser Boston: New York, NY, **1998;** p 1-199.

47. FFTWhttp://www.fftw.org/(accessed Dec. 16, 2018).

48. Patil, B.S., Srinivasan, P.D., Atchison, E., Zhu, H., and Bravo-Suárez, J.J., Design, Modelling, and Application of a Low Void-Volume in Situ Diffuse Reflectance Spectroscopic Reaction Cell for Transient Catalytic Studies. *React. Eng. Chem.* **2018**, (DOI: 10.1039/c8re00302e).

49. Srinivasan, P.D., Nitz, S.R., Stephens, K.J., Atchison, E., and Bravo-Suárez, J.J., Modified Harrick reaction cell for in situ/operando fiber optics diffuse reflectance UV–visible spectroscopic characterization of catalysts. *Applied Catalysis A: General* **2018,** *561*, 7-18.

50. Srinivasan, P.D., Khivantsev, K., Tengco, J.M.M., Zhu, H., and Bravo-Suárez, J.J., Enhanced Ethanol Dehydration on γ-Al2O3 Supported Cobalt Catalyst. *J.Catal.* **2019**, 373, 276-296

51. Meade, M.L., *Lock-in Amplifiers: Principles and Applications*. P. Peregrinus: London, UK, **1983;** p 1-232.

52. Dávila Pintle, J.A., Fourier description of lock-in. *Rev. Mex. Fis. E* **2013,** *59*, 1-7.

53. Silverton, P.L., *Composition Modulation of Catalytic Reactors (Topics in Chemical Engineering, Vol. 11)*. Gordon and Breach Science Publishers: Amsterdam (The Netherlands), **1998;** p 1-596.

54. Reyes, S.C. and Iglesia, E., Frequency response techniques for the characterization of porous catalytic solids. In *Catalysis*, J.J. Spivey and Agarwal, S.K., Eds. The Royal Society of Chemistry: **1994;** Vol. 11, pp 51-92.

55. Tang, K.T., *Mathematical Methods for Engineers and Scientists 3: Fourier Analysis, Partial Differential Equations and Variational Methods*. Springer: Berlin, Germany, **2007;** p 1-440.

56. Santamarina, J.C. and Fratta, D., *Discrete Signals and Inverse Problems: An Introduction for Engineers and Scientists*. Wiley: Chichester, UK, **2005;** p 1-364.

57. James, J.F., *A Student's Guide to Fourier Transforms: With Applications in Physics and Engineering*. 3rd Ed. ed.; Cambridge University Press: Cambridge, UK, **2011;** p 1-146.

58. Lyons, R.G., *Understanding Digital Signal Processing*. Prentice Hall: Upper Saddle River, NJ, **2004;** p 1-665.

59. Silveston, P., Hudgins, R.R., and Renken, A., Periodic operation of catalytic reactors—introduction and overview. *Catalysis Today* **1995,** *25* (2), 91-112.

60. Bernasconi, C.F., *Relaxation kinetics*. Academic Press: London, U.K, **1976;** p 1-288.

61. Bell, A.T. and Hegedus, L.L., *Catalysis under transient conditions, ACS Symposium Series, 178*. American Chemical Society: Washington, D.C., **1982;** p 1-308.

62. Tamaru, K., Dynamic Relaxation Methods in Heterogeneous Catalysis. In *Catalysis: Science and Technology*, J.R. Anderson and Boudart, M., Eds. Springer: Berlin, Germany, **2012;** pp 87-129.

63. Caldin, E.F., The Study of Fast Reactions in Solution. In *Techniques and Applications of Fast Reactions in Solution (NATO Advanced Study Institutes Series (Series C — Mathematical and Physical Sciences))*, W.J.Gettins and Wyn-Jones, E., Eds. Springer: Dordrecht, Holland, **1979;** Vol. 50, pp 1-11.

64. Eigen, M. and De Maeyer, L., Relaxation methods. *Technique of Organic Chemistry* **1963,** *8* (Part II), 895-1054.

65. Bürgi, T. and Baiker, A., Attenuated total reflection infrared spectroscopy of solid catalysts functioning in the presence of liquid-phase reactants. *Advances in Catalysis* **2006,** *50*, 227-283.

66. Ribeiro, F.H., Schach von Wittenau, A.E., Bartholomew, C.H., and Somorjai, G.A., Reproducibility of turnover rates in heterogeneous metal catalysis: Compilation of data and guidelines for data analysis. *Catalysis Reviews* **1997,** *39* (1-2), 49-76.

67. Smith, S.W., *The scientist and engineer's guide to digital signal processing*. 2nd ed.; California Technical Publishing: San Diego, CA, **1997;** p 1-650.

68. Li, B. and Gonzalez, R.D., Design and Construction of a DRIFTS Accessory and an in Situ Heatable Sample Cell. *Applied Spectroscopy* **1998,** *52* (11), 1488-1491.

69. Chiarello, G.L., Nachtegaal, M., Marchionni, V., Quaroni, L., and Ferri, D., Adding diffuse reflectance infrared Fourier transform spectroscopy capability to extended x-ray-absorption fine structure in a new cell to study solid catalysts in combination with a modulation approach. *Review of Scientific Instruments* **2014,** *85* (7), 074102.

70. Schubert, M.M., Häring, T.P., Bräth, G., Gasteiger, H.A., and Behm, R.J., New DRIFTS Cell Design for the Simultaneous Acquisition of IR Spectra and Kinetic Data Using On-Line Product Analysis. *Applied Spectroscopy* **2001,** *55* (11), 1537-1543.

71. Dal Santo, V., Dossi, C., Fusi, A., Psaro, R., Mondelli, C., and Recchia, S., Fast transient infrared studies in material science: development of a novel low dead-volume, high temperature DRIFTS cell. *Talanta* **2005,** *66* (3), 674-682.

72. Marchionni, V., Newton, M.A., Kambolis, A., Matam, S.K., Weidenkaff, A., and Ferri, D., A modulated excitation ED-EXAFS/DRIFTS study of hydrothermal ageing of Rh/Al2O3. *Catalysis Today* **2014,** *229*, 80-87.

73. Zarfl, J., Ferri, D., Schildhauer, T.J., Wambach, J., and Wokaun, A., DRIFTS study of a commercial Ni/gamma-Al2O3 CO methanation catalyst. *Applied Catalysis a-General* **2015,** *495*, 104-114.

74. Haghofer, A., Ferri, D., Fottinger, K., and Rupprechter, G., Who Is Doing the Job? Unraveling the Role of Ga2O3 in Methanol Steam Reforming on Pd2Ga/Ga2O3. *ACS Catalysis* **2012,** *2* (11), 2305-2315.

75. Martin, O., Mondelli, C., Cervellino, A., Ferri, D., Curulla-Ferre, D., and Perez-Ramirez, J., Operando Synchrotron X-ray Powder Diffraction and Modulated-Excitation Infrared Spectroscopy Elucidate the CO2 Promotion on a Commercial Methanol Synthesis Catalyst. *Angewandte Chemie-International Edition* **2016,** *55* (37), 11031-11036.

76. Aguirre, A., Barrios, C.E., Aguilar-Tapia, A., Zanella, R., Baltanas, M.A., and Collins, S.E., In-Situ DRIFT Study of Au-Ir/Ceria Catalysts: Activity and Stability for CO Oxidation. *Topics in Catalysis* **2016,** *59* (2-4), 347-356.

77. Vecchietti, J., Bonivardi, A., Xu, W.Q., Stacchiola, D., Delgado, J.J., Calatayud, M., and Collins, S.E., Understanding the Role of Oxygen Vacancies in the Water Gas Shift Reaction on Ceria-Supported Platinum Catalysts. *ACS Catalysis* **2014,** *4* (6), 2088-2096.

78. del Rio, E., Collins, S.E., Aguirre, A., Chen, X.W., Delgado, J.J., Calvino, J.J., and Bernal, S., Reversible deactivation of a Au/$Ce_{0.62}Zr_{0.38}O_2$ catalyst in CO oxidation: A systematic study of CO2-triggered carbonate inhibition. *Journal of Catalysis* **2014,** *316*, 210-218.

79. Marlin, T.E. and Marlin, T., *Process Control: Designing Processes and Control Systems for Dynamic Performance*. 2nd ed.; McGraw-Hill: New York, NY, **2000;** p 1-1017.

80. Di Cosimo, J.I., Díez, V.K., Xu, M., Iglesia, E., and Apesteguía, C.R., Structure and surface and catalytic properties of Mg-Al basic oxides. *Journal of Catalysis* **1998,** *178* (2), 499-510.

81. DeWilde, J.F., Chiang, H., Hickman, D.A., Ho, C.R., and Bhan, A., Kinetics and Mechanism of Ethanol Dehydration on γ-Al2O3: The Critical Role of Dimer Inhibition. *ACS Catalysis* **2013,** *3* (4), 798-807.

82. Larmier, K., Chizallet, C., Cadran, N., Maury, S., Abboud, J., Lamic-Humblot, A.-F., Marceau, E., and Lauron-Pernot, H., Mechanistic Investigation of Isopropanol Conversion on Alumina Catalysts: Location of Active Sites for Alkene/Ether Production. *ACS Catalysis* **2015,** *5* (7), 4423-4437.

83. Larmier, K., Nicolle, A., Chizallet, C., Cadran, N., Maury, S., Lamic-Humblot, A.F., Marceau, E., and Lauron-Pernot, H., Influence of Coadsorbed Water and Alcohol Molecules on Isopropyl Alcohol Dehydration on gamma-Alumina: Multiscale Modeling of Experimental Kinetic Profiles. *ACS Catalysis* **2016,** *6* (3), 1905-1920.

84. Phung, T.K., Lagazzo, A., Crespo, M.A.R., Escribano, V.S., and Busca, G., A study of commercial transition aluminas and of their catalytic activity in the dehydration of ethanol. *Journal of Catalysis* **2014,** *311*, 102-113.

85. Busca, G., Structural, Surface, and Catalytic Properties of Aluminas. In *Advances in Catalysis, Vol 57*, F.C. Jentoft, Ed. **2014;** Vol. 57, pp 319-404.

86. Busca, G., The surface of transitional aluminas: A critical review. *Catalysis Today* **2014,** *226*, 2-13.

87. Lee, J., Jang, E.J., Jeong, H.Y., and Kwak, J.H., Critical role of (100) facets on gamma-Al_2O_3 for ethanol dehydration: Combined efforts of morphology-controlled synthesis and TEM study. *Applied Catalysis a-General* **2018,** *556*, 121-128.

88. Lee, J., Szanyi, J., and Kwak, J.H., Ethanol dehydration on γ-Al_2O_3: Effects of partial pressure and temperature. *Molecular Catalysis* **2017,** *434*, 39-48.

89. Lee, J., Jang, E.J., and Kwak, J.H., Acid-base properties of Al_2O_3: Effects of morphology, crystalline phase, and additives. *Journal of Catalysis* **2017,** *345*, 135-148.

90. Sheng, P.Y., Bowmaker, G.A., and Idriss, H., The Reactions of Ethanol over Au/CeO2. *Applied Catalysis A: General* **2004,** *261* (2), 171-181.

91. Natal-Santiago, M.A. and Dumesic, J.A., Microcalorimetric, FTIR, and DFT studies of the adsorption of methanol, ethanol, and 2,2,2-trifluoroethanol on silica. *Journal of Catalysis* **1998,** *175* (2), 252-268.

92. Hemelsoet, K., Ghysels, A., Mores, D., De Wispelaere, K., Van Speybroeck, V., Weckhuysen, B.M., and Waroquier, M., Experimental and theoretical IR study of methanol and ethanol conversion over H-SAPO-34. *Catalysis Today* **2011,** *177* (1), 12-24.

93. Gao, J. and Teplyakov, A.V., Surface species formed during thermal transformation of ethanol on ZnO powder. *Journal of Catalysis* **2013,** *300*, 163-173.

94. Phung, T.K. and Busca, G., Diethyl ether cracking and ethanol dehydration: Acid catalysis and reaction paths. *Chemical Engineering Journal* **2015,** *272*, 92-101.

95. Hadjiivanov, K., Identification and Characterization of Surface Hydroxyl Groups by Infrared Spectroscopy. In *Advances in Catalysis, Vol 57*, F.C. Jentoft, Ed. **2014;** Vol. 57, pp 99-318.

96. Digne, M., Sautet, P., Raybaud, P., Euzen, P., and Toulhoat, H., Hydroxyl groups on gamma-alumina surfaces: A DFT study. *Journal of Catalysis* **2002,** *211* (1), 1-5.

97. Alexopoulos, K., Lee, M.-S., Liu, Y., Zhi, Y., Liu, Y., Reyniers, M.-F., Marin, G.B., Glezakou, V.-A., Rousseau, R., and Lercher, J.A., Anharmonicity and Confinement in Zeolites: Structure, Spectroscopy, and Adsorption Free Energy of Ethanol in H-ZSM-5. *The Journal of Physical Chemistry C* **2016,** *120* (13), 7172-7182.

98. Kang, M. and Bhan, A., Kinetics and mechanisms of alcohol dehydration pathways on alumina materials. *Catalysis Science & Technology* **2016,** *6* (17), 6667-6678.

99. Roy, S., Mpourmpakis, G., Hong, D.-Y., Vlachos, D.G., Bhan, A., and Gorte, R.J., Mechanistic Study of Alcohol Dehydration on γ-Al2O3. *ACS Catalysis* **2012,** *2* (9), 1846-1853.

100. Christiansen, M.A., Mpourmpakis, G., and Vlachos, D.G., Density Functional Theory-Computed Mechanisms of Ethylene and Diethyl Ether Formation from Ethanol on γ-Al2O3(100). *ACS Catalysis* **2013,** *3* (9), 1965-1975.

101. Fang, Z., Wang, Y., and Dixon, D.A., Computational Study of Ethanol Conversion on Al_8O_{12} as a Model for γ-Al_2O_3. *The Journal of Physical Chemistry C* **2015,** *119* (41), 23413-23421.

102. Kang, M., DeWilde, J.F., and Bhan, A., Kinetics and Mechanism of Alcohol Dehydration on γ-Al_2O_3: Effects of Carbon Chain Length and Substitution. *ACS Catalysis* **2015,** *5* (2), 602-612.

103. Nobutaka, M., Fabian, M., and Alfons, B., Insight into the Mechanism of the Preferential Oxidation of Carbon Monoxide by Using Isotope-Modulated Excitation IR Spectroscopy. *Chem Cat Chem* **2013,** *5* (8), 2199-2202.

104. Maeda, N., Meemken, F., Hungerbühler, K., and Baiker, A., Selectivity-Controlling Factors in Catalytic Methanol Amination Studied by Isotopically Modulated Excitation IR Spectroscopy. *ACS Catalysis* **2013,** *3* (2), 219-223.

105. Müller, P., Wang, S.-C., Burt, S.P., and Hermans, I., Influence of Metal Doping on the Lewis Acid Catalyzed Production of Butadiene from Ethanol Studied by using Modulated Operando Diffuse Reflectance Infrared Fourier Transform Spectroscopy and Mass Spectrometry. *ChemCatChem* **2017,** *9* (18), 3572-3582.

106. Tsakoumis, N.E., York, A.P.E., Chen, D., and Ronning, M., Catalyst characterisation techniques and reaction cells operating at realistic conditions; towards acquisition of kinetically relevant information. *Catalysis Science & Technology* **2015,** *5* (11), 4859-4883.

107. Savatsky, B.J. and Bell, A.T., Nitric Oxide Reduction by Hydrogen over Rhodium Using Transient Response Techniques. In *Catalysis Under Transient Conditions*, American Chemical Society: **1982;** Vol. 178, pp 105-141.

108. Visconti, C.G., Lietti, L., Manenti, F., Daturi, M., Corbetta, M., Pierucci, S., and Forzatti, P., Spectrokinetic Analysis of the NOx Storage Over a Pt-Ba/Al2O3 Lean NOx Trap Catalyst. *Topics in Catalysis* **2013,** *56* (1-8), 311-316.

109. Thomas, S., Marie, O., Bazin, P., Lietti, L., Visconti, C.G., Corbetta, M., Manenti, F., and Daturi, M., Modelling a reactor cell for operando IR studies: From qualitative to fully quantitative kinetic investigations. *Catalysis Today* **2017,** *283*, 176-184.

Chapter 5. Enhanced ethanol dehydration on γ-Al_2O_3 supported cobalt catalyst

5.1. Introduction

Ethylene is the second largest volume chemical produced in the world [1] with a global production in 2017 of over 150 million metric tons (MMT) [2]; 20% of which is produced in the US [3]; It is used in the production of high-density polyethylene (HDPE, 29%), low-density polyethylene (LDPE, 14%), linear LDPE (LLDPE, 19%), ethylene oxide (15%), vinyls (9%), styrenics (6%), and others (10%) [4]. The main feedstocks for ethylene are ethane (36%), naphtha (43%), and liquefied petroleum gas (LPG, 15%), with small but increasing contributions from coal-to-olefins (CTO) and methanol-to-olefins (MTO) processes [4]. Although production of (bio)ethylene from (bio)ethanol is only about 0.3% of the global capacity [5], it is expected to increase in share as price of oil climbs and bio-based polymers demand increases due to ethanol favorable process advantage of lower energy consumption and greenhouse gas emissions over naphtha, ethane, and LPG feedstocks [6].

In the production of ethylene from ethanol, the reaction has been catalyzed by several types of acidic materials including: 1) phosphoric acid based materials; 2) metal oxides; 3) molecular sieves; and 4) heteropolyacids [7-10]. Among these, γ-Al_2O_3 was one of the first industrial metal oxide catalysts for ethanol dehydration to ethylene due to its relatively low cost, good stability, and high product selectivity and today it is one of the main constituents in some of the commercial catalysts [9, 11]. To carry out the ethanol to ethylene conversion, high temperatures (623-773 K) are usually required for high ethylene yields [7, 8]; however, γ-Al_2O_3 based catalysts have been improved (e.g., for operation at lower temperatures, higher selectivity) by addition of dopants/modifiers or by preparation of mixed metal oxides (e.g., FeO_x/γ-Al_2O_3 [12]; TiO_2/γ-Al_2O_3[13] MgO-Al_2O_3/SiO_2 [7, 8]; SiO_2-Al_2O_3 [14]; La_2O_3/γ-Al_2O_3 [15, 16]). In the past 20 years, there have been significant advances in the understanding of the γ-Al_2O_3 surface structure and their catalytic consequences in the dehydration of alcohols to ethers and olefins, although the catalytic consequences due the presence of additional oxides are not clearly understood [17-33]. For example, it was shown that Lewis acid site (LAS)-Brønsted basic site (BBS) pairs of different strength were required for the conversion of ethanol to ethylene and diethyl ether on Al_2O_3 and MgO-Al_2O_3 mixed oxides [17]. In particular, the conversion of ethanol to ethylene was proposed to occur via a concerted single-step E2 elimination mechanism in samples with high Al_2O_3 content.

Recent DFT calculations on γ-Al_2O_3 model clusters (for dehydrated γ-Al_2O_3 (110)) [22, 34] γ-Al_2O_3 (100) [25], and γ-Al_2O_3 (111) [23] support this E2 mechanistic proposal of ethanol conversion to ethylene on LAS-BBS pair centers likely present in the vicinity of tricoordinated Al sites [22, 23, 25]. These sites are expected to dissociate reactants more easily than tetra- and penta-coordinated Al sites due to their higher acidity [35]. DFT calculations during the dehydration of isopropanol to propylene also found the conversion to be energetically favorable via an E2 mechanism but on Al pentacoordinated sites present on γ-Al_2O_3 (100) facets [26, 27]. The γ-Al_2O_3 (100) facets [24] have been proposed to be more active than (110) and (111), because of (100) facet lower hydration propensity at reaction conditions which favors catalytic activity [26, 27]. A kinetic model based on an E2 mechanism was also found to describe experimental results of ethanol conversion to ethylene on γ-Al_2O_3 [21]. however, kinetic measurements alone could not distinguish between E1 and E2 mechanisms. The E2 mechanism requires the presence of adsorbed ethanol, whereas the E1 mechanism requires the presence of an alkoxide intermediate [17, 27, 30]. The latter mechanism has been also suggested based on ethanol temperature programmed desorption studies [36] and in situ IR under ethanol static conditions on γ-Al_2O_3 [32, 33].

In the conversion of ethanol to diethyl ether, the reaction has been proposed to proceed via an SN2 mechanism between an adsorbed ethanol molecule and an ethoxy species [17, 32], as reported from DFT calculations on pentacoordinated Al sites of γ-Al_2O_3 (100) facet [25]. This SN2 mechanism was also found favorable on γ-Al_2O_3 (111) facet with Al sites covered with ethoxy and OH species [23]. While weaker Lewis acidity than that required for ethylene formation is expected to favor the formation of ether [17, 18, 21], it is probably not the only descriptor for etherification chemistry [24]. The presence of coadsorbed water or ethanol (e.g., to form alcohol-alcohol or alcohol-water dimers, trimers, etc) can also change the nucleophilicity and stability of adsorbed alkoxy species, and in turn affect ether formation [24, 26]. These ethoxy species have also been proposed as intermediate species for ether formation on the basis of IR characterization under ethanol static conditions [32, 33] and kinetic modeling [20, 21]. Isopropanol conversion to di isopropyl ether on γ-Al_2O_3 (111) and (100) facets has also been studied by DFT and found to be more favorable via the SN2 mechanism on pentacoordinated Al on the (100) facet [27]. An interesting finding by these authors was that the same set of active sites, a pentacoordinated Al LAS and a vicinal oxygen basic species, were responsible for olefin and ether formation. Additionally, the number of active sites, which was a function of temperature, hydration, and/or

site poisoning, and the presence and proximity to the Al atom of a vicinal basic oxygen appeared to determine catalytic activity and selectivity [27].

Overall, there have been significant efforts to understand the nature of the active sites and the fundamental aspects that control ethanol conversion and selectivity. In this work, we were particularly interested in developing more active catalysts for dehydration reactions based on modified metal oxides. Our hypothesis was that the addition of acid-basic site pairs by means of co-added transition metals would increase the availability of LAS-BBS pairs and thus the overall catalyst's activity. From a preliminary work on several metal oxides (e.g., SiO_2, Al_2O_3, TiO_2), we discovered that a highly dispersed Co supported on γ-Al_2O_3 resulted in a catalyst that was relatively more active than the original γ-Al_2O_3 support, despite the former's lower Lewis acid site population, which was in contradiction with our original hypothesis and prompted us to elucidate the reasons for the improved activity of the Co-Al_2O_3 catalyst. In this work, we will show by means of ex-situ acidity and basicity characterization, kinetic measurements, and in situ modulation excitation-phase sensitive detection-diffuse reflectance Fourier infrared transform spectroscopy (ME-PSD-DRIFTS) that this highly dispersed Co on γ-Al_2O_3, prepared by the strong electrostatic adsorption (SEA) method, resulted in a catalyst with increased surface area (as a result of opening of occluded pores), and more hydrophobic (reducing water inhibition), which increased the number of active sites that otherwise would have been unavailable for ethanol conversion. We will also show in situ ME-PSD-DRIFTS evidence of terminal and bridging hydroxyls bonded to octahedral and tetrahedral Al and adsorbed ethanol and ethoxide species as possible intermediate species in the conversion of ethanol to diethyl ether and ethylene.

5.2. Experimental section

5.2.1. Catalysts preparation

Cobalt doping of γ-Al_2O_3 was done via the strong electrostatic adsorption (SEA) method [37-39]. The support used was a commercial γ-Al_2O_3 (Sasol, SBa-200). For the doping procedure, the support was subjected to a metal uptake survey across a pH range by immersion in a 100 ppm Co solution of the precursor, hexaamminecobalt(III) chloride (Sigma Aldrich) in water. Prior to addition of the support powder, the solution pH was adjusted by dropwise addition of dilute aqueous hydrochloric acid or ammonium hydroxide 5 N (for pH ≤ 10) and consecutive ammonia

(to pH = 10) and sodium hydroxide 10 N (for pH > 10). The amount of support mixed into the solution was fixed by surface loading (SL), that is, the ratio of support surface to solution volume, at 1000 m^2/L. The slurry was then agitated for 1 h at 140 rpm to ensure contact of the support and solution and that adsorption equilibrium was achieved. The slurry pH at equilibrium was measured after agitation. The Co uptake, or amount of Co adsorbed, was determined from difference of metal concentration measured by ICP-OES (Perkin Elmer Optima 2000 DV) analysis of solution aliquots withdrawn prior to addition of support (initial [Co]), and after agitation and syringe filtration (final [Co]). The Co uptake values were plotted versus equilibrium pH and the pH of peak uptake was used for the scaled-up preparation of final catalysts.

The final SEA prepared catalyst was made by using a larger mass of support powder immersed in a Co precursor solution with limited Co concentration such that adsorption of all Co onto the support will result in a catalyst metal loading of ~0.3 wt%. The initial pH was adjusted to pH ~ 11.5 by addition of concentrated ammonia such that the equilibrium pH will be at peak Co uptake (from the uptake survey provided as Appendix D, and **Figure D.1**). After a contact time of 1 h with agitation, the slurry was filtered, and the solids were recovered, dried at room temperature overnight and then in an oven at 393 K overnight. The concentration of Co in solution was measured using ICP-OES from aliquots withdrawn before addition of support and after equilibrium and the actual loading of Co in the powder was determined by material balance calculations. The dried powder was stored without further treatment (for kinetic tests in fixed bed reactor) or calcined under static air in a muffle furnace with a temperature ramp of 5 K/min from ambient to 623 K and dwell time of 5 h (for surface area, XRD, acidity, basicity, or in situ ME-PSD-DRIFTS). For comparison, a Co (~2%) doped SiO_2 catalyst (SiO_2 Aerosil, Evonik) was also prepared by the SEA method as recently reported [40].

A set of treated γ-Al_2O_3 supports was also prepared for control experiments. The support was immersed in water, without Co precursor, at conditions similar to the corresponding Co-Al_2O_3 catalyst. The solids were recovered by filtration and dried and calcined under the same conditions as the Co catalyst. For comparison, a γ-Al_2O_3 (SBa-200) supported Co catalyst was also made by incipient wetness impregnation (IWI). A calculated amount of hexaamminecobalt(III) chloride to give a catalyst Co loading similar to that in the Co-Al_2O_3 prepared by SEA was dissolved in an amount of water equivalent to the pore volume of the SBa-200. This solution was added dropwise

to the alumina powder. The impregnated support was dried and calcined under the same conditions as the SEA prepared catalyst.

5.2.2. Catalysts characterization

Physical properties. Nitrogen adsorption-desorption isotherms were measured at 77.2 K in an Autosorb-iQ2 analyzer (Quantachrome Instruments). Prior to the physisorption experiment, ~100 mg of calcined catalyst sample was pretreated in vacuum at 573 K (5 K/min) for 5 h. Total surface area, micropore surface area, and mesopore size distribution were determined using the Brunauer-Emmet-Teller (BET), the de-Boer t-plot, and the Barret-Joyner-Halenda (BJH, desorption branch) methods, respectively. Powder X-ray diffraction patterns of calcined samples were collected in a PANalytical Empryrean diffractometer using Cu Kα radiation operating at 45 kV and 40 mA.

Acidity via pyridine-TPD-MS-DRIFTS. Temperature programmed desorption (TPD) studies of adsorbed pyridine were carried out on γ-Al_2O_3 and Co-Al_2O_3 catalysts by in situ diffuse reflectance infrared Fourier transformed spectroscopy (DRIFTS) using a Vertex 70 (Bruker) infrared spectrometer equipped with an MCT detector. Pyridine adsorption was carried out in a Harrick Scientific HVC-DRM-5 high temperature reaction chamber with a detachable dome (HVC-DWM-2) capable of heating the sample to about 773 K under controlled gas atmosphere and with temperature measured at the center of the sample by a thermocouple inserted via the gas outlet line [41]. The reaction chamber was used in combination with Harrick's mirror optics Praying Mantis^{TM} diffuse reflectance accessory (DRP-BR4). Spectra were collected in the 4000-400 cm^{-1} interval with a resolution of 4 cm^{-1} obtained by averaging 64 scans. In a typical experiment, the catalyst sample (45-75 μm) was loaded in the cell and heated in He (UHP, Matheson, 40 NTP cm^3 min^{-1}) to 773 K. Once at this temperature, the gas was switched to O_2 (UHP, Matheson, 40 NTP cm^3 min^{-1}) and the temperature held at 773 K for 1 h. After pretreatment, the gas flow was switched to He and the temperature was lowered to 323 K during which infrared spectra were recorded at every 50 K intervals to be used as baseline for pyridine TPD experiments as described below.

After pretreatment, the catalyst surface was saturated with pyridine at 323 K by injecting 3 μL/h of pyridine (≥ 99.8%, EMD Millipore, P/N: PX2012-7) via a syringe pump in a He carrier gas (40 NTP cm^3/min) as followed by continuous IR spectra measurements. The in situ cell outlet gas was analyzed online through an OmniStar GSD 320 O mass spectrometer (Pfeiffer Vacuum)

at a data acquisition time interval of 1 s. MS calibration was performed by injecting known amounts of pyridine in He. The transfer lines were heated to 433 K to avoid any liquid condensation in the lines. After saturation, the cell was evacuated with a Buchi V-700 vacuum pump for approximately two hours to desorb any physisorbed pyridine from the catalyst surface after which the cell was flushed with He (40 NTP cm^3/min) overnight. After flushing, TPD experiments were carried out by ramping the temperature from 323 to 773 K in He (40 NTP cm^3/min, 10 K/min) and held at the final temperature until complete desorption of pyridine as tracked by m/z = 79 in the MS. Experiments were also performed with SiO_2 sand (45-75 μm, Sigma-Aldrich, P/N 84880) to correct for possible pyridine adsorption in the in situ cell wall. The total (Brønsted+ Lewis) acidity was determined from the amount of pyridine desorbed as tracked by MS, the relative amount of LAS (Lewis acid sites)/BAS (Brønsted acid sites) as obtained from the areas of the in situ DRIFTS peaks at 1449 and 1540 cm^{-1}, respectively, and the ratio of the LAS/BAS integrated molar extinction coefficients of 1.33 [42].

Acidity via NH_3-TPD. Temperature programmed desorption (TPD) studies of adsorbed ammonia (NH_3) were also carried out on the γ-Al_2O_3 and Co-Al_2O_3 catalysts using a Micromeritics Autochem 2910 unit. The catalyst samples (<125 μm, ~70 mg) were pretreated in He (NTP 30 cm^3/min) at 773 K (10 K/min) for 60 min. Upon cooling to 323 K in He, the sample was contacted with pure ammonia (99.99%, Matheson; 15 cm^3/min) for 1 h and flushed with He for 1.5 h to remove weakly adsorbed NH_3. The temperature was then increased to 773 K (10 K/min) in He gas (30 cm^3/min) and held at 773 K for 1.5 h. NH_3 evolution was monitored by MS (OmniStar GSD 320 O, Pfeiffer Vacuum) and quantified by calibration of the MS NH_3 signal (m/z = 17) with NH_3 pulses of known concentration.

Basicity via CO_2-TPD-MS-DRIFTS. The basicity of γ-Al_2O_3 and Co-Al_2O_3 samples was assessed via carbon dioxide temperature programmed desorption (CO_2-TPD) with the same experimental set up and methodology similar to the one described above. The CO_2-TPD-MS-FTIR technique combines conventional CO_2-TPD-MS usually applied for characterization of basic materials with concomitant DRIFTS monitoring of adsorbed CO_2 surface species [43, 44]. Such combination resembles the more common pyridine-TPD-MS-DRIFTS for characterization of catalysts' acid sites [44]. Similar application of CO_2-TPD-MS + FTIR has been previously reported by Di Cosimo

et al. for the characterization of basic sites in Al_2O_3 and $MgAlO_x$ mixed oxides [17, 45]. The surface of the catalyst was saturated by flowing 20% CO_2/He (40 NTP cm^3/min) at 323 K with simultaneous recording of IR spectra. After evacuation and flushing with He, the sample was heated to 773 K (10 K/min) in He flow (40 NTP cm^3/min) to desorb CO_2. MS calibration was performed by injecting known amounts of CO_2.

5.2.3. Catalytic tests

General procedure. Ethanol dehydration measurements were carried out in a downflow fashion in a continuous fixed bed reactor made of 304 SS (1/2" OD, 0.444" ID, 427 mm long, McMaster-Carr, P/N 89895K743). To avoid reaction on the SS reactor walls, an inner quartz tube (8 mm ID x 10 mm OD, 430 mm long, Technical Glass Products) was fitted inside the SS reactor to hold the powdered catalyst samples on a bed of coarse quartz wool (CQ-wool-0.5, Technical Glass Products). The length of the quartz tube was such that once placed inside the SS reactor it could hold O-rings (1.5 mm W x 10 mm ID, McMaster P/N 5233T36) just out of the SS reactor to secure it when the Swagelok fittings were tightened. The reactor was vertically mounted and heated with a temperature controller (GSL-1100X-NT-110-LD, MTI Corp) and high temperature split tube furnace (EQ-OTF1200X-S-H-110V, MTI Corp.) combination. Catalyst samples were sieved to particle sizes in the 45-75 μm range (Mesh # 325 and 200, Hogentogler P/Ns: 1313 and 1310, respectively) and loaded in the quartz tube. A concentric K-type thermocouple (1/16", OMEGA, KMQXL-062G-18) in direct contact with the sample measures the temperature of catalyst packing. Prior to the experiment, the catalysts were pretreated by flowing a gas mixture of 20% O_2 (10.5 NTP cm^3/min) in He (39.5 NTP cm^3/min) at 623 K (1 K/min) for 5 h. Blank runs at typical reaction temperatures in the presence of SiO_2 sand (45-75 μm) confirmed the inertness of the quartz liner. For the reaction studies, ethanol (>99.5%, Sigma-Aldrich, P/N 459844) was injected into the reactor by means of a high-pressure programmable syringe pump (NE-8000X2, New Era Pump Systems) and gastight syringes (Hamilton) via an online ultra-Torr fitting (Swagelok, SS-4-UT-1-2) equipped with a high temperature septum (Restek, P/N 27090). Gases were fed to the reactor by means of calibrated mass flow controllers (Parker, Type 201-FKASVBAA) and a control module (Parker, CM-400). All the transfer lines to the reactor and online gas chromatograph (GC) were heated to 353 K to prevent the liquid condensation. The reactor effluent stream containing

the unreacted reactants and products were sampled and analyzed online with an SRI 8610C GC employing a Rt-Q-BOND PLOT column (30 m x 0.53 mm, 20µm, P/N 19742-6850, RESTEK) and a flame ionization detector (FID). GC signals were quantified by proper calibration standards.

Temperature ramp and steady state measurements. Ethanol dehydration rates were measured in the temperature range of 473-773 K and ambient pressure. For the reaction studies, about 75 mg of catalysts (45-75 µm) were loaded in the quartz tube. The feed mixture usually consisted of 1 kPa of ethanol (120 µL/h) in a He (80 NTP cm^3/min) carrier gas (WHSV ~ 1.26 $(g_{EtOH}/g_{cat})h^{-1}$). Reaction rates were measured at 473, 573, 673 and 773 K after steady state was attained. Steady state operation (conversion and product selectivities) was verified for γ-Al_2O_3 and Co-Al_2O_3 samples for a period of approximately 24 h at 573 K (1 kPa ethanol) to check for any possible catalyst deactivation.

Apparent activation energy and water co-feeding. Catalysts' apparent activation energies for ethylene and diethyl ether formation were calculated at high and low temperature ranges under differential conditions (less than 20% conversion). For the low temperature ranges (433-473 K) the initial reaction rates at each temperature were calculated by varying the space velocities between 1.2 and 2.4 $(g_{EtOH}/g_{cat})h^{-1}$ while keeping the ethanol partial pressure at 1 kPa (He flows ranging from 80-155 NTP cm^3/min; ethanol liquid flows ranging from 120-225 µL/h; catalyst weight of ≈76 mg) and extrapolating the reaction rate to zero residence. For the high temperature range (533-563 K) about 3.5 mg of the catalysts were diluted with 160 mg of SiO_2 sand (45-75 µm) and experiments were conducted by varying the space velocities between 25 and 190 $(g_{EtOH}/g_{cat})h^{-1}$ at constant ethanol partial pressure of 1 kPa (He flow ranging from 320-395 NTP cm^3/min; ethanol liquid flows ranging from 120-800 µL/h). The effect of co-fed water on the product formation rate was studied at 473 K. Liquid ethanol (1-3 kPa, 120-720 µL/h) and deionized HPLC water (0.5-4 kPa, Fisher, P/N W5-4, 20-300 µL/h) were co-fed using two separate pumps and vaporized into a stream of He (80-160 NTP cm^3/h). The initial reaction rates at each partial pressure were calculated by varying the space velocities of ethanol between 1.2 and 7.0 $(g_{EtOH}/g_{cat})h^{-1}$ and extrapolating them to zero residence time.

5.2.4. In situ modulation excitation-phase sensitive detection-diffuse reflectance fourier infrared transform spectroscopy (ME-PSD-DRIFTS)

When characterizing catalysts with in situ FTIR spectroscopy, it is common to encounter spectra that contain baseline shifts, noise, and multiple peaks associated with surface species that are true intermediates, that react slowly or are spectators, and that could accumulate on the surface. Discriminating reactive species and true intermediates from such a mix is a complex task that commonly requires the use of methods to track species temporal changes, for example, as their surface coverage changes with time [46, 47]. Examples of these techniques include: 1) stopped-reactant and jump techniques (e.g., from clean surface to steady state coverage, step change from steady state, etc.) [48-52]. 2) SSITKA coupled with in situ FTIR (that operates at pseudo-steady state chemical potential) [53, 54]; and 3) modulation excitation spectroscopy (MES) techniques (that operate in periodic transient mode around a steady state) [55, 56]. Among these, MES technique such as feed concentration modulation excitation (ME) + phase sensitive detection (PSD) + in situ FTIR spectroscopy is of particular interest. The reason for this is that it allows the sole detection of adsorbed surface species that respond to transient changes in the system while eliminating contributions from spectator and slow reacting species and increasing signal to noise ratio. The method consists of introducing an external periodic perturbation to the catalyst surface, for example, via feed concentration modulation, temperature, or pressure followed by spectra analysis to track likely intermediate species that respond to the perturbation frequency, f(ω=2πf, where ω is the angular frequency). To follow the adsorbed species that respond at the same feed modulation frequency, the infrared spectroscopy response is processed in ways similar to those described for the discrete processing of signals using Fourier transform methods [57, 58]. In the processing of acoustic signals, for example, time-domain signals are processed via Fourier transform (FT) to obtain signals in the frequency domain. After removing signals of undesirable frequencies, a clean signal is obtained by application of an inverse FT (IFT) procedure [59]. For ME-FTIR data, one such method has been described in detail by Baurecht and Fringeli [60] that combines FT and IFT (i.e., PSD approach) by solving:

$$A_k^{\phi_k^{PSD}}(\tilde{\nu}) = \frac{2}{T}\int_o^T A(\tilde{\nu}, t)\sin(k\omega t + \phi_k^{PSD})dt \quad (1)$$

Where $A_k^{\phi_k^{PSD}}(\tilde{\nu})$ is the phase-resolved absorbance spectrum or IFT (phase-domain response) of the periodic time dependent absorbance $A(\tilde{\nu}, t)$ (time-domain response), T is the time length of

one period, ω is the angular modulation frequency, k is a positive integer (where k=1 corresponds to the fundamental frequency, and k > 1 are higher frequency harmonics) [61], and ϕ_k^{PSD} is the demodulation phase angle [56]. For the ME-PSD-IR, the PSD process is usually applied such that Eq. 1 is solved for spectroscopic signals that respond to the same feed modulation frequency, f (for k=1). In general terms, we have implemented a similar PSD procedure by solving $X(\tilde{\nu}, \omega)$, the (complex) continuous FT of the function $x(\tilde{\nu}, t)$:

$$X(\tilde{\nu}, \omega) = \frac{1}{2\pi}\int_{-\infty}^{\infty} x(\tilde{\nu}, t)e^{-i\omega t}dt \quad (2)$$

Where $x(\tilde{\nu}, t)$ can be reconstituted from $X(\tilde{\nu}, \omega)$ by the IFT equation (to the so-called phase domain):

$$x(\tilde{\nu}, t) = \int_{-\infty}^{\infty} X(\tilde{\nu}, \omega)e^{i\omega t}d\omega \quad (3)$$

More specifically, we solved the discrete Fourier transform (DFT) and the inverse DFT (IDFT) as applied to a discrete sequence of time-domain sampled spectra, $x(\tilde{\nu}, r)$, of the continuous variable $x(\tilde{\nu}, t)$ as given by equations 4 and 5 respectively [62]:

$$X(\tilde{\nu}, k) = \frac{1}{N}\sum_{r=0}^{N-1} x(\tilde{\nu}, r)e^{-i(2\pi kr/N)} \quad k = 0, 1, 2, \ldots, (N\text{-}1) \quad (4)$$

$$x(\tilde{\nu}, r) = \sum_{k=0}^{N-1} X(\tilde{\nu}, k)e^{i(2\pi kr/N)} \quad r = 0, 1, 2, \ldots, (N\text{-}1) \quad (5)$$

These equations were solved numerically with a homemade Python (www.python.org) software code for processing of the sampled IR spectra collected during the feed concentration modulation experiments. A schematic representation of the ME-PSD-IR methodology is shown in **Figure 5.1**.

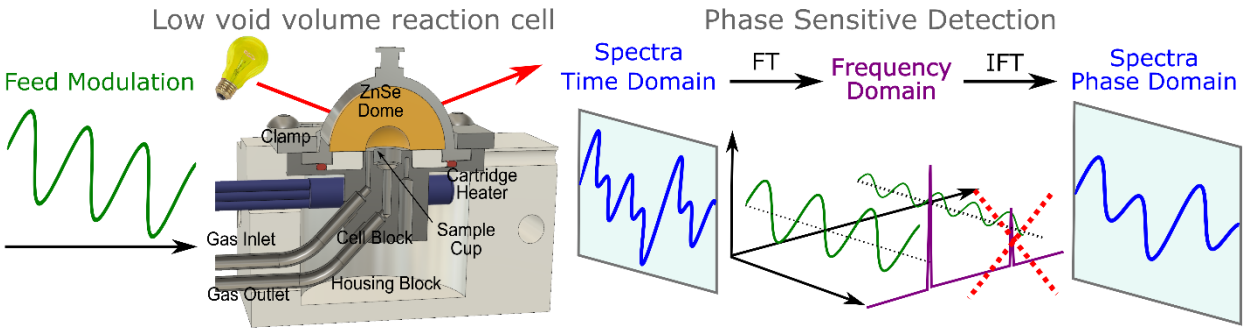

Figure 5.1. General procedure for feed concentration modulation excitation-phase sensitive detection-diffuse reflectance Fourier infrared transform spectroscopy (ME-PSD-DRIFTS). Reproduced from Ref. [62] with permission from the Royal Society of Chemistry.

In this work, the catalysts were characterized by ME-PSD in combination with diffuse reflectance Fourier infrared spectroscopy (ME-PSD-DRIFTS). We have recently reported a detailed and extensive description of the ME-PSD-DRIFTS technique, its principles, implementation, interpretation of results, and limitations [62]. The technique was enabled by a newly designed low void-volume in situ cell (**Figure 5.1**) [63] which permitted rapid exchange of gas feed through the cell within about 1-1.5 s at moderate flow rates (~45 NTP cm^3/min) [41] Such low residence times are similar to those reported in transmission cells and match the sampling time in the infrared spectrometer. The new reaction cell (**Figure 5.1**) resembled Harrick Scientific's HVC reaction cell and was fitted inside Harrick's Praying Mantis™ mirror optics for diffuse reflectance measurements. More details about the reaction cell design(including blueprints), construction, and reaction setup have been recently reported [63]. The reaction setup schematics is shown in **Figure 5.2.**

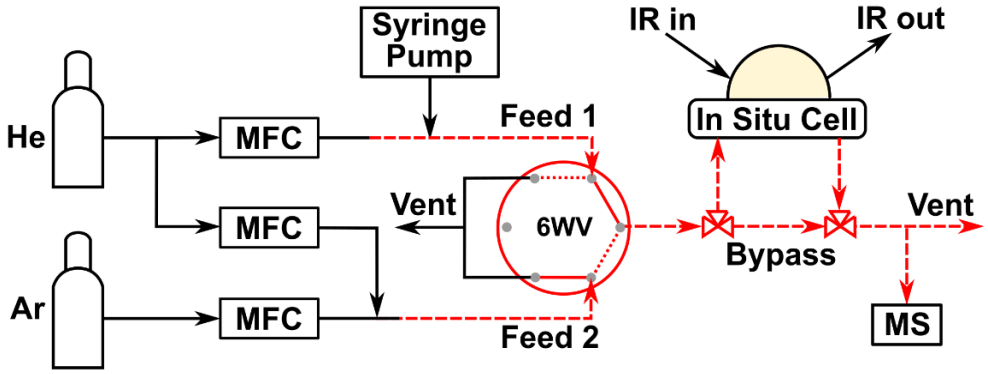

Figure 5.2. Schematics of the in situ DRIFTS reaction setup. MFC =mass flow controller; 6WV = six-way valve (a 4WV could be used instead, but a 6WV is convenient for determining the cell's average residence time via pulse experiments) [41]; IR = infrared; MS = mass spectrometer. Dashed lines and red color indicate that transfer lines are heated to avoid liquid condensation. Adapted from Ref [63] with permission from Royal Society of Chemistry.

Ethanol modulation. In a typical experiment, ~45 mg of (45-75 μm) freshly calcined (623 K, 2 h, static air) catalyst were loaded in the reaction cell and heated to reaction temperature in He (30 NTP cm^3/min)/Ar (10.4 NTP cm^3/min) flow (Feed 2). At the same time, He (40 NTP cm^3/min) and ethanol (60 μL/h of liquid ethanol) were allowed to flow in Feed 1 (~1 kPa ethanol) and vented (**Figure 5.2**, dotted line) before the modulation experiment. All liquid transfer lines were heated to about 353-363 K to avoid condensation. To start the feed concentration modulation, the 6WV

was switched periodically between Feed 2 and Feed 1 every 45 s (via a LabVIEW 2018 VI program routine) to yield a period of 90 s, which was repeated a total of 15 times. The resulting fundamental modulation frequency falls within typical reaction TOFs (f_0 = 1/90 = 0.0111 Hz). DRIFTS spectra are also collected upon starting of the feed modulation approximately every 1 s (16 scans, 4 cm^{-1}) via rapid scan in an FTIR spectrometer (Vector 70, Bruker) equipped with a mercury-cadmium-telluride detector (MCT D316/BP). Spectra are plotted as pseudo-absorbance, log(1/R), where R is the relative reflectance, but they will be noted in all plots as absorbance for simplicity.

Water modulation. A water modulation experiment was also carried out similar to the ethanol modulation described above except that ethanol partial pressure was always 1 kPa, while water was modulated between 0 and 1 kPa. In a typical experiment, Feed 1 was He (40 NTP cm^3/min) and a water/ethanol equimolar mixture (78.5 μL/h of liquid mixture) resulting in a stream with ethanol and water of 1 kPa each and Feed 2 consisted of He (40.4 NTP cm^3/min) and ethanol (60 μL/h of liquid ethanol) yielding a gas flow containing 1 kPa of ethanol. The water concentration modulation started by switching the 6WV periodically between Feed 2 and Feed 1 every 45 s (period of 90 s, feed modulation, f_0, of 0.0111 Hz) for a total of 15 times. IR spectra collection was identical as described for the ethanol modulation experiment.

5.3. Results and discussion

5.3.1. Catalysts characterization

The Co-Al_2O_3 catalyst was prepared by the Strong Electrostatic Adsorption (SEA) method following the techniques described above. This method allowed us to prepare a material that contained highly dispersed Co on γ-Al_2O_3, which is also expected for the low Co content (0.3wt%) in the final Co-Al_2O_3 catalyst. The XRD pattern of the commercial SBa-200 alumina support was characteristic of γ-Al_2O_3 (**Figure 5.3**), whereas that of the Co-Al_2O_3 (SEA) catalyst indicated that it was primarily composed of γ-Al_2O_3, but also contained boehmite (γ-AlO(OH)) and aluminum nitride (AlN). The formation of boehmite and aluminum nitride were the result of the exposure of the alumina support to high pH (~11.5) in the presence of aqueous concentrated ammonia. At this equilibrium pH, which is above the point of zero charge of the support, it appears that the negatively charged alumina surface not only attracts the hexamminecobalt(III) cation, but also the ammonium ion. It is also possible that at the high pH of synthesis, some Al_2O_3 dissolved and

precipitated forming boehmite [64]. Regardless of the mechanism of formation of boehmite and traces of aluminum nitride, which is unclear at present, the main interest of this work was to elucidate the differences in catalytic activity and surface properties between the Co-Al_2O_3 (SEA) and γ-Al_2O_3 as further explored in the following sections.

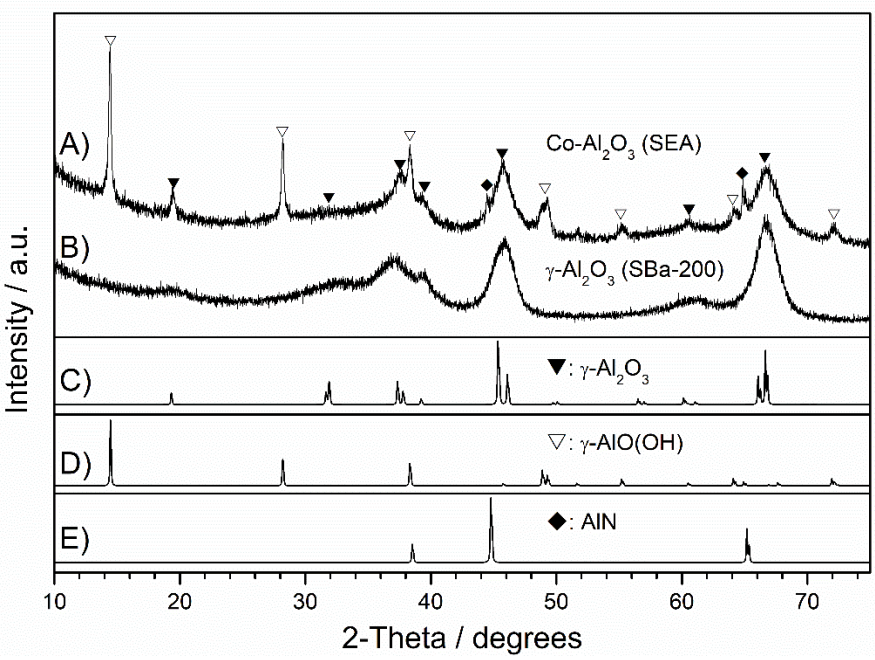

Figure 5.3. X-ray diffraction patterns of: A) calcined (623 K, 5 h, 1 K/min) Co-Al_2O_3 (SEA) and B) γ-Al_2O_3, and of reference materials: C) γ-Al_2O_3 (boehmite-derived, PAN-ICSD reference code: 98-009-9836); D) boehmite (γ-AlO(OH), PAN-ICSD reference code: 98-009-3732); and E) aluminum nitride (AlN, PAN-ICSD reference code: 98-060-8628).

Surface areas, pore volumes, and average pore sizes for the catalysts are presented in **Table 5.1.** The results show that the total specific surface area of the γ-Al_2O_3 (SBa-200) support (189 m^2/g) was smaller than that of the Co-Al_2O_3 catalyst (320 m^2/g). Comparison of the external and micropore surface areas further indicated that the increased in the total surface area was the result of the formation of new micropores. This was a surprising result, but it is consistent with the opening of occluded pores in the bulk of γ-Al_2O_3 crystals. A recent tomography and high-resolution electron microscopic study, for example, demonstrated the presence of a high density of enclosed interconnected pores within the central part of γ-Al_2O_3 particles [65]. Such occluded pores were estimated to contribute to approximately half of the available (although not accessible) surface area in the particle. Our results suggest that the SBa-200 alumina support also contained a

large amount of these occluded pores which opened as a result of the Co doping by the SEA method and subsequent post-treatment. The chemistry of the opening of these pores is unknown at present, but based on the similarity of the textural properties of the γ-Al_2O_3 support treated at similar Co-free SEA conditions (γ-Al_2O_3 (SEA) in **Table 5.1**), it seems that the deposition of the Co precursor, $Co(NH_3)_6Cl_3$, and its decomposition during calcination contributed to the exposure of these previously inaccessible pores to nitrogen during surface area measurements. The average pore diameter of the Co(0.3%)-Al_2O_3 also decreased with respect to the parent γ-Al_2O_3 as a likely result of possible loss of intraparticle and interparticle voids at the high pH of preparation [64]. In what follows, we explore the γ-Al_2O_3 and Co-Al_2O_3 catalysts acidity, basicity, and how these properties affect their reactivity in the dehydration of ethanol in the vapor phase.

Table 5.1. Textural properties of catalysts

Catalyst Sample	Specific surface area (m^2/g)			Pore volume (cm^3/g)	Average pore diameter[c] (nm)
	Total[a]	External[b]	Micropore[b]		
γ-Al_2O_3	189	189	-	0.40	6.6
Co(0.3%)-Al_2O_3 (SEA)	320	175	145	0.26	3.8
γ-Al_2O_3 (SEA)[d]	228	228	-	0.48	6.6

[a] Multipoint BET; [b] t-method; [c] BJH method desorption isotherm; [d] γ-Al_2O_3 treated at similar SEA synthesis conditions of Co(0.3%)-Al_2O_3 (SEA) catalyst, but in absence of Co precursor.

Acidity. Because of their expected activity in ethanol dehydration, the γ-Al_2O_3 and Co-Al_2O_3 were also characterized for acidity using temperature programmed desorption of pyridine, as followed by online mass spectrometry and in situ DRIFTS to determine the total amount of acid sites titrated by pyridine and the proportion of Lewis acid sites (LAS) and Brønsted acid sites (BAS) present in the catalysts. Pyridine adsorption provides a direct estimation of the type of acid sites as its interaction with acid sites leads to distinct bands due to protonated pyridine (i.e., pyridinium ion around 1540-1545 and 1638 cm^{-1}) on BAS, a coordinatively bonded pyridine complex (at around 1449-1452 cm^{-1}) on LAS, or a band common to both (at about 1490 cm^{-1}) [42, 66]. Additionally, a van't Hoff like plot was obtained based on the LAS (the predominant sites on the catalysts) to compare both catalysts' acid strength trends. The results are shown in **Figure 5.4**

Figure 5.4A shows that significant amounts of acid sites are present on the γ-Al_2O_3 (408 μmol pyridine/g_{cat}), however, the acidity amount for the Co-Al_2O_3 as determined by pyridine

adsorption was almost half that of γ-Al_2O_3 despite the low content of Co (0.3 wt%) deposited on the alumina support and larger Co-Al_2O_3 surface area. This is in agreement with XRD results showing the formation of boehmite and aluminum nitride during synthesis in the presence of concentrated NH_4OH as typically reported in the SEA method [37, 40, 67]. The presence of such basic conditions and ammine groups in the Co precursor are likely to affect the acid site distribution in the γ-Al_2O_3 support. As it will be also shown latter by IR, nitrogen moieties remained on the catalyst surface which contributed to a decrease in the acid site count by pyridine and a slight increase in the number of surface basic sites.

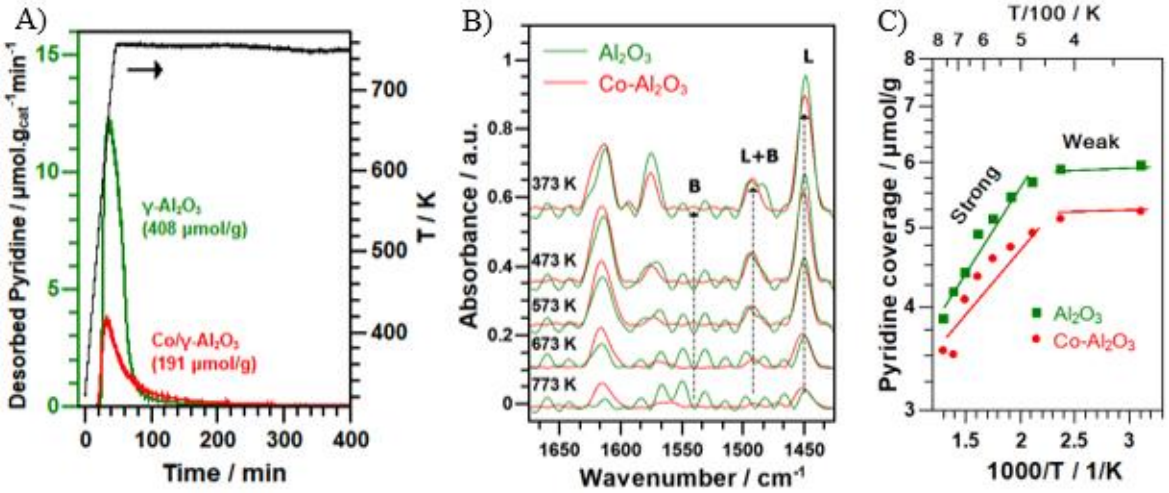

Figure 5.4. Catalysts' acidity characterization by in situ DRIFTS during temperature programmed desorption (TPD) adsorbed of pyridine at 323 K: A) TPD traces as followed by MS (total acidity indicated in parenthesis); B) in situ DRIFTS; C) van't Hoff type plots based on in situ DRIFTS deconvolution of band at 1450 cm^{-1}.

The in situ DRIFTS spectra resulting from the temperature programmed desorption from 373 to 773 K of the catalysts' surface saturated with pyridine is shown in **Figure 5.4B**. From this figure it can be seen that the γ-Al_2O_3 and Co-Al_2O_3 were primarily composed of LAS as shown by the presence of a strong peak at 1449 cm^{-1} and the absence of BAS (no major peak observed around 1540 cm^{-1}). These results are expected for γ-Al_2O_3 based materials, where Al centers serve the role of LAS on which ethanol dehydration can take place on both catalysts. This is in agreement with ethanol and isopropanol conversion on γ-Al_2O_3 based catalysts, where Al and a nearby O species act as strong LAS (sLAS) - weak Brønsted basic site (wBBS) pair centers for alcohol dehydration reactions as evidenced by kinetic experiments [17, 21, 27] and DFT calculations [22-27]. Such

pair sites have been previously proposed for ethanol dehydration where the surface LAS is the Al^{3+} and the weak BBS is the adjacent O^{2-} in the Al^{3+}-O^{2-} pair [17, 68].

Figure 5.4C presents a van't Hoff type plot for γ-Al_2O_3 and Co-Al_2O_3 based on the desorbed amount of pyridine from the band at 1450 cm^{-1} in the in situ DRIFTS spectra and MS results (**Figure 5.4B**). While the pyridine TPD test was not carried out at equilibrium and isosteric conditions, it can provide information on the relative strengths of catalyst sites upon desorption and heat of adsorption after assumption of a pseudo equilibrium [69-71]. We have not attempted quantification from this van't Hoff plot because of the large differences in surface coverages, rather the main interest resided in the qualitative comparison of the slope of the plots (related to the heat of adsorption) to infer possible changes in the strength of the catalyst acid sites. In general, it appears that the LAS present in the γ-Al_2O_3 and Co-Al_2O_3 catalysts had a similar acid strength distribution, which would be expected because of the use of the same support. This suggests that the surface changes on the Co-Al_2O_3 catalyst only affected the density of the acid sites, but not their strength. Based on pyridine adsorption, it also seems that some sites adsorbed pyridine weakly up to about 473 K, whereas other sites adsorbed pyridine more strongly above this temperature. Since ethanol conversion to diethyl ether has been proposed to occur on sites that are of intermediate strength, there does not seem to be major differences in acid site strength on both these catalysts that would justify any major changes to conversion or product selectivity. However, NH_3-TPD characterization (Appendix D, Figure D.2) indicated that the number of acid sites was higher in Co-Al_2O_3 (500 NH_3 μmol/g_{cat}) than in γ-Al_2O_3 (395 NH_3 μmol/g_{cat}). This suggested the presence of Lewis acidity in the Co-Al_2O_3 micropores resulting from the opening of occluded pores that were too small for pyridine titration (kinetic diameter ~5.3-5.9 Å) [72], but large enough for ammonia adsorption (kinetic diameter ~2.6-3.3 Å) [73], some of which are likely to be accessible to ethanol (kinetic diameter ~4.5 Å) [72] adsorption and reaction.

Basicity. A quantitative measure of basic sites density and strength was also obtained by TPD and in situ infrared spectroscopy measurements of preadsorbed CO_2. **Figure 5.5** shows the total basicity of γ-Al_2O_3 and Co-γ-Al_2O_3 catalysts as determined from the amount of CO_2 desorbed as a function of sample temperature. The resulting values show that the presence of surface Co species increases the basicity of the catalyst (98 μmol CO_2/g_{cat}) by about 10% with respect to the bare γ-Al_2O_3 support (89 μmol CO_2/g_{cat}).

Figure 5.5B shows the in situ FTIR spectra of γ-Al_2O_3 and Co-γ-Al_2O_3 as a function of temperature during desorption of CO_2. The spectra presented three major peaks for both catalysts centered around 1230, 1430, and 1660 cm^{-1} which are characteristic of bicarbonate species adsorbed on surface hydroxyl groups. The peaks at around 1230 and 1660 cm^{-1} were due to C-OH bending and O-C-O asymmetric stretching modes, respectively [17]. **Figure 5.5C** also shows van't Hoff type plots obtained from CO_2 desorption as tracked by the 1660 cm^{-1} band. Similar to the LAS results, the plot shows the presence of basic sites of similar strengths on both samples, weak (< 398 K) and stronger sites (> 398 K).

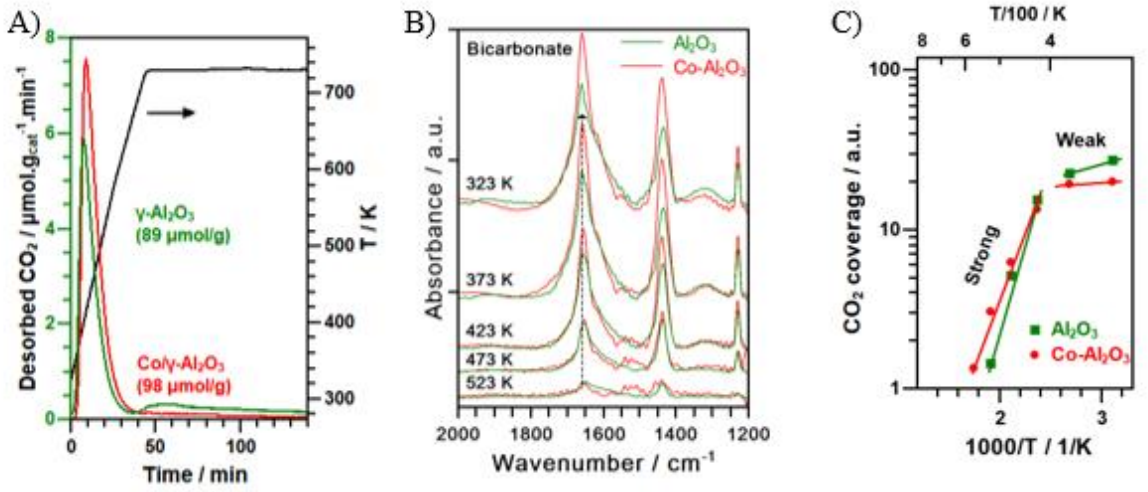

Figure 5.5. Catalysts' basicity characterization by in situ DRIFTS during temperature programmed desorption (TPD) adsorbed of CO_2 at 323 K: A) TPD traces as followed by MS; B) in situ DRIFTS; C) van't Hoff-like plot based on in situ DRIFTS deconvolution of band at 1660 cm^{-1}.

In summary, TPD of adsorbed pyridine and CO_2 indicated that the Co-Al_2O_3 catalyst possessed about half the number of Lewis acid sites (accessible via pyridine adsorption) as those in the original γ-Al_2O_3 support likely because of surface chemical modifications during Co deposition by the SEA synthesis method, which required the use of NH_4OH to adjust the synthesis solution to high pH and a $[Co(NH_3)_6]Cl_3$ precursor. The deposition of Co ammine complexes and their subsequent decomposition led to an increase of over 70% in the specific surface area because of opening of occluded micropores in the γ-Al_2O_3 support. Acid sites titration with ammonia, which possesses a smaller kinetic diameter than pyridine (and ethanol), revealed that the total acidity on the Co-Al_2O_3 was higher than that on the parent γ-Al_2O_3 support as a result of additional

micropore acidity inaccessible to pyridine. XRD results and the slight increase in surface basicity in the Co-Al_2O_3 sample also indicated that some nitrogen containing moieties remained on the catalyst surface. Such surface changes, however, only affected the density of LAS in the original surface area of the γ-Al_2O_3 support, but not its strength distribution.

5.3.2. Reactivity tests

Table 5.2 shows the catalysts' reactivity during ethanol conversion at increasing reaction temperatures. The results indicate that the main products of reaction on γ-Al_2O_3 and Co-Al_2O_3 are diethyl ether and ethylene, whereas acetaldehyde and C3+ hydrocarbons only formed in trace amounts. This product distribution is expected and typical of alumina based catalysts which form diethyl ether and ethylene preferentially at low and high temperatures, respectively [16, 17, 21, 30-33, 74]. The results of **Table 5.2** and **Figure 5.6** also show that ethanol conversion (on a weight basis) was similar for γ-Al_2O_3 and Co-Al_2O_3. However, a closer look at the data showed that Co-Al_2O_3 achieved ethanol conversion and ethylene selectivity similar to γ-Al_2O_3, but at relatively lower temperatures. **Figure 5.6** also shows that the catalysts' conversion and selectivity were relatively high and steady at a reaction temperature of 573 K over a period of 24 h.

It is worth noticing the lack of selectivity for acetaldehyde on the Co-Al_2O_3 catalyst. This is quite unusual as supported cobalt has been reported for ethanol dehydrogenation to acetaldehyde in absence of water (>523 K) [75] and at steam reforming conditions (water/EtOH=3, >773 K) [76, 77], although at low conversions and/or acetaldehyde selectivities below ~30% [78]. These reports, however, only employed catalysts with large Co content (1-22 wt%) and large particle sizes (~3-26 nm), which are significantly different from the Co-Al_2O_3 catalyst, which had only ~0.3 wt% Co and presented isolated or highly dispersed Co(II) ions [40] (Section 3.3). A 2%Co-SiO_2 (SEA) was prepared following the Co-Al_2O_3 SEA synthesis method as recently reported [40]. This catalyst consisted of highly dispersed $Co(II)_1O_4$ sites, but which lacked N moieties (as seen in Co-Al_2O_3) after calcination. The 2%Co-SiO_2 (SEA) catalyst showed lower ethanol conversion than the Co-Al_2O_3 (SEA) but with acetaldehyde selectivity between 30-40% (**Table 5.2**, **Figure D.3**, appendix D), which agreed with previous reports. At present, we do not know the reasons for the lack of Co-Al_2O_3 (SEA) acetaldehyde selectivity and future work will focus on this elucidation. At present, we can only speculate that the first (O *vs* N) and second shell ligand environment (Si

vs Al) of Co probably induce profound changes in its ability to break ethanol C-H bonds required to form acetaldehyde.

Table 5.2. Ethanol conversion (%) and product space-time yield (mmol/g_{cat}/h) at increasing temperatures on several γ-Al_2O_3 based catalysts

T / K	γ-Al_2O_3			0.3%Co-Al_2O_3 (SEA)			γ-Al_2O_3 (SEA treated)			0.3%Co/γ-Al_2O_3 (IWI)			2%Co-SiO_2 (SEA)		
	EtOH	$C_{2=}$	Et_2O (AcH)	EtOH	$C_{2=}$	Et_2O (AcH)	EtOH	$C_{2=}$	Et_2O (AcH)	EtOH	$C_{2=}$	Et_2O (AcH)	EtOH	$C_{2=}$	Et_2O (AcH)
473	23	0.1	5.8 (0.1)	24	0.3	5.9 (0)	0.4	0	0 (0.1)	11	0.1	2 (0.7)	0.1	0	0 (<0.1)
573	97	25	0.1 (0.1)	>99	25	0 (0.1)	2	0.1	0.4 (0.1)	67	7	9 (0.7)	3	0.4	0.1 (0.3)
673	>99	26	0 (0)	>99	25	0 (0)	53	7	5 (1)	99	25	0 (0.3)	51	9	0.2 (4)
773	>99	26	0 (0)	>99	26	0 (0.1)	95	22	0.3 (1)	>99	25	0 (0.3)	96	12	0.1 (11)

Reaction conditions: total pressure = 101.3 kPa, ethanol partial pressure = 1 kPa, ethanol liquid flow rate = 120 μL/h, He carrier flow = 80 NTP cm^3 min^{-1}, catalyst weight ≈ 76 mg. T = reaction temperature, SEA = strong electrostatic adsorption synthesis method, IWI = incipient wetness impregnation synthesis method, EtOH = ethanol, $C_{2=}$ = ethylene, Et_2O = diethyl ether, AcH = acetaldehyde. Trace amounts of C3+ hydrocarbons were usually observed at the highest temperatures.

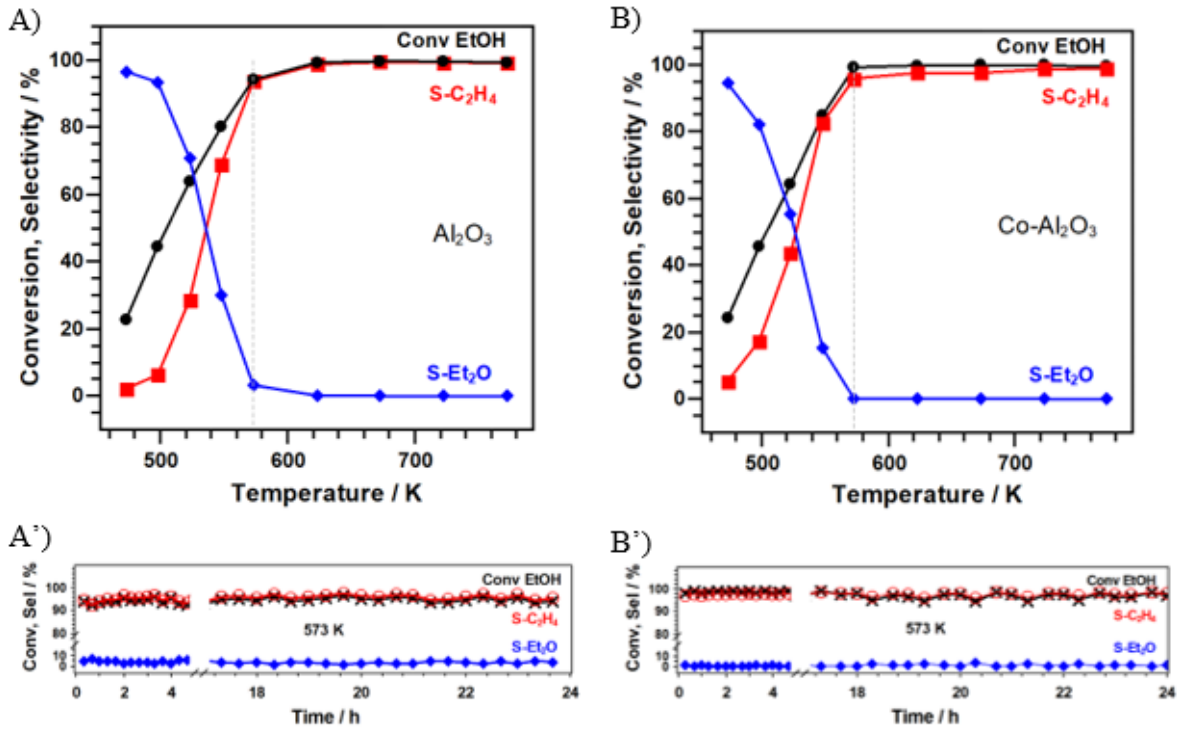

Figure 5.6. Catalytic activity during ethanol dehydration at different temperatures: A) γ-Al_2O_3 and B) Co-Al_2O_3; A') and B') steady state activity of γ-Al_2O_3 and Co-Al_2O_3 at 573 K, respectively. Conv = ethanol conversion; Sel or S = product selectivity; EtOH = ethanol; C_2H_4 = ethylene; Et_2O = diethyl ether. Reaction conditions: He carrier flow = 80 NTP cm^3 min^{-1}; EtOH liquid flow = 120 μL h^{-1}; catalyst weight ≈ 76 mg. Total pressure = 101.3 kPa, EtOH partial pressure ≈ 1 kPa.

We had originally hypothesized that introduction of Co would increase the number of LAS and therefore result in higher activity since LAS present in LAS-BBS pair sites are required for ethanol dehydration reactions [17]. However, the number of LAS present in the Co-Al_2O_3, as determined by pyridine adsorption, was only about half that of the γ-Al_2O_3 support (191 vs 408 μmol/g_{cat}) and the number of BBS increased only moderately (98 vs 89 μmol/g_{cat}). If the ethanol conversion rate is normalized by the total number of acid sites, assuming that all of the acid sites are available and active for reaction, then the Co-Al_2O_3 catalyst will have at least twice the activity of the γ-Al_2O_3. This is quite unexpected, unless the incorporation of Co in the Al_2O_3 support modified the acid sites strength significantly so that their activity also increased accordingly. **Figure 5.4C**, however, showed that acidity strength distribution remained fairly similar. One possible explanation for Co-Al_2O_3 improved activity is the presence of additional LAS in micropores smaller than pyridine size (kinetic diameter ~5.3-5.9 Å). Determination of acid sites

with ammonia support this assertion since the total NH_3 acidity for Co-Al_2O_3 (~500 NH_3 μmol/g_{cat}) was higher than γ-Al_2O_3 (~390 NH_3 μmol/g_{cat}). This is more than double the acidity determined for Co-Al_2O_3 by pyridine adsorption, but it is in line with a similar gain in Co-Al_2O_3 surface area from the opening of occluded pores. Since ammonia kinetic diameter (~2.6-3.3 Å) [73] is smaller than pyridine (~5.3-5.9 Å) [72] N_2 (~3.6 Å) or Ar (~3.4 Å) (usually used for porosity measurements), and even ethanol (~4.5 Å) [72], it is possible that some of these micropore acid sites are also available for ethanol reaction. However, because ethanol kinetic diameter is closer to pyridine's than to ammonia's, it seems that micropore acidity alone cannot explain completely the better activity performance of Co-Al_2O_3. To figure out possible additional reasons for the Co-Al_2O_3 catalyst improved activity, two additional catalysts were prepared and tested: 1) γ-Al_2O_3 support submitted to a Co-free SEA synthesis procedure, to verify if the presence of Co is required; and 2) Co-Al_2O_3 catalyst prepared by incipient wetness impregnation, to check if the SEA synthesis method was needed. The reactivity results during ethanol dehydration reactions for γ-Al_2O_3 (SEA treated) and Co-Al_2O_3 (IWI) are presented in the last columns of **Table 5.2**. For both cases, significantly higher temperatures (> 673 K) were required to achieve the same level of conversion as that obtained by the Co-Al_2O_3 (SEA) catalyst at 573 K. These results indicated that both Co and its incorporation via SEA synthesis method were necessary for achieving higher activity. Up to this point, it seems reasonable to assume that the reason for Co-Al_2O_3 (SEA) higher activity was the result of the opening of occluded pores, whose acidity density compensated the loss of external LAS in γ-Al_2O_3, and not to a change in the strength of LAS. Also, the amount of BBS increased only moderately and neither SEA treatment of the support or Co introduction via DI resulted in improved catalysts.

Up to now, the focus has been on the γ-Al_2O_3 and Co-Al_2O_3 catalyst requirements for ethanol dehydration, namely, the presence of strong LAS-weak BBS pair sites [17, 26, 27]. Therefore, one would expect that increasing the number of strong LAS/ weak BBS pair sites would result in improved catalytic activity. This may be the case for the Co-Al_2O_3 catalyst, but if only a fraction of the micropore acidity is available for ethanol adsorption and reaction (which is reasonable because the kinetic diameter of ethanol is larger than that of NH_3 used to count micropore acidity), then other variables are likely to be at play that have not been considered so far. Additional insights for Co-Al_2O_3 improved catalyst performance may come from prior kinetic studies of alcohols conversion on γ-Al_2O_3. For example, it has been shown that the presence of co-adsorbed water

and/or alcohol in the form of dimers (and possibly trimers) could influence the stability of alkoxy intermediates and thus the formation of ether or olefin product [26]. The presence of such surface adsorbed dimers (e.g., water-water, water-alcohol, alcohol-alcohol) has been shown to be required to explain experimental alcohol reactivity data resulting in kinetic models that are dependent on dimer inhibiting terms [21, 26, 30]. **Figure 5.7** shows a simplified mechanistic model for dehydration of ethanol to ethylene and diethyl ether accounting for possible inhibition by surface adsorbed dimer species. In this mechanism, the rate limiting steps at low to moderate temperatures are assumed to be: 1) dehydration of adsorbed ethanol (or its dissociated form) to ethylene and 2) etherification of two adsorbed ethanol molecules (or an ethanol and a dissociated ethanol) [21, 26, 27] It is worth mentioning that ethylene could also be formed via disproportionation of diethyl ether [33, 79, 80] and this reaction pathway was added to **Figure 5.7** for the sake of completeness. However, we assumed this to be a minor reaction pathway at the studied conditions of relatively low reaction temperatures (<543 K) and low ethanol conversions where ether partial pressure should be small in relation to that of ethanol. For simplicity, we only considered ethanol dehydration pathways to evaluate the possible presence of adsorbed water and alcohol dimers and oligomers. Therefore, the corresponding formation rate equations for ethylene and diethyl ether are given by a generic Langmuir-Hinshelwood with competitive (single) sites model where surface coverages of ether and olefin are assumed to be smaller than those of intermediate species:

$$r_{C2H4} = \frac{\overbrace{k_{C2H4}K_{A1}P_A}^{\text{RDS}}}{[\underbrace{1}_{*} + \underbrace{K_{A1}P_A}_{A^*} + \underbrace{K_{W1}P_W}_{W^*} + \underbrace{K'_{AW}P_AP_W}_{AW^*} + \underbrace{K_{A1}K_{A2}P_A^2}_{AA^*} + \underbrace{K_{W1}K_{W2}P_W^2}_{WW^*}]} \quad (6)$$

$$r_{Et2O} = \frac{\overbrace{k_{Et2O}K_{A1}K_{A2}P_A^2}^{\text{RDS}}}{[\underbrace{1}_{*} + \underbrace{K_{A1}P_A}_{A^*} + \underbrace{K_{W1}P_W}_{W^*} + \underbrace{K'_{AW}P_AP_W}_{AW^*} + \underbrace{K_{A1}K_{A2}P_A^2}_{AA^*} + \underbrace{K_{W1}K_{W2}P_W^2}_{WW^*}]} \quad (7)$$

Where the numerator terms are related to the rate determining step and the denominator terms correspond to the concentration of the indicated adsorbed species (A* and W* for alcohol and water monomer; AW*, AA*, and WW* for alcohol-water, alcohol-alcohol, and water-water dimers, respectively) relative to the concentration of the empty sites (*). Here, * is taken as a macrosite in the form proposed by Larmier et al. [26, 27] including LAS and BBS site pairs. In the denominator expressions, K's are equilibrium constants, $K'_{AW} = K_{AWa} + K_{AWb}$, and k's are forward

rate constants (**Figure 5.7**) [21] From Eqs. 6 and 7, it is expected that different surface concentrations (or coverages) of alcohol and water monomers and dimers will lead to different reaction rates [21] and likely different apparent activation energies [30]. Therefore, it is possible that the differences in activities of γ-Al_2O_3 and Co-Al_2O_3 are also the result of different surface properties leading to different surface concentration of inhibiting species. To gain more insights into the possible reason for Co-Al_2O_3 higher activity, we explore this hypothesis by two different approaches: 1) indirectly, via measurement of apparent activation energies of formation of ethylene and diethyl ether and water inhibition experiments; and 2) directly, via in situ ME-PSD-DRIFTS at reaction conditions that allow observation of surface species that could be directly involved in the reaction mechanism.

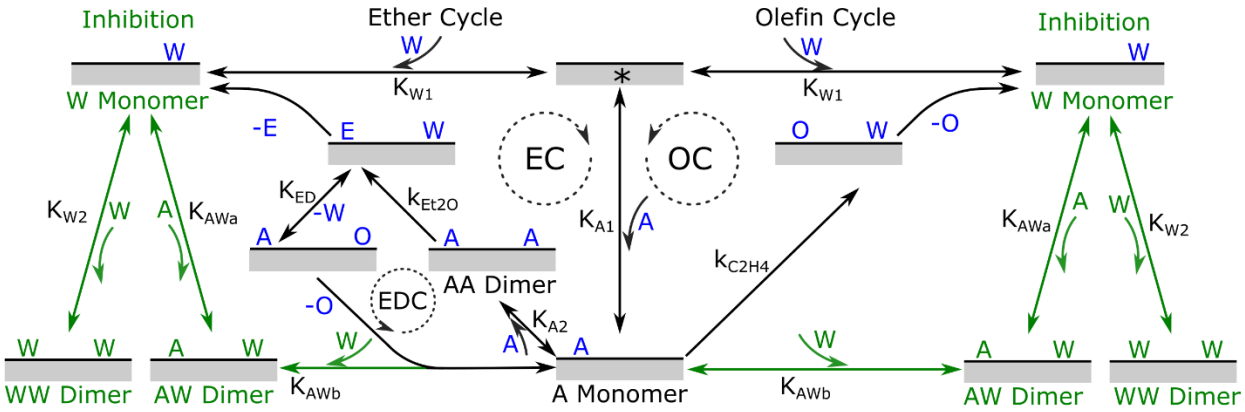

Figure 5.7. Simplified mechanistic pathways for ethanol dehydration on Co-Al_2O_3 and γ-Al_2O_3 catalysts. EC = ether (i.e., diethyl ether) cycle; OC = olefin (i.e., ethylene) cycle; ED = ether disproportionation; EDC = ED cycle; * = active "macrosite"; A = alcohol (i.e., ethanol); AA = alcohol dimer (i.e., ethanol-ethanol dimer); W = water; WW = water-water dimer; AW = alcohol-water dimer (i.e., ethanol-water dimer). Adapted from References [21, 26, 27, 79]

Apparent activation energy. As indicated by Eqs. 6 and 7, it may be possible to vary some surface species coverages on the catalyst by proper selection of reaction conditions, for example, at low temperatures ethanol dimers are expected to populate the surface, whereas monomeric ones would be more favorable at higher temperatures [17, 30]. At these conditions, contributions to the apparent activation energy (E_{App}) could then be correlated to those specific surface species to explain the observed experimental trends. In the case of ethanol dehydration reactions on γ-Al_2O_3, this has been previously reported to explain how surface dimers could affect the apparent activation

energy. For example, Lee et al. [30] found that apparent activation energies for ethylene and diethyl ether formation varied with reaction temperature because of different coverage of surface dimer species. These authors reported apparent activation energies for low (443-459 K) and high (528-543 K) temperatures and for ethanol partial pressures of 0.5 and 2 kPa on γ-Al_2O_3. The reported apparent activation energies at high ($E_{App,HT}$) and low ($E_{App,LT}$) temperatures varied for diethyl ether between 62-84 and 94-96 kJ/mol, respectively, whereas for ethylene they varied between 112-113 and 157-165 kJ/mol, respectively. **Figure 5.8** shows the E_{App} also determined in the present study at low (433-473 K) and high (533-563 K) temperatures (**Figure 5.6**). The obtained $E_{App,HT}$ for diethyl ether (72 kJ/mol) and ethylene (110 kJ/mol) were within the ranges reported by Lee et al.; but the diethyl ether and ethylene $E_{App,LT}$ values were somewhat higher than theirs (124 and 200 kJ/mol vs ~95 and 157-165 kJ/mol). In general, the E_{App} results for diethyl ether and ethylene formation followed Lee et al.'s trends, that is, all E_{App} including γ-Al_2O_3 (**Figure 5.8**, green squares) and Co-γ-Al_2O_3 (**Figure 5.8**, red circles) increased in going from high to low temperatures.

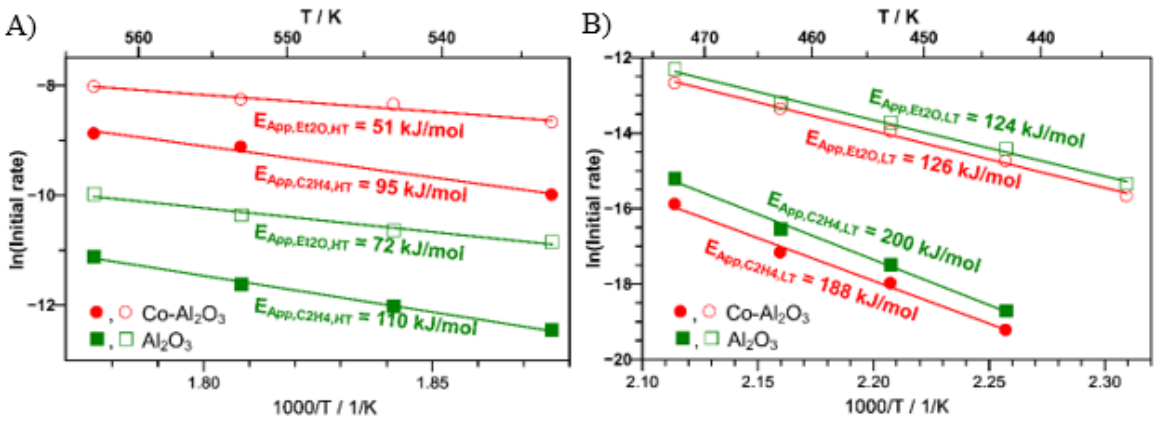

Figure 5.8. Initial diethyl ether (Et_2O, empty symbols) and ethylene (C_2H_4, solid symbols) formation rates (extrapolated to residence time zero, in mol g_{cat}^{-1} s^{-1}) for Co-Al_2O_3 (circles) and γ-Al_2O_3 (squares) during ethanol conversion at: A) high and B) low temperatures. Apparent activation energies (E_{App}) calculated from the slope of best linear were fit to the data as shown in the figure. Reaction conditions: He carrier flow = 80-400 NTP cm^3 min^{-1}; EtOH liquid flow = 120-800 μL h^{-1}; catalyst weight ≈ 76 mg; SV varied between 1.2-190 $(g_{EtOH}/g_{cat})h^{-1}$. Total pressure = 101.3 kPa, EtOH partial pressure ≈ 1 kPa; EtOH conversion range at various SV ≈ 2-20%.

In the low temperature range (< 473 K), the γ-Al_2O_3 and Co-Al_2O_3 catalysts are expected to preferentially form diethyl ether (**Figure 5.6**). At these conditions, the catalyst surface should be covered with ethanol dimer species as expected for the ether conversion pathway (Ether cycle) and as implied from the reported zero reaction rate order dependence on ethanol for ether formation and negative reaction rate order dependence on ethanol for ethylene formation [21, 30]. At the high temperature range (> 528 K), the opposite dependence on ethanol was reported, suggesting that monomer ethanol species are more abundant with increasing temperatures [30]. If the above described surface coverage by these ethanol dimer species (i.e., high AA* at LT and high A* at HT) holds for both γ-Al_2O_3 and Co-Al_2O_3 catalysts, then a preliminary evaluation to the E_{App} contributions from these species can be performed. Then, from Eqs. 6 and 7 it can be shown that:

$$r_{C2H4,LT} = \frac{k_{C2H4}}{K_{A2}P_A} \quad \text{where} \quad E_{App,C2H4,LT} = E_{s,C2H4} + \lambda_{A2} \tag{8}$$

$$r_{C2H4,HT} = k_{C2H4} \quad \text{where} \quad E_{App,C2H4,HT} = E_{s,C2H4} \tag{9}$$

$$r_{Et2O,LT} = k_{Et2O} \quad \text{where} \quad E_{App,Et2O,LT} = E_{s,Et2O} \tag{10}$$

$$r_{Et2O,HT} = k_{Et2O}K_{A2}P_A \quad \text{where} \quad E_{App,Et2O,HT} = E_{s,Et2O}\text{-}\lambda_{A2} \tag{11}$$

Here, *k* is the reaction rate constant for the given surface elementary step, assumed to follow the Arrhenius equation, *K* is the adsorption equilibrium constant, which decreases with temperature by the factor $e^{\lambda/RT}$, E_{App} is the apparent activation energy, E_s is the activation energy for the given surface elementary step, and λ is the heat of chemisorption, which is taken to be independent of temperature [81]. Additionally, both E_s and λ will normally have positive values [81]. A quick inspection of Eqs. 8 and 11 for γ-Al_2O_3 and for Co-Al_2O_3 using the experimental E_{App} obtained in **Figure 5.8** shows that the equalities do not hold. For example, in the case of γ-Al_2O_3: $E_{App,C2H4,LT}(200) > E_{s,C2H4}(110) + \lambda_{A2}(52)$, and for Co-$Al_2O_3$: $E_{App,C2H4,LT}(188) > E_{s,C2H4}(95) + \lambda_{A2}(77)$. These results show that smaller differences in the equality of Eq. 8 are observed for the Co-Al_2O_3 catalyst than for γ-Al_2O_3, suggesting that at least, at low temperatures, additional adsorbed surface species that affect the formation of ethylene (i.e., in the denominator of Eqs. 6 and 7) need to be considered for γ-Al_2O_3. This has been shown to be the case for γ-Al_2O_3 in the dehydration of ethanol at a temperature of 488 K [21] and of isopropanol at 473 K [26],

where, in addition to alcohol-alcohol dimers, alcohol-water and water-water dimers were taken into account to adequately explain the reactivity data. As informed by these results, we explore next the possible inhibition by co-fed water during ethanol conversion at 473 K.

Water co-feeding. The effect of water on the dehydration of alcohols has been investigated by several authors [19, 21, 26, 82]. As shown in **Figure 5.7**, one of the main consequences of addition of water is the inhibition of ether and olefin formation rates as a result of alcohol competitive adsorption for active sites [28]. DeWilde et al. postulated, for example, that the formation of alcohol-water and water-water dimers can inhibit significantly ethanol dehydration [21]. These authors also proposed that at low temperatures formation of alcohol/water or water trimers is required to explain 1-propanol dehydration experimental data [19]. Similarly, Larmier et al. also developed a multiscale model for isopropanol dehydration on γ-Al_2O_3 that required the presence of water-isopropanol and water-water dimers which could affect ether and olefin formation rates [26]. Clearly, the presence of water can have a significant impact in catalyst operation, in particular, at low temperatures [20]. In what interests us here and as shown in the previous paragraph, catalysts' surface species during ethanol conversion at low temperatures will likely involve the presence of alcohol/water and water dimers and/or trimers, whose coverage may differ for the γ-Al_2O_3 and Co-Al_2O_3 catalysts studied in this work. To evaluate the possible presence of water dimers and trimers, water co-feeding experiments (0.5-4 kPa) were carried out at 473 K on γ-Al_2O_3 and for Co-Al_2O_3 at two different ethanol partial pressures (1 and 3 kPa) as shown in **Figure 5.9**.

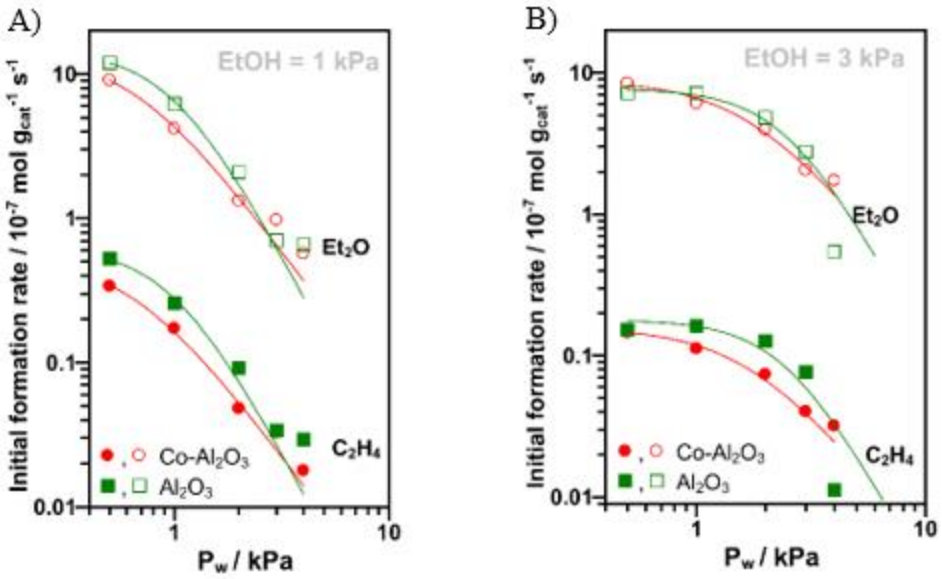

Figure 5.9. Initial diethyl ether (Et_2O, empty symbols) and ethylene (C_2H_4, solid symbols) formation rates (extrapolated to residence time zero, in mol g_{cat}^{-1} s^{-1}) for γ-Al_2O_3 (squares) and Co-Al_2O_3 (circles) during ethanol dehydration at: A) low (1 kPa) and B) high (3 KPa) co-fed water partial pressures. Lines are the results to the best fit of an equation of the form: $r_{i,j} = \alpha_{i,j}/(\beta_{i,j} + \gamma P_W + \delta P_w^2 + \varepsilon P_w^3)$. γ, δ, and ε for γ-Al_2O_3 and Co-Al_2O_3 were (0, 0.68, 0.63) and (0, 3.4, 0), respectively. Reaction conditions: He carrier flow = 80-160 NTP cm^3 min^{-1}; EtOH liquid flow = 120-720 μL h^{-1}; water liquid flow = 20-300 μL h^{-1}; catalyst weight ≈ 76 mg; total SV varied between 1.2 and 7.0 $(g_{EtOH}/g_{cat})h^{-1}$. Total pressure = 101.3 kPa, temperature = 473 K. EtOH conversion range before extrapolation to residence time zero ≈ 1-10%.

As expected, **Figure 5.9** shows that both diethyl ether and ethylene formation rates are inhibited by the presence of co-fed water and that the inhibition is more pronounced at lower ethanol partial pressures. As a first approach to understand these trends, we have fitted the experimental data in **Figure 5.9** to Eqs. 6 and 7. For simplicity, we assumed that ethanol partial pressure did not change significantly (as expected from the relatively low to moderate conversion during these tests), that the surface is completely covered with adsorbed species (at the low temperature of reaction studied) [30], and that trimers are also likely present (as previously proposed for alcohol dehydration reactions at low temperatures) [19]. With these assumptions, the following simplified equations were obtained:

$$r_{C2H4} = \frac{\alpha}{[\beta + \gamma P_W + \delta P_W^2 + \varepsilon P_W^3]} \qquad (12)$$

$$r_{Et2O} = \frac{\alpha'}{[\beta + \gamma P_W + \delta P_W^2 + \varepsilon P_W^3]} \quad (13)$$

Where α ($k_{C2H4}K_{A1}P_A$) and β ($K_{A1}P_A + K_{A1}K_{A2}P_A^2$) and α′ ($k_{Et2O}K_{A1}K_{A2}P_A^2$) are adjustable parameters dependent on ethanol partial pressure (assumed to be fairly constant at the current conditions), and γ ($K_{W1} + K'_{AW}P_A$+ any other term with first order dependence on water partial pressure), δ ($K_{W1}K_{W2}$+ any other term with second order dependence on water partial pressure), and ε ($K_{W1}K_{W2}K_{W3}$) are common parameters to both ethylene and diethyl ether formation rates and which are related to the adsorption equilibrium constants of the various surface species in the denominator of Eqs. 6 and 7. Therefore, the fitted values for γ, δ, and ε could provide preliminary information about the possible presence of adsorbed water species on the studied catalysts. The most salient findings for the best fitted equation were: γ-Al_2O_3 ($\gamma = 0$, $\delta = 0.677$, and $\varepsilon = 0.633$) and Co-Al_2O_3 ($\gamma = 0$, $\delta = 3.40$, and $\varepsilon = 0$), whose corresponding fitted rate data are also shown as solid lines in **Figure 5.9**. Despite the simplicity of the model, it fits the experimental data reasonably well. The results suggest that on γ-Al_2O_3, water is more propense to inhibit the catalyst by forming dimers and trimers in comparison with Co-Al_2O_3 for which only dimers seem to be the most common species. The absence of water trimers on the Co-Al_2O_3 catalyst also seems to indicate that the catalyst surface may be somewhat more hydrophobic than that of the parent γ-Al_2O_3 support because of the Co deposition via the SEA synthesis method. To further explore these observations, in situ DRIFTS results at reaction conditions as coupled with the ME-PSD methodology are described next.

5.3.3. In situ ME-PSD-DRIFTS during ethanol dehydration

Co-Al_2O_3 at 473 K. As mentioned above, the ME-PSD-DRIFTS methodology allows the discrimination of only surface species that respond to periodic perturbations in the gas feed concentration, reaction temperature, or pressure, while eliminating contributions from spectator species. In this work, we have introduced a periodic modulation in the feed concentration by switching between two identical feed (**Figure 5.2**) flow rates (~40 NTP cm^3/min), but with different ethanol concentration. Feed 1 consisted of 1 kPa of ethanol in He (1/100 v/v) and Feed 2 was an inert gas mixture of Ar/He (26/75 v/v). These two feeds were switched in a 6-way valve every 45 s to yield a period of 90 s and a feed modulation of 1/90 = 0.0111 Hz, resulting in a periodic change of the ethanol concentration in the feed around a value close to 0.5 kPa. A feed

modulation of 0.0111 Hz was within the same magnitude of typical TOFs for ethanol dehydration at moderate temperatures.

Figure 5.10 shows the time-domain spectra during the first periodic cycle (0-45 s: He/EtOH(1 kPa) and 45-90 s: Ar/He) of ethanol dehydration on Co-Al_2O_3 at 473 K. The peaks identified in this figure correspond to some of those that respond to the feed modulation (e.g., 3726, 3479, 3235, 2973, 2886, 1388, 1131, and 1053 cm^{-1}) and some that do not (3321, 3125, 2074, and 1955 cm^{-1}). The latter peaks correspond to features that evolve after calcination of the Co-Al_2O_3 prepared via SEA method and can be assigned to remnants of the decomposition of the Co precursor, $[Co(NH_3)_6]Cl_3$. For example, the strong peaks at 3321 and 3125 cm^{-1} can be assigned to amine's NH stretch modes [83-85], whereas the peaks at 2074 and 1955 cm^{-1} are likely the result of NN stretching of Co azido [86-88] and/or nitride [89] moieties. The presence of these compounds is consistent with the observed traces of aluminum nitride in the XRD patterns of Co-Al_2O_3 (SEA) and with the slight increase in the basicity of Co-Al_2O_3 with respect to γ-Al_2O_3 (**Figure 5.5**) and the possible change in catalyst surface hydrophobicity [90]. Additionally, the Co is likely to be present as Co(II) as evidenced by the evolution of IR bands in the 2600-3000 cm^{-1} during catalyst exposure to CO at liquid nitrogen temperature, which are ascribed to the formation of carbonyl complexes with Co(II) ions (Appendix D, Section D.2. and **Figure D.5**). Comparison with CO adsorption on single-site Co(II)/SiO_2 material [40], which produces only one band at 2178 cm^{-1} upon CO adsorption at identical conditions, revealed that on the catalyst surface there are at least 3 different types of Co(II) species at 2199, 2169, and at 2160 cm^{-1}. This indicates that, most likely, isolated or highly dispersed Co(II) ions surrounded by framework γ-Al_2O_3 oxygens and nitrogen are present on the Co-Al_2O_3 catalyst. Since the spectroscopic signatures of these sites are slightly different, it is possible that they are in various crystallographically non-equivalent positions of the γ-Al_2O_3 surface.

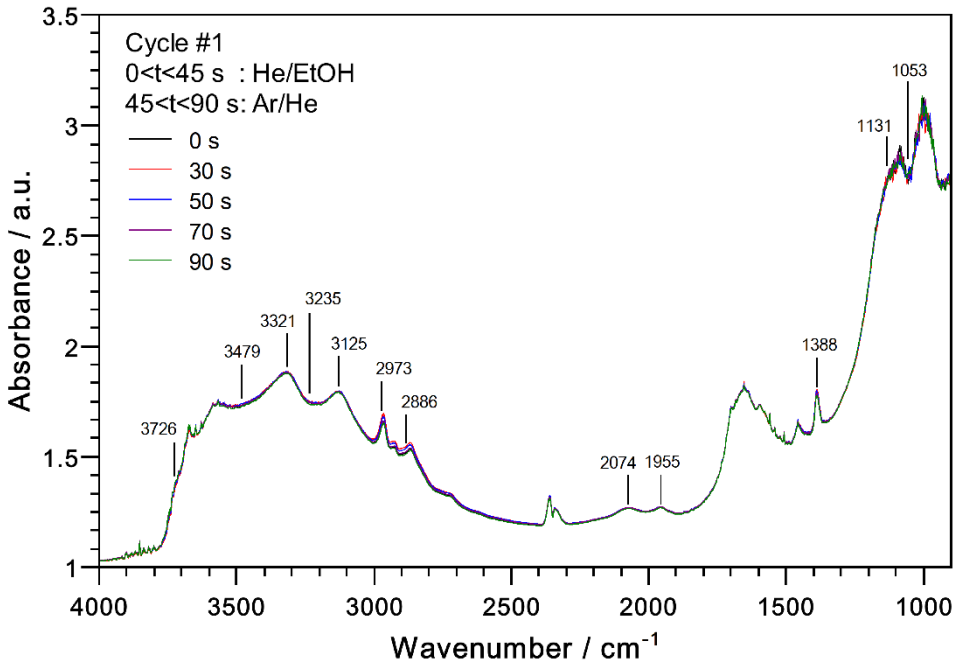

Figure 5.10. In situ time domain DRIFTS spectra during ethanol dehydration on Co-Al_2O_3. Conditions: 473 K, 101.3 kPa, feed modulation from He + Ar → He + EtOH (1 kPa), modulation frequency = 1/90 Hz, total gas flow ~40 NTP cm^3/min, catalyst weight ~45 mg.

Figure 5.11 presents the in situ ME-PSD-DRIFTS during ethanol dehydration reaction on Co-Al_2O_3 catalyst at 473 K. **Figure 5.11A** and **B** show the contour and trace views of the phase domain spectra after IFT of ME-PSD data, which includes only the species that responded to the fundamental modulation frequency (f_0=0.0111 Hz). The contour plot allows a quick visual evaluation of the major changes occurring during ethanol conversion, in this case, over one modulation period of 90 s, as indicated by the y-axis. While the actual modulation waveform is not a sine wave, this was added to the contour plot (**Figure 5.11A**) to quickly identify regions where low and high concentration of ethanol in the feed are expected and which could correlate to changes in the surface species. For example, between 25-65 s, where the concentration of ethanol in the gas feed is high, the surface is mainly covered with ethanol derived species as inferred from the CH stretching at 2800-3000 cm^{-1}. These species seem to be associated to undissociated ethanol and ethoxide species as indicated by the intense signal about 1390 cm^{-1}, among others (**Figure 5.11B**) [32]. Concomitantly, Al hydroxyl groups interacted with these ethanol derived species as shown by the marked blue color around 3750 cm^{-1}, indicating a negative signal with respect to the average value during the periodic feed oscillation. Additionally, adsorbed water and ethanol

bonded to hydroxyl groups were visible at high ethanol gas phase concentration (orange regions around 3450 and 3200 cm^{-1}). The opposite observations can be also made when the concentration of ethanol is low (i.e., 60-90 s) because of the symmetry of the phase-domain spectra around a mid-concentration reference value.

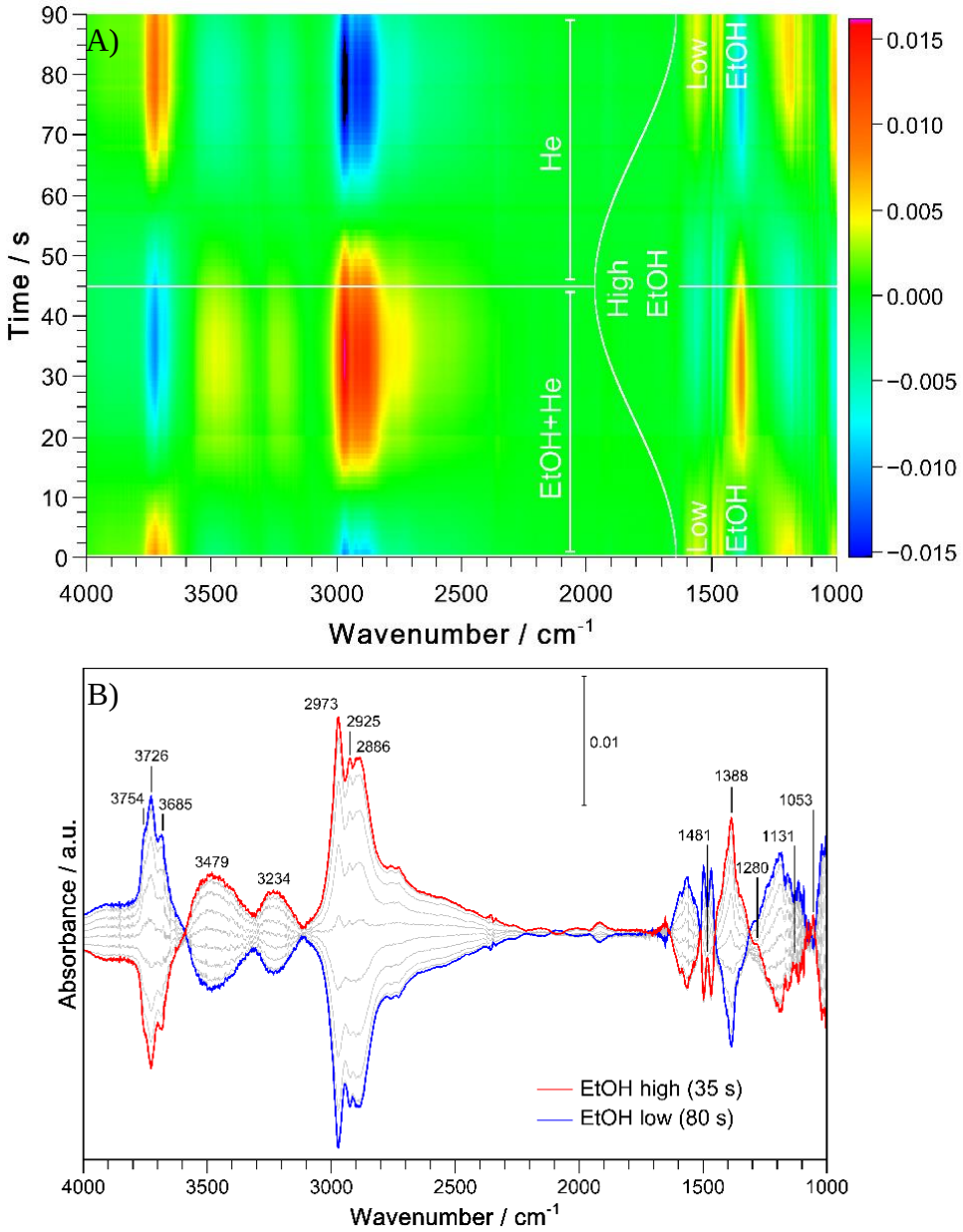

Figure 5.11. In situ ME-PSD-DRIFTS spectra during ethanol conversion on Co-Al_2O_3 at 473 K. A) Phase domain contour plot; B) Phase domain trace plot. Conditions: 473 K, 101.3 kPa, feed modulation from He + Ar → He + EtOH (1 kPa), modulation frequency = 1/90 Hz, total gas flow ~40 NTP cm^3/min, catalyst weight ~45 mg. Phase angle = (time in s/90)×360°. EtOH sine wave feed composition curve added to guide the eye.

Table 5.3. Summary of FTIR assignments

Band / cm^{-1}	Assignment	Species	Refs
3755	HO-μ_1-(Al_{IV}, Al_{VI}) (100)	Al_2O_3 terminal OH	[91-94]
3725	HO-μ_1-Al_V (110)	Al_2O_3 terminal OH	[91-94]
3685	HO-(μ_2, μ_3)-Al_V (110)	Al_2O_3 bridging OH	[91-94]
~3480	HO-μ_3-Al_{VI} (100)	H bonded hydroxyl	[91-94]
3300-3450	-	W_3, A_2W, A_3 trimers	[95, 96]
3250-3450	-	A_3W tetramers	[96]
~3230	HO-μ_1-Al_{IV} (110)	H bonded hydroxyl	[94, 97]
3150-3300	ν(CH)	Ads. Ethanol dimer	[98]
2970	$\nu_{as}(CH_3)$	Ethanol, Ethoxide	[99-102]
2930	$\nu_s(CH_3)$, $\nu_{as}(CH_2)$	Ethanol, Ethoxide	[99-102]
2890	$\nu_s(CH_2)$	Ethanol, Ethoxide	[99-102]
~1480	$\delta_{as}(CH_2)$	Ethanol, Ethoxide	[99, 100]
~1440	$\delta_{as}(CH_3)$	Ethanol, Ethoxide	[33, 99-104]
~1390	$\delta_s(CH_3)$	Ethanol, Ethoxide	[33, 99-104]
~1360	$\delta_s(CH_2)$	Ethoxide	[99]
~1330	$\omega(CH_2)$	Ethoxide	[99]
~1280	δ(COH)	Ethanol	[33, 99, 104]
~1170	ν(CC)	Ethanol	[32, 105]
~1125	ν(CO), ν(CC)	Ethoxide	[103, 104]
~1055	ν(CO)	Ethanol, Ethoxide	[32, 33, 99]
~1035	ν(CO)	Ethoxide	[99]

Symbols: μ_1 = terminal; μ_2 = bridging; μ_3 = triply bridging; Al_{IV} = bonded on tetrahedral Al; Al_V = bonded on penta-coordinated Al; Al_{VI} = bonded on octahedral Al; W_3 = water trimer; A_2W = alcohol-alcohol-water trimer; A_3 = alcohol trimer; A_3W = alcohol-alcohol-alcohol-water tetramer; ν = stretching (ν_s = symmetric; ν_{as} = asymmetric); δ = bending (δ_s = symmetric; δ_{as} = asymmetric); ω = wagging.

More specific observations can be made from individual in situ ME-PSD-DRIFTS traces shown in **Figure 5.11B**. This figure also details temporal changes over the 1000-4000 cm^{-1} frequency range. In contrast with the time domain plot (**Figure 5.10**), the surface species shown in this plot respond to the feed concentration modulation and are, therefore, possible reaction intermediates. At the reaction temperature of the plot (473 K), the main product of reaction is diethyl ether (**Table 5.2**, **Figure 5.6**). The following peaks were observed in **Figure 5.11B**: 2973, 2925, 2886, 1481, 1388, 1280, and 1053 cm^{-1}, assigned to adsorbed ethanol and 2973, 2925, 2886, 1481, 1388, 1131, and 1053 cm^{-1}, assigned to an incipient ethoxide species. This latter species lacks strong characteristic peaks in the region below 1100 cm^{-1} (e.g., 1131 cm^{-1}) and the observed

peak's frequency magnitude was just above noise level (Appendix D, **Table D.1-D.4.**). These results are consistent with the conversion of ethanol to diethyl ether via an SN2 mechanism involving an ethanol and an incipient ethoxide species as supported by DFT calculations on γ-Al_2O_3 (100) [25], (111), [23] and (110) facets, kinetics, and IR characterization under static conditions. While there is no definitive agreement on the assignment of γ-Al_2O_3 hydroxyl groups from IR frequency positions [91-93], the most currently accepted species are listed in **Table 5.3.** Interestingly, terminal (3754 and 3726 cm^{-1}) and bridging (3685 cm^{-1}) hydroxyls bonded to Al_{IV} and Al_V present in γ-Al_2O_3 (100) and (110) facets responded to feed modulation and therefore are likely to be directly involved in ethanol dehydration reactions. In γ-Al_2O_3, (110), (100), and (111) surfaces are the most predominant at approximately 75, 15, and 10% density, respectively [106]. While the presence of (111) facets is not manifested in the IR results, they cannot be ruled out as (110) surfaces have been shown to reconstruct and form nanoscale (111) facets [65]. Additionally, adsorption of ethanol and water to surface Al hydroxyls is also evidenced by distinct bands due to ethanol and water H-bonded to surface hydroxyls in terminal (3224 cm^{-1}) and triply (3479 cm^{-1}) bridging positions on tetrahedral and octahedral Al.

γ-Al_2O_3 at 473 K. **Figure 5.12** presents the in situ ME-PSD-DRIFTS spectra during ethanol dehydration on γ-Al_2O_3 at 473 K. Similar to what was observed on Co-Al_2O_3 catalyst, the γ-Al_2O_3 surface was also covered with adsorbed ethanol (2968, 2925, 2880, 1448, 1388, weak 1280, and very weak 1063 cm^{-1}, see Appendix D, **Table D.1-D.4.**) and incipient ethoxide (2968, 2925, 2880, 1448, 1388, and very weak 1137, 1063, and 1033 cm^{-1}, see Appendix D, **Table D.1-D.4.**) species which interacted with terminal and bridging hydroxyls in Al_{IV} and Al_V (3754, 3741, 3720, and 3680 cm^{-1}). These results also indicate that ethanol dehydration to diethyl ether occurs via an SN2 mechanism on γ-Al_2O_3 in agreement with previous reports [17, 18, 21, 22, 25, 32-34]. One of the major differences on γ-Al_2O_3 (**Figure 5.12A**) with respect to the Co-Al_2O_3 catalyst (**Figure 5.11A**), however, is the significantly higher amount of species adsorbed on the γ-Al_2O_3 surface as evidenced from the deep orange color (broad band) in the 3500-3000 cm^{-1} range at high ethanol concentrations in the feed gas. This result is in line with our expectation that the Co-Al_2O_3 surface is more hydrophobic and less susceptible to ethanol and water inhibition than that of γ-Al_2O_3 (**Figure 5.9**). The presence of terminal (3224 cm^{-1}) and triply (3479 cm^{-1}) bridging positions on Al_{IV} (110) and Al_{VI} (100), respectively, is no longer discernible on γ-Al_2O_3 indicating that ethanol

and water molecules covered the surface to a larger extent than Co-Al_2O_3 by forming dimers, trimers, and possibly tetramers that inhibit ethanol dehydration reactions and whose IR fingerprints fall within the broad 3500-3000 cm^{-1} band. This is also in agreement with prior ethanol, n-propanol, and isopropanol dehydration kinetic and multiscale modeling studies on γ-Al_2O_3 which required the presence of surface adsorbed dimers (e.g., water-water, water-alcohol, alcohol-alcohol) and trimers to satisfactorily explain the experimental kinetic results [19, 21, 26, 30].

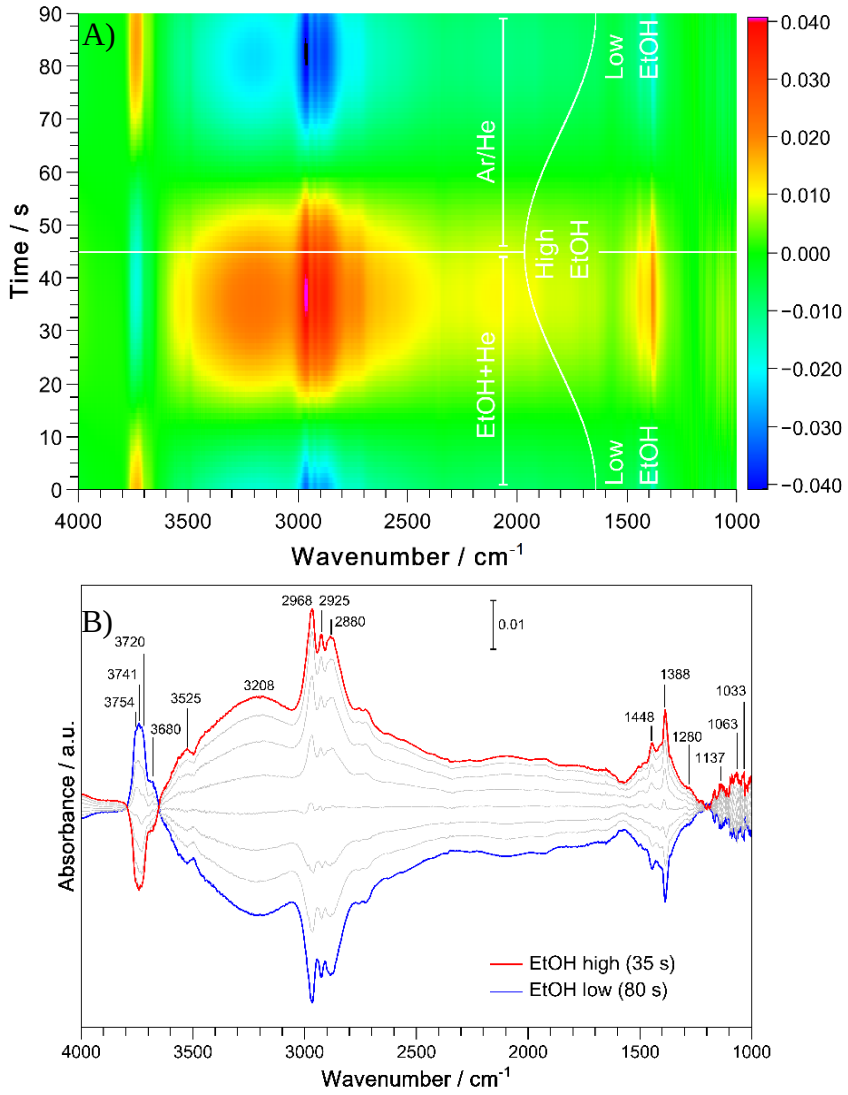

Figure 5.12. In situ ME-PSD-DRIFTS spectra during ethanol conversion on γ-Al_2O_3 at 473 K. A) Phase domain contour plot; B) Phase domain trace plot. Conditions: 473 K, 101.3 kPa, feed modulation from He +Ar → He + EtOH (1 kPa), modulation frequency = 1/90 Hz, total gas flow ~40 NTP cm^3/min, catalyst weight ~45 mg. Phase angle = (time in s/90)×360°. EtOH sine wave feed composition curve added to guide the eye.

Overall, we confirmed by means of in situ ME-PSD-DRIFTS that the Co-Al_2O_3 catalyst possesses surface properties that make it more hydrophobic and resistant to inhibition by water and ethanol than γ-Al_2O_3 at 473 K. As shown above, the highly dispersed Co on alumina prepared by the SEA method contained Co centers that upon calcination resulted in Co containing nitrogen moieties (derived from $Co(NH_3)_6Cl_3$ precursor), which appear to primarily affect the catalyst surface hydrophobicity, but not the energetics of the reaction, in agreement with previous proposals that water function is to block sites, without affecting reaction activation energies [22, 26]. Such surface tuning of hydrophobicity points out to alternative strategies to improving catalyst performance in catalyst formulations that are water inhibited by means of simple post synthesis modifications. These experiments, however, do not allow to determine the precise location of these Co species, but it is hypothesized that they may adsorb at undercoordinated or vacancy sites including those reported by Busca [92] at the (110)/(100) corner terminations of lamellar or fibrous γ-Al_2O_3 crystals and/or defect sites on (110) terminations such as those proposed by Sautet and co-workers [107]. Water modulation experiments during ethanol conversion described in Section 3.4 will show that water adsorption at 473 K occurs on all hydroxyls at the (100) and (110) facets, in support of the above hypothesis.

Despite the apparent loss of half of the total pyridine titrated acid sites in γ-Al_2O_3 by Co deposition, it is possible that some of the sites lost were not kinetically relevant. Bhan and co-workers estimated the active site density for diethyl ether formation to be at best 0.1 sites/nm^2 [21]. which would correspond to roughly 8% the number of sites in the γ-Al_2O_3 studied here. Therefore, if 50% of the original acid sites lost during Co-Al_2O_3 synthesis are not kinetically relevant that would still leave sites available for alcohol reaction. We also speculate that Co species adsorption at or near (110) or (110)/(100) facet terminations opens up neighboring sites active for ethanol dehydration as suggested by the slight increase of the 3685 cm^{-1} band (**Figure 5.11B**) in Co-Al_2O_3 with respect to that in γ-Al_2O_3. This assertion is supported by additional water ME-PSD-DRIFTS experiments described later in Section 3.4 showing a high Co dispersion on (110) and (100) Al_2O_3 facets resulting in similar water coverage for both Co-Al_2O_3 and γ-Al_2O_3 catalysts.

The surface response of Al hydroxyls groups on Co-Al_2O_3 and γ-Al_2O_3 is also in agreement with previous proposals that γ-Al_2O_3 (100) facet is relevant for ethanol dehydration reactions [28, 31] as shown by the response of the 3754 cm^{-1} peak in **Figure 5.11**, however, the concomitant changes to the 3726 and 3685 cm^{-1} peaks also point out to a more complex dynamics in ethanol

dehydration involving other Al hydroxyl types on different facets [32, 92], as evidenced here thanks to in situ ME-PSD-DRIFTS experiments at reaction conditions. These results raise new questions on the role of different hydroxyl sites which could be addressed by additional systematic studies, beyond the scope of the present work, for example, on γ-Al_2O_3 structures with controlled facets [31] combined with kinetic experiments [19, 21] and in situ spectroscopic experiments such as those described here which should provide more clear evidence on the nature of active sites involved in ethanol and alcohol dehydration reactions on γ-Al_2O_3 based materials.

Co-Al_2O_3 and γ-Al_2O_3 at 543 K. For the sake of completeness, we also performed in situ ME-PSD-DRIFTS of ethanol dehydration on Co-Al_2O_3 and γ-Al_2O_3 at a higher temperature (543 K). The obtained ME-PSD-DRIFTS trace views are shown in **Figure 5.13**. Similar to the lower temperature in situ spectroscopic study (**Figure 5.11**), the results on Co-Al_2O_3 at 543 K also showed adsorption of ethanol derived species including ethanol and ethoxide species. Ethanol species are evident from the bands at 2964, 2922, 2864, 1386, 1289, 1176, and 1068 cm^{-1} due to stretching and bending of CH_x, COH, and CO groups as well as 3495 and 3228 cm^{-1} due ethanol H-bonded to surface hydroxyl groups HO-μ_3-Al_{VI} (100) and HO-μ_1-Al_{IV} (110). Incipient ethoxide species are observed from similar bands (2964, 2922, 2864, 1386, 1334, 1140, and 1035 cm^{-1}). Both species are also expected as both diethyl ether and ethylene are formed at this temperature. Water adsorption at smaller coverages is also evident from the bands at 3495 and 3228 cm^{-1}, which are of lower intensity than those observed at 473 K. In terms of adsorption sites, it appears that more terminal OH in Al_{IV} and Al_{VI} (3754 cm^{-1}) are available for reaction at the higher temperature. It is unclear as to why this is the case, as (100) facets are less propense to water adsorption than (110) and (111) facets [65, 106] and should have been available in significant proportions at low and higher temperatures. One possibility, is that as a result of less water and ethanol coverage at higher temperature some new under-coordinated or vacancy sites at, for example, (110)/(100) facets, as proposed by Busca [92], are now available for ethanol conversion at 543 K. These sites could be present at the external surface or the new micropores of the support which are now accessible to ethanol.

A)

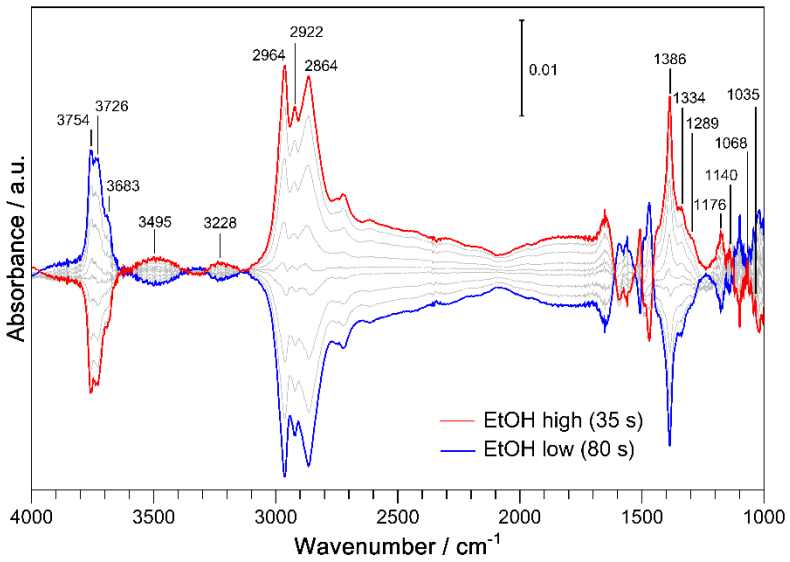

B)

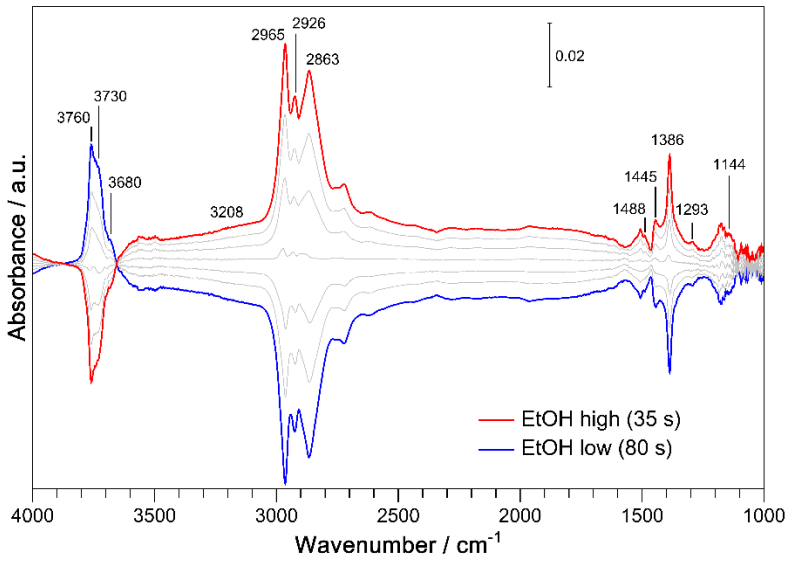

Figure 5.13. In situ ME-PSD-DRIFTS spectra during ethanol conversion at 543 K. Trace plot of: A) Co-Al_2O_3 and B) γ-Al_2O_3. Conditions: 543 K, 101.3 kPa, feed modulation from He + Ar → He + EtOH (1 kPa), modulation frequency = 1/90 Hz, total gas flow ~40 NTP cm^3/min, catalyst weight ~45 mg. Phase angle = (time in s/90)×360°. EtOH sine wave feed composition curve added to guide the eye.

On γ-Al_2O_3, ethanol (2965, 2926, 2863, 1488, 1445, 1386, and 1293 cm^{-1}) and ethoxide (2965, 2926, 2863, 1488, 1445, 1386, and weak 1144 cm^{-1}) species were also observed. However, ethoxide peaks below 1100 cm^{-1} were hardly noticeable as they confounded with the noise level (Appendix D, **Table D.1-D.4.**). As expected, adsorption of ethanol and water on the γ-Al_2O_3 surface is significantly lower at 543 than 473 K as noted from the lower intensity of the 3000-3500 cm^{-1} broad band. In comparison with Co-Al_2O_3's 3495 and 3228 cm^{-1} peaks, the slight sloped band

in the same frequency range that buries these peaks in γ-Al_2O_3, suggests that ethanol and water are still present in amounts moderately higher than on Co-Al_2O_3, but significantly less than what was observed at 473 K. These results are also in agreement with the observed ethylene selectivity dependence on reaction temperature for both catalysts as shown in **Figure 5.6** and **Figure D.4** in Appendix D, where water inhibition becomes less relevant with increasing temperature. Additionally, while diethyl ether is very likely to form via a SN2 mechanism, the results from Figure 5.13 do not permit discrimination between E1 and E2 mechanisms for the formation of ethylene since the former requires ethoxide species and the latter adsorbed ethanol, both of which are detected on both γ-Al_2O_3 and Co-Al_2O_3 catalysts at the studied reaction conditions.

5.3.4. In situ water ME-PSD-DRIFTS during ethanol dehydration

Co-Al_2O_3 and γ-Al_2O_3 at 473 K. To evaluate the effect of co-fed water on catalysts surface species in situ water ME-PSD-DRIFTS during ethanol conversion at 473 K was carried out. In this experiment, ethanol feed concentration was maintained constant at ~1 kPa, while water concentration was varied periodically by switching between two feed streams at 0 and 1 kPa. **Figure 5.14A** shows the results for the Co-Al_2O_3 catalyst. In this figure, features characteristic of Al hydroxyl groups (~3700-3770 cm^{-1}), adsorbed water and ethanol (~3230 and ~3490 cm^{-1}), adsorbed ethanol and ethoxy species (~2870-2960 cm^{-1}), and water (~1640 cm^{-1}) are evident as previously found in ethanol modulation experiments (**Figure 5.11** and **Figure 5.12**). Because of the presence of co-fed water, the C-H stretching region due to ethanol and ethoxy species appeared distorted and difficult to read. However, these C-H stretching bands are more evident near the mid-concentration of water (**Figure 5.14A,** black middle trace) indicating adsorption of ethanol derived species on Al hydroxyls (which are out-of-phase) as discussed above. This figure also shows competitive adsorption of water and ethanol for all Al hydroxyl sites, regardless of the facet or facets where they are located, as evidenced by the synchronized peaks for water (in-phase) and hydroxyls (~3230, ~3490, and ~3700-3770 cm^{-1}) at both high and low concentrations of water (**Figure 5.14A,** red and blue traces). This result is expected and in agreement with the inhibition effect of water on ethanol conversion rates discussed in Section 3.2. When identical experiments were performed on γ-Al_2O_3, similar observations are also made (**Figure 5.14B**). Notably, as presented in **Figure 5.12**, a broader and more intense 3100-3500 cm^{-1} region evolved at high water

contents because of γ-Al_2O_3 lower hydrophobicity than Co-Al_2O_3. Additionally, the identical trends for adsorption of water on all Al hydroxyl sites strongly suggest that Co deposited on all Al_2O_3 surface, and not just on specific sites. As a consequence, it is expected that at the studied conditions (i.e., 473 K, EtOH = 1 kPa, water < 1 kPa), product selectivities should not be affected as a result of water adsorption which is confirmed in **Figure 5.9** and **Figure D.6**, Appendix D.

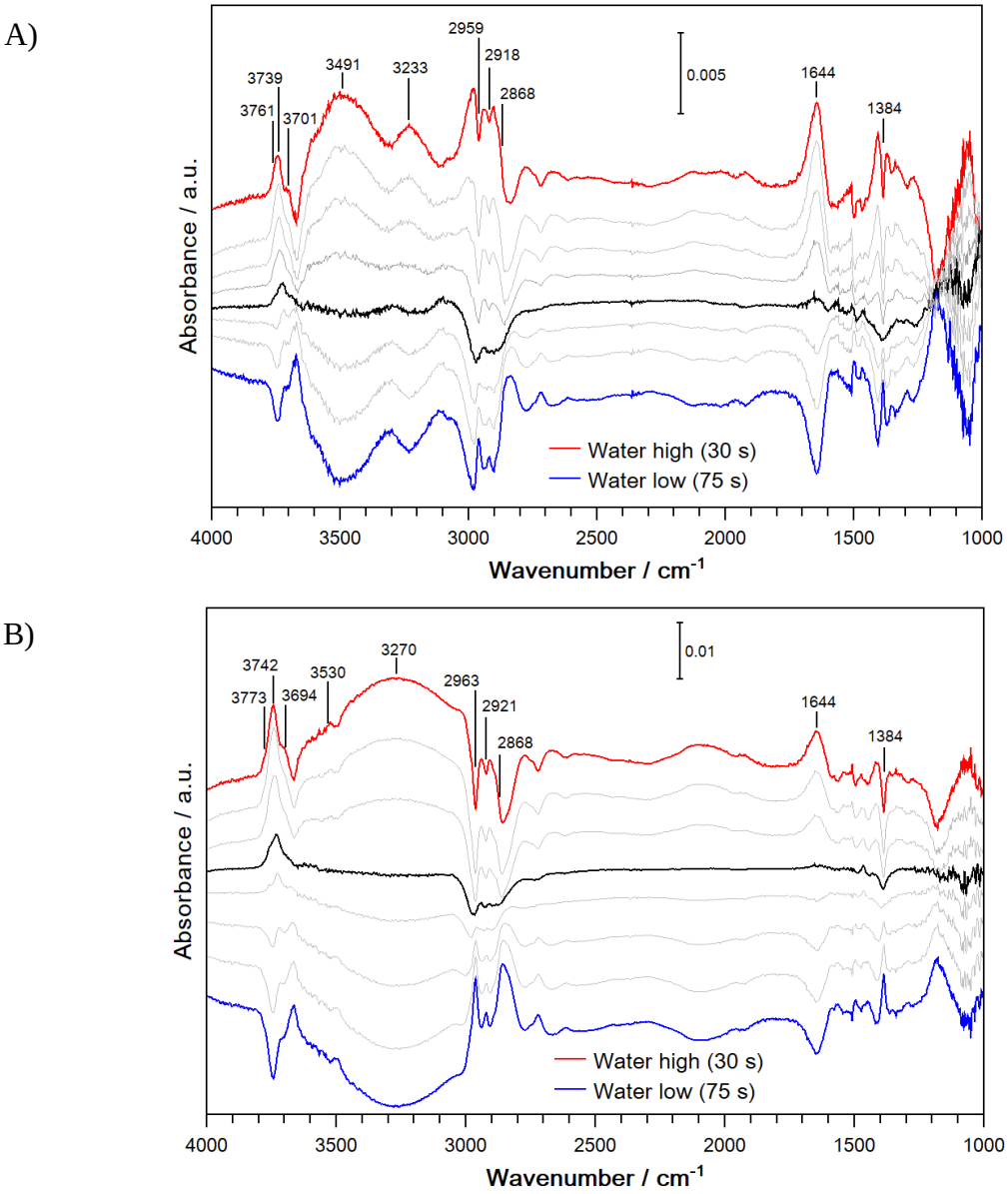

Figure 5.14. In situ water ME-PSD-DRIFTS spectra during ethanol conversion at 473 K. Phase domain plot for: A) Co-Al_2O_3 and B) γ-Al_2O_3. Conditions: 473 K, 101.3 kPa, feed modulation from He + EtOH (1 kPa) → He + EtOH (1 kPa) + H_2O (1 kPa), modulation frequency = 1/90 Hz, total gas flow ~40 NTP cm^3/min, catalyst weight ~45 mg. Phase angle = (time in s/90)×360°. Spectra were displaced vertically to facilitate reading.

Overall, this work presented a commercial γ-Al_2O_3 (SBa-200) catalyst modified by small amounts of cobalt (0.3%) via the strong electrostatic adsorption synthesis method which allowed the deposition of highly dispersed ammine containing Co species. The decomposition of these ammine Co complexes during calcination opened γ-Al_2O_3 occluded pores, resulting in an increased surface area. The remaining surface nitrogen containing Co moieties appeared to modify the catalyst surface such that water inhibition was minimized during ethanol dehydration, and which also possibly led to the creation of new active sites in their vicinity. This resulted in a Co-Al_2O_3 catalyst that could achieve similar ethanol conversion and ethylene selectivity at temperatures lower than the corresponding γ-Al_2O_3 support. The nature and location of these new sites, however, is yet to be determined, but it is likely that they are located in the newly created micropores larger than the kinetic diameter of ethanol as well as near undercoordinated or vacancy sites at the (110)/(100) or (110) terminations such as those recently proposed by Busca [92] and Sautet and co-workers [107]. While the number of acid sites were counted using TPD of adsorbed pyridine or NH_3 at low temperature, the resulting values will not likely correspond to those at reaction conditions (even when matching the starting TPD temperature) because of ethanol and products competition for acid sites. Additionally, as shown in this work, pyridine or NH_3 titration will only provide lower and upper bound limits for acid site count on Co-Al_2O_3 as their kinetic diameters are larger and smaller, respectively, than that of ethanol. An alternative approach, which is currently explored in our group, is the in situ determination of acid sites available for ethanol adsorption and reaction by steady-state isotopic-transient kinetic analysis (SSITKA) during a switch from 12C-labeled ethanol to 13C-labeled ethanol at different reactions conditions, for example, as reported by Davis and co-workers [108, 109].

While the results in the present work are encouraging for ethanol dehydration reactions at low to moderate temperatures, additional testing is required for comparison with commercial catalysts at practical conditions of high temperature and high ethanol conversion, where performance is evaluated, among others, on their deactivation rate and by-products formation (i.e., higher hydrocarbons), in particular, when catalysts become deactivated. Additionally, while the reported Co-Al_2O_3 catalyst was not optimized, it is possible that further post-treatments may recover most of the lost external acidity, thus increasing further its activity in acid-based or other reactions that require Lewis acid sites and some degree of catalyst surface hydrophobicity.

5.4. Conclusions

In this work, we report a γ-Al_2O_3 support modified by deposition of highly dispersed cobalt species via the strong electrostatic adsorption (SEA) synthesis method. The resulting Co-Al_2O_3 possessed higher surface area because of additional micro porosity resulting from occluded pores in the γ-Al_2O_3 support that likely opened during calcination of the deposited ammine Co precursor complex. The Co-Al_2O_3 catalyst presented about half the original Lewis acidity (counted with pyridine adsorption) of the γ-Al_2O_3 support and a slight increase in basicity due to the presence of nitrogen containing Co moieties on the catalyst surface. Acidity measurement via NH_3-TPD indicated that both catalysts have similar acid site count due to micropore acidity available to NH_3 but not to pyridine during titration. However, not all micropore acid sites are expected to be available for reaction as the kinetic diameter of NH_3 (~2.6-3.3 Å) is smaller than that of ethanol (~4.5 Å). The deposition of Co species on γ-Al_2O_3 changed the hydrophobic properties in the Co-Al_2O_3 catalyst making it more resistant to water inhibition and thus opening additional active sites previously unavailable for ethanol dehydration. The new Co-Al_2O_3 catalyst could achieve similar ethanol conversion and dehydration selectivity to ethylene at lower temperatures than the parent γ-Al_2O_3 support. Measurement of apparent activation energies from initial ethanol formation reaction rates at relatively low (433-473 K) and high (533-563 K) temperatures showed that adsorbed dimer species were required to explain the experimental observations. Further, water co-feeding experiments during ethanol conversion at 473 K also confirmed the need for water dimers and trimers to satisfactorily explain the inhibition trends. In situ modulation excitation-phase sensitive detection-DRIFTS (ME-PSD-DRIFTS) experiments at 473 and 543 K confirmed that the Co-Al_2O_3 surface was significantly less covered by adsorbed ethanol and water species than the γ-Al_2O_3 surface. Additionally, evidence was also shown from in situ ethanol and water ME-PSD-DRIFTS for the participation of adsorbed ethanol and ethoxide species as well as terminal and bridging hydroxyls bonded to octahedral and tetrahedral Al on Al_2O_3 (100) and (110) facets as possible reaction intermediates in the conversion of ethanol to diethyl ether and ethylene as well as competitive adsorption of water and ethanol. Overall, the results of this work highlight the need for use of careful consideration of the combined role of active sites requirements, kinetic dependences, and in situ characterization in the design of catalysts for alcohol conversion reactions.

This work was published in ***Journal of Catalysis***, 2019, 373, 276-296 (DOI: 10.1016/j.jcat.2019.03.024).

5.5. References

1. Technology Roadmap: Energy and GHG Reductions in the Chemical Industry via Catalytic Processes.**2013**,1-60; https://www.iea.org/publications/freepublications/publication/Chemical_Roadmap_2013_Final_WEB.pdf
2. Lewandowski, S., Asia Chemical Conference: Ethylene-Global. **2016**, 1-31;https://cdn.ihs.com/www/pdf/Steve-Lewandowski-Big-Changes-Ahead-for-Ethylene-Implications-for-Asia.pdf.
3. Lippe, D., Uncertainty looms for US olefins industry. *Oil & Gas J.* **2018,** *116 (3)* (3), in: https://www.ogj.com/articles/print/volume-116/issue-3.html
4. Direct Oil and Gas to Ethylene - The Search for the Holy Grail,**2017,**1-36http://www.wraconferences.com/wp-content/uploads/2017/01/Direct-Oil-Gas-to-Ethylene-Advantageous-Technologies-or-False-Dawns-draft.pdf.
5. Broeren, M., Simbolotti, G., Tosato, G., and Gielen, D., Production of Bio-ethylene. **2013,** (Technology Policy Brief I13), 1-9.
6. Technology Roadmap: Energy and GHG Reductions in the Chemical Industry via Catalytic Processes**2013**,138;https://www.iea.org/media/freepublications/technologyroadmaps/TechnologyRoadmapCatalyticProcessesAnnexes.pdf.
7. Zhang, M. and Yu, Y., Dehydration of Ethanol to Ethylene. *Industrial & Engineering Chemistry Research* **2013,** *52* (28), 9505-9514.
8. Fan, D., Dai, D.-J., and Wu, H.-S., Ethylene Formation by Catalytic Dehydration of Ethanol with Industrial Considerations. *Materials* **2013,** *6* (1), 101.
9. Gallo, J.M.R., Bueno, J.M.C., and Schuchardt, U., Catalytic Transformations of Ethanol for Biorefineries. *Journal of the Brazilian Chemical Society* **2014,** *25* (12), 2229-2243.
10. Mohsenzadeh, A., Zamani, A., and Taherzadeh, M.J., Bioethylene Production from Ethanol: A Review and Techno-economical Evaluation. *ChemBioEng Reviews* **2017,** *4* (2), 75-91.

11. Hulea, V., Toward Platform Chemicals from Bio-Based Ethylene: Heterogeneous Catalysts and Processes. *ACS Catalysis* **2018,** *8* (4), 3263-3279.
12. El-Katatny, E.A., Halawy, S.A., Mohamed, M.A., and Zaki, M.I., Recovery of ethene-selective FeOx/Al2O3 ethanol dehydration catalyst from industrial chemical wastes. *Applied Catalysis A: General* **2000,** *199* (1), 83-92.
13. Chen, G., Li, S., Jiao, F., and Yuan, Q., Catalytic dehydration of bioethanol to ethylene over TiO_2/γ-Al_2O_3 catalysts in microchannel reactors. *Catalysis Today* **2007,** *125* (1), 111-119.
14. Takahara, I., Saito, M., Inaba, M., and Murata, K., Dehydration of ethanol into ethylene over solid acid catalysts. *Catalysis Letters* **2005,** *105* (3-4), 249-252.
15. Garbarino, G., Wang, C., Valsamakis, I., Chitsazan, S., Riani, P., Finocchio, E., Flytzani-Stephanopoulos, M., and Busca, G., Acido-basicity of lanthana/alumina catalysts and their activity in ethanol conversion. *Applied Catalysis B: Environmental* **2017,** *200*, 458-468.
16. Garbarino, G., Prasath Parameswari Vijayakumar, R., Riani, P., Finocchio, E., and Busca, G., Ethanol and diethyl ether catalytic conversion over commercial alumina and lanthanum-doped alumina: Reaction paths, catalyst structure and coking. *Applied Catalysis B: Environmental* **2018,** *236*, 490-500.
17. Di Cosimo, J.I., Díez, V.K., Xu, M., Iglesia, E., and Apesteguía, C.R., Structure and surface and catalytic properties of Mg-Al basic oxides. *Journal of Catalysis* **1998,** *178* (2), 499-510.
18. Kang, M. and Bhan, A., Kinetics and mechanisms of alcohol dehydration pathways on alumina materials. *Catalysis Science & Technology* **2016,** *6* (17), 6667-6678.
19. Kang, M., DeWilde, J.F., and Bhan, A., Kinetics and Mechanism of Alcohol Dehydration on γ-Al_2O_3: Effects of Carbon Chain Length and Substitution. *ACS Catalysis* **2015,** *5* (2), 602-612.
20. DeWilde, J.F., Czopinski, C.J., and Bhan, A., Ethanol Dehydration and Dehydrogenation on γ-Al2O3: Mechanism of Acetaldehyde Formation. *ACS Catalysis* **2014,** *4* (12), 4425-4433.
21. DeWilde, J.F., Chiang, H., Hickman, D.A., Ho, C.R., and Bhan, A., Kinetics and Mechanism of Ethanol Dehydration on γ-Al2O3: The Critical Role of Dimer Inhibition. *ACS Catalysis* **2013,** *3* (4), 798-807.

22. Roy, S., Mpourmpakis, G., Hong, D.-Y., Vlachos, D.G., Bhan, A., and Gorte, R.J., Mechanistic Study of Alcohol Dehydration on γ-Al2O3. *ACS Catalysis* **2012,** *2* (9), 1846-1853.
23. Christiansen, M.A., Mpourmpakis, G., and Vlachos, D.G., DFT-driven multi-site microkinetic modeling of ethanol conversion to ethylene and diethyl ether on γ-Al2O3(111). *Journal of Catalysis* **2015,** *323*, 121-131.
24. Jenness, G.R., Christiansen, M.A., Caratzoulas, S., Vlachos, D.G., and Gorte, R.J., Site-Dependent Lewis Acidity of γ-Al2O3 and Its Impact on Ethanol Dehydration and Etherification. *The Journal of Physical Chemistry C* **2014,** *118* (24), 12899-12907.
25. Christiansen, M.A., Mpourmpakis, G., and Vlachos, D.G., Density Functional Theory-Computed Mechanisms of Ethylene and Diethyl Ether Formation from Ethanol on γ-Al2O3(100). *ACS Catalysis* **2013,** *3* (9), 1965-1975.
26. Larmier, K., Nicolle, A., Chizallet, C., Cadran, N., Maury, S., Lamic-Humblot, A.F., Marceau, E., and Lauron-Pernot, H., Influence of Coadsorbed Water and Alcohol Molecules on Isopropyl Alcohol Dehydration on gamma-Alumina: Multiscale Modeling of Experimental Kinetic Profiles. *ACS Catalysis* **2016,** *6* (3), 1905-1920.
27. Larmier, K., Chizallet, C., Cadran, N., Maury, S., Abboud, J., Lamic-Humblot, A.-F., Marceau, E., and Lauron-Pernot, H., Mechanistic Investigation of Isopropanol Conversion on Alumina Catalysts: Location of Active Sites for Alkene/Ether Production. *ACS Catalysis* **2015,** *5* (7), 4423-4437.
28. Kwak, J.H., Mei, D., Peden, C.H.F., Rousseau, R., and Szanyi, J., (100) facets of γ-Al2O3: The Active Surfaces for Alcohol Dehydration Reactions. *Catalysis Letters* **2011,** *141* (5), 649-655.
29. Kwak, J.H., Lee, J., Szanyi, J., and Peden, C.H.F., Modification of the acid/base properties of γ-Al2O3 by oxide additives: An ethanol TPD investigation. *Catalysis Today* **2016,** *265*, 240-244.
30. Lee, J., Szanyi, J., and Kwak, J.H., Ethanol dehydration on γ-Al2O3: Effects of partial pressure and temperature. *Molecular Catalysis* **2017,** *434*, 39-48.
31. Lee, J., Jang, E.J., Jeong, H.Y., and Kwak, J.H., Critical role of (100) facets on gamma-Al2O3 for ethanol dehydration: Combined efforts of morphology-controlled synthesis and TEM study. *Applied Catalysis a-General* **2018,** *556*, 121-128.

32. Phung, T.K., Lagazzo, A., Crespo, M.A.R., Escribano, V.S., and Busca, G., A study of commercial transition aluminas and of their catalytic activity in the dehydration of ethanol. *Journal of Catalysis* **2014,** *311*, 102-113.
33. Phung, T.K. and Busca, G., Diethyl ether cracking and ethanol dehydration: Acid catalysis and reaction paths. *Chemical Engineering Journal* **2015,** *272*, 92-101.
34. Fang, Z., Wang, Y., and Dixon, D.A., Computational Study of Ethanol Conversion on Al_8O_{12} as a Model for γ-Al_2O_3. *The Journal of Physical Chemistry C* **2015,** *119* (41), 23413-23421.
35. Maresca, O., Allouche, A., Aycard, J.P., Rajzmann, M., Clemendot, S., and Hutschka, F., Quantum study of the active sites of the γ-alumina surface: chemisorption and adsorption of water, hydrogen sulfide and carbon monoxide on aluminum and oxygen sites. *Journal of Molecular Structure: THEOCHEM* **2000,** *505* (1), 81-94.
36. Lee, J., Jang, E.J., and Kwak, J.H., Acid-base properties of Al_2O_3: Effects of morphology, crystalline phase, and additives. *Journal of Catalysis* **2017,** *345*, 135-148.
37. D'Souza, L., Jiao, L., Regalbuto, J.R., Miller, J.T., and Kropf, A.J., Preparation of silica- and carbon-supported cobalt by electrostatic adsorption of Co(III) hexaammines. *Journal of Catalysis* **2007,** *248* (2), 165-174.
38. Liu, Q. Rational Synthesis of Catalysts for Biomass Conversion. Dissertation, University of South Carolina, Columbia, South Carolina, **2017**.
39. Regalbuto, J.R., Strong Electrostatic Adsorption of Metals onto Catalyst Supports. In *Catalyst Preparation: Science and Engineering*, J.R. Regalbuto, Ed. Taylor and Francis/CRC Press: **2007;** pp 297-318.
40. Khivantsev, K., Biancardi, A., Fathizadeh, M., Almalki, F., Grant, J.L., Tien, H.N., Shakouri, A., Blom, D.A., Makris, T.M., Regalbuto, J.R., Caricato, M., and Yu, M., Catalytic N-H Bond Activation and Breaking by a Well-Defined (Co1O4)-O-II Site of a Heterogeneous Catalyst. *Chemcatchem* **2018,** *10* (4), 736-742.
41. Srinivasan, P.D., Nitz, S.R., Stephens, K.J., Atchison, E., and Bravo-Suárez, J.J., Modified Harrick reaction cell for in situ/operando fiber optics diffuse reflectance UV–visible spectroscopic characterization of catalysts. *Applied Catalysis A: General* **2018,** *561*, 7-18.

42. Emeis, C.A., Determination of integrated molar extinction coefficients for infrared-absorption bands of pyridine adsorbed on solid acid catalysts. *Journal of Catalysis* **1993,** *141* (2), 347-354.
43. Hattori, H., Heterogeneous Basic Catalysis. *Chemical Reviews* **1995,** *95* (3), 537-558.
44. Hill, I.M., Hanspal, S., Young, Z.D., and Davis, R.J., DRIFTS of Probe Molecules Adsorbed on Magnesia, Zirconia, and Hydroxyapatite Catalysts. *The Journal of Physical Chemistry C* **2015,** *119* (17), 9186-9197.
45. Di Cosimo, J.I., Apesteguía, C.R., Ginés, M.J.L., and Iglesia, E., Structural requirements and reaction pathways in condensation reactions of alcohols an MgyAlOx catalysts. *Journal of Catalysis* **2000,** *190* (2), 261-275.
46. Tamaru, K., *Dynamic heterogeneous catalysis*. Academic Press: New York, NY, **1978;** p pp 1-140.
47. Oyama, S.T. and Li, W., Absolute determination of reaction mechanisms by in situ measurements of reaction intermediates. *Topics in Catalysis* **1999,** *8* (1), 75-80.
48. Oyama, S.T. and Zhang, W., True and spectator intermediates in catalysis: The case of ethanol oxidation on molybdenum oxide as observed by in situ laser Raman spectroscopy. *Journal of the American Chemical Society* **1996,** *118* (30), 7173-7177.
49. Kondratenko, E.V., Using time-resolved methods to monitor and understand catalytic oxidation reactions. *Catalysis Today* **2010,** *157* (1–4), 16-23.
50. Bravo-Suárez, J.J., Bando, K.K., Lu, J.I., Haruta, M., Fujitani, T., and Oyama, S.T., Transient technique for identification of true reaction intermediates: Hydroperoxide species in propylene epoxidation on gold/titanosilicate catalysts by X-ray absorption fine structure spectroscopy. *Journal of Physical Chemistry C* **2008,** *112* (4), 1115-1123.
51. Gott, T. and Oyama, S.T., A general method for determining the role of spectroscopically observed species in reaction mechanisms: Analysis of coverage transients (ACT). *Journal of Catalysis* **2009,** *263* (2), 359-371.
52. Reed, C., Xi, Y., and Oyama, S.T., Distinguishing between reaction intermediates and spectators: A kinetic study of acetone oxidation using ozone on a silica-supported manganese oxide catalyst. *Journal of Catalysis* **2005,** *235* (2), 378-392.

53. Meunier, F.C., The power of quantitative kinetic studies of adsorbate reactivity by operando FTIR spectroscopy carried out at chemical potential steady-state. *Catalysis Today* **2010,** *155* (3), 164-171.
54. Kalamaras, C.M., Americanou, S., and Efstathiou, A.M., "Redox" vs "associative formate with -OH group regeneration" WGS reaction mechanism on Pt/CeO_2: Effect of platinum particle size. *Journal of Catalysis* **2011,** *279* (2), 287-300.
55. Müller, P. and Hermans, I., Applications of Modulation Excitation Spectroscopy in Heterogeneous Catalysis. *Industrial & Engineering Chemistry Research* **2017,** *56* (5), 1123-1136.
56. Urakawa, A., Bürgi, T., and Baiker, A., Sensitivity enhancement and dynamic behavior analysis by modulation excitation spectroscopy: Principle and application in heterogeneous catalysis. *Chemical Engineering Science* **2008,** *63* (20), 4902-4909.
57. Newland, D.E., *An Introduction to Random Vibrations and Spectral Analysis*. Longman: Mineola, NY, **1984;** p 1-477.
58. Lyons, R.G., *Understanding Digital Signal Processing*. Prentice Hall: Upper Saddle River, NJ, **2004;** p 1-665.
59. Karam, M., Khazaal, H.F., Aglan, H., and Cole, C., Noise Removal in Speech Processing Using Spectral Subtraction. *J. Signal Inf. Proc.* **2014,** *5* (2), 32-41.
60. Baurecht, D. and Fringeli, U.P., Quantitative modulated excitation Fourier transform infrared spectroscopy. *Review of Scientific Instruments* **2001,** *72* (10), 3782-3792.
61. Marchionni, V., Ferri, D., Krocher, O., and Wokaun, A., Increasing the Sensitivity to Short-Lived Species in a Modulated Excitation Experiment. *Analytical Chemistry* **2017,** *89* (11), 5802-5810.
62. Srinivasan, P.D., Patil, B.S., Zhu, H., and Bravo-Suárez, J.J., Application of modulation excitation-phase sensitive detection-DRIFTS for in situ/operando characterization of heterogeneous catalysts. *Reaction Chemistry & Engineering* **2019,** *DOI: 10.1039/C9RE00011A*.
63. Patil, B.S., Srinivasan, P.D., Atchison, E., Zhu, H., and Bravo-Suárez, J.J., Design, Modelling, and Application of a Low Void-Volume in Situ Diffuse Reflectance Spectroscopic Reaction Cell for Transient Catalytic Studies. *React. Eng. Chem.* **2019,** *DOI: 10.1039/C8RE00302E*.

64. Trimm, D.L. and Stanislaus, A., The control of pore size in alumina catalyst supports: A review. *Applied Catalysis* **1986,** *21* (2), 215-238.
65. Kovarik, L., Genc, A., Wang, C., Qiu, A., Peden, C.H.F., Szanyi, J., and Kwak, J.H., Tomography and High-Resolution Electron Microscopy Study of Surfaces and Porosity in a Plate-like γ-Al2O3. *The Journal of Physical Chemistry C* **2013,** *117* (1), 179-186.
66. Tamura, M., Shimizu, K.-i., and Satsuma, A., Comprehensive IR study on acid/base properties of metal oxides. *Applied Catalysis A: General* **2012,** *433-434*, 135-145.
67. Hu, B., Getsoian, A., Schweitzer, N.M., Das, U., Kim, H., Niklas, J., Poluektov, O., Curtiss, L.A., Stair, P.C., Miller, J.T., and Hock, A.S., Selective propane dehydrogenation with single-site Co-II on SiO2 by a non-redox mechanism. *Journal of Catalysis* **2015,** *322*, 24-37.
68. Diez, V.K., Apesteguia, C.R., and Di Cosimo, J.I., Effect of the chemical composition on the catalytic performance of MgyAlOx catalysts for alcohol elimination reactions. *Journal of Catalysis* **2003,** *215* (2), 220-233.
69. Dulaurent, O., Nawdali, M., Bourane, A., and Bianchi, D., Heat of adsorption of carbon monoxide on a Ru/Al2O3 catalyst using adsorption equilibrium conditions at high temperatures. *Applied Catalysis A: General* **2000,** *201* (2), 271-279.
70. Bourane, A., Dulaurent, O., Chandes, K., and Bianchi, D., Heats of adsorption of the linear CO species on a Pt/Al2O3 catalyst using FTIR spectroscopy: Comparison between TPD and adsorption equilibrium procedures. *Applied Catalysis A: General* **2001,** *214* (2), 193-202.
71. Bianchi, D., A Contribution to the Experimental Microkinetic Approach of Gas/Solid Heterogeneous Catalysis: Measurement of the Individual Heats of Adsorption of Coadsorbed Species by Using the AEIR Method. *Catalysts* **2018,** *8* (7), 265.
72. Wu, H., Gong, Q., Olson, D.H., and Li, J., Commensurate Adsorption of Hydrocarbons and Alcohols in Microporous Metal Organic Frameworks. *Chemical Reviews* **2012,** *112* (2), 836-868.
73. Kanezashi, M., Yamamoto, A., Yoshioka, T., and Tsuru, T., Characteristics of ammonia permeation through porous silica membranes. *AIChE Journal* **2010,** *56* (5), 1204-1212.

74. Escribano, V.S., Garbarino, G., Finocchio, E., and Busca, G., gamma-Alumina and Amorphous Silica-Alumina: Structural Features, Acid Sites and the Role of Adsorbed Water. *Topics in Catalysis* **2017,** *60* (19-20), 1554-1564.
75. Ribeiro, R.U., Liberatori, J.W.C., Winnishofer, H., Bueno, J.M.C., and Zanchet, D., Colloidal Co nanoparticles supported on SiO2: Synthesis, characterization and catalytic properties for steam reforming of ethanol. *Applied Catalysis B: Environmental* **2009,** *91* (3), 670-678.
76. Da Silva, A.L.M., den Breejen, J.P., Mattos, L.V., Bitter, J.H., de Jong, K.P., and Noronha, F.B., Cobalt particle size effects on catalytic performance for ethanol steam reforming – Smaller is better. *Journal of Catalysis* **2014,** *318*, 67-74.
77. Ferencz, Z., Varga, E., Puskás, R., Kónya, Z., Baán, K., Oszkó, A., and Erdőhelyi, A., Reforming of ethanol on Co/Al2O3 catalysts reduced at different temperatures. *Journal of Catalysis* **2018,** *358*, 118-130.
78. Bichon, P., Haugom, G., Venvik, H.J., Holmen, A., and Blekkan, E.A., Steam reforming of ethanol over supported Co and Ni catalysts. *Topics in Catalysis* **2008,** *49* (1-2), 38-45.
79. DeWilde, J.F. and Bhan, A., Kinetics and site requirements of ether disproportionation on gamma-Al2O3. *Applied Catalysis a-General* **2015,** *502*, 361-369.
80. Kostetskyy, P. and Mpourmpakis, G., Structure-activity relationships in the production of olefins from alcohols and ethers: a first-principles theoretical study. *Catalysis Science & Technology* **2015,** *5* (9), 4547-4555.
81. Satterfield, C.N., *Heterogeneous Catalysis in Industrial Practice*. 2nd ed.; McGraw-Hill: New York, NY, **1991**.
82. De Mourgues, L., Peyron, F., Trambouze, Y., and Prettre, M., Kinetics of the catalytic dehydration of 2-propanol. *Journal of Catalysis* **1967,** *7* (2), 117-125.
83. Bertin, E.P., Penland, R.B., Mizushima, S., Curran, C., and Quagliano, J.V., Infrared absorption studies of inorganic coorganic coordination complexes .20. cobalt (III) ammine complexes containing some coordinated anions. *Journal of the American Chemical Society* **1959,** *81* (15), 3818-3821.
84. Mikuli, E., Migdal-Mikuli, A., Gorska, N., Wrobel, S., Sciesinski, J., and Sciesinska, E., Phase transition and molecular motions in Co(NH3)(6) (ClO4)(3) studied by differential

scanning calorimetry and infrared spectroscopy. *Journal of Molecular Structure* **2003,** *651*, 519-524.

85. Villalba, M.E.C., Navaza, A., Dupont, N., Marrot, J., Varetti, E.L., and Aymonino, P.J., Crystal structure of Co(NH3)(5)NO3 (NO3)(PF6) center dot 1.5H(2)O and the vibrational bands of its normal and (NO3)-N-15-enriched cation. *Journal of Chemical Crystallography* **2007,** *37* (8), 573-577.
86. Fujita, J., Nakamoto, K., and Kobayashi, M., Infrared Spectra of Metallic Complexes. I. The Effect of Coördination on the Infrared Spectra of Ammine, Rhodanato and Azido Complexes. *Journal of the American Chemical Society* **1956,** *78* (14), 3295-3297.
87. Massoud, S.S., Spectroscopic characterization for the geometrical-isomers of azido amine cobalt (III) complexes. *Polyhedron* **1994,** *13* (22), 3127-3134.
88. Druding, L.F., Wang, H.-C., Cohen, R.E., and Sancilio, F.D., The triamines of cobalt[III].II.infrared and nuclear magnetic resoannce spectra of some azido complexes. *Journal of Coordination Chemistry* **1973,** *3* (1), 105-112.
89. Andrews, L., Citra, A., Chertihin, G.V., Bare, W.D., and Neurock, M., Reactions of Laser-Ablated Co and Ni Atoms with Nitrogen Atoms and Molecules. Infrared Spectra and DFT Calculations of Metal Nitride Molecular Species and Complexes. *The Journal of Physical Chemistry A* **1998,** *102* (15), 2561-2571.
90. Zenkin, S., Kos, S., and Musil, J., Hydrophobicity of Thin Films of Compounds of Low-Electronegativity Metals. *Journal of the American Ceramic Society* **2014,** *97* (9), 2713-2717.
91. Hadjiivanov, K., Identification and Characterization of Surface Hydroxyl Groups by Infrared Spectroscopy. *Advances in Catalysis* **2014,** *57*, 99-318.
92. Busca, G., The surface of transitional aluminas: A critical review. *Catalysis Today* **2014,** *226*, 2-13.
93. Busca, G., Structural, Surface, and Catalytic Properties of Aluminas. *Advances in Catalysis* **2014,** *57*, 319-404.
94. Digne, M., Sautet, P., Raybaud, P., Euzen, P., and Toulhoat, H., Hydroxyl groups on gamma-alumina surfaces: A DFT study. *Journal of Catalysis* **2002,** *211* (1), 1-5.

95. Nedic, M., Wassermann, T.N., Larsen, R.W., and Suhm, M.A., A combined Raman- and infrared jet study of mixed methanol-water and ethanol-water clusters. *Physical Chemistry Chemical Physics* **2011,** *13* (31), 14050-14063.

96. Lee, Y.-F., Kelterer, A.-M., Matisz, G., Kunsági-Máté, S., Chung, C.-Y., and Lee, Y.-P., Infrared absorption of methanol-water clusters (CH3OH)n(H2O), n = 1–4, recorded with the VUV-ionization/IR-depletion technique. *The Journal of Chemical Physics* **2017,** *146* (14), 144308.

97. Al-Abadleh, H.A. and Grassian, V.H., FT-IR study of water adsorption on aluminum oxide surfaces. *Langmuir* **2003,** *19* (2), 341-347.

98. Alexopoulos, K., Lee, M.-S., Liu, Y., Zhi, Y., Liu, Y., Reyniers, M.-F., Marin, G.B., Glezakou, V.-A., Rousseau, R., and Lercher, J.A., Anharmonicity and Confinement in Zeolites: Structure, Spectroscopy, and Adsorption Free Energy of Ethanol in H-ZSM-5. *The Journal of Physical Chemistry C* **2016,** *120* (13), 7172-7182.

99. Sheng, P.Y., Bowmaker, G.A., and Idriss, H., The Reactions of Ethanol over Au/CeO2. *Applied Catalysis A: General* **2004,** *261* (2), 171-181.

100. Natal-Santiago, M.A. and Dumesic, J.A., Microcalorimetric, FTIR, and DFT studies of the adsorption of methanol, ethanol, and 2,2,2-trifluoroethanol on silica. *Journal of Catalysis* **1998,** *175* (2), 252-268.

101. Hemelsoet, K., Ghysels, A., Mores, D., De Wispelaere, K., Van Speybroeck, V., Weckhuysen, B.M., and Waroquier, M., Experimental and theoretical IR study of methanol and ethanol conversion over H-SAPO-34. *Catalysis Today* **2011,** *177* (1), 12-24.

102. Gao, J. and Teplyakov, A.V., Surface species formed during thermal transformation of ethanol on ZnO powder. *Journal of Catalysis* **2013,** *300*, 163-173.

103. Dömök, M., Tóth, M., Raskó, J., and Erdőhelyi, A., Adsorption and reactions of ethanol and ethanol–water mixture on alumina-supported Pt catalysts. *Applied Catalysis B: Environmental* **2007,** *69* (3), 262-272.

104. Hussein, G.A.M., Sheppard, N., Zaki, M.I., and Fahim, R.B., Infrared spectroscopic studies of the reactions of alcohols over group IVB metal oxide catalysts. Part 3.-Ethanol over TiO_2, ZrO_2 and HfO_2, and general conclusions from parts 1 to 3. *Journal of the Chemical Society, Faraday Transactions* **1991,** *87* (16), 2661-2668.

105. Li, D., Bui, P., Zhao, H.Y., Oyama, S.T., Dou, T., and Shen, Z.H., Rake mechanism for the deoxygenation of ethanol over a supported Ni2P/SiO2 catalyst. *Journal of Catalysis* **2012,** *290*, 1-12.

106. Digne, M., Sautet, P., Raybaud, P., Euzen, P., and Toulhoat, H., Use of DFT to achieve a rational understanding of acid-basic properties of gamma-alumina surfaces. *Journal of Catalysis* **2004,** *226* (1), 54-68.

107. Wischert, R., Laurent, P., Coperet, C., Delbecq, F., and Sautet, P., gamma-Alumina: The Essential and Unexpected Role of Water for the Structure, Stability, and Reactivity of "Defect" Sites. *Journal of the American Chemical Society* **2012,** *134* (35), 14430-14449.

108. Birky, T.W., Kozlowski, J.T., and Davis, R.J., Isotopic transient analysis of the ethanol coupling reaction over magnesia. *Journal of Catalysis* **2013,** *298*, 130-137.

109. Hanspal, S., Young, Z.D., Shou, H., and Davis, R.J., Multiproduct Steady-State Isotopic Transient Kinetic Analysis of the Ethanol Coupling Reaction over Hydroxyapatite and Magnesia. *ACS Catalysis* **2015,** *5* (3), 1737-1746.

Chapter 6. Conclusions and Recommendations

6.1. Conclusions

Two powerful characterization techniques based on gold surface plasmon resonance (Au SPR) and ME-PSD-DRIFTS were developed to understand: a) the oxygen adsorption properties of supported gold catalysts in presence of flowing oxygen and during CO oxidation at reaction conditions and b) catalyst active sites and surface intermediate species of catalyzed reactions including ethanol dehydration on modified Al_2O_3, respectively. This dissertation has led to several advances, fundamental insights, and potential applications in heterogeneous catalysis as listed below:

1. A commercial Harrick diffuse reflectance reaction cell was successfully modified for application of rapid transients in situ UV-Vis spectroscopic studies.
2. A residence time distribution methodology was developed to study the flow dynamics of in situ reaction cells.
3. A thermal experimental and simulation study on the modified in situ cell pointed out to significant heat losses reflected by a significant gradient between the sample bed and the heater temperatures.
4. The utility of the modified in situ/operando fiber optics diffuse reflectance cell was demonstrated for monitoring temporal changes of gold catalysts exposed to oxidizing (O_2) and reducing (H_2) environments at high temperature. More specifically, rapid changes to the gold surface plasmon resonance peak in the visible region were observed on switching from O_2 to H_2 gas as a likely result of O_2 reduction and/or desorption, a process that was fully reversible and reproducible over several cycles and an extended period.
5. A simple characterization technique based on gold surface plasmon resonance (Au SPR) named oxygen gold plasmon sensing (O_2-GPS) was developed to estimate the oxygen adsorption properties of supported gold catalysts at reaction conditions.
6. A simple charge transfer model based on the support's dielectric constant and Drude's free electron model for gold nanoparticles dielectric function was employed to estimate the relative charge transfer change from/to gold during oxygen adsorption and titration with hydrogen.

7. A correlation was found between charge transfer from gold to oxygen and gold nanoparticle size suggesting that for reducible and nonreducible supports oxygen adsorption primarily occurred at the Au-support perimeter.
8. Evidence was provided for oxygen participation at the Au-support perimeter and CO or CO_x intermediate species on surface gold atoms in rate limiting steps with reducible and nonreducible supports during CO oxidation reaction.
9. Application of modulation excitation-phase sensitive detection-diffuse reflectance Fourier transform spectroscopy (ME-PSD-DRIFTS) via discrete Fourier transform (DFT)/inverse discrete Fourier transform (IDFT) was described in detail including a general mathematical framework, basic guidelines for planning, running, and interpreting ME-PSD-DRIFTS results.
10. The described DFT/IDFT procedure can be applied to any periodic modulation and to any input modulation waveform (not just sine and square waveforms as previously reported in literature) introduced as a perturbation in the reaction system. In practice, this is quite convenient as a single software code can be used to handle ME-PSD responses regardless of the type of perturbation.
11. Modification of a γ-Al_2O_3 support by highly dispersed cobalt species via the strong electrostatic adsorption (SEA) synthesis method that changed the hydrophobic properties in the Co-Al_2O_3 catalyst making it more resistant to water inhibition and thus opening additional active sites previously unavailable for ethanol dehydration, which was used as test reaction.
12. Spectroscopic evidence was shown from in situ ethanol and water ME-PSD-DRIFTS for the participation of adsorbed ethanol and ethoxide species and terminal and bridging hydroxyls bonded to octahedral and tetrahedral Al on Al_2O_3 (100) and (110) facets as possible reaction intermediates in the conversion of ethanol to diethyl ether and ethylene as well as competitive adsorption of water and ethanol.

6.2. Recommendations for future work

6.2.1. Gold-support and particle size effects

Our study also rises additional questions regarding the enhancement of catalytic activity when reducible supports are used as the amount of charge transfer (or adsorbed oxygen) does not fully account for the significantly different catalytic activity. We hypothesize that support acid-base

properties and presence of oxygen vacancies may be at play as they could influence the adsorption/desorption of O_2 and CO or CO_x derived intermediates which could adsorb strongly on active sites and inhibit the reaction. The simple in situ Au SPR technique developed here along with future kinetic and in situ/operando spectroscopies (e.g., IR, Raman) should shed additional light to our understanding of gold-support effects, particle size, and reactant/product inhibition in CO and other oxidation reactions enabled by gold catalysts.

6.2.2. Kinetic studies of deactivating catalysts through ME-PDS-DRIFTS

New information of surface species could be afforded from the study of kinetics of rapidly deactivating catalysts by analysis of the broadening of frequency signals analogous to NMR relaxation techniques in the frequency domain. Since ME-PSD has only been applied to stable catalysts, ME-PSD-DRIFTS can provide new understanding on the active sites and surface species involved during the deactivation of catalysts.

6.2.3. Combination of SSITKA with ME-PSD-DRIFTS

As in situ/operando spectroscopic studies become more routine, there is a need to move from qualitative to quantitative studies. This is no easy task because of the difficulties in the calibration of spectroscopic signals. Combination of SSITKA with ME-PSD-DRIFTS will undoubtedly represent a powerful combination to explore reaction intermediate species and their kinetics. In this natural evolution from in situ to operando and from spectroscopic to spectrokinetic studies, careful consideration should be given to the reaction cell and reaction conditions (i.e., operation in absence of mass and heat transfer limitations). As discussed in this work, low void-volume DR cells and proper choice of modulation frequency and amplitude change can help simplify kinetic models to obtain information on rate constants of individual elementary steps. Kinetic studies in the transient conditions and in combination with kinetic models that consider surface species can also serve as inspiration for further quantitative developments of ME-PSD-DRIFTS.

6.2.4. Alcohol dehydration studies on highly dispersed Co-Al_2O_3

Alcohol dehydration can be efficiently catalyzed by alumina surfaces, but the nature of active sites, mechanisms and the key parameters to tune both the activity and alkene selectivity remain a matter of debate. The results of the work on ethanol dehydration studies, illustrated the

need for use of careful consideration of the combined role of active sites requirements, kinetic dependences, and in situ characterization of catalysts for other alcohol conversion reactions like isopropanol dehydration or other reactions that require acid sites, but with a catalyst surface that is somewhat hydrophobic.

Appendix A

Table A.1. Residence time distribution characteristics through the reaction cell system with large (w/o beads ~ 12.5 cm^3) and reduced empty volume (w/ beads ~ 3.5 cm^3)

Gas	**$t_{m,r}$ (σ) (s)**	**t $RTD_{90\%}$ (s)**	**$\tau_{p,r}$ (s)**	**$\tau_{p,b}$ (s)**	**$t_{m,1}$ (s)**	**$t_{m,2}$ (s)**
Ar (w/o beads)	15.4 (14.5)	22.6	3.2	2.0	8.0	4.2
Ar (w/ beads)	11.0 (14.2)	17.8	3.0	2.0	3.8	4.2
CO_2 (w/o beads)	15.9 (14.6)	23.7	3.3	2.3	8.5	4.1
CO_2 (w/ beads)	11.5 (12.8)	18.7	2.9	2.3	4.5	4.1

$t_{m,r}$ = mean residence time of pulse gas to reach MS detector (via in situ reaction cell), σ = standard deviation, t RTD90% = residence time required for 90% of the pulse gas to reach the MS detector, $\tau_{p,r}$ = space time for a plug flow reactor: tubing line before in situ reactor, $\tau_{p,b}$ = space time for a plug flow reactor: tubing line bypassing in situ reactor, $t_{m,1}$ = mean residence time of pulse gas through in situ reactor based on an ideal CSTR, $t_{m,2}$ = mean residence time of pulse gas in mass spectrometer before reaching detector based on an ideal CSTR. Experimental conditions: He carrier 120 cm^3/min, 50 μL gas pulse, 1 bar, 25 °C, reaction cell without (cell dead volume ~12.5 cm^3) or with glass beads (cell dead volume ~3.5 cm^3).

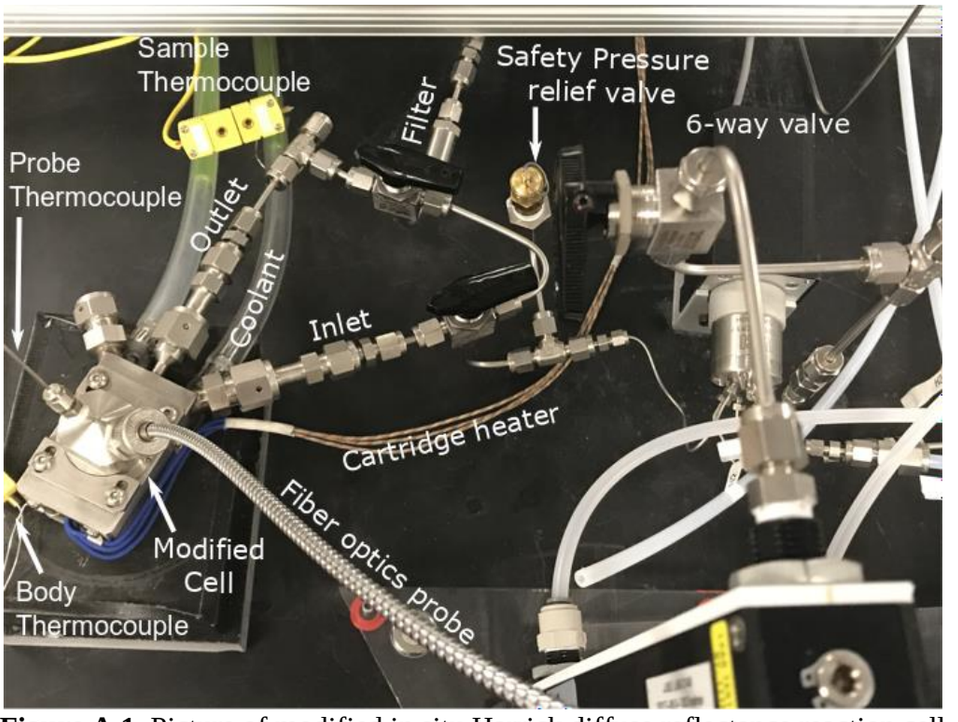

Figure A.1. Picture of modified in situ Harrick diffuse reflectance reaction cell

A.1. VBA code for finding maximum peak position in UV-Vis spectra

The code below is used to find the maximum peak in the measured UV-Vis spectra. It is worth noting that many spectra are taken an analyzed as they are sample every ~2 seconds, resulting in approximately 900 spectra per gas trial (~30 min). The data has been saved for each gas independently to minimize the number of scans to analyze and the size of the excel file produced. StellarNet software exports a file than can be open in Excel with columns representing the different acquired spectra (**Figure A.2**, appendix A).

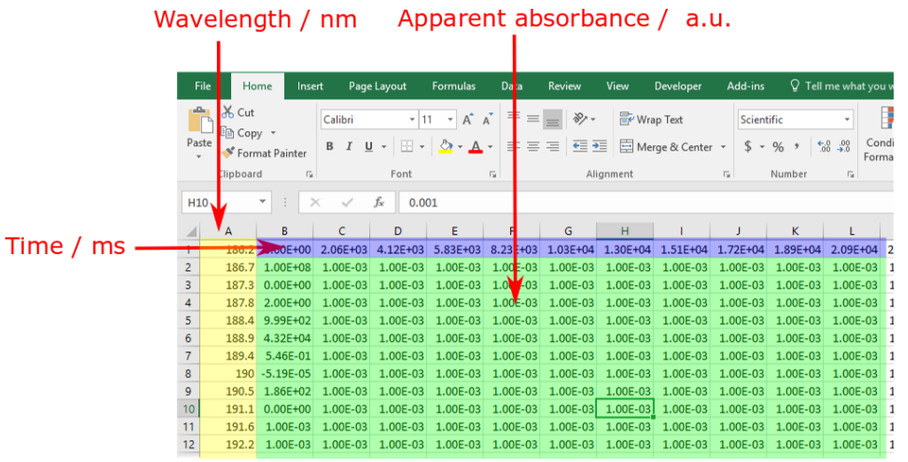

Figure A.2. Excel screenshot of collected UV-Vis data from StellarNet SpectraWiz® software

The following VBA code is used in and Excel macro to analyze each spectra series by fitting the region around the maximum to a polynomial of order 5th and find the corresponding maximum. A figure is produced that plots the maximum peak position vs the run number

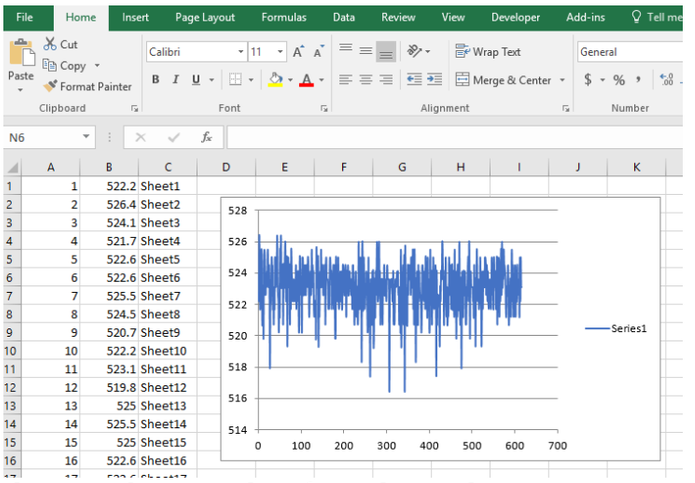

Figure A.3. Excel screenshot sample of resulting plasmon resonance peak maximum determined via the VBA Excel macro

```
Sub NewSpectrometerMacro()



Dim n As Long
Dim i As Long
Dim WkBook As Workbook
Dim SheetA As Worksheet
```

```
Set WkBook = ActiveWorkbook
Set SheetA = WkBook.Worksheets(1)
n = SheetA.Cells(1, Columns.Count).End(xlToLeft).Column
SheetA.Activate

For i = 2 To n
WkBook.Worksheets.Add After:=WkBook.ActiveSheet
SheetA.Range("A1:A2051").Copy
WkBook.Worksheets(i).Range("A1").PasteSpecial Paste:=xlPasteValues
SheetA.Columns(i).Copy
WkBook.Worksheets(i).Range("B1").PasteSpecial Paste:=xlPasteValues

Range("C16:C451").Value = Range("A612:A1047").Value

   Range("D16").Select
   Application.CutCopyMode = False
   ActiveCell.FormulaR1C1 = "=RC[-1]^2"
   Selection.AutoFill Destination:=Range("D16:D451"), Type:=xlFillDefault
   Range("E16").Select
   ActiveCell.FormulaR1C1 = "=RC[-2]^3"
   Selection.AutoFill Destination:=Range("E16:E451"), Type:=xlFillDefault
   Range("F16").Select
   ActiveCell.FormulaR1C1 = "=RC[-3]^4"
   Selection.AutoFill Destination:=Range("F16:F451"), Type:=xlFillDefault
   Range("G16").Select
   ActiveCell.FormulaR1C1 = "=RC[-4]^5"
   Selection.AutoFill Destination:=Range("G16:G451"), Type:=xlFillDefault



   Range("H16:H451").Value = Range("B612:B1047").Value

   Range("E6").Select
   Application.CutCopyMode = False
   ActiveCell.FormulaR1C1 = ""
   Range("D6:I6").Select
   Selection.FormulaArray = _
      "=LINEST(H16:H451,C16:G451,,TRUE)"
   Range("I16").Select
   ActiveCell.Formula = _
      "=$D$6*C16^5+$E$6*C16^4+$F$6*C16^3+$G$6*C16^2+$H$6*C16+$I$6"
```

```
    Selection.AutoFill Destination:=Range("I16:I451"), Type:=xlFillDefault

    Range("J16:J451").Value = Range("C16:C451").Value
    Range("K16:K451").Value = Range("H16:H451").Value
    Range("L16:L451").Value = Range("I16:I451").Value

    Range("L6").Select
    ActiveCell.Formula = "=MAX(I16:I451)"
    Range("M6").Select
    ActiveCell.Formula = _
       "=INDEX(C16:C451,Match(Max(I16:I451),I16:I451,0))"

    Range("J16:L451").Select

    Dim rData As Range
    Set rData = Selection

    Dim Chart As Chart
    Dim sheet As Worksheet

    Set sheet = ActiveWorkbook.Worksheets(i)
    Set Chart = sheet.Shapes.AddChart.Chart
    Chart.ChartType = xlXYScatterSmoothNoMarkers
    Chart.SetSourceData Source:=rData

WkBook.Worksheets(i).Activate
Next

    Dim a As Long
    a = WkBook.Worksheets.Count
    ActiveWorkbook.Sheets.Add After:=ActiveWorkbook.Worksheets(a)

    Dim t As Long
    t = WkBook.Worksheets.Count

    WkBook.Sheets(t).Activate

    For i = 2 To n
    Range("A" & i - 1).Value = i - 1
    ActiveWorkbook.Worksheets(i).Range("M6").Copy
    ActiveWorkbook.Worksheets(t).Range("B" & i - 1).PasteSpecial Paste:=xlPasteValues
```

```
    Application.CutCopyMode = False
    ActiveWorkbook.Worksheets(t).Range("C" & i - 1).Value =
ActiveWorkbook.Worksheets(i).Name
    Next

    Range("A1:B" & n).Select

    Dim ChartF As Chart
    Dim SheetF As Worksheet
    Dim rDataF As Range

    Set rDataF = Selection
    Set SheetF = ActiveWorkbook.Worksheets(t)
    Set ChartF = SheetF.Shapes.AddChart.Chart
    ChartF.ChartType = xlXYScatterSmoothNoMarkers
    ChartF.SetSourceData Source:=rDataF

    WkBook.Worksheets(t).Name = "Graph"

End Sub
```

Appendix B

B.1. Nitrogen physisorption

Nitrogen adsorption-desorption isotherms were measured at 77 K using an Autosorb-iQ_2 analyzer (Quantachrome Instruments). Prior to the physisorption, about 50 mg of the sample was loaded in a 9 mm wide sample cell (P/N 74200-9L, Quantachrome Instruments) and heated in vacuum at 573 K for 3 h at a rate of 5 K/min. After degassing, the sample was back-filled with helium and the analysis was carried out with a standard method consisting of 21 adsorption points and 19 desorption points.

B.2. SEM-EDX elemental analysis

The surface morphology and elemental composition on the sample was analyzed with a Versa 3D dual beam Scanning Electron Microscope (SEM)/Focused Ion Beam (FEI) with a silicon drift EDX detector (Oxford Instruments) at an accelerating voltage of 10 kV.

B.3. X-ray diffraction

Powder X-ray diffraction patterns of catalyst samples were collected in a PANalytical Empryrean diffractometer using Cu Kα radiation operating at 45 kV and 40 mA.

B.4. Modeling of gold nanoparticles and site coordination statistics calculations

Site coordination statistics calculations were performed using the top slice of a truncated octahedron model on a (111) plane as that shown in Figure . The calculation formulas were previously reported by Carlsson et al. [1] and are summarized next.

Table B.1. Surface area, pore volume, and average pore size of supports.

Material	**Source**	**BET specific surface area (m^2/g)**	**Pore volume (cm^3/g)**	**BJH desorption average pore size (nm)**
SiO_2	Grace, Davisil XWP 1000A	47	0.63	54
Al_2O_3	NorPro, SA31132	74	0.46	25
ZrO_2 (monoclinic)	Alfa Aesar, 43814	69	0.31	18
ZnO	Strem, 30-1405	12	0.08	27
TiO_2 (P25)	Aldrich, 718467	59	0.36	24

Table B.2. Surface area, pore volume, and average pore size of supported gold catalysts.

Material	Au wt%	Cat wt[a] (mg)	BET specific surface area (m^2/g)	Pore volume (cm^3/g)	BJH desorption average pore size (nm)
Au/SiO_2	1.08 ± 0.31	36	45	0.63	56
Au/Al_2O_3	0.78 ± 0.13	46	64	0.40	25
Au/ZrO_2	1.08 ± 0.17	89	60	0.28	19
Au/ZnO	0.94 ± 0.18	87	13	0.15	45
Au/TiO_2 (P25)	1.10 ± 0.08	52	58	0.56	38
Au/TiO_2 (Strem, 79-0165)	0.95 ± 0.13	63	48	0.37	31

[a] Weight of catalyst used in in situ UV-Vis/reactivity tests

Table B.3. Average and standard deviation of Au SPR peak position of gold catalysts during O_2/He/H_2 adsorption cycles at 398 K[a]

Material	λ_{SPR} (nm) 1: in O_2	λ_{SPR} (nm) 2: in He after O_2	λ_{SPR} (nm) 3: in H_2	λ_{SPR} (nm) 4: in He after H_2
Au/SiO_2	517.1 (0.3)	516.7 (0.3)	514.9 (0.3)	515.2 (0.3)
Au/Al_2O_3	526.1 (0.4)	525.3 (0.3)	522.5 (0.3)	522.9 (0.3)
Au/ZrO_2	528.5 (0.9)	527.0 (0.8)	522.9 (0.7)	523.5 (0.8)
Au/ZnO	543.3	541.2	531.9	534.5

	(1.0)	(0.9)	(0.8)	(0.9)
Au/TiO_2 (P25)	574.8 (1.0)	571.9 (1.0)	566.3 (0.7)	568.2 (0.8)
Au/TiO_2 (Strem, 79-0165)	575.2 (0.8)	569.6 (1.0)	552.4 (0.9)	554.8 (0.8)

[a] Average of 3 cycles (2 for He after H_2) shown in **Figure 3.3**

Table B.4. Top (layers) surface and bulk atoms (excluding interface) calculation formulas.

Description	**Acronym**	**CN**	**Formula (m>2, l = m+1)**
Corner	tS-C	6	$\text{tS-C} = 12$
Edge (hexagonal face-hexagonal face)	tS-EHH	7	$\text{tS-EHH} = 3(m-2) + 6(l-m-1)$
Edge (hexagonal face-square face)	tS-EHS	7	$\text{tS-EHS} = 12(m-2)$
Square face	tS-SF	8	$\text{tS-SF} = 3(m-2)^2$
Hexagonal face	tS-HF	9	$\text{tS-HF} = -\frac{3}{2}m^2 + 9ml - \frac{33}{2}m - 12l + 25$
Bulk	B_t	12	$B_t = -m^3 - \frac{1}{3}l^3 + \frac{9}{2}m^2l + \frac{3}{2}ml^2 - \frac{9}{2}m^2 - 18ml + \frac{53}{2}m + \frac{28}{3}l - 16$
Total top surface atoms	n_{tS}	6-9	n_{tS}=tS-C + tS-EHH + tS-EHS + tS-SF + tS-HF
Total top atoms	n_t		$n_t = n_{tS} + B_t$

Nomenclature:
m = number of atoms in a single edge

l = number of atom layers in a particle
CN = coordination number
d = apparent particle diameter

Table B.5. Interface (bottom layer) surface and bulk atoms calculation formulas.

Description	**Acronym**	**CN**	**Formula (m>2, l = m+1)**
Corner	iS-C	5	iS-C $= 6$
Edge (hexagonal face-outward sloping)	iS-EHO	6	iS-EHO $= 3(m + l - 3)$
Edge (hexagonal face-inward sloping)	iS-EHI	7	iS-EHI $= 3(l - 2)$
Bulk (interface)	B_i	9	$B_i = \frac{9}{2}m^2 - l^2 + 3ml - \frac{33}{2}m - l + 12$
Total surface interface atoms	n_{iS}	5-7	n_{iS} = iS-C + iS-EHO + iS-EHI
Total interface atoms	n_i		$n_i = n_{iS} + B_i$

Nomenclature:
m = number of atoms in a single edge
l = number of atom layers in a particle
CN = coordination number
d = apparent particle diameter

Table B.6. Apparent diameter and dispersion calculation formulas.

Description	**Acronym**	**CN**	**Formula (m>2, l = m+1)**
Top hexagon average side length	S_t	-	$S_t = (m - 1)$
Interface hexagon average side length	S_i	-	$S_i = \mathbf{1.5}(\boldsymbol{m} - \mathbf{1})$
Particle average hexagon side length	S	-	$S = 0.5(S_t + S_i)$
Particle average hexagon diameter (nm)	d_H	-	$d_H = 2S \times 0.2884$ Gold atomic diameter = 0.2884 nm
Particle average apparent diameter (nm)	d	-	$d = d_H + 0.2884$
Total atoms	n_T	-	$n_T = n_t + n_i$
Total surface atoms	n_S	5-9	$n_S = n_{tS} + n_{iS}$
Fraction of total surface atoms (Dispersion)	D_S	5-9	$D_S = n_S/n_T$
Fraction of total top surface atoms	D_{tS}	6-9	$D_{tS} = n_{tS}/n_T$
Fraction of interface (perimeter) surface atoms	D_i	5-7	$D_i = n_{iS}/n_T$
Fraction of interface surface corner atoms	D_{iSC}	5	$D_{iSC} = (iS\text{-}C)/n_T$
Fraction of top surface corner atoms	D_{tSC}	6	$D_{tSC} = (tS\text{-}C)/n_T$

Nomenclature:
m = number of atoms in a single edge
l = number of atom layers in a particle
CN = coordination number
d = apparent particle diameter

Table B.7. Detailed results of site statistics for Au NPs using formulas from **Table B.4.** to **B.7.**

	A	B	C	D	E	F	G	H	I	J	K	L	M	N	O	P	Q	R	S	T	U	V
1	**Site Statistics Top Slice of Truncated Octahedron Supported on a (111) Plane**																					
2																						
3	m	number of atoms in a single edge		m>2		J. Phys. Chem. B 2006, 110, 11, 5286 (Formulas in Supporting Information File)																
4	l=m+1	number of atom layers in a particle				Anna Carlsson, Anna Puig-Molina, and Ton V. W. Janssens																
5						http://pubs.acs.org/doi/suppl/10.1021/jp0569537																
6				m																		
7		Top Layers Surface and Bulk Atoms	CN	2	3	4	5	6	7	8	9	10	11	12	13	14	15	16	17	18	19	20
8	tS-C	Corner	6	12	12	12	12	12	12	12	12	12	12	12	12	12	12	12	12	12	12	12
9	tS-EHH	Edge HF-HF	7	0	3	6	9	12	15	18	21	24	27	30	33	36	39	42	45	48	51	54
10	tS-EHS	Edge HF-SF	7	0	12	24	36	48	60	72	84	96	108	120	132	144	156	168	180	192	204	216
11	tS-SF	Square Face	8	0	3	12	27	48	75	108	147	192	243	300	363	432	507	588	675	768	867	972
12	tS-HF	Hexagonal Face	9	4	22	55	103	166	244	337	445	568	706	859	1027	1210	1408	1621	1849	2092	2350	2623
13	Bt	Bulk	12	3	30	109	268	535	938	1505	2264	3243	4470	5973	7780	9919	12418	15305	18608	22355	26574	31293
14	ntS	Total Top Surface		16	52	109	187	286	406	547	709	892	1096	1321	1567	1834	2122	2431	2761	3112	3484	3877
15	nt	Total Top		19	82	218	455	821	1344	2052	2973	4135	5566	7294	9347	11753	14540	17736	21369	25467	30058	35170
16		Interface Surface and Bulk Atoms	CN																			
17	iS-C	Corner	5	6	6	6	6	6	6	6	6	6	6	6	6	6	6	6	6	6	6	6
18	iS-EHO	Edge HF-OS	6	0	6	12	18	24	30	36	42	48	54	60	66	72	78	84	90	96	102	108
19	iS-EHI	Edge HF-IS	7	3	6	9	12	15	18	21	24	27	30	33	36	39	42	45	48	51	54	57
20	Bi	Bulk	9	3	19	48	90	145	213	294	388	495	615	748	894	1053	1225	1410	1608	1819	2043	2280
21	niS	Total Interface Surface		9	18	27	36	45	54	63	72	81	90	99	108	117	126	135	144	153	162	171
22	ni	Total Interface		12	37	75	126	190	267	357	460	576	705	847	1002	1170	1351	1545	1752	1972	2205	2451
23		Total Atoms in Particle																				
24	nT	Total Atoms		31	119	293	581	1011	1611	2409	3433	4711	6271	8141	10349	12923	15891	19281	23121	27439	32263	37621
25	nS	Total Surface		25	70	136	223	331	460	610	781	973	1186	1420	1675	1951	2248	2566	2905	3265	3646	4048
26	St	Top Hx Average Side Length		1	2	3	4	5	6	7	8	9	10	11	12	13	14	15	16	17	18	19
27	Si	Interface Hx Aver Side Length		1.5	3	4.5	6	7.5	9	10.5	12	13.5	15	16.5	18	19.5	21	22.5	24	25.5	27	28.5
28	S	Particle Aver Hx Side Length		1.25	2.5	3.75	5	6.25	7.5	8.75	10	11.25	12.5	13.75	15	16.25	17.5	18.75	20	21.25	22.5	23.75
29	dH	Particle Aver Hx Diameter, nm		0.72	1.44	2.16	2.88	3.61	4.33	5.05	5.77	6.49	7.21	7.93	8.65	9.37	10.09	10.82	11.54	12.26	12.98	13.70
30	d	Particle App Diameter, nm		1.01	1.73	2.45	3.17	3.89	4.61	5.34	6.06	6.78	7.50	8.22	8.94	9.66	10.38	11.10	11.82	12.55	13.27	13.99
31		Dispersion	CN																			
32	DS	Fraction Surface Atoms nS/nT	5-9	8.06E-01	5.88E-01	4.64E-01	3.84E-01	3.27E-01	2.86E-01	2.53E-01	2.27E-01	2.07E-01	1.89E-01	1.74E-01	1.62E-01	1.51E-01	1.41E-01	1.33E-01	1.26E-01	1.19E-01	1.13E-01	1.08E-01
33	DtS	Fraction Surface Top Atoms ntS/nT	6-9	5.16E-01	4.37E-01	3.72E-01	3.22E-01	2.83E-01	2.52E-01	2.27E-01	2.07E-01	1.89E-01	1.75E-01	1.62E-01	1.51E-01	1.42E-01	1.34E-01	1.26E-01	1.19E-01	1.13E-01	1.08E-01	1.03E-01
34	Di	Fract Interface Surf At niS/nT	5-7	2.90E-01	1.51E-01	9.22E-02	6.20E-02	4.45E-02	3.35E-02	2.62E-02	2.10E-02	1.72E-02	1.44E-02	1.22E-02	1.04E-02	9.05E-03	7.93E-03	7.00E-03	6.23E-03	5.58E-03	5.02E-03	4.55E-03
35	DiSC	Fract Int Surf Corner At tS-C/nT	5	1.94E-01	5.04E-02	2.05E-02	1.03E-02	5.93E-03	3.72E-03	2.49E-03	1.75E-03	1.27E-03	9.57E-04	7.37E-04	5.80E-04	4.64E-04	3.78E-04	3.11E-04	2.60E-04	2.19E-04	1.86E-04	1.59E-04
36	DtSC	Fract Top Surf Corner At tS-C/nT	6	3.87E-01	1.01E-01	4.10E-02	2.07E-02	1.19E-02	7.45E-03	4.98E-03	3.50E-03	2.55E-03	1.91E-03	1.47E-03	1.16E-03	9.29E-04	7.55E-04	6.22E-04	5.19E-04	4.37E-04	3.72E-04	3.19E-04

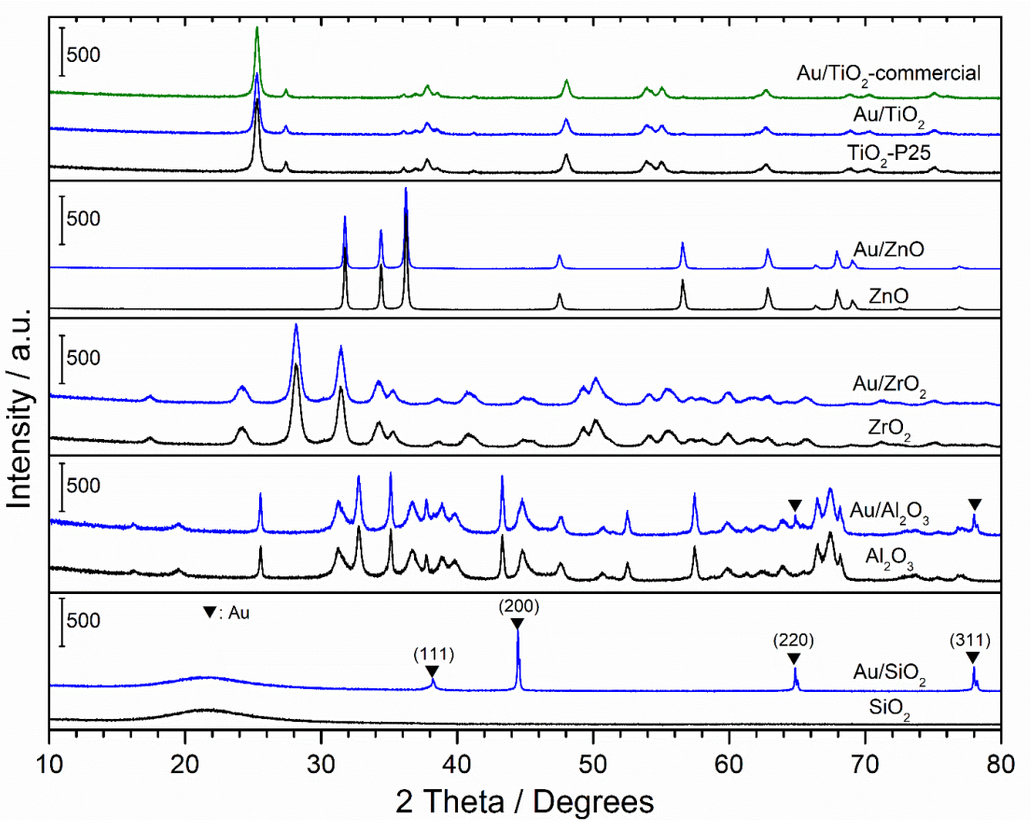

Figure B.1. X-ray diffractograms of supports (SiO_2, Al_2O_3, ZrO_2, ZnO, and TiO_2 (P25) in (**Table B.1**) and supported Au catalysts (Au/SiO_2, Au/Al_2O_3, Au/ZrO_2, Au/ZnO, and Au/TiO_2 (P25) in Table B.2).

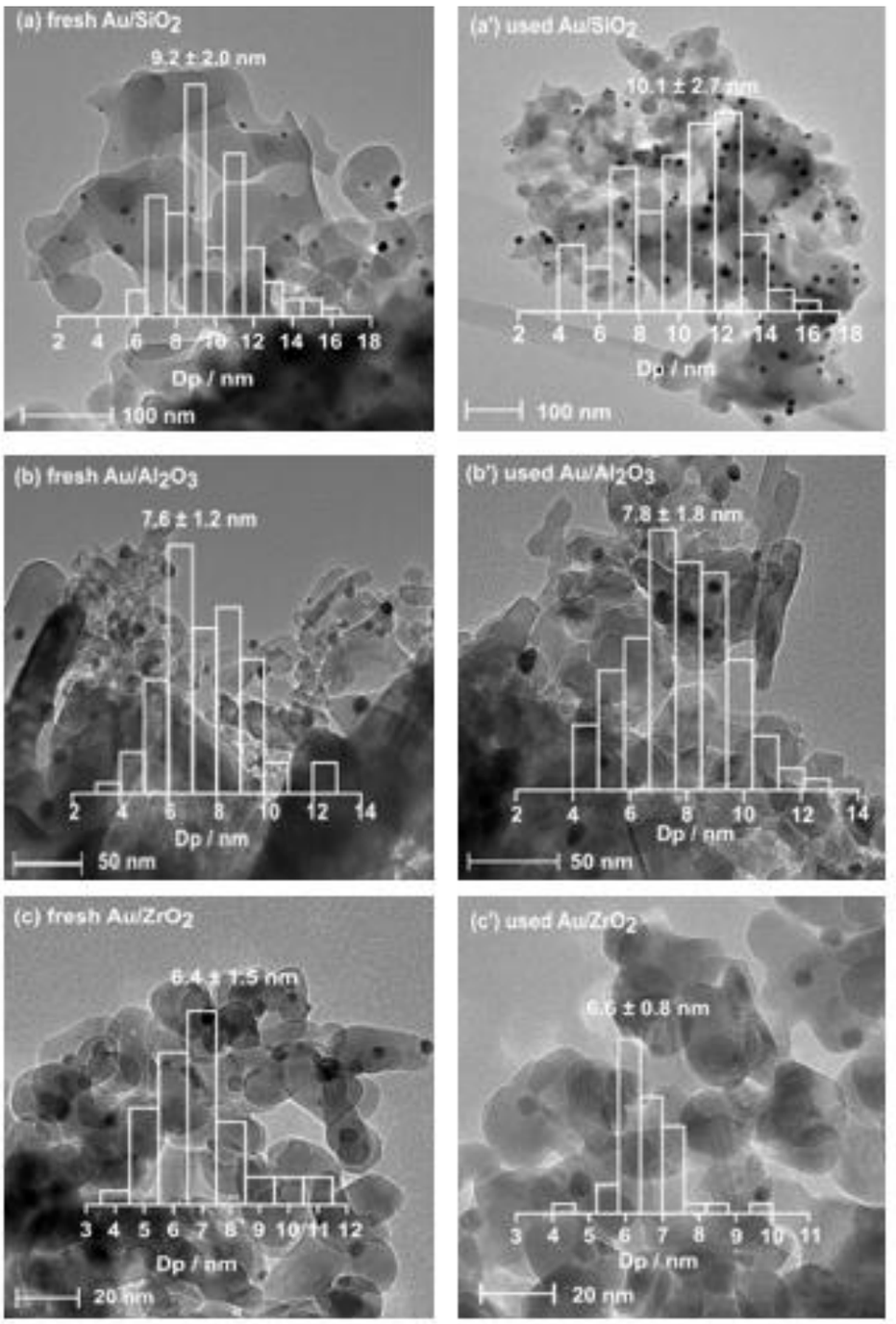

Figure B.2. TEM images of calcined Au catalysts: a) fresh Au/SiO_2; a') used Au/SiO_2; b) fresh Au/Al_2O_3; b') used Au/Al_2O_3; c) fresh Au/ZrO_2; and c') used Au/ZrO_2.

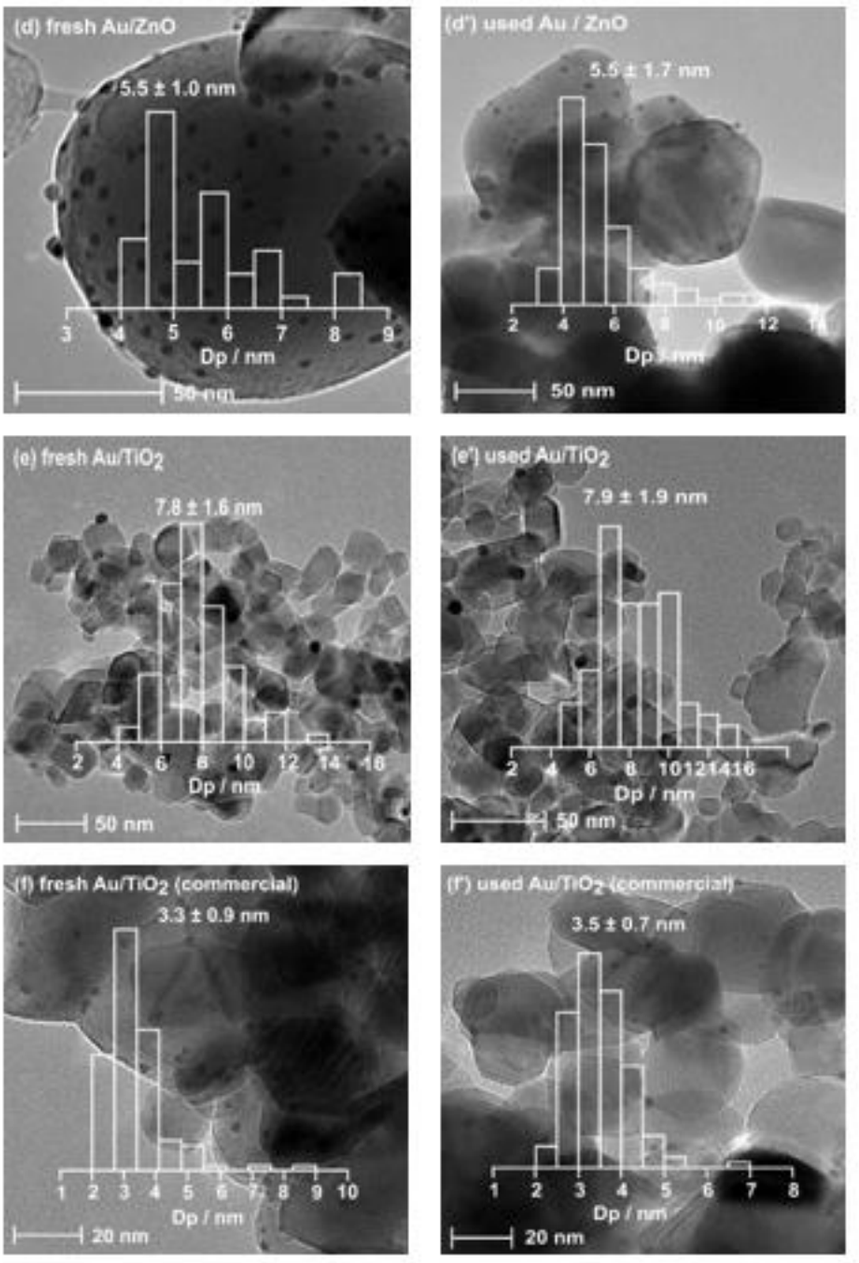

Figure B.2 (continued). TEM images of calcined Au catalysts: d) fresh Au/ZnO; d') used Au/ZnO; e) fresh Au/TiO_2 (P25); e') used Au/TiO_2 (P25); f) fresh Au/TiO_2 (commercial, Strem 79-0165); and f') used Au/TiO_2 (commercial, Strem 79-0165).

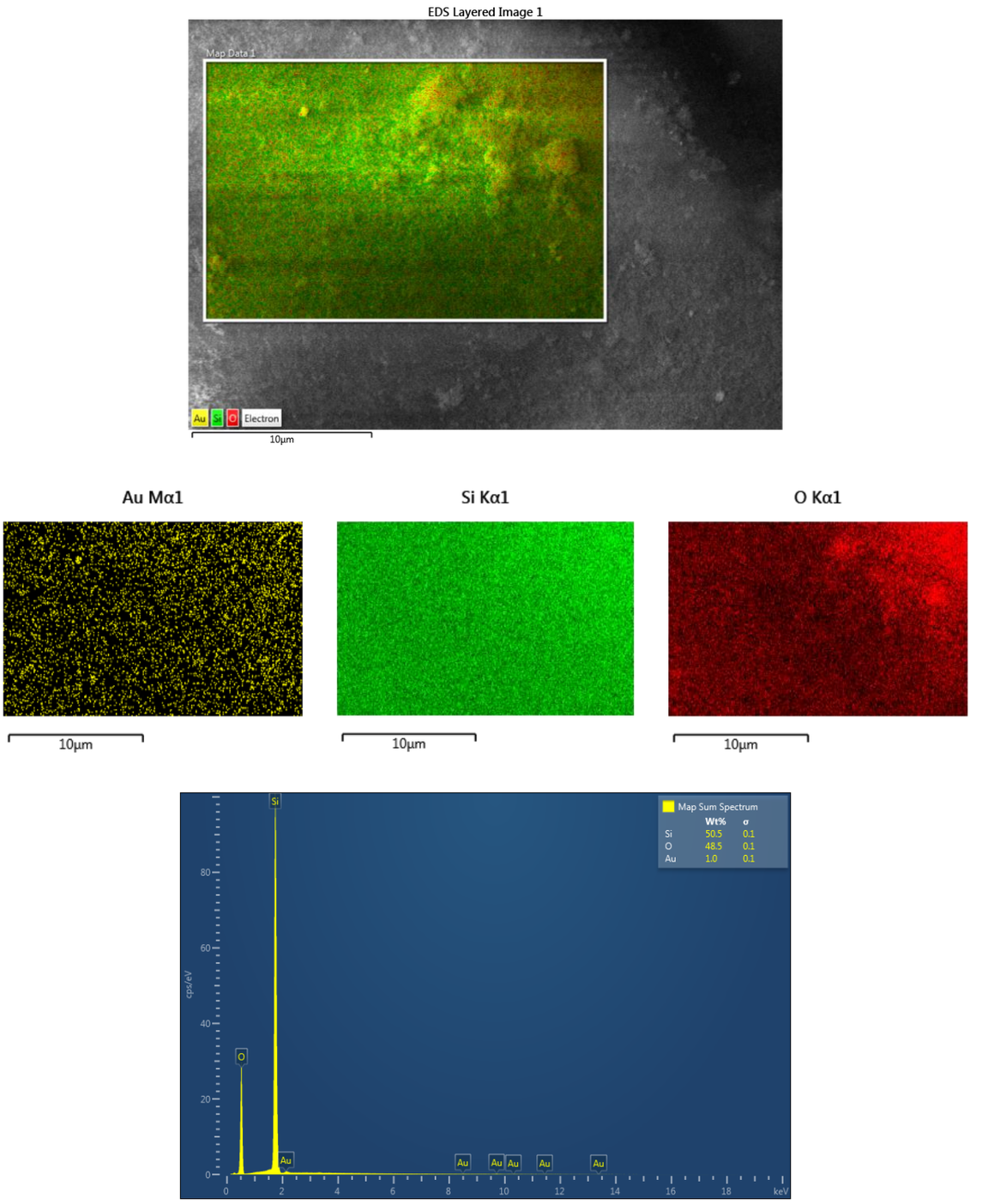

Figure B.1. Au/SiO_2 SEM-EDX elemental mapping and analysis sample. Au average content = 1.08 ± 0.31 wt% from average of 5 different spots (showing only 1 for illustration)

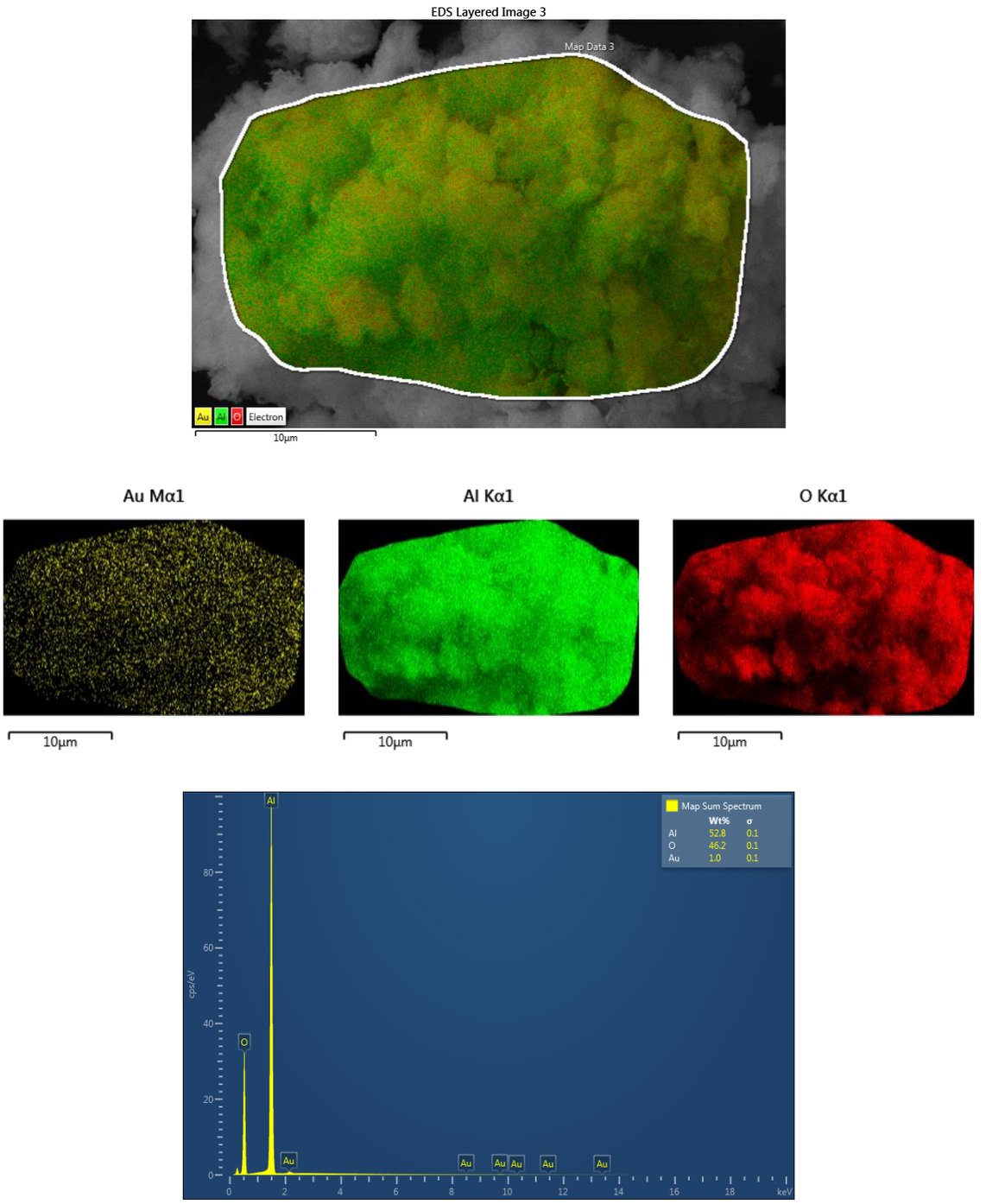

Figure B.4. Au/Al_2O_3 SEM-EDX elemental mapping and analysis sample. Au average content = Au 0.78 ± 0.13 wt% from average of 5 different spots (showing only 1 for illustration).

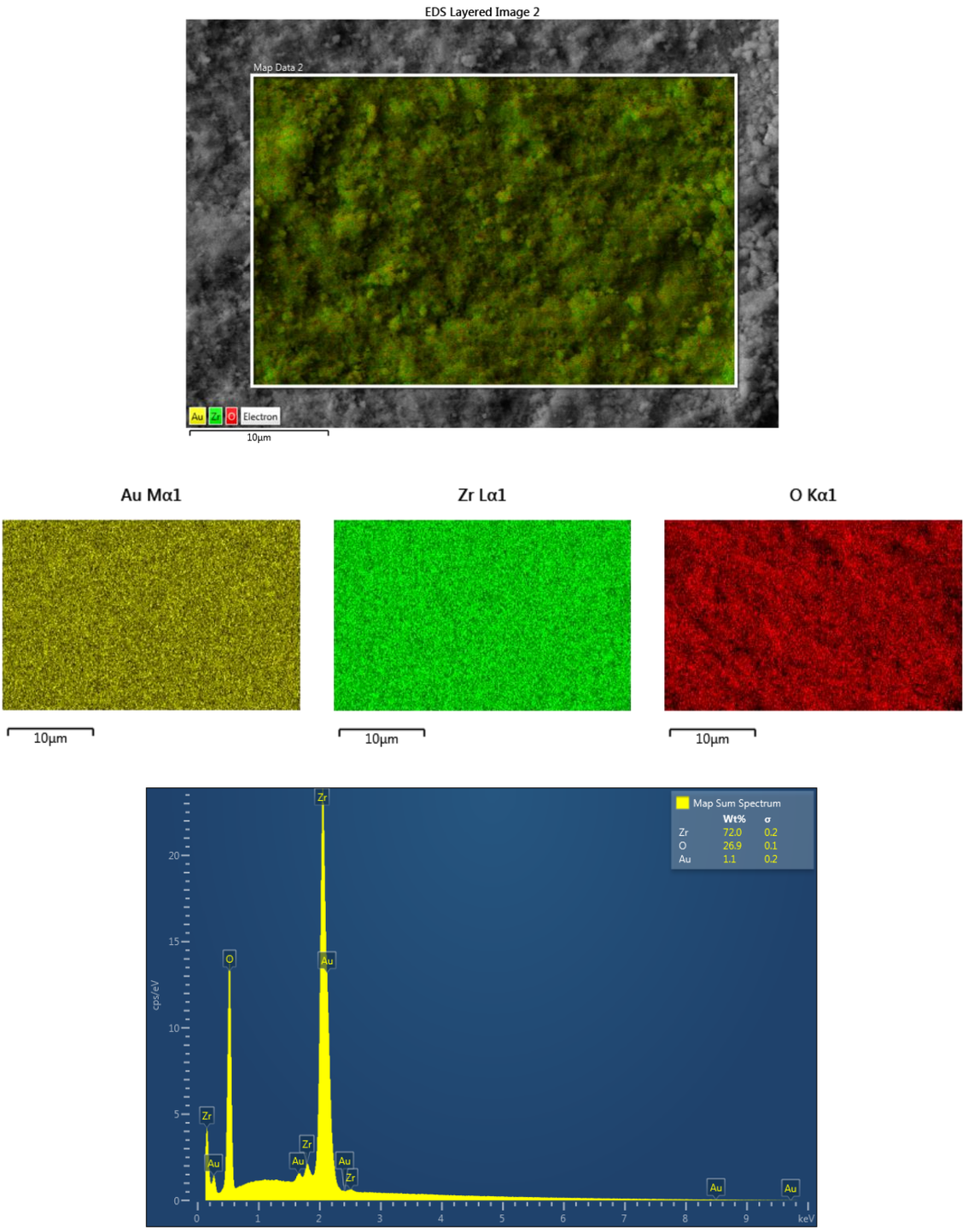

Figure B.5. Au/ZrO_2 SEM-EDX elemental mapping and analysis sample. Au average content = Au 1.08 ± 0.17 wt% from average of 5 different spots (showing only 1 for illustration).

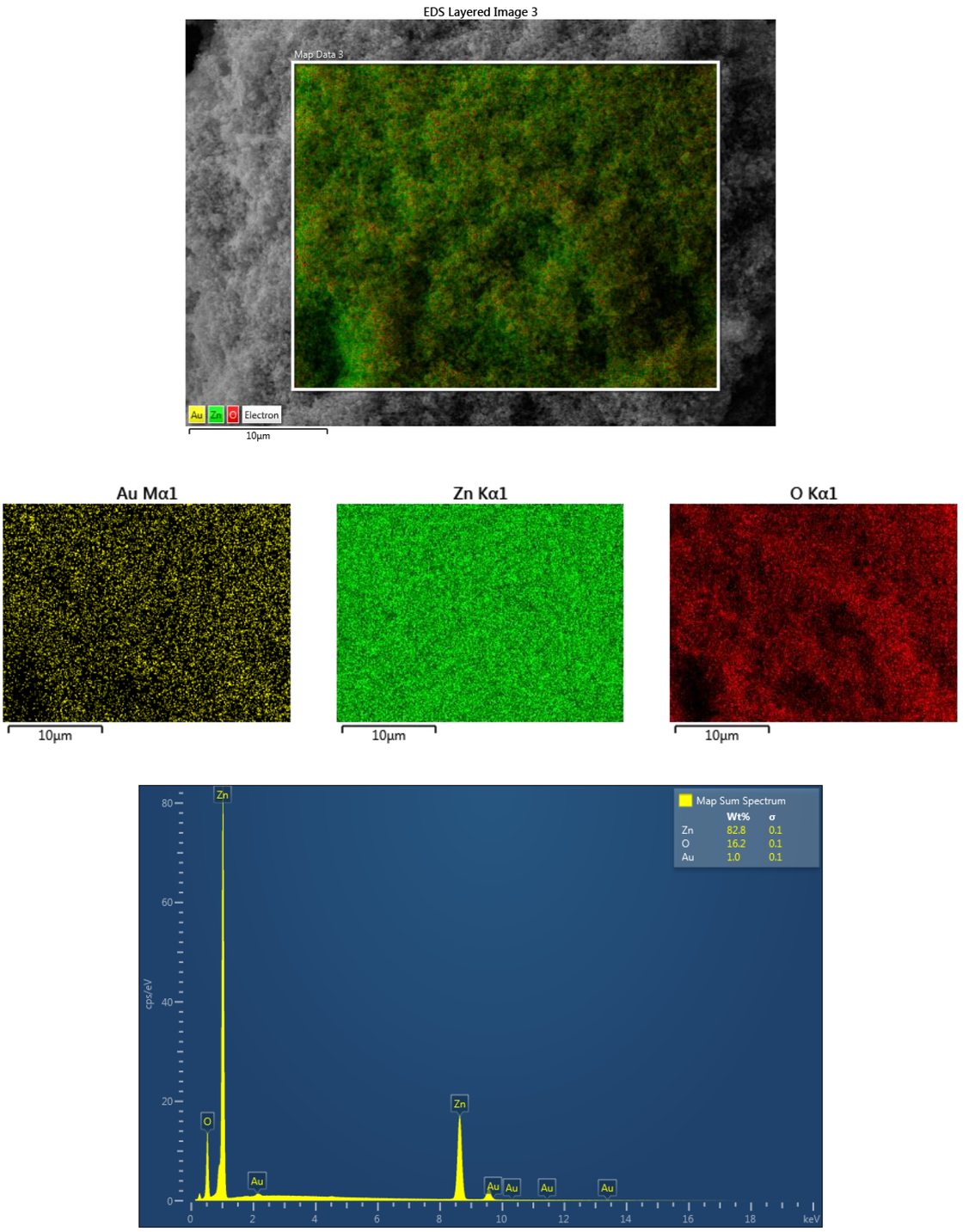

Figure B.6. Au/ZnO SEM-EDX elemental mapping and analysis sample. Au average content = Au 0.94 ± 0.18 wt% from average of 5 different spots (showing only 1 for illustration).

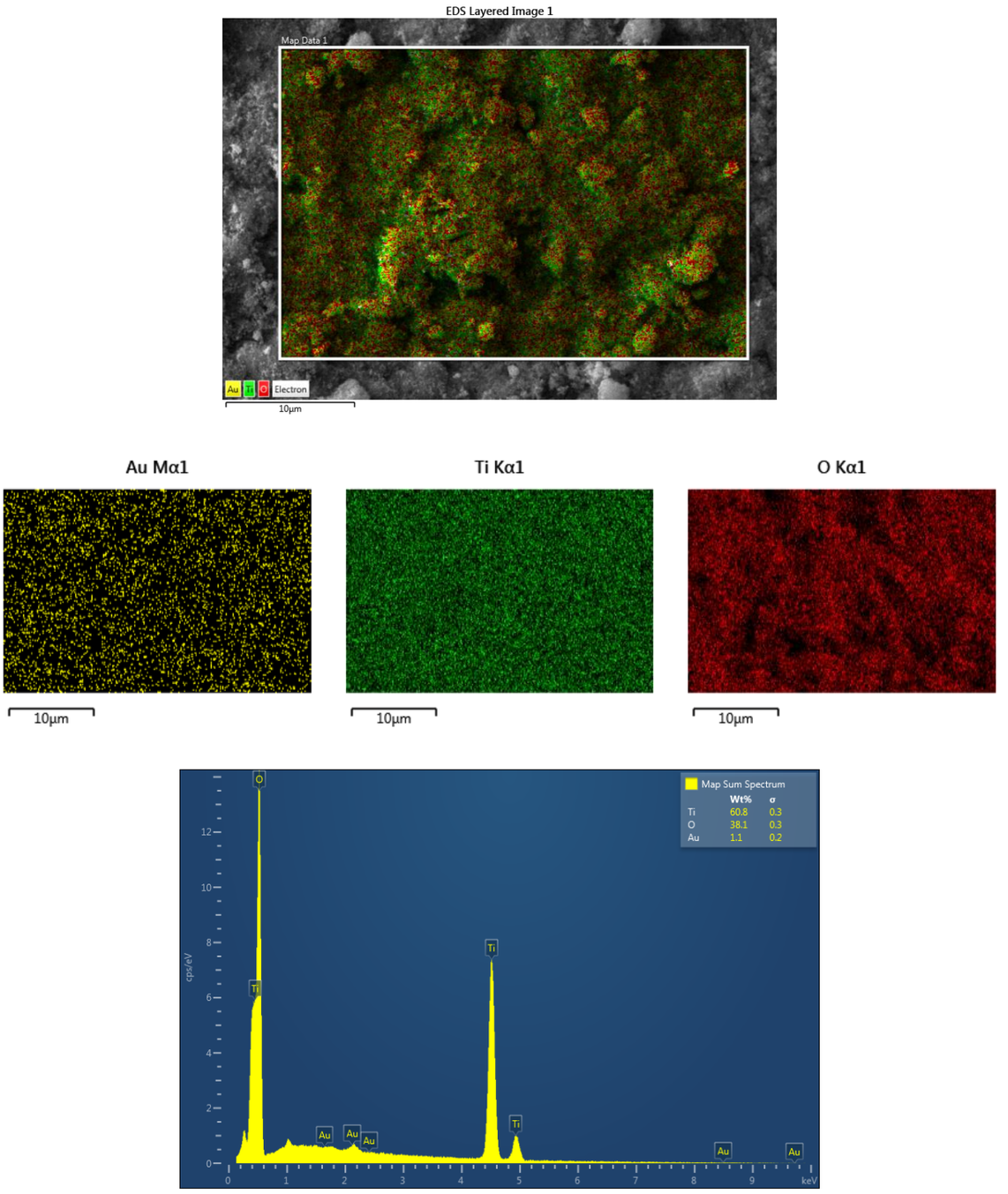

Figure B.7. Au/TiO_2 (P25) SEM-EDX elemental mapping and analysis sample. Au average content = Au 1.10 ± 0.08 wt% from average of 5 different spots (showing only 1 for illustration).

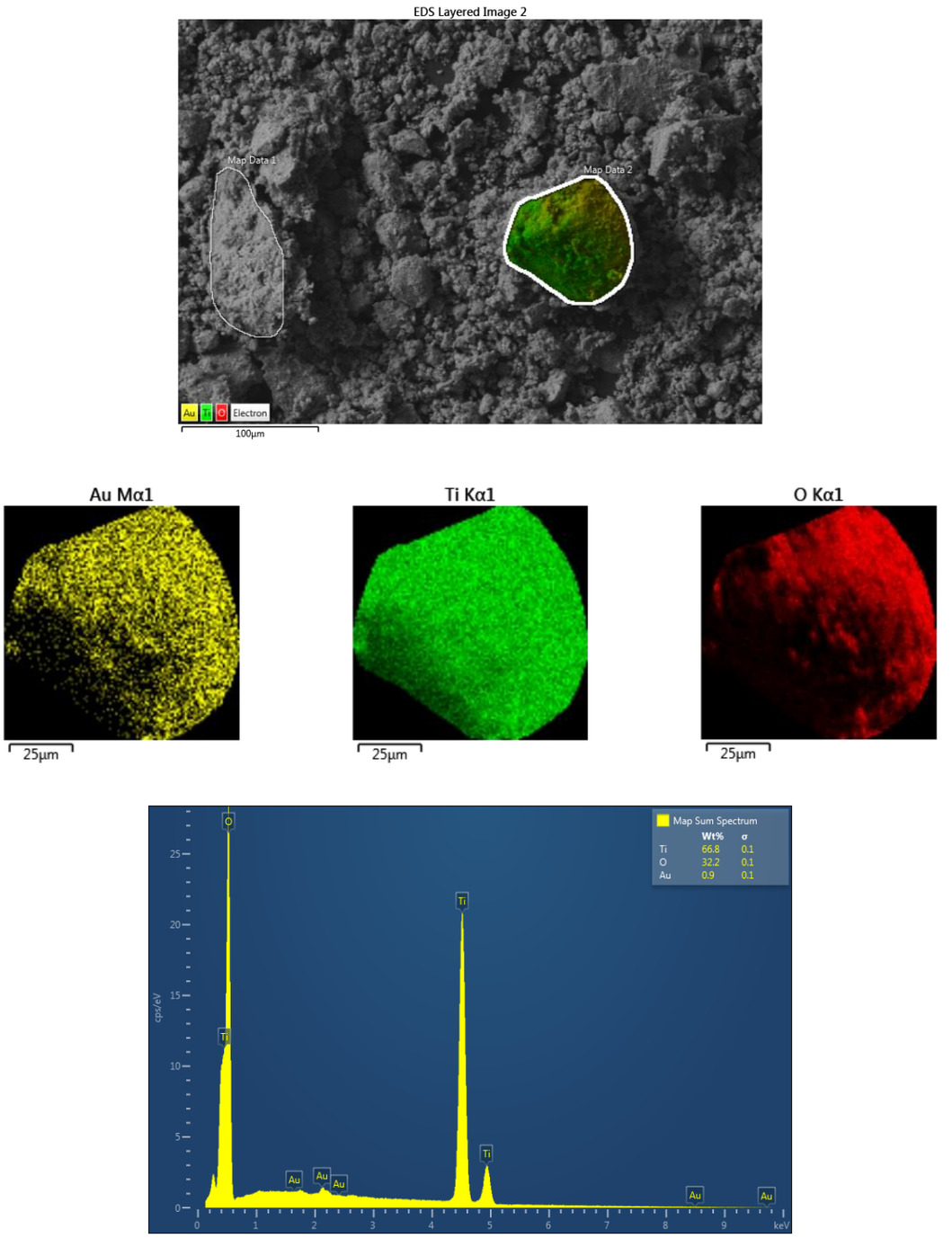

Figure B.8. Au/TiO_2 (Strem) SEM-EDX elemental mapping and analysis sample. Au average content = Au 0.95 ± 0.13 wt% from average of 5 different spots (showing only 1 for illustration).

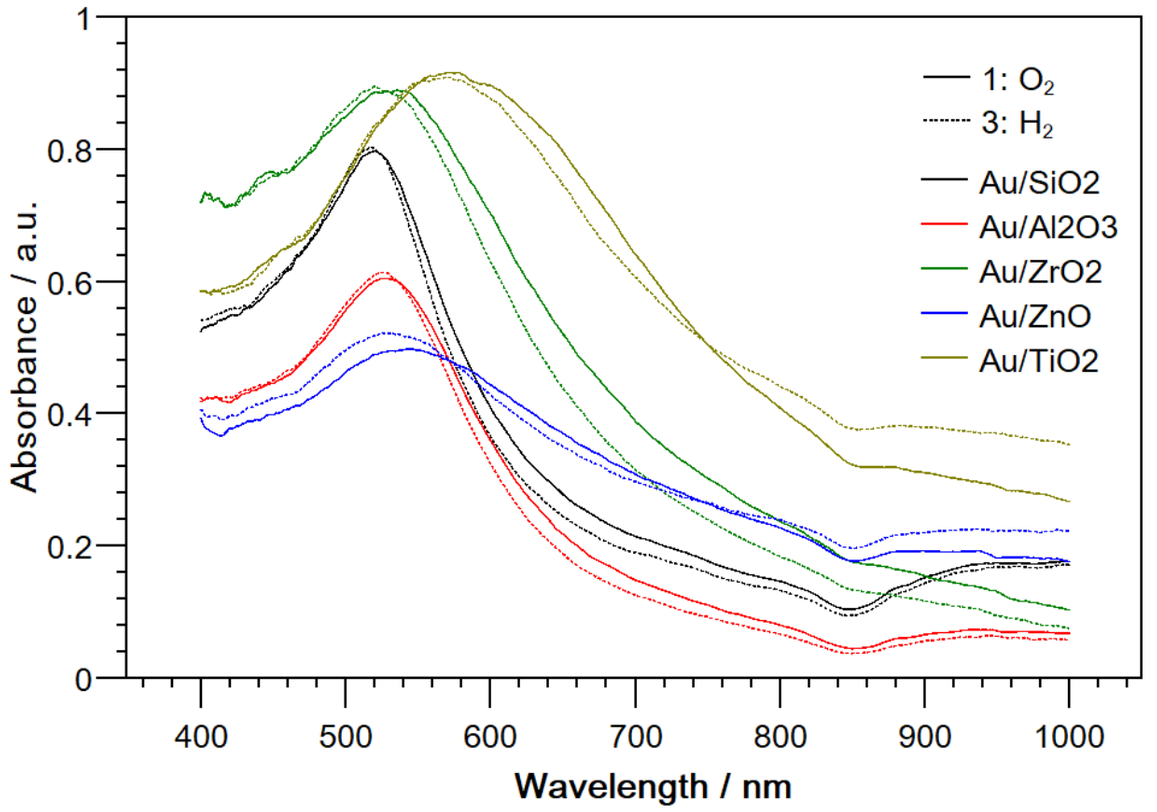

Figure B.9. In situ UV-Vis spectra of Au/SiO_2, Au/Al_2O_3, Au/ZrO_2, Au/ZnO, and Au/TiO_2 under O_2 and H_2 gas atmospheres at 125 °C.

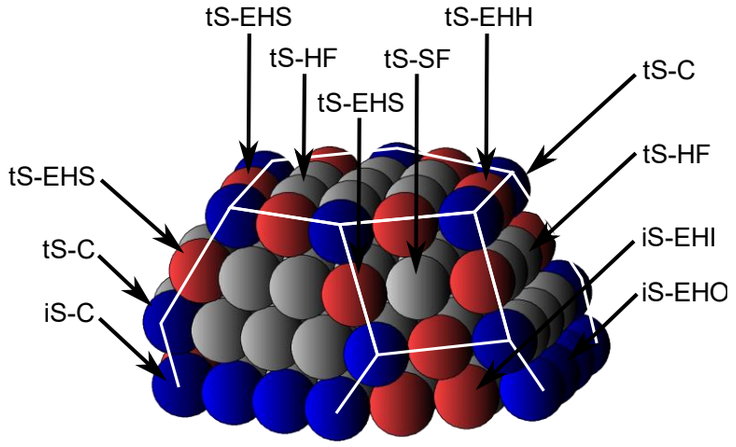

Figure B.10. Top slice of a truncated octahedron model for site statistics of gold nanoparticles (m = 3, l = m+1). Acronyms: S: top surface atoms; I: interface atoms; EHS-edge (hexagonal face-square face) atoms; EHH: edge (hexagonal face-hexagonal face) atoms; HF: hexagonal face atoms; SF: square face atoms; EHI: edge (hexagonal face inward sloping); EHO: (hexagonal face outward sloping).

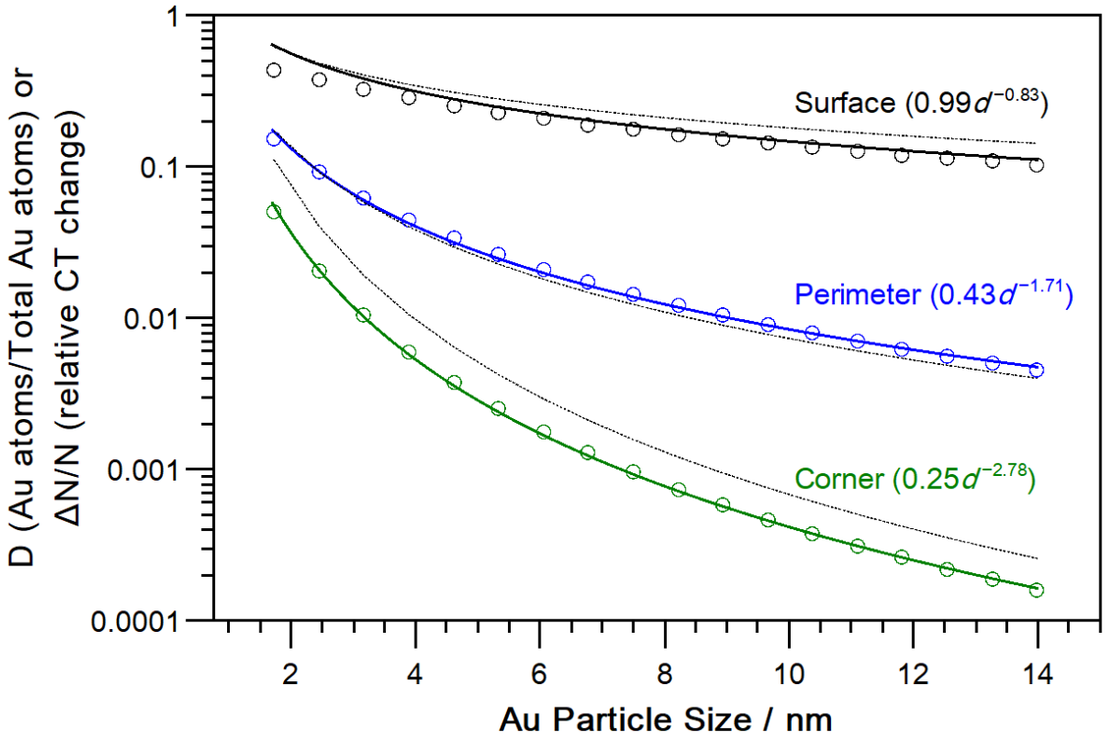

Figure B.11. Fraction of top surface (excluding perimeter), perimeter, and corner (perimeter only) atoms with respect to total Au atoms in a particle as a function of gold particle size for a top slice of a truncated octahedron with m number of side atoms and m+1 atom layers supported on a (111) plane.

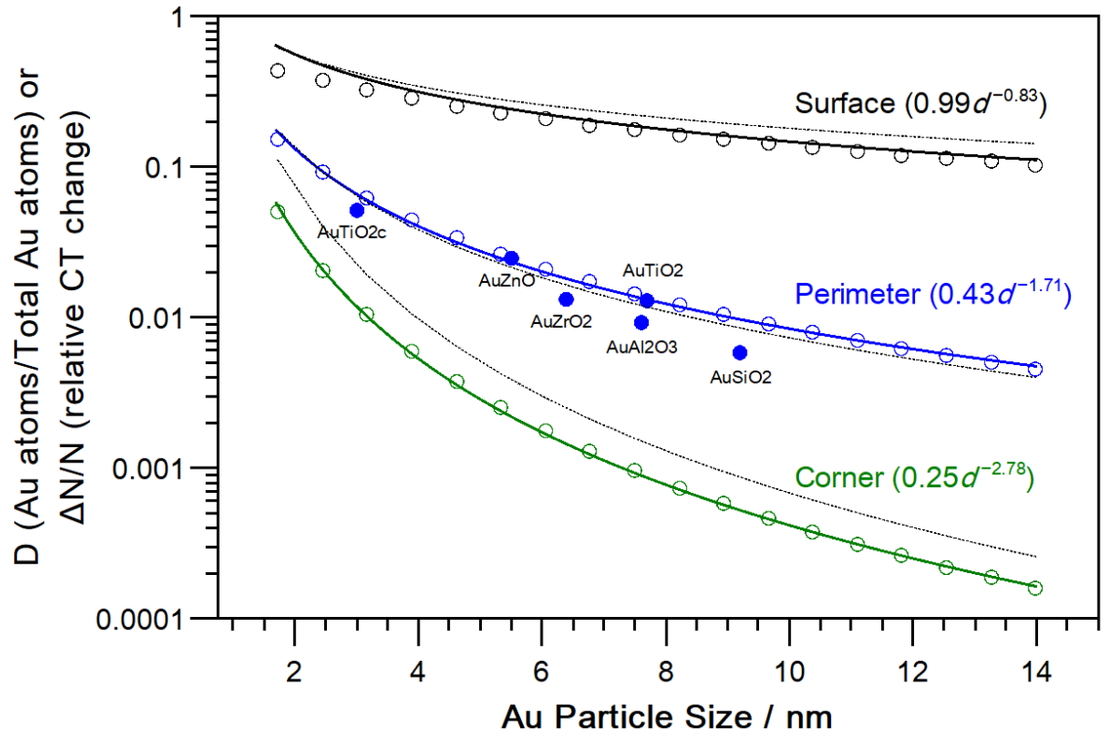

Figure B.12. Correlation between gold average particle diameter *vs* dispersion (D) = fraction of surface gold atoms with respect to the total amount of Au in a NP (empty symbols) and $\Delta N/N$ = fraction of electron density change (charge transfer, CT) from Au SPR peaks (Equation 3, **Table B.3**) in He after flowing O_2 and H_2 (solid blue symbols) on gold catalysts at 398 K. Here, D is the dispersion or fraction of surface sites which are proportional to $1/d^m$, where d is the average gold nanoparticle size in nm and m=0.83 for the (top) surface atoms (coordination number = 6−9), m=1.71 for perimeter atoms (coordination number = 5−7), or m=2.78 for corner (perimeter) atoms (coordination number = 5). Values of m were determined from atom statistics for a gold nanoparticle modeled as the top slice of a truncated octahedron (detailed calculations can be found in the Supporting Information, **Tables B.4-B.7**) [1]. For comparison, the corresponding site statistics for a Au nanoparticle with truncated cuboctahedra geometry was

also added (dotted line) as reported by Ribeiro and co-workers: Surface ($0.90d^{-0.70}$), Perimeter ($0.90d^{-1.8}$), and Corner ($0.90d^{-2.9}$) [2].

B.5. Derivation of the relationship between gold nanoparticles plasmon absorption position (λ_m) and support refractive index (n_0) in supported gold catalysts.

In analogy with colloidal dilute systems containing small adsorbing nanoparticles, we derived the corresponding relationship between gold nanoparticle plasmon peak position and the refractive index of the medium they are imbedded. In such systems, absorption is given by the attenuation of a light beam of intensity I_o over a path length d:

$$A = log_{10}\left(\frac{I_o}{I_d}\right) = N_p C_{ext} d/2.303 \tag{B22}$$

Where N_p is the number of particles per unit volume and C_{ext} is the extinction cross section of a single particle [5]. For particles smaller than the wavelength of light imbedded in a medium of refractive index n_0, it has been shown that C_{ext} is [5, 6]:

$$C_{ext} = \frac{24\pi^2 R^3 n_0^3}{\lambda} \frac{\epsilon_2}{(\epsilon_1 + 2n_0^2)^2 + \epsilon_2^2} \tag{B23}$$

Where R is the radius of a spherical nanoparticle, λ is the wavelength, ϵ_1 and ϵ_2 are the real and imaginary parts of the dielectric function ($\epsilon = \epsilon_1 + i\epsilon_2$). Here, the dielectric constant of the nonabsorbing matrix was taken as $\epsilon_m = n_0^2$.[5, 6] For many metals, the bulk plasma frequency is dominated by the free electron behavior. At such conditions, the dielectric function's real and imaginary part are well described by Drude's free electron model of the form:[5, 6]

$$\epsilon_1 = \epsilon^{\infty} - \frac{4\pi N e^2 \lambda^2}{(2\pi c)^2 m_e} \tag{B24}$$

$$\epsilon_2 = \frac{4\pi N^2 e^4 \lambda^3}{(2\pi c)^3 m_e^2 \sigma_0} \tag{B25}$$

Where ϵ^{∞} is the high frequency dielectric constant due to interband and core transitions, c is the velocity of light, and σ_0 is the dc (at zero frequency) electrical conductivity of the metal [5-7]: Substitution of Equations B24 and B25 in Equation B23 gives [6]:

$$C_{ext} = \frac{12\pi^2 R^3 n_0^3 c}{\sigma_0} \frac{\lambda^2}{(\lambda_m^2 - \lambda^2)^2 + \lambda^6/\lambda_a^2} \tag{B26}$$

Where, λ_m is the approximate wavelength at which maximum absorption occurs. Also:

$$\lambda^2 = {(2\pi c)^2 m_e}/{4\pi N e^2} \tag{B27}$$

$$\lambda_a = {2\lambda_p^2 \sigma_0}/{c} \tag{B28}$$

$$\lambda_p^2 = {(2\pi c)^2}/{\omega_p^2} \tag{B29}$$

$$\omega_p^2 = \frac{N e^2}{m_e \epsilon_0} \tag{B30}$$

Where λ_p is the metal's bulk plasma wavelength [5], ω_p is the bulk plasmon frequency, N is the concentration of conduction electrons, e is their electronic charge, m_e is their effective electron mass, and ϵ_0 is the permittivity of vacuum.[8, 9].

Since Equation B26 has a Lorentzian shape, its full width at one-half the maximum (FWHM) of absorption can be approximated by:

$$FWHM \approx \frac{\lambda_m^2}{\lambda_a} = \frac{(\epsilon^\infty + 2n_0^2)c}{2\sigma_0} \tag{B31}$$

After substitution of λ_a and rearranging:

$$\lambda_m^2 = \lambda_p^2(\epsilon^\infty + 2n_0^2) = \lambda_p^2\epsilon^\infty + \lambda_p^2(2n_0^2) \tag{B32}$$

B.6. Derivation of the relationship between gold nanoparticles plasmon absorption position shift (λ_m) and charge transfer (N).

The real part of the Drude's dielectric function in Equation B24 can be also expressed as a function of frequencies [5, 9]:

$$\epsilon_1 = \epsilon^\infty - \frac{\omega_p^2}{\omega^2} \tag{B33}$$

Upon charge transfer to the gold NPs, the dielectric function changes due to changes to the plasma frequency (Equation B30) and can be expressed as:[5, 9]

$$\epsilon_1 = \epsilon^\infty - \frac{\omega_p^2 + \Delta\omega_p^2}{\omega^2} \tag{B34}$$

The absorption modes of a small metal NP of arbitrary shape consists of several plasmon modes that in general fulfill:[5, 9]

$$(1 - L)\epsilon_m + L\epsilon_1 = 0 \tag{B35}$$

Where L is a shape-dependent depolarization factor and $\epsilon_m = n_0^2$. Combining Equations B27, B30, B34, and B35 results in:

$$(1 - L)\epsilon_m + L\epsilon^\infty - L\frac{\lambda^2}{\lambda_p^2}\left(1 + \frac{\Delta N}{N}\right) = 0 \tag{B36}$$

Here, λ is the measured SPR peak wavelength, N is the electron density of the metal, and ΔN is the change in the nanoparticle electron density. After rearranging Equation B36 for λ^2:

$$\lambda^2 = \frac{\lambda_p^2[\epsilon^\infty + (1/L - 1)\epsilon_m]}{\left(1 + \frac{\Delta N}{N}\right)} = \frac{\lambda_m^2}{\left(1 + \frac{\Delta N}{N}\right)} \tag{B37}$$

The numerator term is equivalent to the right term of Equation B32 that defines λ_m^2. Therefore, subtracting λ_m^2 from both sides of Equation B32 and rearranging, yields:

$$\frac{\lambda_m^2 - \lambda^2}{\lambda_m^2} = 1 - \frac{1}{\left(1 + \frac{\Delta N}{N}\right)} \approx \frac{\Delta N}{N}\left[1 - \frac{\Delta N}{N} + \cdots\right] \tag{B38}$$

The right side of Equation B38 is approximated by a Taylor series. In the case when ΔN/N << 1, then:

$$\frac{\lambda_m^2 - \lambda^2}{\lambda_m^2} \approx \frac{\Delta N}{N} \tag{B39}$$

Equation B39 shows that the relative change of the squared SPR peak position with respect to a reference wavelength, in this case, the expected ideal Drude's model value, is proportional to the electron charge transferred to/from the gold NP.

From Equation B37 and following a similar procedure, it can be also shown that:

$$\frac{\lambda_m - \lambda}{\lambda_m} = 1 - \frac{1}{\left(1 + \frac{\Delta N}{N}\right)^{1/2}} \approx \frac{\Delta N}{2N}\left[1 - \frac{3}{4}\frac{\Delta N}{N} + \cdots\right] \quad \text{(B40)}$$

$$\frac{\lambda_m - \lambda}{\lambda_m} \approx \frac{\Delta N}{2N} \quad \text{(B41)}$$

Equation B41 shows that for small changes of the relative charge transfer, $\Delta N/N << 1$, the relative change of the SPR peak position with respect to a reference λ_m value is proportional to half the relative charge transfer to/from the gold NP.

B.7. CO conversion vs adsorbed oxygen relationship

In most cases, the CO conversion should tend to zero at decreasing values of $\Delta N/N \times n_{Au}$, except in the case when the reaction rate dependence is zero order with respect to oxygen. The in situ cell used in this work can be fairly described as a CSTR reactor as we have demonstrated recently [10]. For CO oxidation, the CSTR design equation is given by:

$$-r_{CO} = F_{CO}X_{CO}/V$$

Where $-r_{CO}$ is CO conversion rate per unit volume of reactor, F_{CO} is the volumetric flow rate of CO, X_{CO} is CO conversion, and V is the reactor volume.

CO conversion reaction rate can be also expressed by the general power rate law:

$$-r_{CO} = kP_{CO}^{a}P_{O2}^{b}$$

Combining these two equations:

$$F_{CO}X_{CO}/V = kP_{CO}^{a}P_{O2}^{b}$$

Or

$$X_{CO} = (kV/F_{CO})P_{CO}^{a}P_{O2}^{b}$$

Where k is the reaction rate constant and P_i is the partial pressure of component *I*.

In **Figure 3.7**., $\Delta N/N \times n_{Au}$ is proportional to the amount of adsorbed O_2 on Au and which is a function of P_{O2} (e.g., via a Langmuir adsorption model, $\theta_{O2} = K_{O2}P_{O2}/(1 + K_{O2}P_{O2})$, where θ_{O2} is the O_2 coverage). Therefore, from the previous equation, X_{CO} will be zero when P_{O2} tends to zero for almost all cases except when the rate dependence is zero order on oxygen (b = 0). In that case CO conversion is independent of the amount $\Delta N/N \times n_{Au}$ and should result in a constant value. In oxidation reactions, the reaction rate dependence on O_2 for CO oxidation on gold catalysts is often a positive non-zero value [11], indicating its involvement in reaction rate controlling steps. Therefore, on the reported catalysts in **Figure 3.7**, whose supports are inactive for CO oxidation, CO conversion will become zero for $\Delta N/N \times n_{Au}$ equal to zero.

B.8. References

1. Carlsson, A., Puig-Molina, A., and Janssens, T.V.W., New Method for Analysis of Nanoparticle Geometry in Supported fcc Metal Catalysts with Scanning Transmission Electron Microscopy. *The Journal of Physical Chemistry B* **2006,** *110* (11), 5286-5293.
2. Shekhar, M., Wang, J., Lee, W.S., Williams, W.D., Kim, S.M., Stach, E.A., Miller, J.T., Delgass, W.N., and Ribeiro, F.H., Size and Support Effects for the Water-Gas Shift Catalysis over Gold Nanoparticles Supported on Model Al2O3 and TiO2. *Journal of the American Chemical Society* **2012,** *134* (10), 4700-4708.
3. Kotobuki, M., Leppelt, R., Hansgen, D.A., Widmann, D., and Behm, R.J., Reactive oxygen on a Au/TiO2 supported catalyst. *Journal of Catalysis* **2009,** *264* (1), 67-76.
4. Widmann, D., Liu, Y., Schuth, F., and Behm, R.J., Support effects in the Au-catalyzed CO oxidation - Correlation between activity, oxygen storage capacity, and support reducibility. *Journal of Catalysis* **2010,** *276* (2), 292-305.
5. Mulvaney, P., Surface Plasmon Spectroscopy of Nanosized Metal Particles. *Langmuir* **1996,** *12* (3), 788-800.
6. Doremus, R.H., Optical Properties of Small Gold Particles. *The Journal of Chemical Physics* **1964,** *40* (8), 2389-2396.
7. Doyle, W.T., Absorption of Light by Colloids in Alkali Halide Crystals. *Phys. Rev.* **1958,** *111* (4), 1067-1072.
8. Kreibig, U. and Vollmer, M., *Optical properties of metal clusters*. Springer: Berlin (Germany), **1995;** p 1-553.
9. Mulvaney, P., Pérez-Juste, J., Giersig, M., Liz-Marzán, L.M., and Pecharromán, C., Drastic Surface Plasmon Mode Shifts in Gold Nanorods Due to Electron Charging. *Plasmonics* **2006,** *1* (1), 61-66.
10. Srinivasan, P.D., Nitz, S.R., Stephens, K.J., Atchison, E., and Bravo-Suárez, J.J., Modified Harrick reaction cell for in situ/operando fiber optics diffuse reflectance UV–visible spectroscopic characterization of catalysts. *Applied Catalysis A: General* **2018,** *561*, 7-18.
11. Aguilar-Guerrero, V. and Gates, B.C., Kinetics of CO Oxidation Catalyzed by Supported Gold: A Tabular Summary of the Literature. *Catalysis Letters* **2009,** *130* (1-2), 108-120.

Appendix C

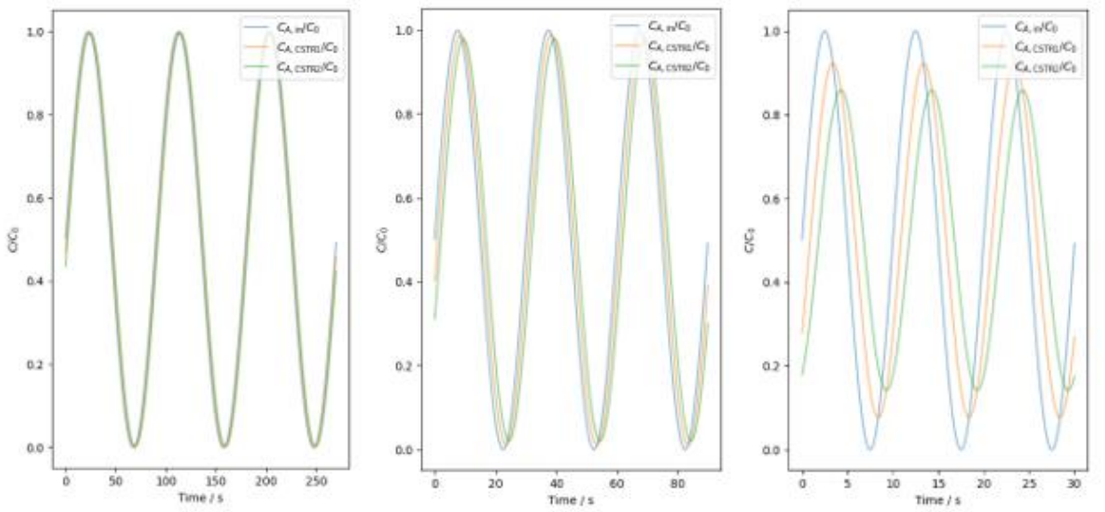

Figure C.1. Residence time distribution simulation of two CSTR reactors in series by inducing a sine waveform with a periodic concentration change in the feed with periods of: A) 90 s, B) 30 s, and C) 10 s. First reactor simulates a small void-volume reaction cell (τ_1 = 1 s) and the second simulates the mass spectrometer mixing chamber. Concentration exiting CSTR #1 = orange, solid line; concentration exiting CSTR #2 = black, dotted line. Conditions: (CSTR #1 average residence time) τ_1 = 1 s; (CSTR #2 average residence time) τ_2 = 1 s; (feed modulation low relative concentration) C_{low}/Co = 0; (feed modulation high relative concentration) C_{high}/Co = 1.

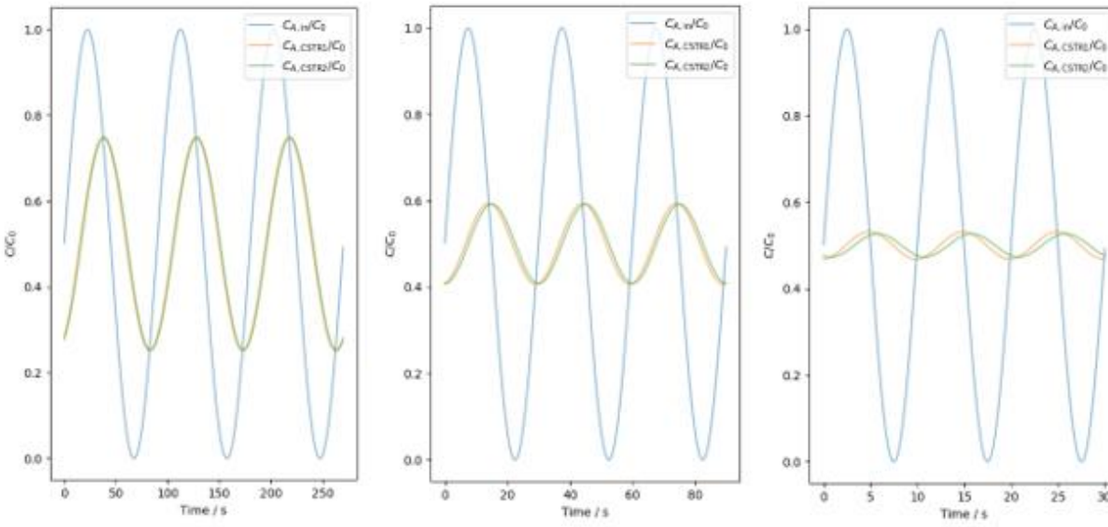

Figure C.2. Residence time distribution simulation of two CSTR reactors in series by inducing a sine waveform with a periodic concentration change in the feed with periods of: A) 90 s, B) 30 s, and C) 10 s. First reactor simulates a large void-volume reaction cell (τ_1 = 25 s) and the second simulates the mass spectrometer mixing chamber. Concentration exiting CSTR #1 = orange, solid line; concentration exiting CSTR #2 = black, dotted line. Conditions: (CSTR #1 average residence time) τ_1 = 25 s; (CSTR #2 average residence time) τ_2 = 1 s; (feed modulation low relative concentration) C_{low}/Co = 0; (feed modulation high relative concentration) C_{high}/Co = 1.

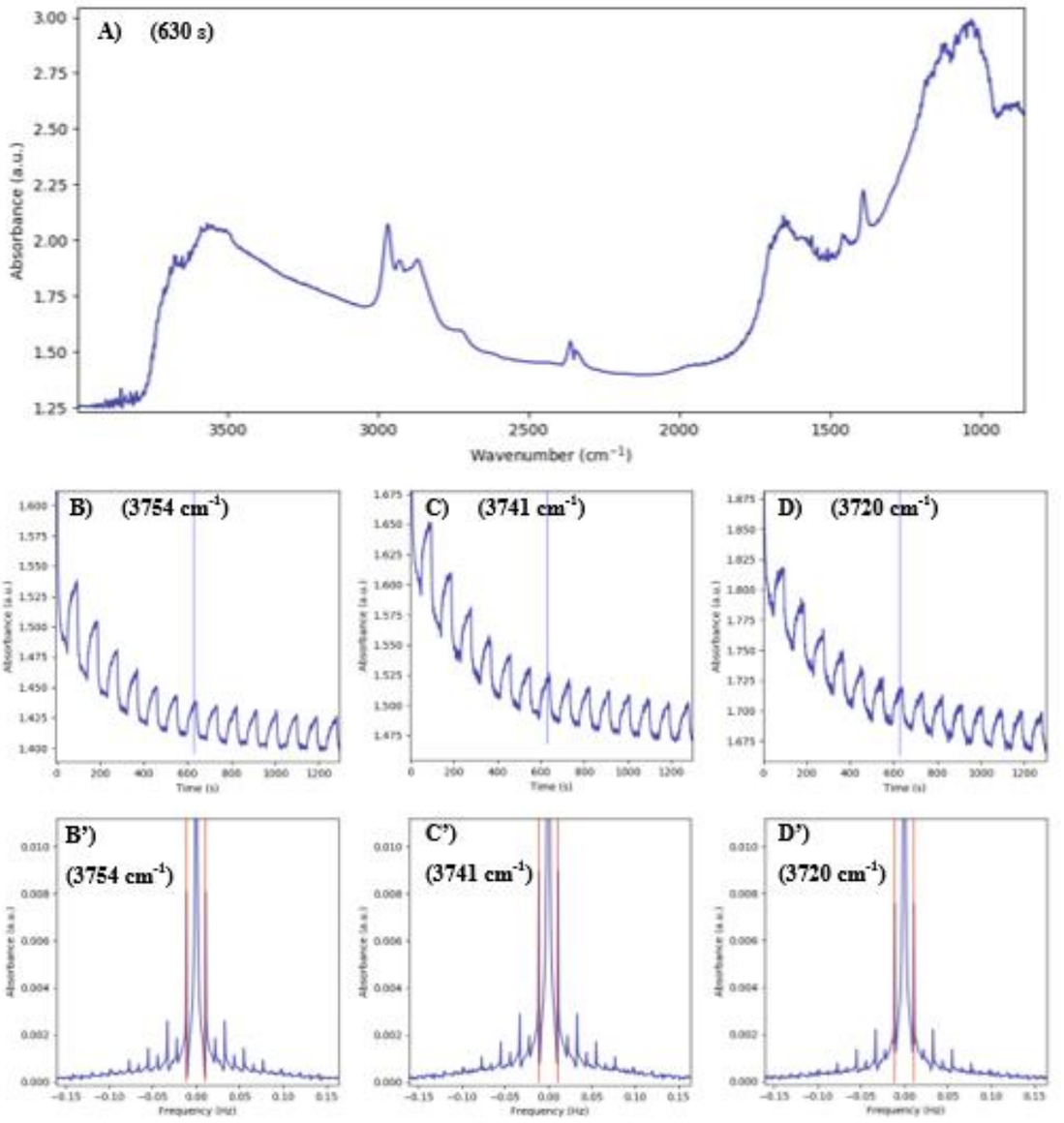

Figure C.3. In situ ME-PSD-DRIFTS spectra during ethanol conversion on γ-Al_2O_3. A) Time domain (TD) spectrum at 630 s; TD response at: B) 3754 cm^{-1}; C) 3741 cm^{-1}; D) 3720 cm^{-1} (blue line at 630 s); FD plot at 630 s and: B') 3754 cm^{-1}; C') 3741 cm^{-1}; D') 3720 cm^{-1} (red lines at $1f_0$). Conditions: 473 K, 101.3 kPa, feed modulation from He/Ar → He + EtOH (1 kPa), modulation frequency = 1/90 Hz (period = 90 s), total gas flow ~45 NTP cm^3/min, catalyst weight ~45 mg. Phase angle = (time in s/period in s)×360°.

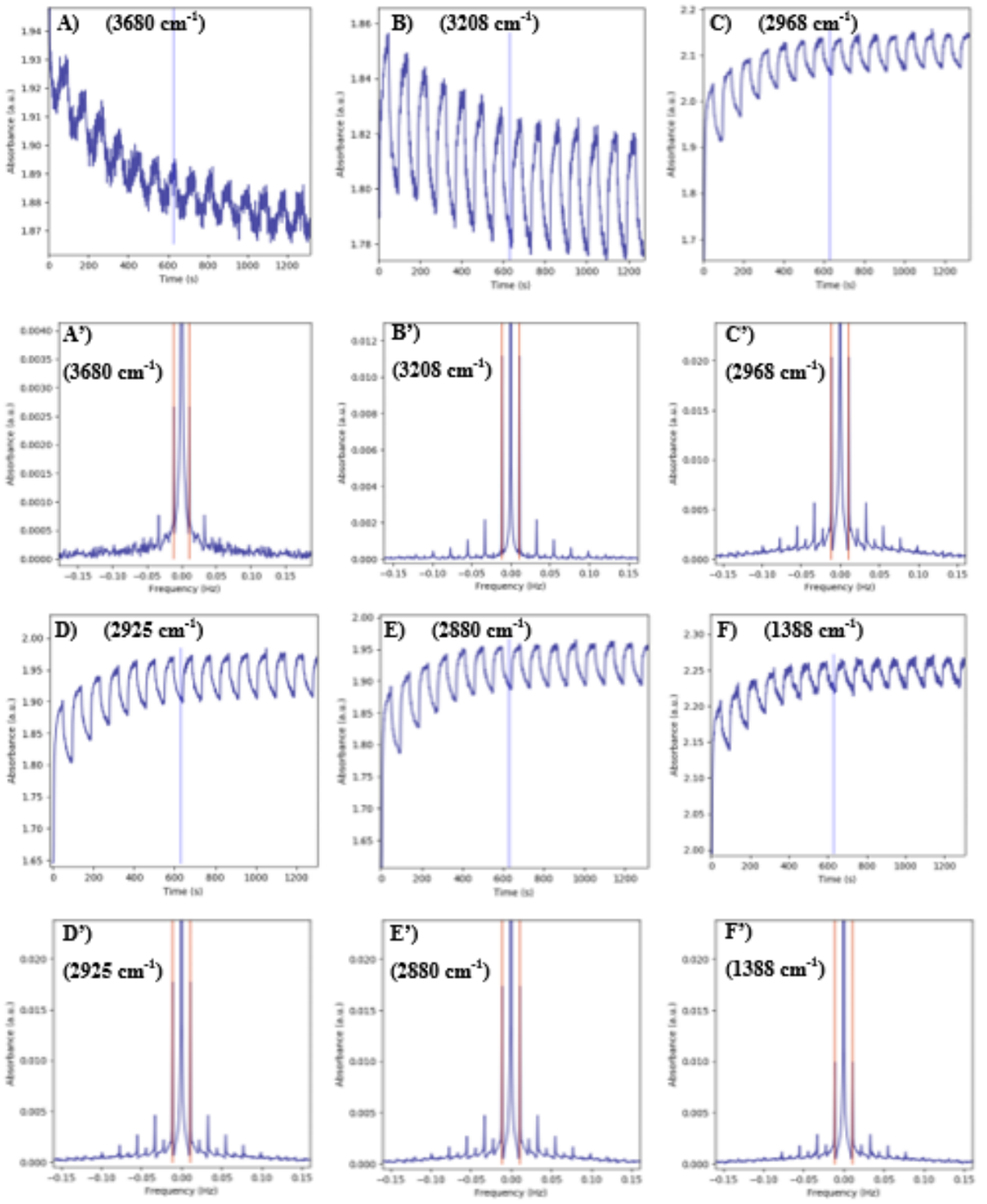

Figure C.4. In situ ME-PSD-DRIFTS spectra during ethanol conversion on γ-Al_2O_3. TD response at: A) 3680 cm^{-1}; B) 3208 cm^{-1}; C) 2968 cm^{-1}; D) 2925 cm^{-1}; E) 2880 cm^{-1}; F) 1388 cm^{-1} (blue line at 630 s); FD plot at 630 s and: A') 3680 cm^{-1}; B') 3208 cm^{-1}; C') 2968 cm^{-1}; D') 2925 cm^{-1}; E') 2880 cm^{-1}; F') 1388 cm^{-1} (red lines at $1f_0$); Conditions: same as in **Figure C.3.**

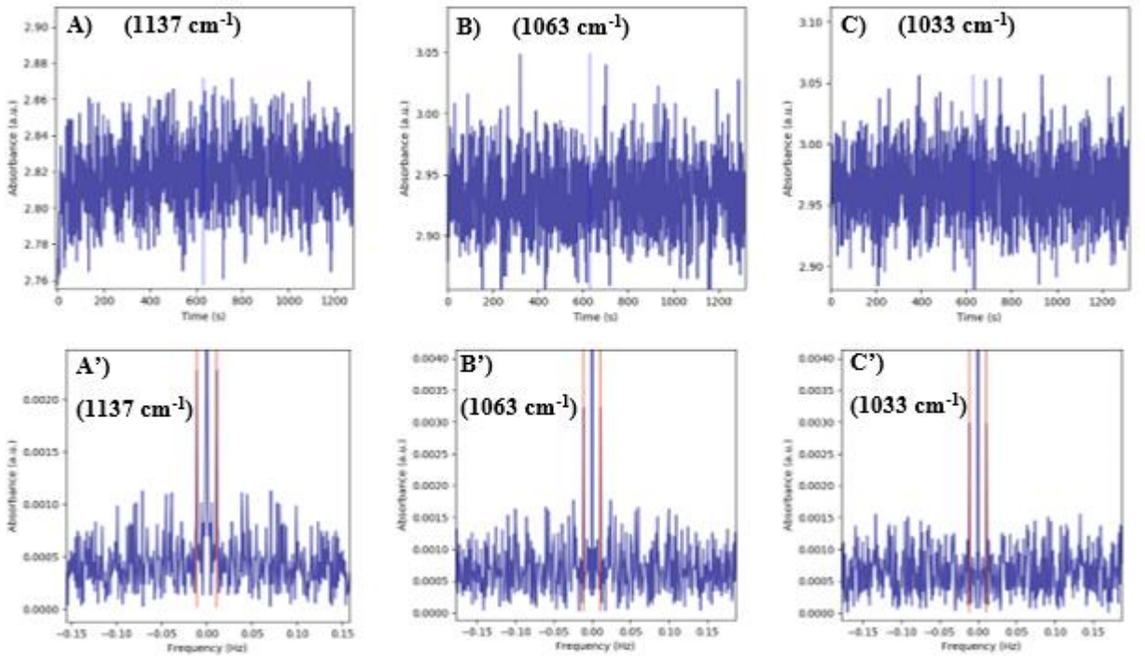

Figure C.5. In situ ME-PSD-DRIFTS spectra during ethanol conversion on γ-Al_2O_3. TD response at: A) 1137 cm^{-1}; B) 1063 cm^{-1}; C) 1033 cm^{-1} (blue line at 630 s); FD plot at 630 s for: A') 1137 cm^{-1}; B') 1063 cm^{-1}; C') 1033 cm^{-1} (red lines at $1f_0$); Conditions: same as in **Figure C.3.**

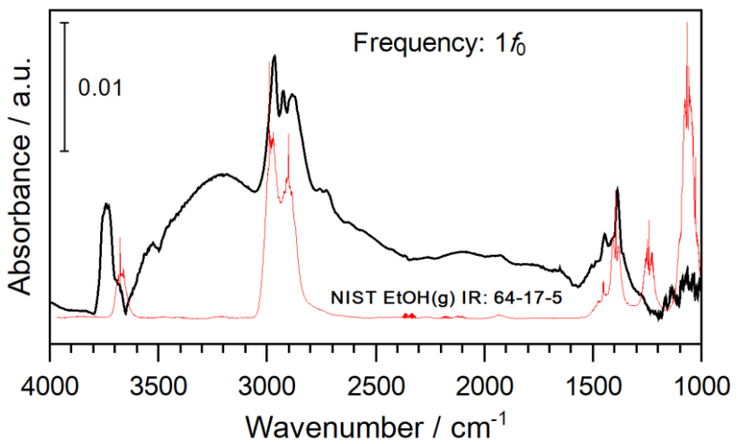

Figure C.6. Phase domain magnitude plot (showing all positive observed peaks) at a frequency of 0.011 Hz. Conditions: 473 K, 101.3 kPa, feed modulation from He/Ar → He + EtOH (1 kPa), modulation frequency = 1/90 Hz, total gas flow ~45 NTP cm^3/min, catalyst weight ~45 mg. Phase angle = (radians/2π)×360°. A scaled gas phase EtOH IR spectrum is shown for comparison to verify absence of EtOH gas phase contributions to the phase domain spectra.

C.1. Modelling of feed modulation and reaction cell frequency response in a two CSTR in series model (no reaction)

1. Fourier series for waveforms with fundamental angular frequency ω_0 and bounded by [−1, 1]:

Square wave

$$f(t) = \frac{4}{\pi}\sum_{k=1}^{\infty}\frac{\sin[(2k\text{-}1)\omega_0 t]}{2k\text{-}1} = \frac{2}{\pi i}\sum_{k=-\infty}^{\infty}\frac{\exp[i(2k\text{-}1)\omega_0 t]}{2k\text{-}1} \qquad \text{C1}$$

2. The transformation of each component in the Fourier series ($z_n \exp(i\omega_n t)$) through two CSTRs is performed individually in the *s*-domain via Laplace transform:

$$L\{z_n \exp(i\omega_n t)\} = \frac{z_n}{s\text{-}i\omega_n} \qquad \text{C2}$$

For a CSTR model:

$$\tau\frac{dc_{out}}{dt} = c_{in}\text{-}c_{out} \xrightarrow{L} \tau[sC_{out}\text{-}c_{out}(t=0)] = C_{in}\text{-}C_{out} \qquad \text{C3}$$

Its transfer function is:

$$T^L(s) = \frac{1}{1+\tau s} \qquad \text{C4}$$

Its initial condition is:

$$I^L(s) = \frac{\tau f_0}{1+\tau s} \qquad \text{C5}$$

The output components with angular frequency ω_n from the first and the second CSTRs are:

$$F_{n,1}^L(s) = \frac{z_n}{s\text{-}i\omega_n}\frac{1}{1+\tau_1 s} \qquad \text{C6}$$

$$F_{n,2}^L(s) = \frac{z_n}{s\text{-}i\omega_n}\frac{1}{1+\tau_1 s}\frac{1}{1+\tau_2 s} \qquad \text{C7}$$

Additional terms are generated from initial conditions:

$$F_{init,1}^L(s) = \frac{\tau_1 c_{init,1}}{1+\tau_1 s} \qquad \text{C8}$$

$$F_{init,2}^L(s) = \frac{\tau_1 c_{init,1}}{(1+\tau_1 s)(1+\tau_2 s)} + \frac{\tau_2 c_{init,2}}{1+\tau_2 s} \qquad \text{C9}$$

The inverse Laplace transforms of the expressions are:

$$f_{n,1}(t) = z_n\frac{\exp(i\omega_n t) - \exp\left(-\frac{t}{\tau_1}\right)}{1+i\omega_n\tau_1} \qquad \text{C10}$$

$$f_{n,2}(t) = \begin{cases} z_n\left[\dfrac{\exp(i\omega_n t) - \dfrac{t}{\tau_1}\exp\left(-\dfrac{t}{\tau_1}\right)}{(1+i\omega_n\tau_1)^2} - \dfrac{\exp\left(-\dfrac{t}{\tau_1}\right)}{1+i\omega_n\tau_1}\right], & \tau_1 = \tau_2; \\ z_n\left[\dfrac{\exp(i\omega_n t)}{(1+i\omega_n\tau_1)(1+i\omega_n\tau_2)} + \dfrac{\exp\left(-\dfrac{t}{\tau_1}\right)}{(\tau_2-\tau_1)(1+i\omega_n\tau_1)} + \dfrac{\exp\left(-\dfrac{t}{\tau_2}\right)}{(\tau_1-\tau_2)(1+i\omega_n\tau_2)}\right], & \tau_1 \neq \tau_2 \end{cases} \quad \text{C11}$$

$$f_{init,1}(t) = c_{init,1}\exp\left(-\frac{t}{\tau_1}\right) \quad \text{C12}$$

$$f_{init,2}(t) = \begin{cases} c_{init,1}\dfrac{t}{\tau_1}\exp\left(-\dfrac{t}{\tau_1}\right) + c_{init,2}\exp\left(-\dfrac{t}{\tau_2}\right), & \tau_1 = \tau_2; \\ \dfrac{c_{init,1}\tau_1}{\tau_1-\tau_2}\left[\exp\left(-\dfrac{t}{\tau_1}\right) - \exp\left(-\dfrac{t}{\tau_2}\right)\right] + c_{init,2}\exp\left(-\dfrac{t}{\tau_2}\right), & \tau_1 \neq \tau_2 \end{cases} \quad \text{C13}$$

3. Finally, applying the last four equations to any input with the Fourier series

$$f_{in}(t) = \sum_{n=0}^{N} z_n \exp(i\omega_n t) \quad \text{C14}$$

Assuming initial concentrations in the two CSTRs are $c_{init,i}$ $(i = 1,2)$, the outputs from the CSTRs are:

$$f_{out,i}(t) = f_{init,i}(t) + \sum_{n=0}^{N} f_{n,i}(t) \quad \text{C15}$$

Note that the exponential terms with the form $\exp\left(-\frac{t}{\tau_i}\right)$ decays to negligible level after the signals are periodic. Beyond $t = 5\max(\tau_1, \tau_2)$, the following approximations may be used $[\exp(-5) < 0.7\%]$

$$f_{n,1}(t) = z_n\frac{\exp(i\omega_n t)}{1+i\omega_n\tau_1} \quad \text{C16}$$

$$f_{n,2}(t) = z_n\frac{\exp(i\omega_n t)}{(1+i\omega_n\tau_1)(1+i\omega_n\tau_2)} \quad \text{C17}$$

$$f_{init,1}(t) = f_{init,2}(t) = 0 \quad \text{C18}$$

4. The following Fourier series are used to calculate the outputs from the CSTRs after the modulation is steady.

Square wave

$$f_{in}(t) = \frac{2}{\pi i}\sum_{k=-\infty}^{\infty}\frac{\exp[i(2k-1)\omega_f t]}{2k-1} \quad \text{C19}$$

$$f_1(t) = \frac{2}{\pi i} \sum_{k=-\infty}^{\infty} \frac{\exp[i(2k\text{-}1)\omega_f t]}{(2k\text{-}1)[1 + i(2k\text{-}1)\omega_f \tau_1]} \qquad \text{C20}$$

Type equation here.

$$f_2(t) = \frac{2}{\pi i} \sum_{k=-\infty}^{\infty} \frac{\exp[i(2k\text{-}1)\omega_f t]}{(2k\text{-}1)[1 + i(2k\text{-}1)\omega_f \tau_1][1 + i(2k\text{-}1)\omega_f \tau_2]} \qquad \text{C21}$$

Table C.1. Feed modulation forms and outputs in two CSTR in series model (no reaction), CSTR1=in situ cell, CSTR2=MS

Fourier Series Waveform	Initial outputs	Output from CSTR1	Output from CSTR2
Sine wave $f(t) = \sin(\omega_0 t)$ $= \frac{1}{2i}[\exp(i\omega_0 t) - \exp(-i\omega_0 t)]$	$f_{in}(t) = \frac{1}{2i}[\exp(i\omega_0 t) - \exp(-i\omega_0 t)]$	$f_1(t) = \frac{1}{2i}\left[\frac{\exp(i\omega_0 t)}{1 + i\omega_0\tau_1} - \frac{\exp(-i\omega_0 t)}{1 - i\omega_0\tau_1}\right]$	$f_2(t) = \frac{1}{2i}\left[\frac{\exp(i\omega_0 t)}{(1 + i\omega_0\tau_1)(1 + i\omega_0\tau_2)} - \frac{\exp(-i\omega_0 t)}{(1 - i\omega_0\tau_1)(1 - i\omega_0\tau_2)}\right]$
Cosine wave $f(t) = \cos(\omega_0 t)$ $= \frac{1}{2}[\exp(i\omega_0 t) + \exp(-i\omega_0 t)]$	$f_{in}(t) = \frac{1}{2}[\exp(i\omega_0 t) + \exp(-i\omega_0 t)]$	$f_1(t) = \frac{1}{2}\left[\frac{\exp(i\omega_0 t)}{1 + i\omega_0\tau_1} + \frac{\exp(-i\omega_0 t)}{1 - i\omega_0\tau_1}\right]$	$f_2(t) = \frac{1}{2}\left[\frac{\exp(i\omega_0 t)}{(1 + i\omega_0\tau_1)(1 + i\omega_0\tau_2)} + \frac{ex}{(1 - i\omega_0$
Square wave $f(t) = \frac{4}{\pi}\sum_{k=1}^{\infty}\frac{\sin[(2k-1)\omega_0 t]}{2k-1}$ $= \frac{2}{\pi i}\sum_{k=-\infty}^{\infty}\frac{\exp[i(2k-1)\omega_0 t]}{2k-1}$	$f_{in}(t) = \frac{2}{\pi i}\sum_{k=-\infty}^{\infty}\frac{\exp[i(2k-1)\omega_0 t]}{2k-1}$	$f_1(t)$ $= \frac{2}{\pi i}\sum_{k=-\infty}^{\infty}\frac{\exp[i(2k-1)\omega_0 t]}{(2k-1)[1 + i(2k-1)\omega_0\tau_1]}$	$f_2(t)$ $= \frac{2}{\pi i}\sum_{k=-\infty}^{\infty}\frac{\exp[i(2k-1)\omega_0 t]}{(2k-1)[1 + i(2k-1)\omega_0\tau_1][1 + i$
Sawtooth wave $f(t) = \frac{2}{\pi}\sum_{k=1}^{\infty}\frac{(-1)^{k+1}\sin(k\omega_0 t)}{k}$ $= \frac{1}{\pi i}\sum_{k=-\infty,k\neq 0}^{\infty}\frac{(-1)^{k+1}\exp(ik\omega_0 t)}{k}$	$f_{in}(t)$ $= \frac{1}{\pi i}\sum_{k=-\infty,k\neq 0}^{\infty}\frac{(-1)^{k+1}\exp(ik\omega_0 t)}{k}$	$f_1(t) = \frac{1}{\pi i}\sum_{k=-\infty}^{\infty}\frac{(-1)^{k+1}\exp(ik\omega_0 t)}{k(1 + ik\omega_0\tau_1)}$	$f_2(t) = \frac{1}{\pi i}\sum_{k=-\infty}^{\infty}\frac{(-1)^{k+1}\exp(ik\omega_0 t)}{k(1 + ik\omega_0\tau_1)(1 + ik\omega_0\tau_2)}$
Triangle wave $f(t)$ $= \frac{8}{\pi^2}\sum_{k=1}^{\infty}\frac{(-1)^{k+1}\sin[(2k-1)\omega_0 t]}{(2k-1)^2}$ $= \frac{4}{\pi^2 i}\sum_{k=-\infty}^{\infty}\frac{(-1)^{k+1}\exp[(2k-1)\omega_0 t]}{(2k-1)^2}$	$f_{in}(t)$ $= \frac{4}{\pi^2 i}\sum_{k=-\infty}^{\infty}\frac{(-1)^{k+1}\exp[(2k-1)\omega_0 t]}{(2k-1)^2}$	$f_1(t)$ $= \frac{4}{\pi^2 i}\sum_{k=-\infty}^{\infty}\frac{(-1)^{k+1}\exp[i(2k-1)\omega_0 t]}{(2k-1)^2[1 + i(2k-1)\omega_0\tau_1]}$	$f_2(t)$ $= \frac{4}{\pi^2 i}\sum_{k=-\infty}^{\infty}\frac{(-1)^{k+1}\exp[i(2k-1$ $(2k-1)^2[1 + i(2k-1)\omega_0\tau_1][1 -$

Appendix D

D.1. Strong Electrostatic Adsorption

The results of the cobalt uptake survey on γ-Al^{2}O$_3$ are shown in **Figure D.1**. The resulting plots show uptake of the hexaamminecobalt(III) cation (CoHA) at equilibrium pH above the point of zero charge of the support.[1, 2] This is due to deprotonation of surface hydroxyl groups, imparting a negative charge on the surface of the support and electrostatically attracting positively charged CoHA.[3, 4] As an amount of Co uptake is needed to give 0.3 wt% metal loading on the final catalyst, equilibrium pH values above 10.0 are enough to ensure strong interaction between the surface and precursor complex.

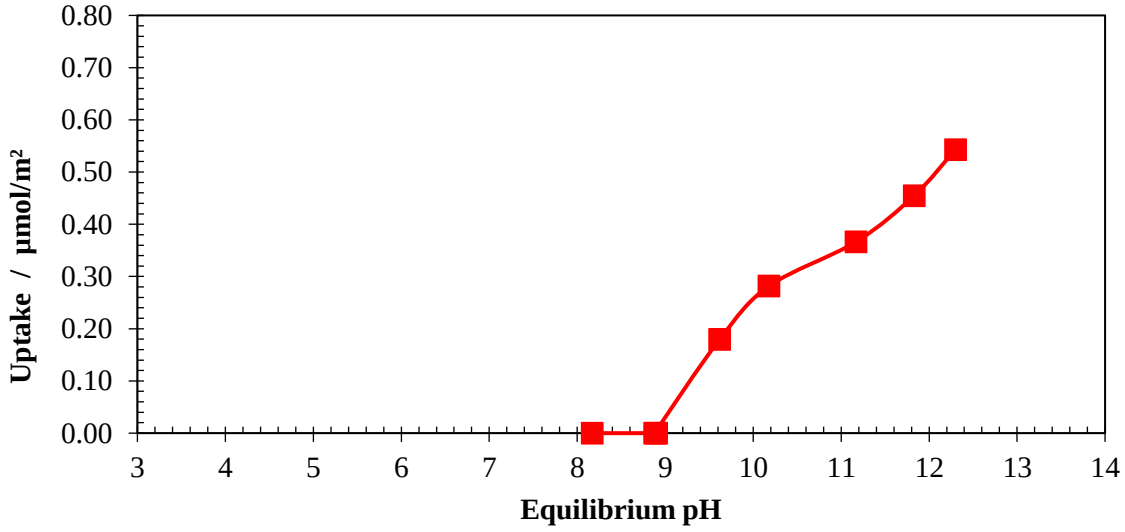

Figure D.1. SEA uptake survey of CoHA on γ-Al$_2$O$_3$ (SBa-200).

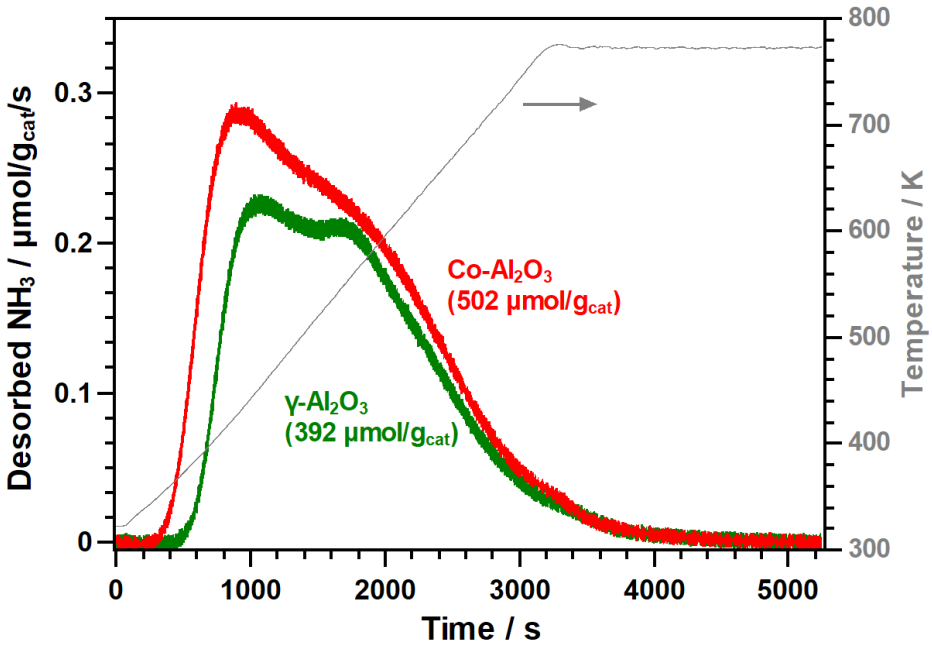

Figure D.2. Co-Al_2O_3 and γ-Al_2O_3 catalysts' acidity characterization by temperature programmed desorption of adsorbed ammonia (NH_3-TPD).

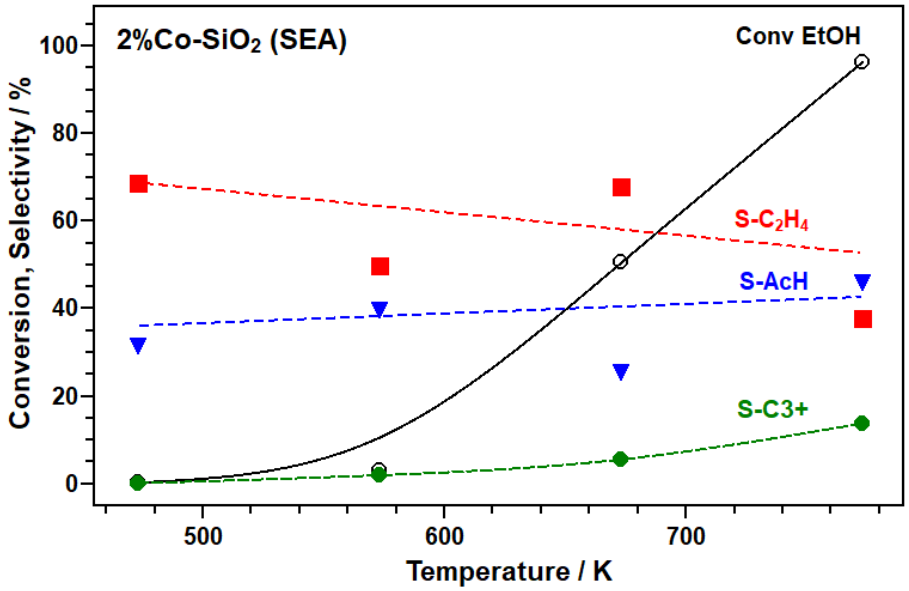

Figure D.3. 2%Co-SiO_2 (SEA) catalytic activity during ethanol dehydration at different temperatures. Conv = conversion; S = product selectivity; EtOH = ethanol; C_2H_4 = ethylene; AcH = acetaldehyde. Reaction conditions: He carrier flow = 80 NTP cm^3 min^{-1}; EtOH liquid flow = 120 µL h^{-1}; catalyst weight ≈ 75 mg. Total pressure = 101.3 kPa, EtOH partial pressure ≈ 1 kPa.

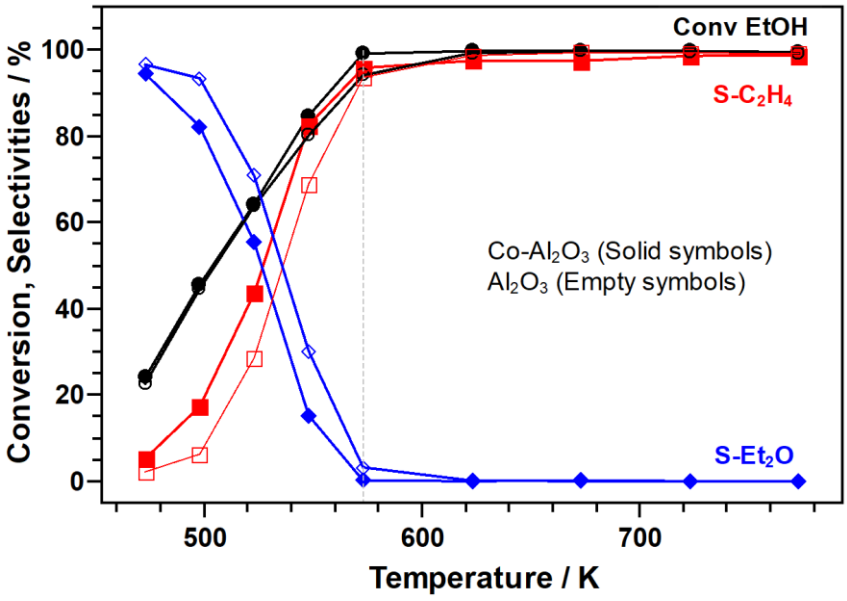

Figure D.4. γ-Al_2O_3 (empty symbols) and Co-Al_2O_3 (solid symbols) catalytic activity during ethanol dehydration at different temperatures. Conv = conversion; S = product selectivity; EtOH = ethanol; C_2H_4 = ethylene; Et_2O = diethyl ether. Reaction conditions: He carrier flow = 80 NTP cm^3 min^{-1}; EtOH liquid flow = 120 µL h^{-1}; catalyst weight ≈ 76 mg. Total pressure = 101.3 kPa, EtOH partial pressure ≈ 1 kPa.

D.2. FTIR Spectroscopy of Adsorbed CO.

A Nicolet Nexus 470 spectrometer equipped with a MCT-B detector cooled by liquid nitrogen was used to collect spectra with a resolution of 2 cm^{-1}, averaging 64 scans per spectrum. Each powder sample was pressed into a self-supported wafer with a density of approximately 20 mg/cm^2 and mounted in a home-made cell connected to a gas distribution manifold.

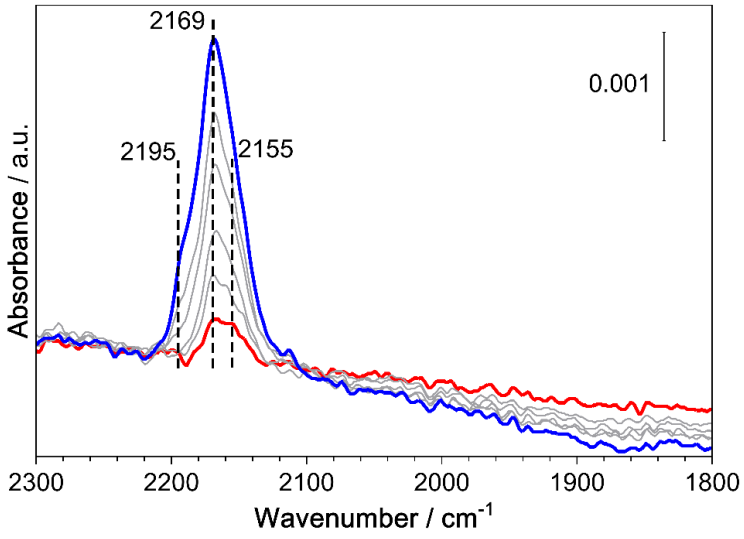

Figure D.5. FTIR spectra during CO pulses at 100 K on Co-Al_2O_3 catalyst. Three peaks are present at: 2195, 2169, and 2155 cm^{-1} indicating at least 3 types of Co(II) spcies on the surface of Co-Al_2O_3 catalyst.

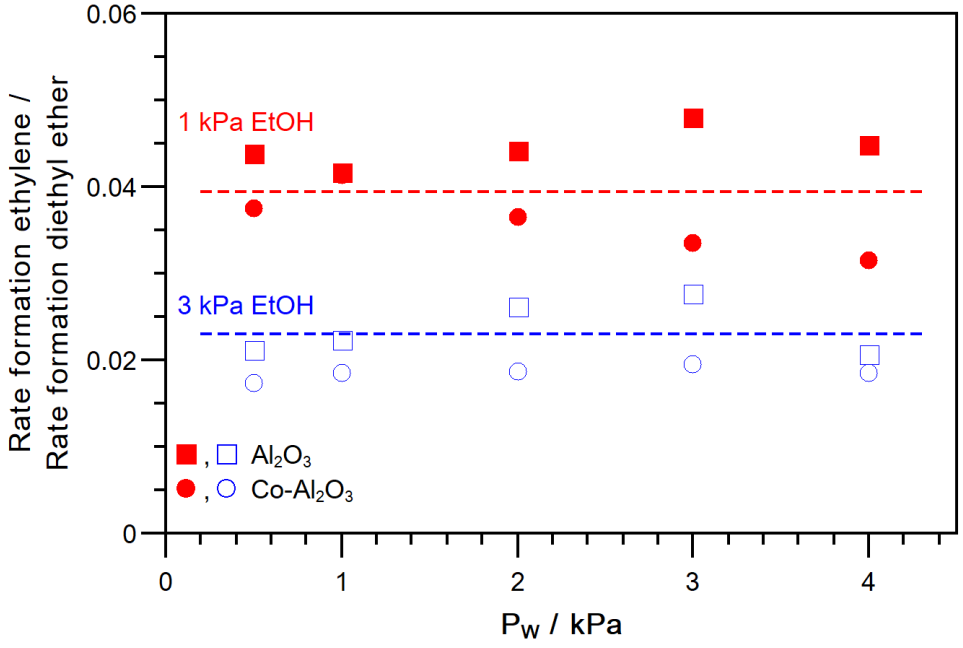

Figure D.6. γ-Al_2O_3 (empty symbols) and Co-Al_2O_3 (solid symbols) catalytic activity during ethanol dehydration at different temperatures. Conv = ethanol conversion; Sel or S = product selectivity; EtOH = ethanol; C_2H_4 = ethylene; Et_2O = diethyl ether. Reaction conditions: He carrier flow = 80 NTP cm^3 min^{-1}; EtOH liquid flow = 120 μL h^{-1}; catalyst weight ≈ 76 mg. Total pressure = 101.3 kPa, EtOH partial pressure ≈ 1 kPa.

Table D.1. In situ ME-PSD-DRIFTS during ethanol dehydration on Co-Al_2O_3 at 473 K: Peak position (left column) vs peak frequency magnitude (right column)

1481	ID: 04440
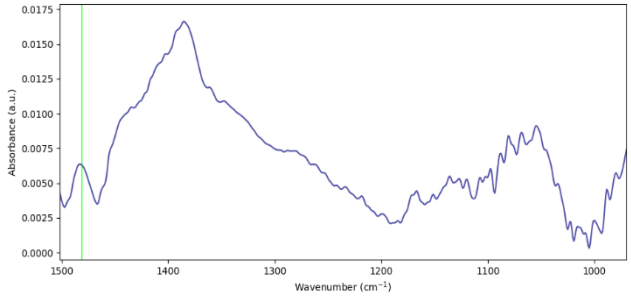	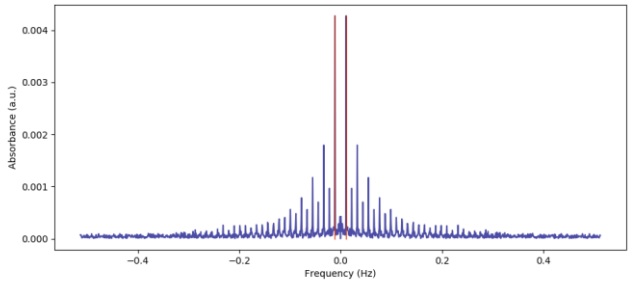
1388	
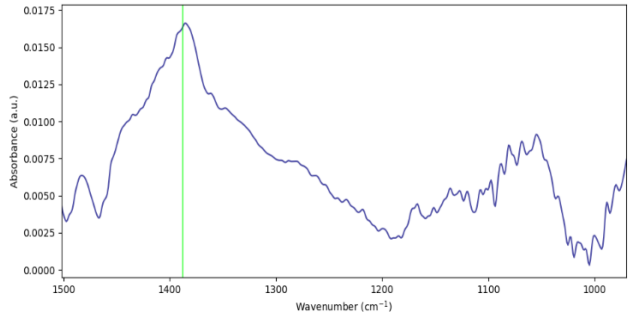	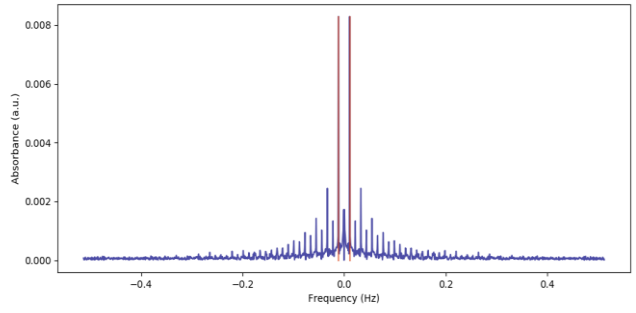
1280	
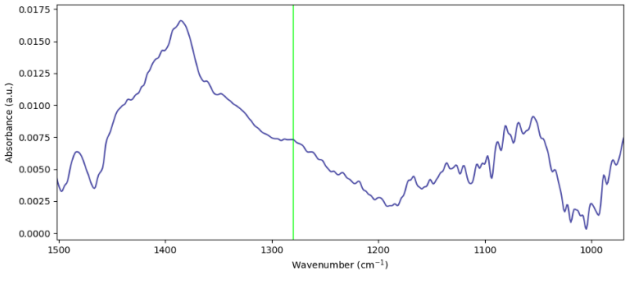	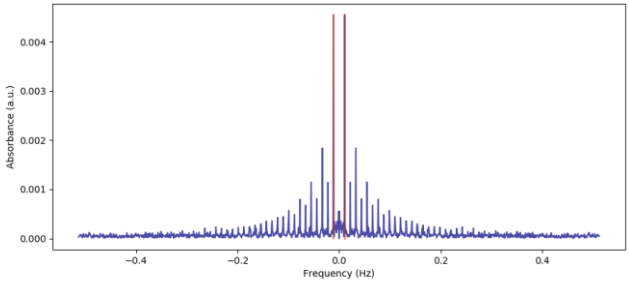
1131	

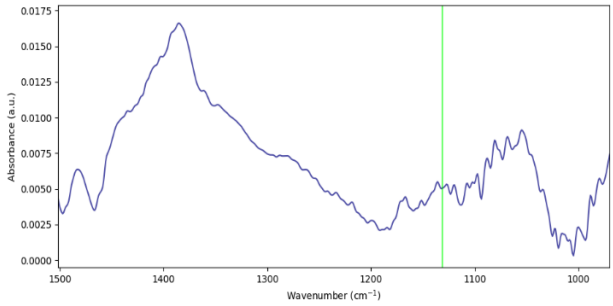	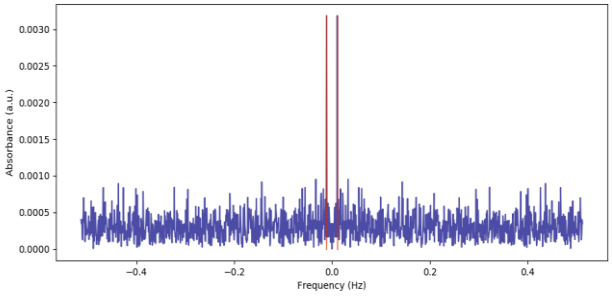
1053	
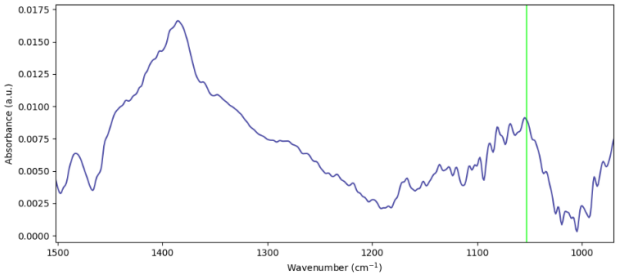	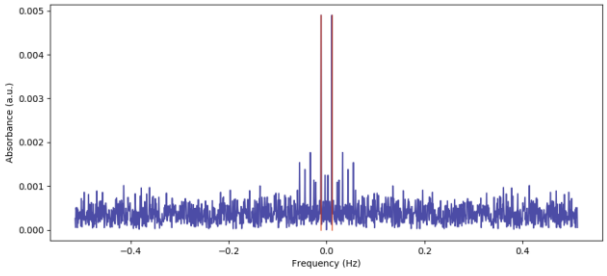

Table D.2. In situ ME-PSD-DRIFTS during ethanol dehydration on Al_2O_3 at 473 K: Peak position (left column) vs peak frequency magnitude (right column)

1448	ID: 04413
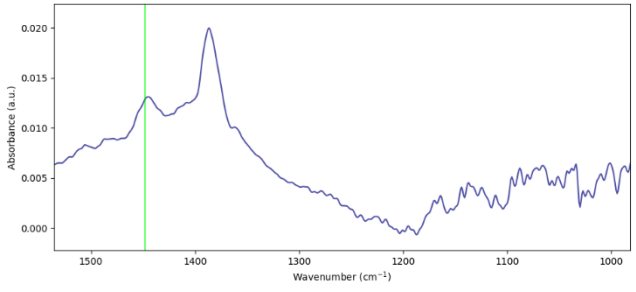	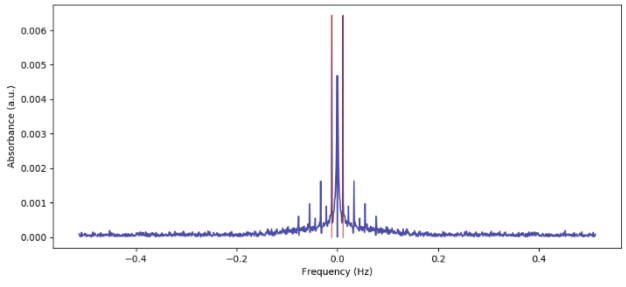
1388	

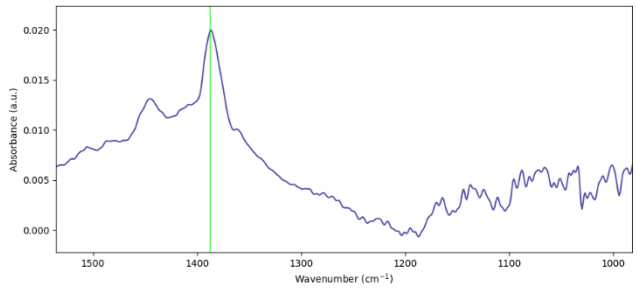	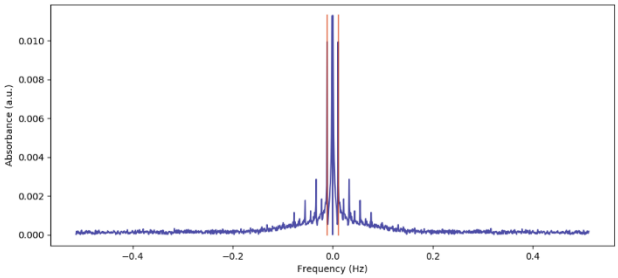
1280	
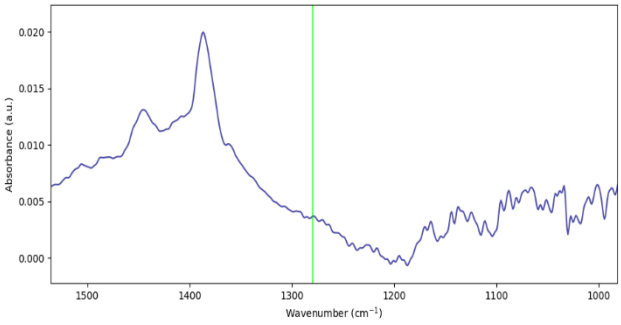	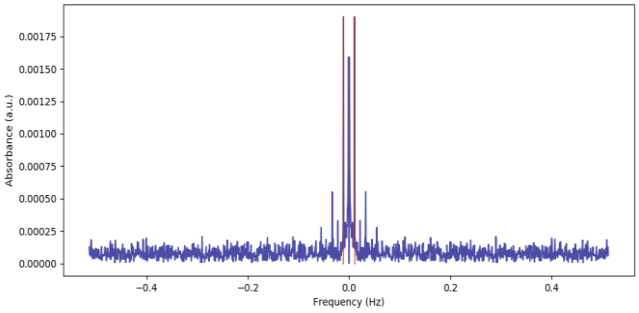
1137	
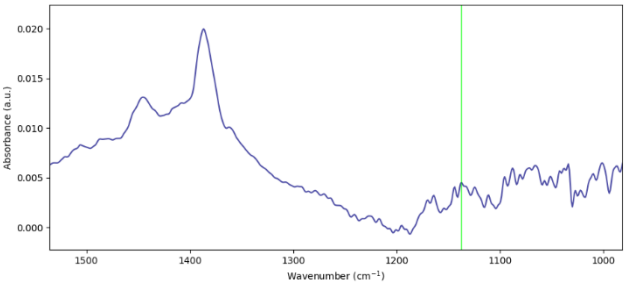	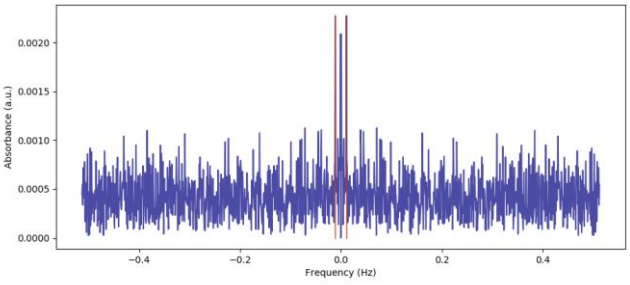
1063	

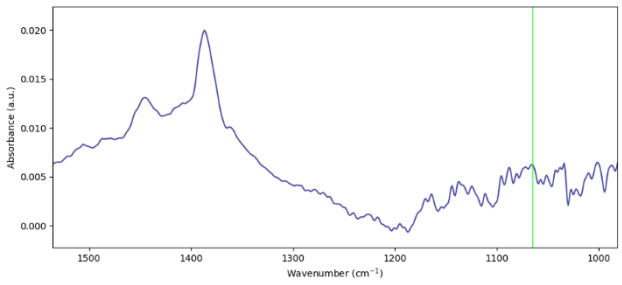	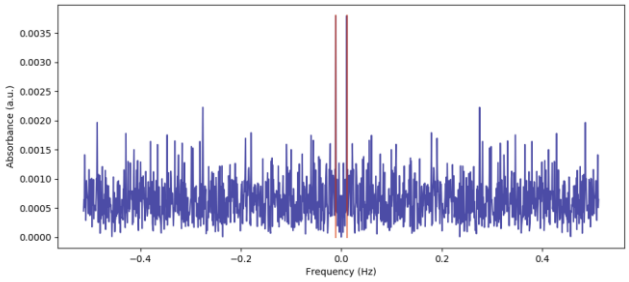
1033	
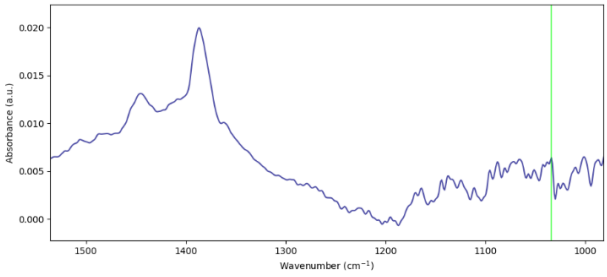	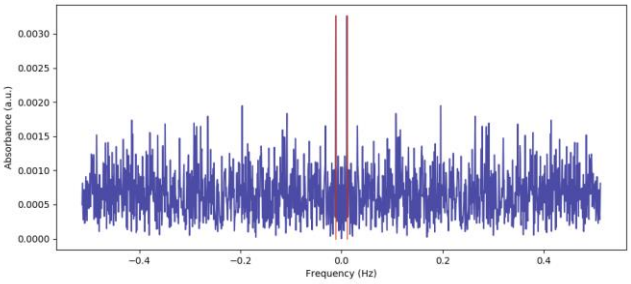

Table D.3. In situ ME-PSD-DRIFTS during ethanol dehydration on Co-Al_2O_3 at 543 K: Peak position (left column) vs peak frequency magnitude (right column)

1386	04441
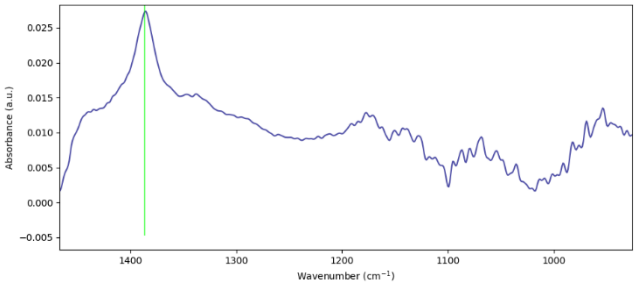	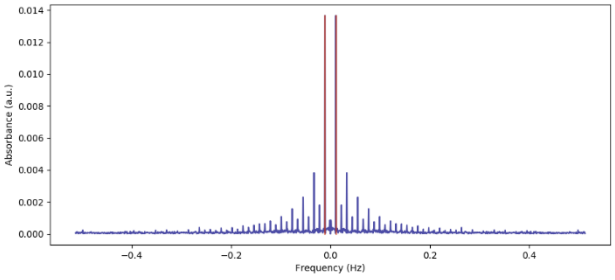
1334	

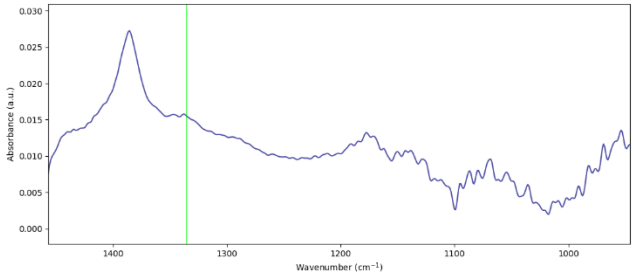	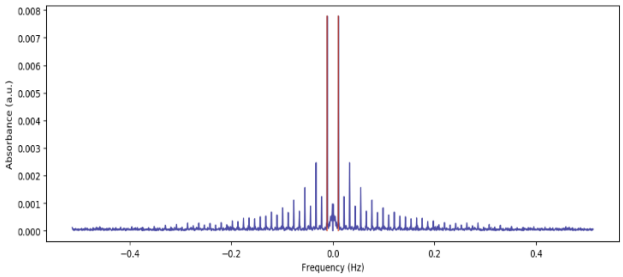
1289	
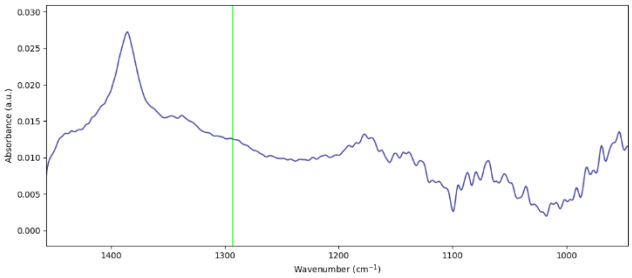	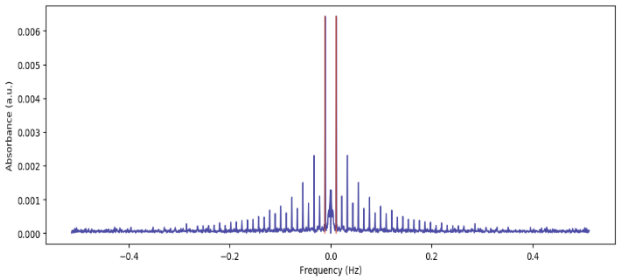
1176	
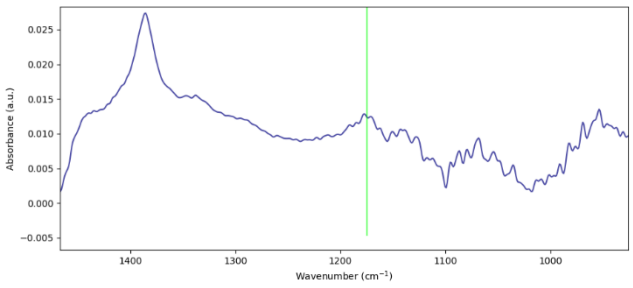	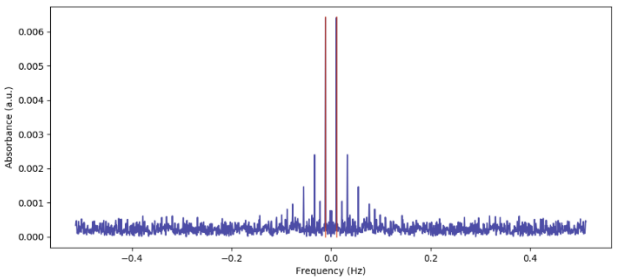
1140	
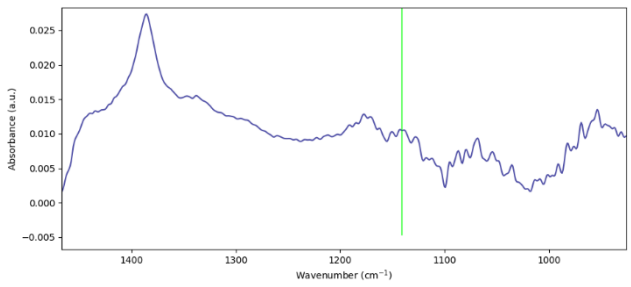	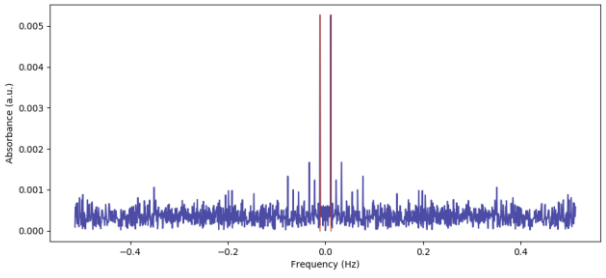
1068	

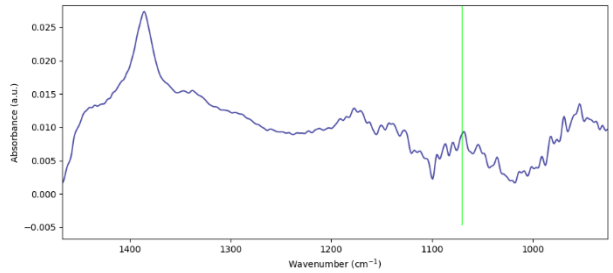	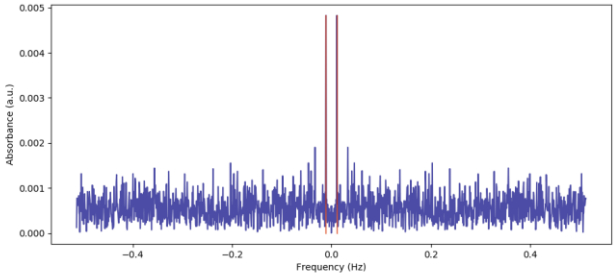
1035	
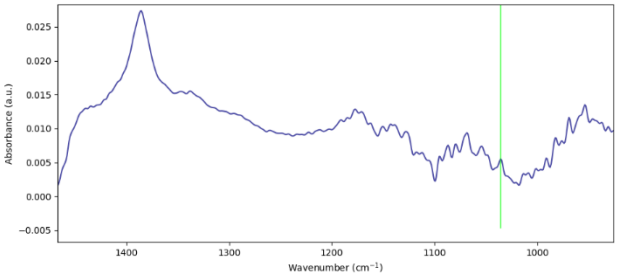	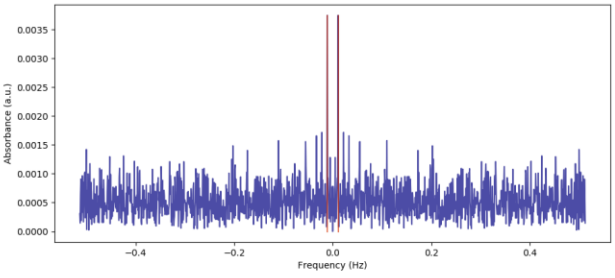

Table D.4. In situ ME-PSD-DRIFTS during ethanol dehydration on γ-Al_2O_3 at 543 K: Peak position (left column) vs peak frequency magnitude (right column)

1488	ID: 04414
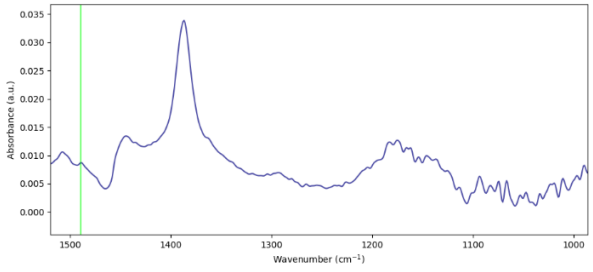	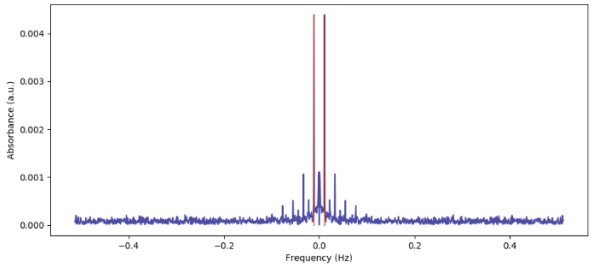
1445	

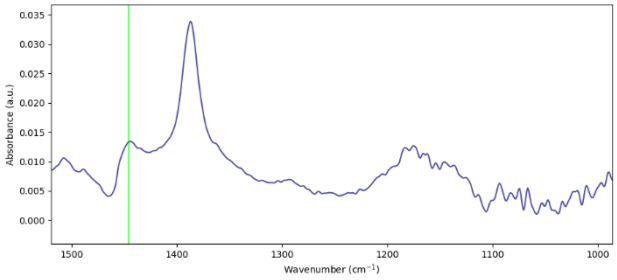	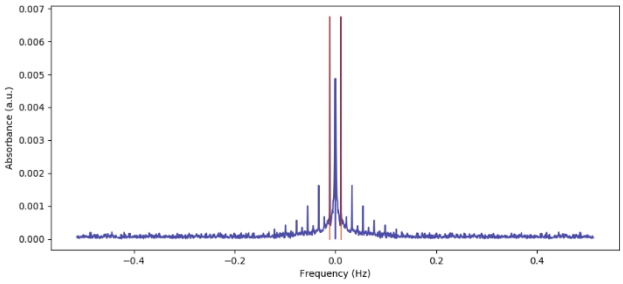
1386	
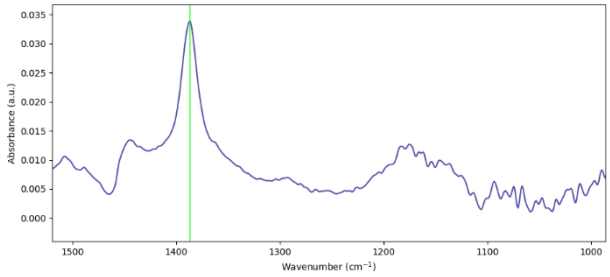	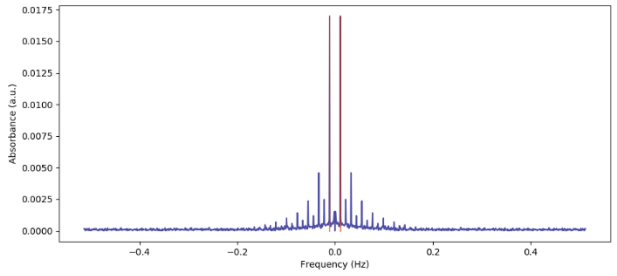
1293	
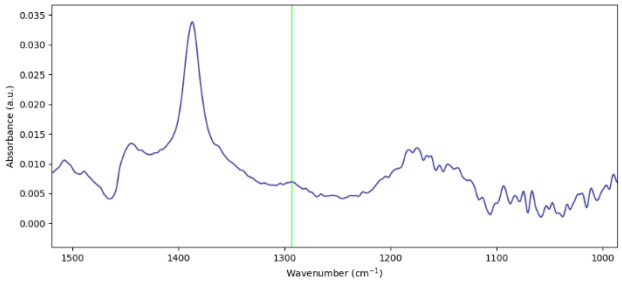	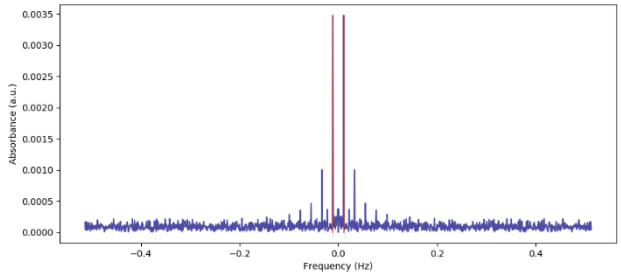
1144	
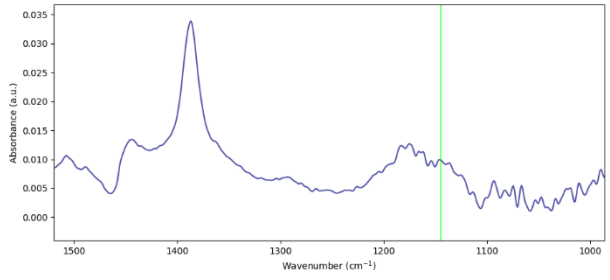	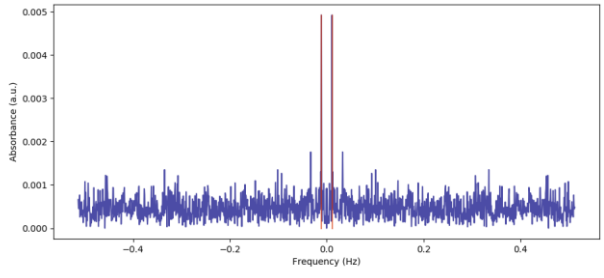
1065	

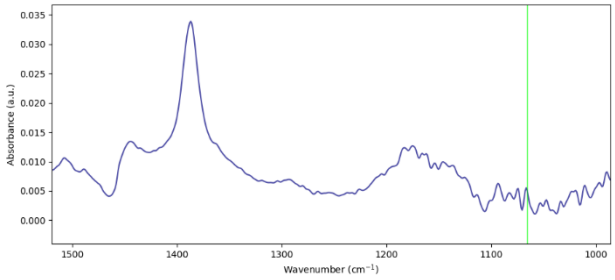	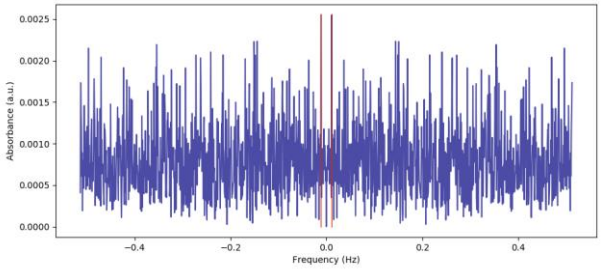
1024	
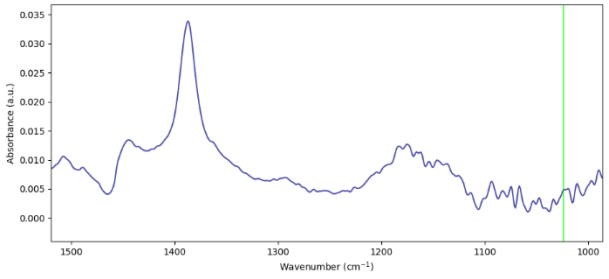	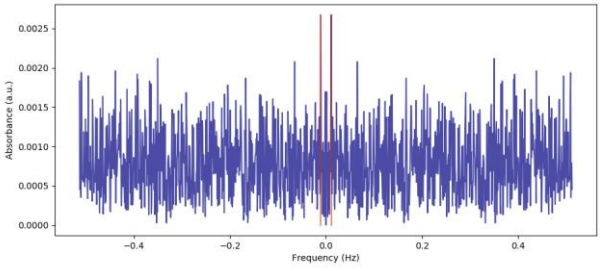

D.3. References

1. Liu, Q. Rational Synthesis of Catalysts for Biomass Conversion. Dissertation, University of South Carolina, Columbia, South Carolina, **2017**.
2. D'Souza, L., Jiao, L., Regalbuto, J.R., Miller, J.T., and Kropf, A.J., Preparation of silica- and carbon-supported cobalt by electrostatic adsorption of Co(III) hexaammines. *Journal of Catalysis* **2007,** *248* (2), 165-174.
3. Regalbuto, J.R., Strong Electrostatic Adsorption of Metals onto Catalyst Supports. In *Catalyst Preparation: Science and Engineering*, J.R. Regalbuto, Ed. Taylor and Francis/CRC Press: **2007;** pp 297-318.
4. D'Souza, L. and Regalbuto, J.R., Strong electrostatic adsorption for the preparation of Pt/Co/C and Pd/Co/C bimetallic electrocatalysts. In *Studies in Surface Science and Catalysis*, M.D.S.H.P.A.J.J.A.M. E.M. Gaigneaux and Ruiz, P., Eds. Elsevier: **2010;** Vol. Volume 175, pp 715-718.

Publications

1. Bravo-Suárez, J.J.; **Srinivasan**, **P.D**. Design Characteristics of in Situ and Operando UV-Visible and Vibrational Spectroscopic Reaction Cells for Heterogeneous Catalysis, ***Catal. Rev.- Sci. Eng***., **2017**, 1–151, DOI: 110.1080/01614940.01612017.01360071
2. **Srinivasan, P.D**.; Nitz, S.R.; Stephens, K.J.; Atchison, E.; Bravo-Suárez, J.J. Modified Harrick Reaction Cell for in situ/Operando Fiber Optics Diffuse Reflectance UV–Visible Spectroscopic Characterization of Catalysts. ***Appl. Catal., A.***, **2018**, 561, 7-18.
3. Patil, B.S.; **Srinivasan, P.D**.; Zhu, H.; Atchison, E.; Bravo-Suárez, J.J. Design, Modeling and Applications of a Low Void-Volume in Situ Diffuse Reflectance Spectroscopic Reaction Cell for Transient Catalytic Studies ***React. Chem. Eng***., **2019**, DOI: 10.1039/C8RE00302E
4. Medina, J.C.; Figueroa, M.; Manrique, R.; Rodriguez-Pereira, J.; **Srinivasan, P.D**.; Bravo-Suárez, J.J.; Baldovino Medrano, V.G.; Jimenez, R.; Karelovic, A. Catalytic consequences of Ga promotion on Cu for CO_2 hydrogenation to methanol ***Catal. Sci. & Technol*****. 2017**, 7, 3375-3387.
5. **Srinivasan, P.D**.; Patil, B.S.; Zhu, H.; Bravo-Suárez, J.J. Application of Modulation Excitation - Phase Sensitive Detection -DRIFTS for in Situ/Operando Characterization of Heterogeneous Catalysts (***React. Chem. Eng***. *Accepted **2019***)
6. **Srinivasan, P.D**.; Khivantsev, K.; Tengco, J.; Zhu, H.; Bravo-Suárez, J.J. Enhanced Ethanol Conversion to Ethylene on Supported Single Site Co Catalysts (***J***. ***Catal***. *Accepted **2019***)

Presentations

1. **Srinivasan, P.D**.; Khivantsev, K.; Tengco, J.; Zhu, H.; Bravo-Suárez, J.J. "ME-PSD-DRIFTS Studies of Single Site Cobalt Supported on Alumina Catalysts for Ethanol Dehydration Reaction" 2019 GPCS Annual Meeting in Bartlesville, OK, April 12, 2019.
2. **Srinivasan, P.D.**; Zhu, H.; Bravo Suárez, J.J. "Enhanced Ethanol Conversion to Ethylene on Supported Single Site Co Catalysts" 256th ACS National Meeting, Boston, MA, Aug 19-23, 2018

3. **Srinivasan, P.D.**; Zhu, H.; Bravo Suárez, J.J. "Spectroscopic Elucidation of the Nature and Strength of Catalysts Acid Sites in the Conversion of Ethanol" Gordon Research Conference, New London, NH, June 24-29, 2018
4. Bravo-Suárez, J.J.; **Srinivasan**, **P.D**. ″In Situ/Operando Reaction Cells: Limitations and Opportunities in the UV-Vis and IR Characterization of Catalysts″ 2018 AIChE Annual Meeting in Pittsburgh, PA. Oct 28 - Nov 2, 2018
5. **Srinivasan, P.D.**; Bravo-Suárez, J.J. "Novel Reaction Cell Design for Simultaneous in Situ Diffuse Reflectance UV-Vis and FTIR Spectroscopies: Application to CO Oxidation on Gold Catalysts" ACS Midwest Regional Meeting, Lawrence, KS, Oct 20, 2017.
6. **Srinivasan, P.D**.; Ramirez, M.; Bravo-Suárez, J.J. "In Situ FTIR studies of Ethanol Conversion on Zr-KIT-5 and Zr-KIT-6 Catalysts" 2017 AIChE Annual Meeting in Minneapolis, MN.
7. **Srinivasan, P.D**.; Bravo-Suárez, J.J. "In Situ Au Plasmon Resonance UV-Vis Spectroscopy as a tool for prediction of Catalytic Activity" 25th North American Catalysis Society meeting, Denver, CO, 2017
8. **Srinivasan, P.D.;** Bravo-Suárez, J.J.; "In Situ UV-Vis Diffuse Reflectance Spectroscopy for Characterization of Gold-Metal Oxide Interactions" 252nd ACS National Meeting, Philadelphia, PA, Aug 21-25, 2016
9. **Srinivasan, P.D.;** Ofosu, T.; Ho, S.; Ramirez, M.; Bravo-Suárez, J.J.; "In Situ & Operando UV-Vis and FTIR Spectroscopies for Understanding Catalyst Active Sites" Gordon Research Conference, New London, NH, June 12-17, 2016
10. **Srinivasan, P.D.**; Bravo-Suárez, J.J. "Improved Design of a Commercial Diffuse Reflectance Reactor for In Situ Ultraviolet-Visible Spectroscopy Studies", 251st ACS National Meeting, San Diego, CA, Mar 13-17, 2016

Copyright permissions

Copyright Clearance Center RightsLink®

Home | Account Info | Help

Title:	Design characteristics of in situ and operando ultraviolet-visible and vibrational spectroscopic reaction cells for heterogeneous catalysis
Author:	Juan J. Bravo-Suárez, , , et al
Publication:	Catalysis Reviews
Publisher:	Taylor & Francis
Date:	Sep 25, 2017

Logged in as:
PRIYA DARSHINI SRINIVASAN
Account #:
3001058524
LOGOUT

Rights managed by Taylor & Francis

Thesis/Dissertation Reuse Request

Taylor & Francis is pleased to offer reuses of its content for a thesis or dissertation free of charge contingent on resubmission of permission request if work is published.

Copyright Clearance Center RightsLink®

Home | Account Info | Help

Title:	Modified Harrick reaction cell for in situ/operando fiber optics diffuse reflectance UV–visible spectroscopic characterization of catalysts
Author:	Priya D. Srinivasan,Steven R. Nitz,Kyle J. Stephens,Ed Atchison,Juan J. Bravo-Suarez
Publication:	Applied Catalysis A: General
Publisher:	Elsevier
Date:	5 July 2018

Logged in as:
PRIYA DARSHINI SRINIVASAN
Account #:
3001058524
LOGOUT

© 2018 Elsevier B.V. All rights reserved.

Please note that, as the author of this Elsevier article, you retain the right to include it in a thesis or dissertation, provided it is not published commercially. Permission is not required, but please ensure that you reference the journal as the original source. For more information on this and on your other retained rights, please visit: https://www.elsevier.com/about/our-business/policies/copyright#Author-rights

Application of modulation excitation-phase sensitive detection-DRIFTS for *in situ*/operando characterization of heterogeneous catalysts

P. D. Srinivasan, B. S. Patil, H. Zhu and J. J. Bravo-Suárez, *React. Chem. Eng.*, 2019, Advance Article , **DOI:** 10.1039/C9RE00011A

If you are not the author of this article and you wish to reproduce material from it in a third party non-RSC publication you must formally request permission using Copyright Clearance Center. Go to our Instructions for using Copyright Clearance Center page for details.

Authors contributing to RSC publications (journal articles, books or book chapters) do not need to formally request permission to reproduce material contained in this article provided that the correct acknowledgement is given with the reproduced material.

.

.

If you are the author of this article you do not need to formally request permission to reproduce figures, diagrams etc. contained in this article in third party publications or in a thesis or dissertation provided that the correct acknowledgement is given with the reproduced material.

.

.

If you are the author of this article you still need to obtain permission to reproduce the whole article in a third party publication with the exception of reproduction of the whole article in a thesis or dissertation.

.

.

Information about reproducing material from RSC articles with different licences is available on our Permission Requests page.

Copyright Clearance Center RightsLink®

Home | Create Account | Help

Title: Enhanced ethanol dehydration on γ-Al2O3 supported cobalt catalyst

Author: Priya D. Srinivasan,Konstantin Khivantsev,John Meynard M. Tengco,Hongda Zhu,Juan J. Bravo-Suárez

Publication: Journal of Catalysis

Publisher: Elsevier

Date: May 2019

© 2019 Elsevier Inc. All rights reserved.

LOGIN

If you're a copyright.com user, you can login to RightsLink using your copyright.com credentials.

Already a RightsLink user or want to learn more?

Please note that, as the author of this Elsevier article, you retain the right to include it in a thesis or dissertation, provided it is not published commercially. Permission is not required, but please ensure that you reference the journal as the original source. For more information on this and on your other retained rights, please visit: https://www.elsevier.com/about/our-business/policies/copyright#Author-rights